MATERIAL AND STRUCTURAL ENHANCEMENTS TO SPIN TRANSFER PHENOMENA IN NANOPILLAR SPIN-VALVE DEVICES

A Dissertation

Presented to the Faculty of the Graduate School

of Cornell University

in Partial Fulfillment of the Requirements for the Degree of

Doctor of Philosophy

by

Patrick M. Braganca

January 2009

MATERIAL AND STRUCTURAL ENHANCEMENTS TO SPIN TRANSFER PHENOMENA IN NANOPILLAR SPIN-VALVE DEVICES

Patrick M. Braganca, Ph.D.

Cornell University 2009

This thesis focuses on work performed to fabricate spin valve nanopillar devices with low spin transfer reversal currents suitable for magnetic memory applications. Fabricating nanopillars into small area ellipses with low saturation magnetization ferromagnets is shown to be an effective strategy for reducing reversal currents while maintaining the thermal stability of the nanomagnet. Pulsed current switching experiments performed on devices with a 4.5 nm thick permalloy free layer show switching current amplitudes ranging from 0.4 mA for a 100 ns pulse to 2 mA for a 1 ns pulse.

I have also examined the role that micromagnetic effects can play in spin transfer reversal processes. Using micromagnetic simulations, a spatially non-uniform spin current with a component polarized partially out of the plane is shown to enhance the spin-torque efficiency acting upon a reversing nanomagnet. I verified this enhancement experimentally in devices with a tapered nanopillar geometry that generates a spin current polarized partially out of plane.

The micromagnetic configurations induced in these tapered nanopillars are also conducive to exciting spin torque driven magnetization oscillations in the absence of an external magnetic field. In addition, by using a small hard axis field the frequencies of oscillations excited in both layers can be tuned such that phase locking occurs between the free and reference layer mediated by spin polarized currents interacting between the layers. This locking phenomenon is characterized

by measured RF voltage signals with large integrated powers and extremely narrow linewidth on the order of 1 HZ.

Finally, I have described a fabrication process for patterning a nanopillar structure with a third contact made to any point within a thin-film multilayer stack, providing the means to apply independent electrical biases to two separate parts of the structure. Here, I have demonstrated a joint magnetic spin valve/tunnel junction structure sharing a common free layer nanomagnet contacted by this third electrode. This three-terminal structure provides a strategy for developing spin-torque magnetic random access memory (ST-RAM) cells which avoids the need to apply large voltages across a magnetic tunnel junction during the writing step, while retaining the benefits of a high-impedance magnetic tunnel junction for read-out.

BIOGRAPHICAL SKETCH

Patrick M. Braganca was born July 8, 1978 to Patricio and Maria Braganca in Somerville, NJ. As a young child, he dreamed of two possible career paths, either traveling the world as a paleontologist, digging up dinosaur fossils, or as an astronomer gazing at the stars and planets. Over time, these aspirations led to an interest in the sciences and in understanding the physical world that persists to this day. He spent his childhood growing up in Somerville, eventually attending Somerville High School, where he past the time pursuing his multiple interests in music (playing a mean drum) and science. On graduating high school, he was accepted to the honors program at Rutgers University in New Brunswick, NJ. Early in his time there, he made the critical decision to focus on studying physics, and eventually graduated with High Honors in 2001. At that point, it was off to Cornell to begin his graduate work in the Applied and Engineering Department, where he hoped to really make a difference in improving technological applications. After joining Robert Buhrman's group, he went through the usual trials and tribulations associated with graduate school, receiving his M.S. in 2005 and his Ph.D. in 2008. He looks forward to his future challenges as a postdoctoral researcher at Hitachi Global Storage Technologies and will continue to strive to explore magnetic systems with an eye towards potential applications.

"You who find this, I charge you to carry on my work"

— The Punisher's War Journal

ACKNOWLEDGEMENTS

No one person can hope to function in graduate school without the assistance and guidance of a larger community. I am honored and blessed to have gotten a chance to interact with these special people on a daily basis, and have become a better scientist because of it.

First of all, I would like to thank my advisor Robert Buhrman, for giving me the freedom to explore the various avenues of nanomagnetics that I have ventured into. Bob has been a valuable resource to me both personally and professionally, and his insights into my experimental results have shaped my concept of approaching and analyzing a physical problem. I am truly grateful for the time and effort that Bob has spent in guiding my career, and feel grateful that I was able to learn from him in my time at Cornell. I would also like to thank the other members of my special committee, Dan Ralph and Bruce Van Dover. Dan's emphasis on clear and precise explanations of our results has influenced my approach to reporting the concepts involved in our experiments, and has improved the quality of more than one of my publications. I was also lucky enough to learn concepts of magnetism and other electric and optical properties from Bruce in my time at Cornell, and I couldn't have had a better advisor for my minor emphasis.

Whether I was repairing a turbopump, shooting the breeze at CNF, or discussing the behavior of the device I just measured, the other members of the Buhrman group have always been there with support and advice. In particular, I would like to thank Ilya Krivorotov for being a tremendous resource to me in my early days with the group, especially in helping me to find a project that would evolve into much of what is covered in this thesis. Ilya's intelligence, inquisitive nature, and kindness of heart are truly inspirational, and have motivated me to be better as a scientist and a person. He has since moved onto the faculty of the

University of California - Irvine and I look forward to seeing great things from him both now and in the future. I must also especially thank Andrew Perrella, my big brother in lab and out, who was always there to lend me a hand whenever I needed it. Many a night I spent talking about life, work, and everything in between with Andrew over a beer, or dinner with him and his wonderful wife Fern. In 2006, Andrew passed away due to complications from cancer, and although I am deeply saddened by the loss of one of my best friends, I do not regret the opportunity I was given to get to know, for however brief, one of the most sincere people I have ever met. Last, but certainly not least, I would like to thank John Read, my fellow coworker, collaborator, and housemate, who has put up with my shenanigans for the last 4 years. John is a brilliant scientist who has been a tremendous springboard for many of my crazy ideas, and I hope that I have been able to fill that role for him as well. I have also enjoyed sitting around our house and discussing all manner of non-physics related topics, from religion, to philosophy, and even sports. I would also be remiss to not thank John for bringing his cat Lola into my life, who has been my furry bundle of joy. Even on the darkest of days, Lola has been a bright spot for me, and I owe a great debt to her and John for that.

Other members of the group who deserve special thanks are Ozhan Ozatay and Nathan Emley. Ozhan and I collaborated often in his time here, and he was a great help to me in both fabrication of devices and analysis of my experimental results. He was also a valuable lunch and dinner companion on most days, and could procure much better tea than I could ever hope to find. I look forward to once again working with Ozhan in my next incarnation as a postdoctoral researcher at Hitachi GST. Nathan acted as my mentor when I started with the group, and I appreciate the freedom he gave me in finding solutions to the problems he set before me. From Nathan, I acquired a strong sense of how to approach a problem

in nanofabrication and develop a process for patterning a device. These skills have served me well continuing to this day, so I am eternally indebted to Nathan for them. I also must thank him for his initial work in patterning three terminal devices, which sparked my curiosity in the project and led to the discuss in chapter 7. Other members of the group I would like to thank include Phil Mather, who's eternal optimism was contagious, Eileen Tan, who always kept me laughing, Eric Ryan, and Greg Fuchs. I thank both Vlad Pribiag and Oukjae Lee for their assistance with both macrospin and micromagnetic simulations, without which much of my analysis would not be possible. Finally, for the younger students that I have not had a chance to interact much with, namely Praveen Gowtham, Luqiuo Liu, Hsinwei Tseng, and Yun Li, I thank them for continuing the legacy that myself and the students before me contributed to, and I wish them the best of luck in their future endeavors. From the Ralph group, I would like to thank Jack Sankey and Sergei Kiselev. Both of these fine fellows brought a sense of fun to the pursuit of knowledge that we all undertake, and although they were unconventional, they were definitely appreciated. I also thank Kiran Thandani for useful conversations on hard axis field dynamics, from which we were able to build a picture of the phenomena discussed in Chapter 6.

The three terminal device discussed in Chapter 7 would never have moved past a concept on a sheet of paper without the effort and ingenuity of Jordan Katine and Hitachi GST. I thank him for his insights and contributions to that project and look forward to working with him in my time at HGST. Also, I must thank Jeff Childress and Daniele Mauri for contributing to the project by depositing the complicated multilayer structures involved in the device. Phil Rice and Eugene Delenia from IBM Almaden were extremely helpful in the TEM microscopy of the device, and for that I am extremely grateful. With respect to fabrication, I would

also like to thank the wonderful staff of the CNF, especially Rob Ilic, Alan Bleier, and John Triechler, who were all extremely helpful with the e-beam processing I developed for low I_c nanopillars.

To conclude, I would like to express my appreciation for my parents Patricio and Maria Braganca, who have always been supportive of me and have pushed me to be the best I can be in everything that I do, helping me to become the person I am today.

TABLE OF CONTENTS

LIST OF TABLES

LIST OF FIGURES

CHAPTER 1

INTRODUCTION

The advent of spin based electronic devices, or spintronic devices as they are more commonly known, represents a significant advancement in present day technologies. Whether these spintronic devices operate using a coupling of electron spin and charge, or simply using the spin alone, they incorporate several enhancements over conventional charge-based semiconductor electronics, such as fast processing speeds, nonvolatile data storage, higher integration density, and decreased power consumption [1]. Many of these devices are still in an early stage of development, offering significant opportunities for studying both the basic physics governing device performance and engineering considerations with materials and device configurations. These opportunities are most clearly illustrated by considering the evolution of the computer hard drive read head. Beginning in 1956 [2], IBM introduced the first hard disk drive, which utilized an inductive coil similar to those in tape recorders, to perform both read and write processes on magnetic storage media. With the pioneering discovery of the giant magnetoresistance (GMR) effect [3, 4] in 1988, development of thin film read heads occurred fairly rapidly, leading to the commercial introduction of GMR read heads in 1996. This advance in read head technology more than doubled the annual growth rate of storage density from 25% to more than 60% per year [2, 5] (see Fig. 1). More recently, investigations of tunneling magnetoresistance [6] have led to the development of magnetic tunnel junction (MTJ) devices incorporating an insulating Al_2O_3 or MgO tunnel barrier sandwiched between two metallic ferromagnetic electrodes. MTJs have not only maintained the growth rate in storage density required by the recording industry [7], but contributed to the commercial release of magnetic random access memory (MRAM) by Freescale Semiconductors [8]. These examples

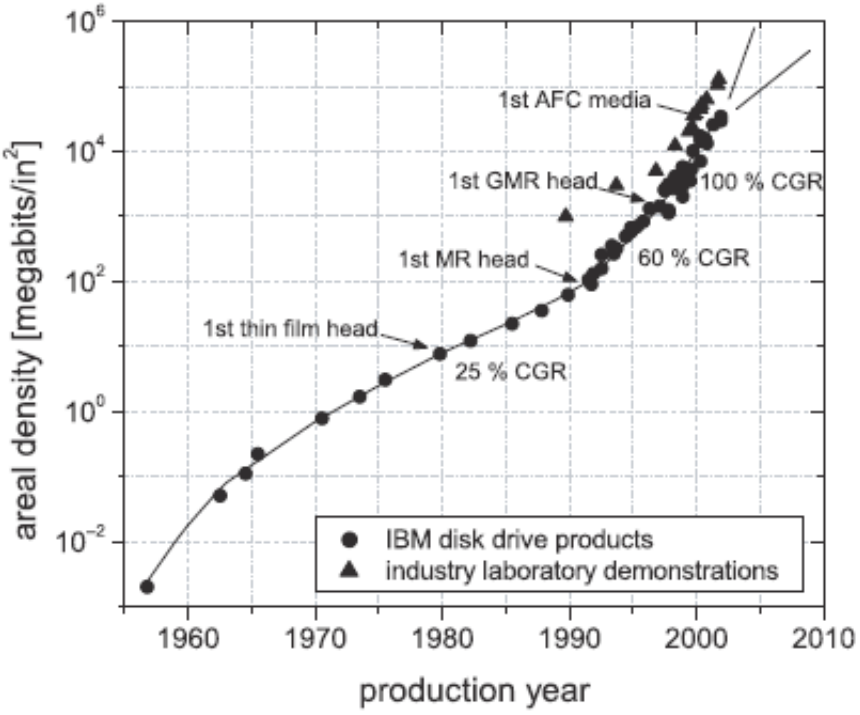

Figure 1.1: Hard disk areal density vs. production year. Advances in read head technology driven by research in nanomagnetics, such as GMR, have led to large increases in the annual growth rate. Figure taken from [2].

serve to illustrate the impact basic physics research in nanomagnetics has had on driving technology and on society as a whole, a fact recently acknowledged by the awarding of the 2008 Nobel Prize in physics to Fert and Grunberg for the discovery of GMR.

Magnetotransport effects are made possible due to Zeeman splitting of the majority and minority spin bands in ferromagnets. This splitting leads to an imbalance of spin states at the ferromagnet's Fermi level, causing the magnet to act as a spin filter, which can be exploited to generate spin polarized currents. Spin filtering leads to spin dependent transmission probabilities for electrons impinging upon the ferromagnet, an effect which is the underlying mechanism for GMR, where the resistance of a magnetic device is dependent on the orientation of a

ferromagnet's moment. More recently, it was shown that a spin polarized current could be used to excite a dynamic response of a ferromagnet's moment through an exchange of spin angular momentum from the current into the magnet, an effect known as spin transfer [9]. Interest in spin transfer has exploded in the past 5 years, due opportunities in both exploring basic physics and developing new spintronic technologies. Here, I describe spin transfer studies geared mainly towards designing low switching current systems for possible MRAM applications.

In chapter 2, I begin with a description of how spin dependent band structure in ferromagnetic metals results in magnetotransport effects such as those mentioned above. These phenomena are the basis for spintronic devices such as hard disk read heads, and continue to spawn proposals for future devices and technologies. I will review currently established technologies, such as the aforementioned read heads, and discuss opportunities in both memory and communication applications made possible through the use of spin transfer. A discussion of alternative spintronic technologies involving the use of semiconductors will be included, where semiconductors are an attractive option for application since they should integrate well into current CMOS technologies and eliminate magnetic noise mechanisms intrinsic to ferromagnetic systems. Finally, possible directions for future spin transfer and spintronic device applications will be explored.

The creation of new spintronic devices requires an integrated approach of fabrication and characterization, repeated iteratively until completion. As such, the importance of a proper understanding of the principles of nanofabrication cannot be understated. Chapter 3 includes a discussion of the various fabrication contributions I have made to the group during my term at Cornell. Several different nanomagnetic systems have been used to study spin transfer effects, such as point

contacts [10, 11], but here I will focus on nanopillar structures consisting of a ferromagnet/Cu/ferromagnet trilayer, a system commonly called a spin valve. My first significant contribution involved developing electron beam lithography procedures geared towards producing very small area, high aspect area elliptical patterns for the purpose of fabricating low critical current spin valve nanopillars for the high speed magnetization reversal experiments discussed in Chapter 4. I will comment on both pattern design and exposure considerations for obtaining these extremely useful types of shapes. Additionally, I dedicated a significant amount of time characterizing properties of hydrogen silsesquioxane (HSQ), a spin-on glass that can be used as both a negative tone electron beam resist and a self-planarizing insulating layer. I will present results indicating that the low sensitivity of HSQ makes it particularly suited for patterning complicated nanostructures with small tolerances in spacing between features. To conclude, I will outline a nanopillar process using HSQ to replace PECVD deposited silicon oxide as an insulating layer. By its self-planarizing properties, HSQ removes the necessity for ion mill planarizing steps required in our current nanofabrication process.

Chapter 4 deals with the development of spin valve nanopillars with low spin transfer reversal currents. By using theoretical calculations of the expected critical currents, we developed a simple strategy for designing these type of devices utilizing low saturation magnetization M_s nanomagnets patterned into small area shapes. Possible applications for these devices also require that the reversing ferromagnet maintain a certain level of thermal stability, which was accommodated by designing these patterns with large aspect ratios. Experiments using DC and pulsed currents indicate that thermal effects can play a significant role in assisting magnetization reversal for time scales above ~ 10 ns. A NiFe alloy is shown to be a particularly effective material for these applications, as the magnetization for this material

minimizes I_c while providing a significant energy barrier U_A required for thermal stability. Macrospin simulation fits to pulse reversal results gives us additional insights into the physics governing spin transfer reversal in these systems.

As chapter 4 discusses spin transfer reversal in a macrospin picture, chapter 5 approaches reversal in a micromagnetic regime, where the magnetization of the nanomagnet is not constrained to be spatially uniform. Here, I discuss a tapered nanopillar structure in which curling of the reference layer magnetization results in a spatially nonuniform spin current polarized partially out of plane interacting with the free layer. Spin transfer reversal using in-plane and out-of-plane polarized currents is explored using macrospin simulations and compared to micromagnetic simulations of this tapered nanopillar, indicating that this nonuniform spin current is effective in increasing spin transfer efficiency and decreasing reversal currents. Experimental results in devices tapered due to shadowing effects during ion mill definition verify this enhancement in reversal efficiency, as well as a beneficial effect on spin accumulation in the devices which leads to increased symmetry in the reversal currents for switching the free layer from antiparallel to parallel with respect to the reference layer (AP-P) or (P-AP). Finally, I will propose a design for a three magnetic layer device similar to that proposed by Greg Fuchs [12], which micromagnetic simulations indicate could be an enabling device for magnetic memory applications.

Chapter 6 concentrates on persistent magnetization dynamics excited within the tapered nanopillar described in chapter 5. GMR oscillations induced by the magnetization dynamics have potential uses as on-chip oscillators for a variety of applications, such as communications or radar. For these applications, excitation of the magnetization in zero or small magnetic fields is an extremely desirable char-

acteristic, however, typical spin transfer devices examined in a macrospin picture require large ($> .1$ T) fields to excite dynamics. There are micromagnetic states that lend themselves to small field oscillations, as recently illustrated in vortex oscillators [13, 14]. The reference layer in these tapered nanopillars orients itself into one of these states, as both experimental and micromagnetic results indicate. Here, oscillations occur within the reference layer with small ($< .02$ T) fields along the easy axis of the nanomagnet, resulting in frequencies between 5.5 and 6.5 GHz, which are much larger than those shown previously in vortex oscillators.

Other important parameters for oscillator applications include the integrated power and linewidth of the output. Application of a hard axis field across a tapered nanopillar is shown to produce extremely high power signals, with linewidths down to 2 MHz, approaching theoretical predictions [15]. This serendipitous effect occurs due to an ideal ratio of anisotropies between the two ferromagnets, leading to phase locking between the oscillating moments of both layers for a range of currents and hard axis fields. This locking effect precludes the existence of other modes, which would act to broaden the linewidth due to transitions between modes, otherwise know as mode hopping. In addition, application of a hard axis field promotes an extremely large angle oscillation of the magnetization, which serves to provide the large integrated power and further ensure narrow linewidths. These phenomena are explored with micromagnetic simulations and a strategy for designing high power, narrow linewidth oscillations by means of spin transfer oscillations is presented, which ideally could be incorporated into magnetic tunnel junction devices to maximize output power.

Chapter 7 picks up on the previous work of Nathan Emley [16], who examined the concept of fabricating a three terminal spin transfer device capable of integrat-

ing an all metallic spin valve and a MTJ. Such a structure would eliminate wear out issues common to repeated spin transfer writing in tunnel junctions while retaining the large TMR signals from the MTJ during readout. Here, I take a different approach than Nathan, incorporating the more commonly used transmission mode of spin transfer rather than reflection mode. A subtractive fabrication process involving several aligned electron beam lithography steps is outlined. Micromagnetic simulations show that reversal occurs by nucleation of a reversal domain followed by sweeping a domain wall across the free layer. This indicates that angular momentum transferred at the interface of the free layer is more effective than exchange pressure exerted by current flowing laterally through the free layer, which would lead to a large asymmetry in reversal currents. Devices fabricated at Hitachi Global Storage Technologies verify these simulation results, and indicate that in fact, this device can be controllably fabricated to allow detection of magnetization reversal by current flowing through the spin valve to be detected by the MTJ. Although these devices still require further device refinement to optimize device performance, these results are encouraging, and show that a three terminal device could be effectively fabricated and utilized in memory applications.

Finally, I conclude my dissertation in chapter 8 with a summary of the important aspects of device design and fabrication discussed within. Additionally, I will comment on the implications of my results and possible avenues for further research involving micromagnetic studies and fabrication of new nanomagnetic systems.

REFERENCES

[1] Wolf S.A., Awschalom D.D., Buhrman R.A., Daughton J.M., von Molnár S., Roukes M.L., Chtchelkanova A.Y., & Treger D.M., Spintronics: A spin-based electronics vision for the future, *Science* **294**, 1488 (2001).

[2] Moser A., Takano K., Margulies D.T., Albrecht M., Sonobe Y., Ikeda Y., Sun S., & Fullerton E.E, Magnetic recording: advancing into the future, *J. Phys. D: Appl. Phys.* **35**, R157 (2002).

[3] Baibich M.N., Broto J.M., Fert A., Van Dau F.N., Petroff F., Eitenne P., Creuzet G., Friederich A., & Chazelas J., Giant magnetoresistance of (001)Fe/(001)Cr magnetic superlattices, *Phys. Rev. Lett.* **61**, 2472 (1988).

[4] Binasch, G., Grünberg, P., Saurenbach, F. & Zinn, W., Enhanced magnetoresistance in layered magnetic structures with antiferromagnetic interlayer exchange, *Phys. Rev. B* **39**, 4828 (1989).

[5] Chappert C., Fert A., & Van Dau F.N., The emergence of spin electronics in data storage, *Nat. Mater.* **6**, 813 (2007).

[6] Moodera J.S., Kinder L.R., Wong T.M., & Meservey R., Large magnetoresistance at room temperature in ferromagnetic thin film tunnel junctions, *Phys. Rev. Lett.* **74**, 3273 (1995).

[7] Mao S., et al., Commercial TMR heads for hard disk drives: characterization and extendibility at 300 gbit/in, *IEEE Trans. Magn.* **42**, 97 (2006).

[8] http://http://media.freescale.com/phoenix.zhtml?c=196520&p=irol-newsArticle&ID=880030&highlight=MRAM

[9] Slonczewski J.C., Current-driven excitation of magnetic multilayers, *J. Magn. Magn. Mater* **159**, L1 (1996).

[10] Tsoi M., Jansen A.G., Bass J., Chiang W.-C., Seck M., Tsoi V., & Wyder P., Excitation of a Magnetic Multilayer by an Electric Current, *Phys. Rev. Lett.* **80**, 4281 (1998).

[11] Myers E.B., Ralph D.C., Katine J.A., Louie R.N., & Buhrman R.A., Current-induced switching of domains in magnetic multilayer devices, *Science* **285**, 867 (1999).

[12] Fuchs G.D., Krivorotov I.N., Braganca P.M., Emley N.C., Garcia A.G.F., Ralph D.C., & Buhrman R.A., Adjustable spin torque in magnetic tunnel junctions with two fixed layers, *Appl. Phys. Lett.* **86**, 152509 (2005).

[13] Pribiag V.S., Krivorotov I.N., Fuchs G.D., Braganca P.M., Ozatay O., Sankey J.C., Ralph D.C., & Buhrman R.A., Magnetic vortex oscillator driven by d.c. spin-polarized current, *Nat. Phys.* **3**, 498 (2007).

[14] Pufall M.R., Rippard W.H., Schneider M.L., & Russek S.E., Low-field current-hysteretic oscillations in spin-transfer nanocontacts, *Phys. Rev. B* **75**, 140404 (2007).

[15] Sankey J.C., Krivorotov I.N., Kiselev S.I., Braganca P.M., Emley N.C., Buhrman R.A., & Ralph D.C., Mechanisms limiting the coherence time of spontaneous magnetic oscillations driven by dc spin-polarized currents, *Phys. Rev. B* **72**, 224427 (2005).

[16] Emley N.C., Ph.D. thesis, Cornell University (2005).

CHAPTER 2

TECHNOLOGICAL ADVANCES IN MAGNETOELECTRONICS: PAST, PRESENT, AND FUTURE

Throughout the course of history, the properties of ferromagnetic materials have been exploited in a multitude of applications, ranging from the compass needles used for navigation in 11th century China to more recent uses in magnetic storage devices such as computer hard drives and random access memory. These ferromagnets exhibit a spontaneous magnetization due to an alignment of atomic moments caused by internal short range magnetic interactions otherwise known as the exchange field. As a result, these materials can generate and interact with magnetic fields, such as when a compass needle rotates to point along the Earth's magnetic field. Recent advances in thin film deposition have led to the discovery of magnetotransport effects such as giant magnetoresistance (GMR) and spin transfer, which occur as conduction electrons traverse through thin ferromagnetic layers. In this chapter, I will focus on the physical origins of these effects and their consequences for current and prospective technologies in the fields of both computer storage and communications.

A qualitative understanding of ferromagnetism in the transition metals mentioned below is relatively straightforward if we consider these systems on the atomic scale. In isolated atoms, Hund's rules govern the the occupation of nearly degenerate electron levels in a manner meant to minimize energy. Hund's first rule states that electrons with the same spin orientation are to be placed into partially filled atomic orbitals before adding electrons of the opposite spin state. The motivation for this strategy comes from the fact that the Pauli exclusion principle states that electrons with the same spin orientation tend to stay further apart on average,

reducing the energy associated with Coulomb repulsion between the electrons; the energy reduction is referred to as the atomic exchange energy. For isolated atoms, contributions to the atomic magnetic moment can come from non-zero spin values due to partially filled orbital levels and/or non-zero values of orbital angular momentum. Extending this picture to the case of a solid material, interactions with neighboring atoms lead to a hybridization of electron states and the formation of bands, which act to suppress the formation of moments in two ways. First, these band tend to break the spherical symmetry of each atom's environment, leading to a quenching of the orbital angular momentum. Second, band structure inhibits spin polarization as there is an associated energy cost to promote unpolarized electrons to a higher unoccupied energy state in order to align their spins. However, in 3-d transition metals such as Co, Fe, or Ni, there is strong exchange splitting of the majority and minority electron spin states, so that these metals remain strongly ferromagnetic even after band formation.

Moving to a mesoscopic scale, a whole new range of phenomena becomes unveiled in these ferromagnets, as short range exchange interactions give way to longer range forces induced by magnetostatic fields. To minimize the energy of the the system in this case, the magnetization typically deviates from a spatially uniform or *macrospin* state, to one in which the local moments of different spatial regions orient themselves in different directions with respect to one another. These *micromagnetic* configurations can play a significant role in defining the characteristics of a nanomagnetic system and are explored in Chapters 5 and 6 of this dissertation. Another interesting consequence of these materials caused by their band structure is that electrons with spin parallel to the moment of a ferromagnet are preferentially transmitted through that ferromagnet, resulting in spin polarized currents. In systems consisting of two or more ferromagnets, these spin polarized

currents are generated and interact with other layers, affecting the electron transport properties in these magnetic nanostructures.

Finally, the consequences of these magnetotransport effects can be evaluated on a macroscopic scale if we consider the technological uses for these nanomagnetic systems. Hard drive read heads have revolutionized computer storage, which has been crucial in the expansion of the internet and numerous other economic sectors. More recently, the drive to establish a nonvolatile memory technology with fast read/write speeds, high densities, and low power consumption has led to the development of field switched magnetic random access memory (MRAM) [1], with uses in automotive and computer server applications. With the prediction and experimental verification of the spin momentum transfer effect [2–6], the development of MRAM written directly using spin polarized currents began in earnest and continues today. Additionally, these nanomagnetic systems have been shown to be ideal candidates for generating RF signals for use in a wide array of communications and oscillatory signal generation applications. In this chapter, I will cover these magnetotransport effects and the mechanisms behind them in more detail, as well as discuss technological systems exploiting these effects, from their inception to current developments and beyond.

2.1 Magnetotransport Effects in Magnetic Multilayers

2.1.1 Spin Filtering in NM/FM Systems

Ferromagnets are natural systems for observing spin dependent transport effects as exchange splitting of the majority and minority spin bands acts to preferentially

transmit electrons of one spin type, effectively spin polarizing electric currents passed through the magnet. A relatively simple definition for this spin polarization P can be given by considering the density of states for majority spin ($\uparrow$) and minority spin ($\downarrow$) electrons:

$$P = \frac{g_\uparrow(E_F) - g_\downarrow(E_F)}{g_\uparrow(E_F) + g_\downarrow(E_F)}, \tag{2.1}$$

where $g_\uparrow(E_F)$ and $g_\downarrow(E_F)$ are the density of states for spin-$\uparrow$ and spin-$\downarrow$ electrons at the Fermi energy, respectively. For a normal metal such as Cu with an equal density of states for both spin bands, we expect $P = 0$, however, in ferromagnets, this is not the case due to the exchange splitting. An example of this is shown in Fig. 2.1a, which shows the calculated band structures of Fe, Co, and Ni. At the Fermi energies indicated by the dotted lines in the figure, we clearly see an imbalance in the states available for spin-$\uparrow$ and spin-$\downarrow$ electrons, from which we expect some polarization of the current. The exact nature of spin polarization within these ferromagnets is much more complex, as electron mobilities differ for different bands crossing the Fermi level, but for the purposes of exploring these effects, this qualitative model is more than sufficient.

The majority of these polarization processes occur mainly at the interface of a magnetic layer, and can be examined more thoroughly by considering electrons flowing from a nonmagnetic metal (NM) directly into a ferromagnetic (FM) layer. In this case, the NM/FM interface acts as a preferential filter for one spin orientation, due mainly to the differences in band structure between the two layers as shown in Fig. 2.1b. Here, the current in the NM is unpolarized because the spin states at the Fermi level are equal, but electrons incident upon the NM/FM interface transmit though and reflect off the interface with different probabilities as there are more available states at the Fermi energy for one spin state in the FM. This effect not only polarizes the current, but also results in spin momentum

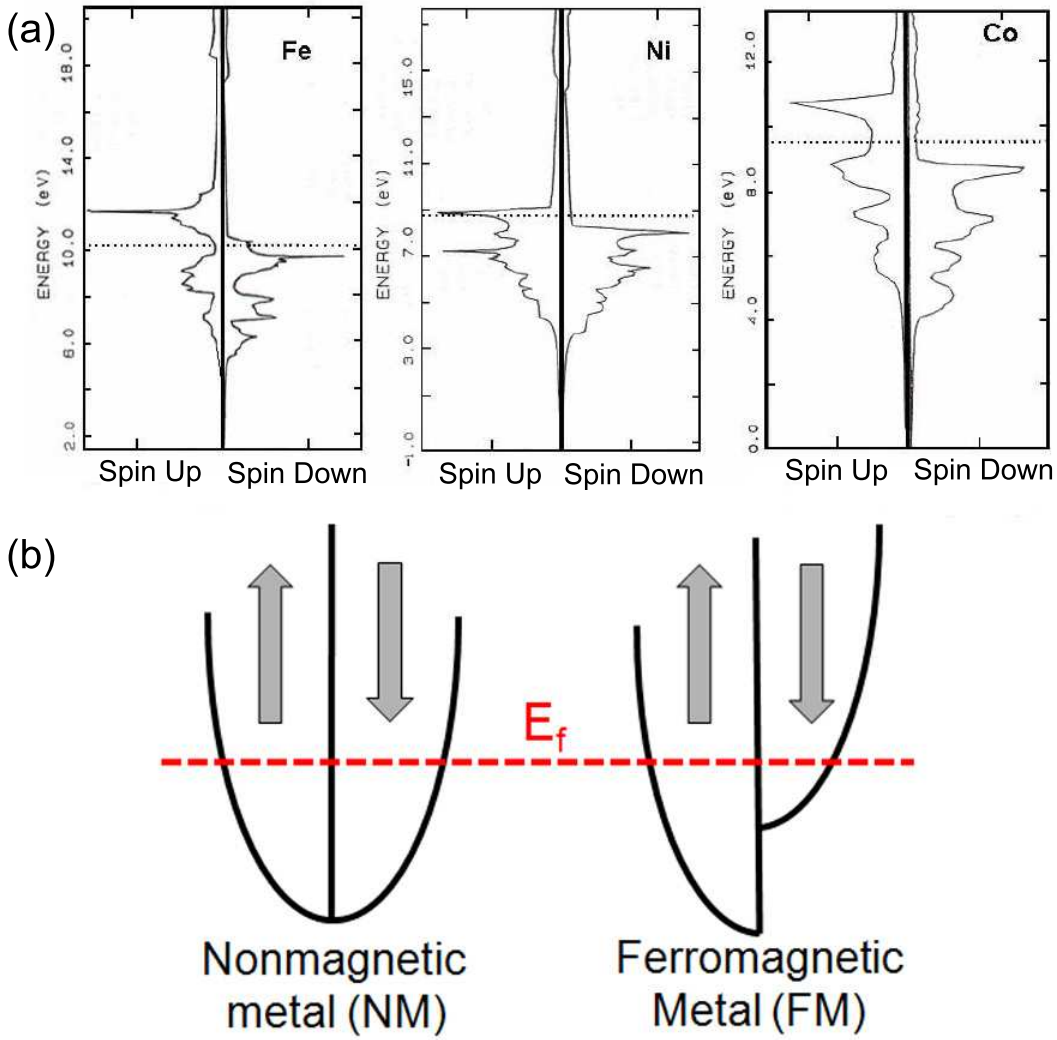

Figure 2.1: (a) Total density of states as a function of electron energy for Ni, Fe and Co obtained from first principles band structure calculations [7]. The dotted line shows the Fermi level. Due to exchange splitting of the spin bands, the occupation of electron states are spin dependent. This asymmetry in the number of states available for different spins to scatter into gives rise to spin-polarized currents. (b) Band diagram for a NM/FM interface. Band splitting in the ferromagnet leads to an asymmetry in electrons states at the Fermi level for the two spin states, such that reflection and transmission of electrons at the interface are spin dependent, which is the origin of magnetotransport effects.

transfer effects, where the component of electron spin lost during the polarization process is exerted as a torque on the moment. In the following discussion, I will discuss these effects in a quantum mechanical framework proposed by Stiles and Zangwill [8, 9], which I have found to be one of the most enlightening treatment of magnetotransport phenomena.

Consider the NM/FM system shown in Fig. 2.2, with the electric current traveling in the $\hat{x}$ direction and the magnetization of the ferromagnet oriented along $\hat{z}$. To simplify the calculations, we assume a free-electron description is adequate for modeling the conduction electrons of the system. Although this assumption is not quantitatively correct, it does capture the qualitative behavior of magnetotransport in the system. Choosing the electron spin quantization axis to be parallel to $\vec{M}$, we can write the electron wavefunction as:

$$\psi = \left[cos\frac{\theta}{2} e^{-i\phi/2} |\uparrow> + sin\frac{\theta}{2} e^{i\phi/2} |\downarrow> \right] e^{ik_x x} e^{i\vec{q}\cdot\vec{R}} \tag{2.2}$$

where θ and ϕ are spherical coordinates defining the electron's spin orientation, $\vec{k} = [k_x, \vec{q}]$ is the electron wavevector satisfying the condition $\frac{\hbar k^2}{2m} = E_F$, and $\vec{r} = [x, \vec{R}]$ is the position vector of the electron. The total wave function can be written as the sum of the spin up and down wavefunctions $\psi = \psi_\uparrow + \psi_\downarrow$, so we can now consider the contributions from individual spin states. Placing the NM/FM interface at x=0, we can treat this as a quantum mechanical scattering problem and consider electrons incident upon the interface, which are then free to reflect back from the interface or transmit through the magnet. The spin dependent wavefunctions now become:

$$\psi_\uparrow = cos\frac{\theta}{2} e^{-i\phi/2} |\uparrow> \begin{cases} (e^{ik_x x} + R_\uparrow e^{-ik_x x}) e^{i\vec{q}\cdot\vec{R}} & \text{if } x < 0; \\ T_\uparrow e^{ik_x^\uparrow x} e^{i\vec{q}\cdot\vec{R}} & \text{if } x > 0. \end{cases} \tag{2.3}$$

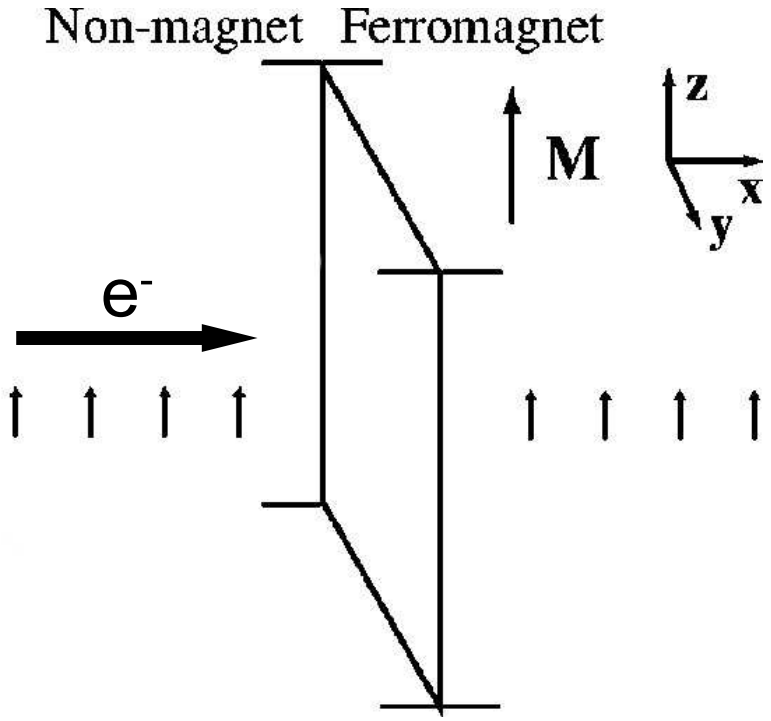

Figure 2.2: Model for discussion of electron reflection and transmission off NM/FM interface. Electrons travel in the $\hat{x}$ direction with spin quantized in the $\hat{z}$ direction, which is also the easy axis of the ferromagnet's moment. Figure taken from [9]

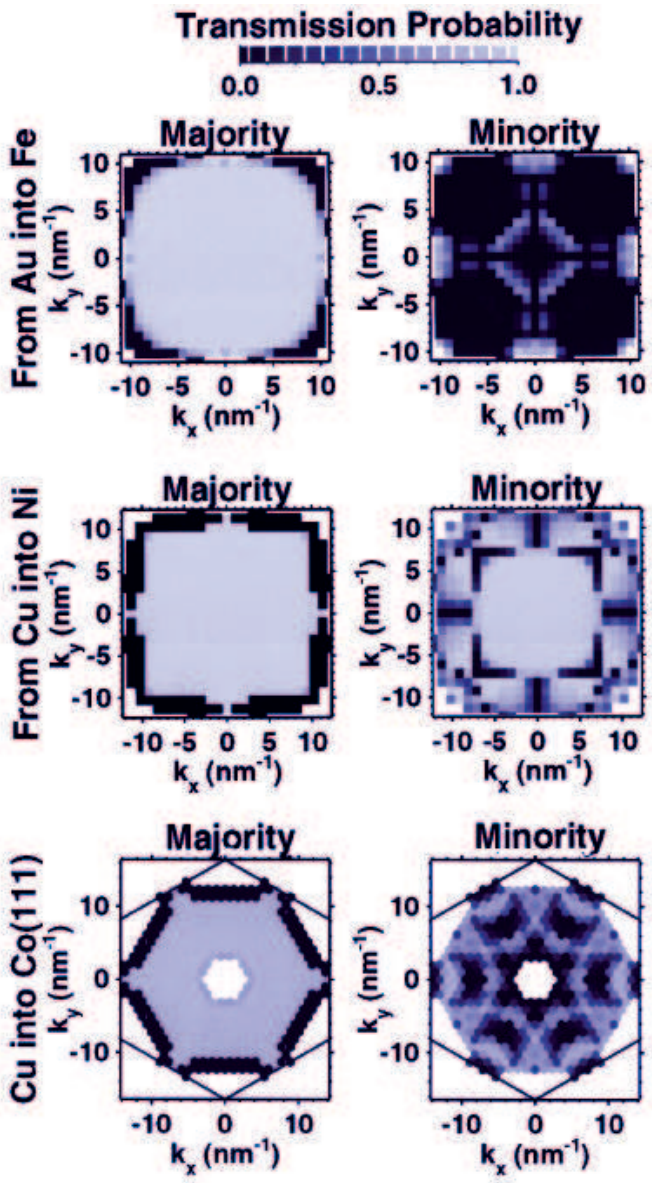

Figure 2.3: Transmission probabilities for various NM/FM interfaces calculated from first principles band structure calculations. These calculations verify the difference in transmission probabilities for majority and minority electrons which give rise to magnetotransport effects like GMR and spin transfer. Figures taken from [10]

$$\psi_\downarrow = sin\frac{\theta}{2}e^{i\phi/2}|\downarrow> \begin{cases} (e^{ik_x x} + R_\downarrow e^{-ik_x x})e^{i\vec{q}\cdot\vec{R}} & \text{if } x < 0; \\ T_\downarrow e^{ik_x^\downarrow x}e^{i\vec{q}\cdot\vec{R}} & \text{if } x > 0. \end{cases} \tag{2.4}$$

where $T_\uparrow$, $T_\downarrow$, $R_\uparrow$, and $R_\downarrow$ are transmission and reflection amplitudes for the respective spin states and are not dependent on θ or ϕ. I also note that the spin up and down component do not propagate with the same wavevectors for $x > 0$ as their kinetic energies depend on the exchange potential energy in the ferromagnet. Solving for these amplitudes involve solving this scattering problem with boundary conditions maintaining continuity of ψ and $\frac{d\psi}{dx}$ at x=0. Using this condition, we find:

$$T_\uparrow = \frac{2k_x(q)}{k_x(q) + k_x^\uparrow(q)}, \tag{2.5}$$

$$R_\uparrow = \frac{k_x(q) - k_x^\uparrow(q)}{k_x(q) + k_x^\uparrow(q)}, \tag{2.6}$$

where $k_x(q) = \sqrt{k_F^2 - q^2}$, $k_x^\uparrow(q) = \sqrt{(k_F^\uparrow)^2 - q^2}$ and $k_x^\uparrow(q)$ is imaginary if $q^2 > (k_x^\uparrow)^2$ for reflected components. Similar expressions exist for down spin components. The associated reflection and transmission *probabilities* are then:

$$R^{\uparrow,\downarrow}(q) = |R_{\uparrow,\downarrow}(q)|^2, \tag{2.7}$$

$$T^{\uparrow,\downarrow}(q) = \frac{k_x^{\uparrow,\downarrow}(q)}{k_x(q)}|T_{\uparrow,\downarrow}(q)|^2, \tag{2.8}$$

which satisfy $T^{\uparrow,\downarrow} + R^{\uparrow,\downarrow} = 1$.

From these expressions, we can clearly see that the transmission and reflection probability of the incident electrons are spin dependent. Fig. 2.3 shows spin dependent transmission probabilities for various NM/FM interfaces calculated taking the band structure of the materials into account. Using these results, we can clearly see that the interface acts as a filter for one electron spin state, preferentially polarizing the current passing through the layers. Measurements of spin polarization

in Co films [11] have shown that $\sim 75\%$ of the bulk polarization occurs within two monolayers of the film, confirming that spin filtering resulting in spin polarized currents occurs predominantly due to spin dependent scattering at FM interfaces as a results of band mismatches.

2.1.2 Giant Magnetoresistance (GMR)

An important consequence of spin polarized currents and spin dependent scattering is the giant magnetoresistance (GMR) effect, which relates the resistance of a FM/NM/FM system to the relative orientation of the ferromagnets' moments with respect to one another. This effect was first demonstrated in Fe/Cr/Fe multilayers by Baibich *et al.* [12] and Binasch *et al.* [13] (see Fig. 2.4). In these experiments, the applied current used to measure device resistance was applied in a direction parallel to the plane of the deposited films, in the so called current-in-plane (CIP) configuration, where only some of the electrons actually scatter off the NM/FM interfaces while others move completely laterally through the bulk of the layers. A more efficient strategy proposed by Pratt *et al.* [14] involved applying the current perpendicular to the film plane (CPP) so that all the electrons are forced to interact with the NM/FM interfaces. This not only yields much larger changes in device resistance for different relative magnetization orientations, but also is less sensitive to sample inhomogeneities introduced during layer deposition, which made this configuration more suitable for examining the fundamental physics of spin-polarized transport. As all my measurements in the following chapters involve CPP measurements, I will focus on this configuration.

The origin of this resistance change can be understood by considering the FM/NM/FM system shown in Fig. 2.5a,b. Valet and Fert [15] modeled these

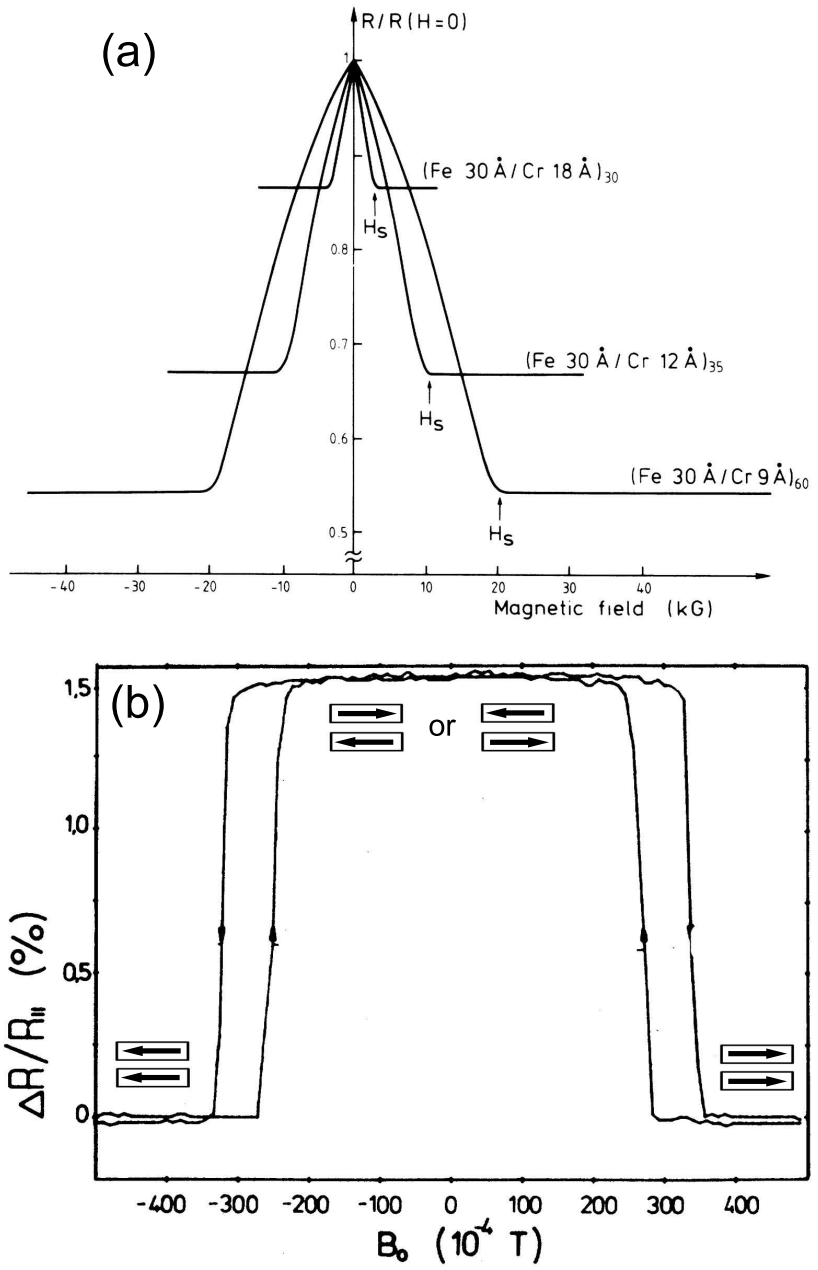

Figure 2.4: (a) Magnetoresistance of 3 Fe/Cr superlattices at 4.2 K. The current and applied field are along the same axis in the plane of the layers. Figure taken from [12] (b) Magnetoresistance of a Fe/Cr/Fe trilayer at room temperature. Figure taken from [13].

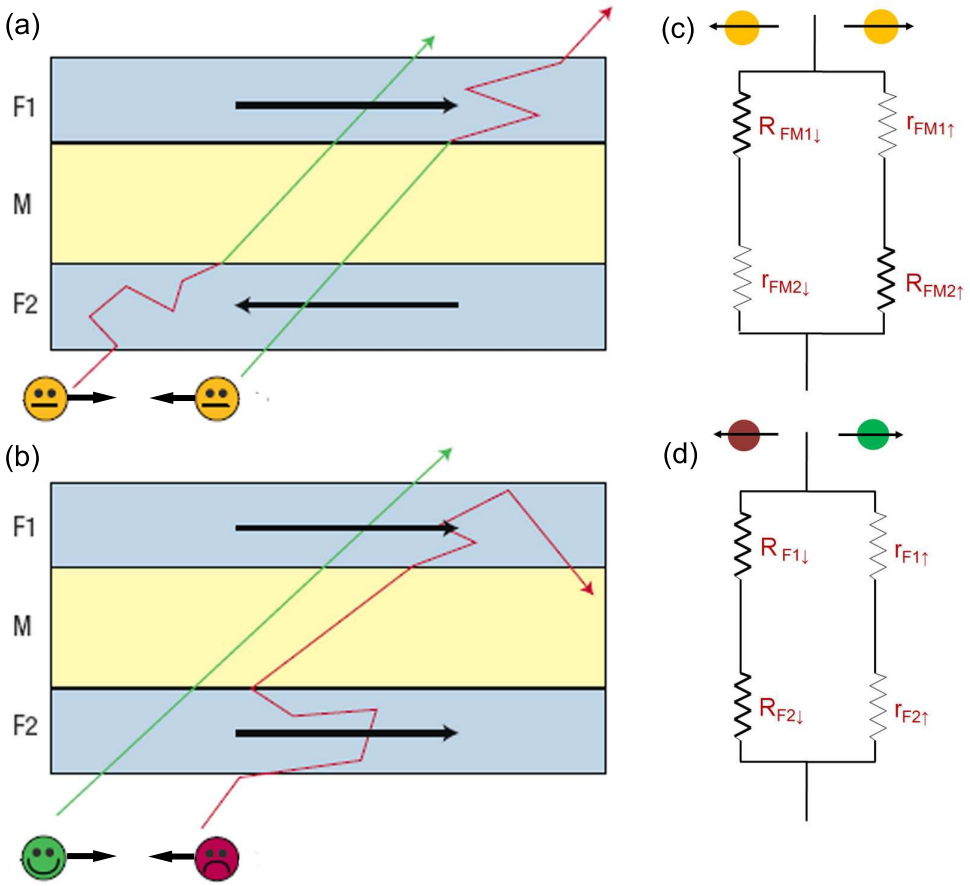

Figure 2.5: (a) Schematic diagram of electron transport through a spin valve with the ferromagnetic layers oriented antiparallel with respect to one another. In this case, both spin-up and spin-down electrons undergo collisions in either F1 or F2, which can be modeled using the two channel parallel resistor circuit shown in (c), where there is a high resistance element for both spin channels, leading to an overall higher resistance than for a parallel alignment. (b) When the ferromagnets are aligned parallel to one another, electrons of one spin type are free to transmit through both layers, effectively seeing a low resistance shunt as depicted in (d). The difference in resistance between these two states is referred to as magnetoresistance. Figure modified from [40].

structures using a two spin channel parallel resistor model, as depicted in Fig. 2.5c,d. Here, the spin dependent resistance of a ferromagnetic layer is r for electrons with spin parallel to the moment and R for electrons with spin antiparallel to the moment, where $R > r$. For the case where the moments are antiparallel (Fig. 2.5a), both spin states preferentially scatter off of one of the FM interfaces, leading to a large resistance R being present in both spin channels, as shown in Fig. 2.5c. Conversely, for the case where the moments are parallel (Fig. 2.5b), the spin state aligned with both moments see a low resistance channel (Fig. 2.5d), effectively shunting electrons with that spin orientation, resulting in a low resistance state. The change in resistance between these two states ΔR defines the GMR ratio (in percent):

$$GMR\ ratio = \frac{\Delta R}{R_{AP}} = \frac{R_{AP} - R_P}{R_{AP}}. \tag{2.9}$$

For misalignments angles between parallel and antiparallel configurations, the resistance takes intermediate values defined by the equation:

$$R(\theta) \approx R_P + \Delta R \cdot \frac{1 - cos\ \theta}{2}. \tag{2.10}$$

This metallic trilayer system has been referred to as a spin valve. In practice, we stabilize one of the ferromagnets by either exchange coupling it with an antiferromagnet or making its volume much larger than the second ferromagnet, which acts to enhance the coercive field of that layer. This reference layer then acts as a polarizer for the incident current due to spin dependent scattering. The polarized current transmits through the thin NM layer and interacts with the second ferromagnet, which is free to rotate, and is therefore called the free layer. As such, GMR is an important probe for magnetization reversal and dynamics experiments as the device resistance provides an indication of the free layer magnetization orientation.

2.1.3 Spin Momentum Transfer

An additional effect of significant importance arising from spin dependent scattering in magnetic multilayers is the spin momentum transfer effect. This effect can be seen as a consequence of the polarizing mechanism, whereby unpolarized electrons transmitted through the NM/FM interface tend to reorient their spins along the magnetization direction of the ferromagnet. By Newton's third law, the angular momentum lost by the electron is transmitted to the ferromagnet as a torque, in order to conserve angular momentum in the system. I return to the formalism of Stiles and Zangwill introduced above to show these interactions in more detail and refer you to Fig. 2.2 for details of the coordinate system.

We can quantum mechanically define a spin current density to be

$$\mathbf{Q}(\vec{r}) = \sum_{i,\sigma,\sigma'} Re[\psi^*_{i\sigma}(\vec{r})\mathbf{s}_{\sigma,\sigma'} \otimes \hat{\mathbf{v}}\psi_{i\sigma'}(\vec{r})], \tag{2.11}$$

where $\psi_{i,\sigma}$ are occupied single particle wavefunctions with state i and spin index σ, $\hat{\mathbf{v}}$ is the velocity operator ($= -\frac{i\hbar}{m}\nabla$), and $\mathbf{s} = (\hbar/2)\vec{\sigma}$, where $\vec{\sigma}$ is a vector whose Cartesian components are the three Pauli matrices. The spin current density is extremely useful in examining changes in spin orientation brought on by scattering at the NM/FM interface. Assuming that the free electron like conduction electrons move only along $\hat{x}$ (i.e. 1D transport), we can compute the x components of the spin current density tensor Q_{jx}, where j represents any of the three spin axes, assumed to be along $\hat{x}$, $\hat{y}$, or $\hat{z}$. Using the wavefunctions describe above in the section on spin filtering, electrons incident on the interface have spin current density components:

$$Q^{in}_{xx} = \frac{\hbar}{2} v_x sin\ \theta\ cos\ \phi, \tag{2.12}$$

$$Q^{in}_{yx} = \frac{\hbar}{2} v_x sin\ \theta sin\ \phi, \tag{2.13}$$

$$Q_{zx}^{in} = \frac{\hbar}{2} v_x cos\ \theta, \tag{2.14}$$

where θ and ϕ are coordinates describing the spin orientation of an unpolarized electron. The spin current density for reflected and transmitted spins are more complicated due to the exchange splitting within the ferromagnet:

$$Q_{xx}^{ref} = -\frac{\hbar}{4}|v_x| sin\ \theta\ Re[R_\uparrow^* R_\downarrow e^{i\phi}], \tag{2.15}$$

$$Q_{yx}^{ref} = -\frac{\hbar}{4}|v_x| sin\ \theta\ Im[R_\uparrow^* R_\downarrow e^{i\phi}], \tag{2.16}$$

$$Q_{zx}^{ref} = -\frac{\hbar}{2}|v_x|[cos^2\ \frac{\theta}{2}|R_\uparrow|^2 - sin^2\ \frac{\theta}{2}|R_\downarrow|^2], \tag{2.17}$$

$$Q_{xx}^{trans} = \frac{\hbar}{4}\frac{v_x^\uparrow + v_x^\downarrow}{2} sin\ \theta\ Re[T_\uparrow^* T_\downarrow e^{i\phi} e^{i(k_x^\downarrow - k_x^\uparrow)x}], \tag{2.18}$$

$$Q_{yx}^{trans} = \frac{\hbar}{4}\frac{v_x^\uparrow + v_x^\downarrow}{2} sin\ \theta\ Im[T_\uparrow^* T_\downarrow e^{i\phi} e^{i(k_x^\downarrow - k_x^\uparrow)x}], \tag{2.19}$$

$$Q_{zx}^{trans} = \frac{\hbar}{2} v_x^\uparrow cos^2\ \frac{\theta}{2}|T_\uparrow|^2 - \frac{\hbar}{2} v_x^\downarrow sin^2\ \frac{\theta}{2}|T_\downarrow|^2. \tag{2.20}$$

A complete understanding of the spin current behavior in this system requires numerical analysis of these equations, but we can still use some simple observations to qualitatively examine the origins of spin transfer in these systems. By substituting in the values of $T_{\uparrow,\downarrow}$ and $R_{\uparrow,\downarrow}$ calculated above, it can be shown that $Q_{zx}^{in} = Q_{zx}^{trans} - Q_{zx}^{ref}$, so that spin components parallel to the magnetization directions are conserved during the scattering process, telling us that there is no torque associated with the transport of longitudinal spin currents. The transverse spin current components Q_{xx} and Q_{yx} are only conserved if $R_\uparrow = R_\downarrow$ and $T_\uparrow = T_\downarrow$, which is not the case for a ferromagnet. Since the component of transverse spin lost in the filtering process must be conserved, it becomes transmitted to the ferromagnet as a torque acting upon the moment.

A second source of transverse spin discontinuity occurs when the product $R_\uparrow^* R_\downarrow$ is not positive real. This leads to a factor of $R_\uparrow^* R_\downarrow = |R_\uparrow^* R_\downarrow| e^{i\Delta\phi}$ being included in

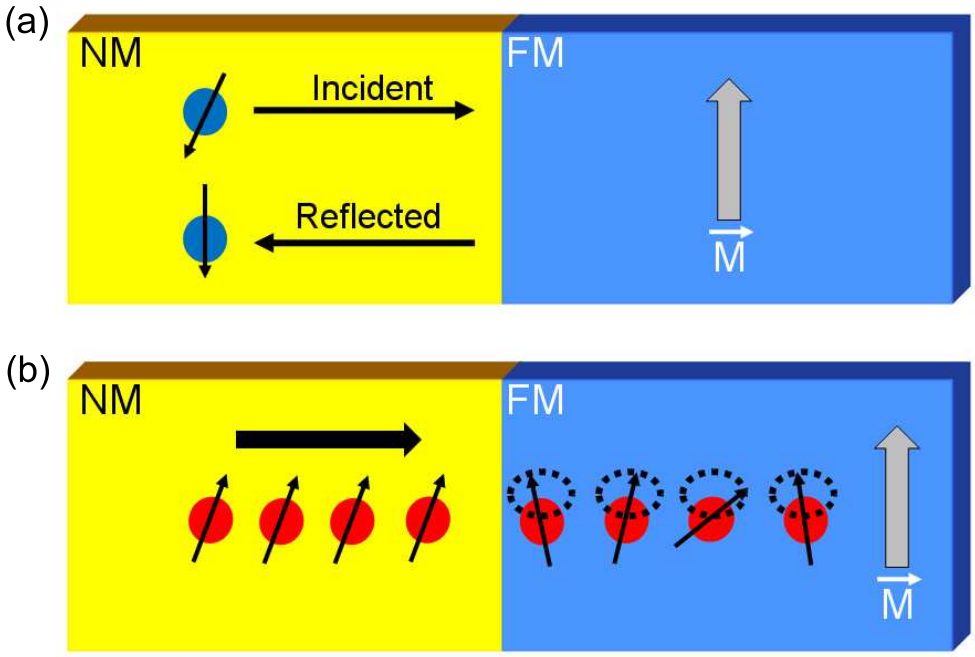

Figure 2.6: (a) Spin torque exerted on a ferromagnet by electron reflection. Reflected electrons undergo a rotation of their spin. The component of the electron spin transverse to the ferromagnet's moment is then transmitted as a torque acting on the moment. (b) Spin torque exerted on a ferromagnetic by averaging. Due to the difference in k-vectors for majority and minority spins, electrons transmitted into the ferromagnet precess around the ferromagnet's moment with a range of different frequencies. By averaging over the entire ensemble of transmitted electrons, the component of electron spin transverse to the ferromagnet's moment is lost and transferred as a torque acting upon the moment.

Eqns. 1.15-16. This phase angle adds to the azimuthal angle ϕ used to describe the spin orientation of the electron's initial state, indicating that reflected electrons can undergo a *rotation* in spin state during interfacial scattering as shown in Fig. 2.6a, which has been calculated [9] to be surprisingly large. In fact, for the calculation in [9], the spin directions can undergo $\sim 180°$ reversal from reflection off the interface, a consequence that will become more important when I discuss current induced magnetization reversal. The resulting spin current discontinuity from this rotation mechanism adds to the torque exerted on the magnetization by spin filtering.

Finally, a third and final source of spin torque is generated by the transmitted transverse spin current. Since $k_x^{\uparrow} \neq k_x^{\downarrow}$ in the ferromagnet, this introduces a spatially varying phase factor to Eqns. 1.18-19, which acts to rotate Q_{xx} into Q_{yx} and vice versa as electrons transmit through the ferromagnet, introducing a *spin precession* about the magnetization axis for the electrons as shown in Fig. 2.6b. These spatial precession frequencies vary rapidly over the Fermi surface, so by summing over the entire electron ensemble transmitted through the ferromagnet, the component of transverse spin current averages out to zero. In other words, an electric current entering a ferromagnet with a transverse component of spin polarization exits the layer with zero transverse component. This loss of angular momentum once again gives rise to a torque that acts upon the magnetization. As this averaging occurs within a few monolayers of the NM/FM interface, I note that this precessional mechanism can still be considered an interfacial effect, as are the other two mechanisms discussed here. This illustrates the importance of maintaining clean interfaces during multilayer deposition for devices fabricated to examine spin transfer effects.

2.1.4 Current Induced Magnetization Dynamics

Current interest in spin transfer results from the ability to manipulate the moment of a ferromagnet solely through the use of an electric current. I have covered the mechanisms involved in transferring angular momentum from conduction electrons to the ferromagnet, but this is one-half of the total process. To complete the picture, we have to examine the range of magnetization dynamics excited in the ferromagnet as a results of applying a current, which is described by the Landau-

Lifshitz-Gilbert (LLG) equation [2],

$$\frac{d\hat{m}}{dt} = \gamma \cdot \hat{m} \times \vec{H}_{eff} - \alpha \cdot \hat{m} \times \frac{d\hat{m}}{dt} - \left(\frac{\gamma\hbar}{2e}\right) \frac{\eta I}{|\vec{m}|} \cdot \hat{m} \times (\hat{p} \times \hat{m}) \tag{2.21}$$

This formula is a summation of all the torques acting upon a ferromagnet's moment $\vec{m}$ such that a dynamic response $\frac{d\hat{m}}{dt}$ is excited in the ferromagnet. The first cross product term is the Larmor precessional torque (τ_H) exerted on the moment by magnetic fields, which acts to excite precession of $\vec{m}$ around the effective magnetic field $\vec{H}_{eff}$. $\vec{H}_{eff}$ includes contributions from externally applied fields, demagnetization fields, Oersted fields, and magnetostatic fields generated by edge charges (i.e. dipole fields) on magnetic layers in close proximity to $\vec{m}$, such as the reference layer in a spin valve structure. γ is the electron gyromagnetic ratio.

The second cross product term is the damping torque (τ_d), a dissipative term that acts as a restoring force upon the precessing $\vec{m}$ to return the magnetization back to its equilibrium position. This term is referred to as the Gilbert damping term, first proposed by T. L. Gilbert in 1955 [16] in order to take large damping values into account and bring the theory closer to experimental results. α is a phenomenological term also referred to as the Gilbert damping constant, which establishes the strength of the damping acting on $\vec{m}$ and can consist of components intrinsic and extrinsic to the particular ferromagnet. Intrinsic contributions to the damping have been attributed to spin-orbit coupling [17] in the ferromagnet, and values on the order of 0.01 have been determined for various ferromagnets from ferromagnetic resonance experiments. More recently, two extrinsic damping mechanisms increasing overall damping have been proposed, both resulting from patterning considerations for nanomagnetic devices. The first was theoretically proposed by Tserkovnyak *et. al* [18, 19] and involves the generation of spin current from the precession of a ferromagnet's moment. This spin current is free to flow out of the ferromagnet into adjacent layers acting as spin sinks, dissipating

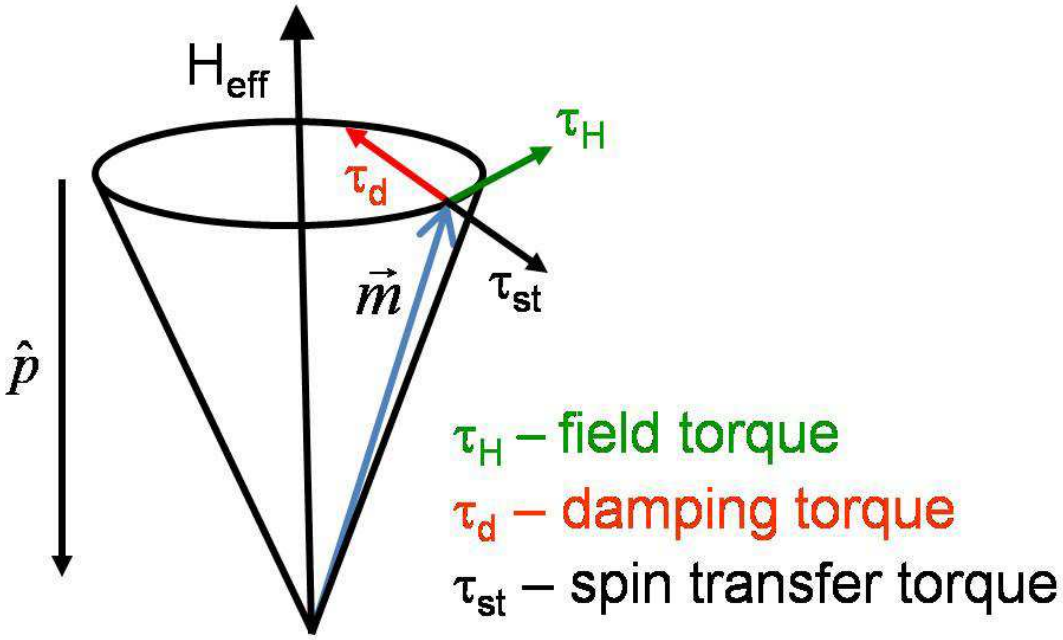

Figure 2.7: Torque acting upon the magnetization as defined by the LLG equation. τ_H is a field torque that causes Larmor precession of the magnetization around the effective magnetic field H_{eff}. τ_d is a damping torque acting as a restoring force on the magnetization to return it back to it's equilibrium position. τ_{st} is the spin transfer torque that can oppose or enhance the damping torque depending on the spin polarization direction $\hat{p}$ and the current polarity.

angular momentum outside of the ferromagnet. This *spin pumping* effect has been experimentally verified [20] using FMR measurements. Alternative mechanisms for extrinsic damping come from antiferromagnetic oxides formed on the sidewalls of patterned nanostructures, which have been shown [21, 22] to form grains that antiferromagnetically couple to the ferromagnet, and act to dissipate angular momentum.

The third and final cross product term in the LLG equation describes the spin torque (τ_{st}) imparted on $\vec{m}$ by DC current I spin polarized in the $\hat{p}$ direction, where η is the percentage of spin polarization. As shown in Eqn. 1.21, the dependence of spin torque amplitude on the misalignment angle θ between $\hat{m}$ and $\hat{p}$ goes as the sine of θ. However, theoretical models [2, 23, 24] and experimental results [25] point to a more complicated dependence on misalignment angle. Although it is still unclear as to the proper form for this angular dependence, I offer some thoughts in Chapter 4 based on experiment observations from pulsed current magnetization reversal experiments.

The interactions of all three torque components are shown in Fig. 2.7. Here, τ_H acts perpendicular to the precessional orbit, driving oscillations of $\vec{m}$, while τ_d attempts to restore $\vec{m}$ back to equilibrium along $\vec{H}_{eff}$. The spin torque τ_{st} either increases the overall effective damping or acts as an "anti-damping" term depending on the polarity of the incident spin current. Magnetization excitations occur when this "anti-damping" spin transfer pumps energy into the magnet faster than the damping can remove it. When the spin torque is equal and opposite to the damping torque, only τ_H remains, driving the magnetization into a persistent precessional state for as long as the spin torque is applied. The current value at which this occurs is referred to as the critical current I_c for the turn-on of dynamics;

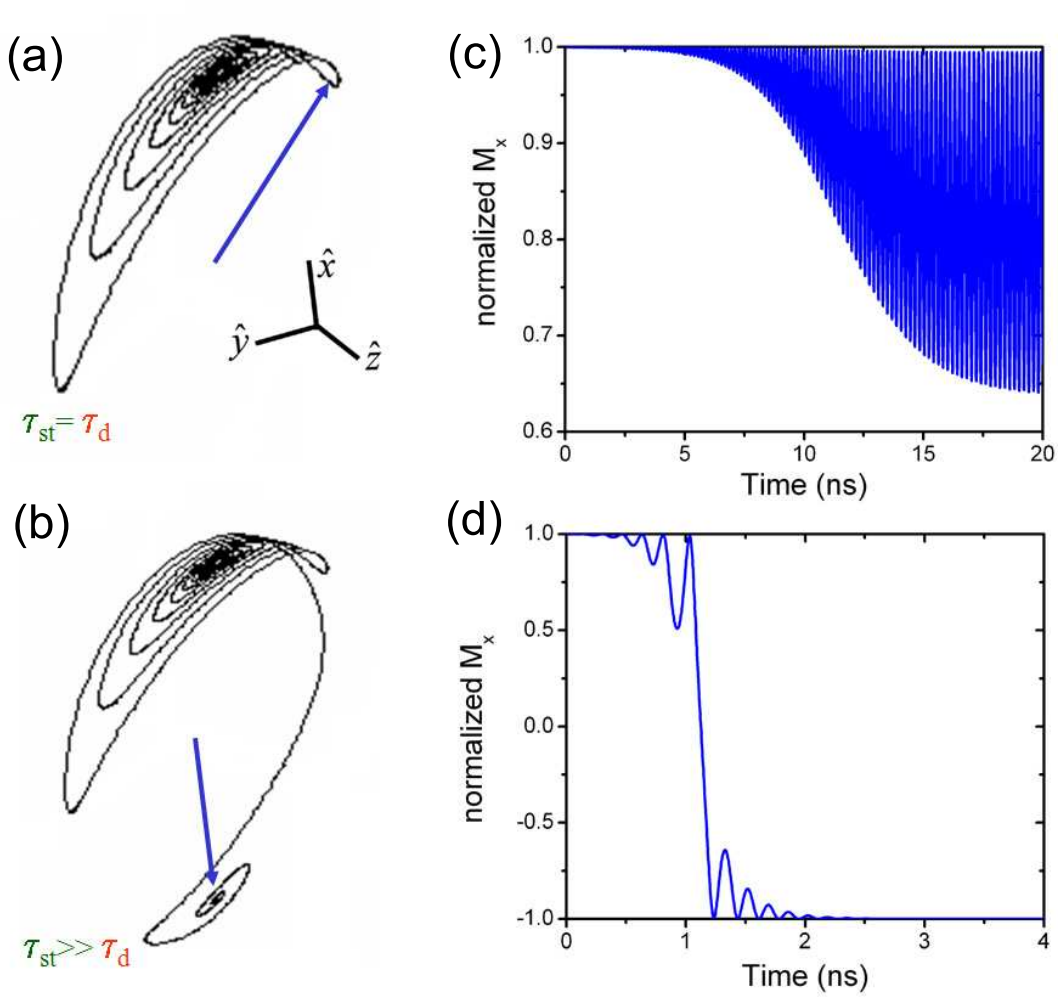

Figure 2.8: (a) Macrospin simulation for $I = I_c$. Here, the spin torque cancels the damping torque, resulting in persistent oscillations of the magnetization around it's equilibrium position (b) Macrospin simulation for $I > I_c$, making that the spin torque greater than the damping torque. Here, the precession amplitude increases over time until the magnetization develops a net component opposite to its original easy-axis orientation, at which point the spin torque causes the nanomagnet to settle rapidly into a quiescent magnetically-reversed state. (c),(d) Plots of M_x vs. time for the simulations shown in (a),(b).

assuming the magnetizations of both ferromagnets are in-plane [2, 26]:

$$I_c^{\pm} = \frac{\alpha}{\eta^{\pm}} \left(\frac{2e}{\hbar} \right) M_s V \left[H_{eff} + 2\pi M_{eff} \right], \tag{2.22}$$

where $I_c^{\pm}$ is the critical current for the onset of dynamics when the reference and free layers are nearly parallel/anti-parallel, α is the Gilbert damping parameter, e is the electron charge, M_s is the saturation magnetization of the free layer, V the free layer volume, H_{eff} the effective field acting on the free layer, $4\pi M_{eff}$ is its effective demagnetization field (typically $4\pi M_{eff} >> H_{eff}$), and $\eta^{\pm}$ is the spin torque efficiency parameter, which varies with the alignment angle θ between the free and reference magnets. An example of these precessions calculated using LLG simulations of a spatially uniform $\vec{m}$ is shown in Fig. 2.8a,c. For larger values of spin torque, the precessions begin to grow in amplitude until the nanomagnet moment develops a net component opposite to its original easy-axis orientation, at which point the spin torque causes the nanomagnet to settle rapidly into a quiescent magnetically-reversed state as shown by the simulation results in Fig. 2.8b,d.

In practice, observing spin transfer phenomena requires a nanomagnetic system such as a FM/NM/FM spin valve structure. As the spin torque imparted by a single electron is only a fraction of the total angular momentum required to overcome damping, the incident electric current must be significantly spin polarized to induce enough scattering events to excite the free layer magnetization. This function is performed by the reference layer of the spin valve. From Eqn. 1.21, we see that the sign of the current polarity required to ensure that spin torque cancels the damping depends on the relative alignment between the free and reference layer magnetizations, as the spin polarization axis of the current is determined by the reference layer moment. Fig. 2.9 illustrates this concept, where for an antiparallel alignment of the moments (Fig 2.9a), the unpolarized current first travels

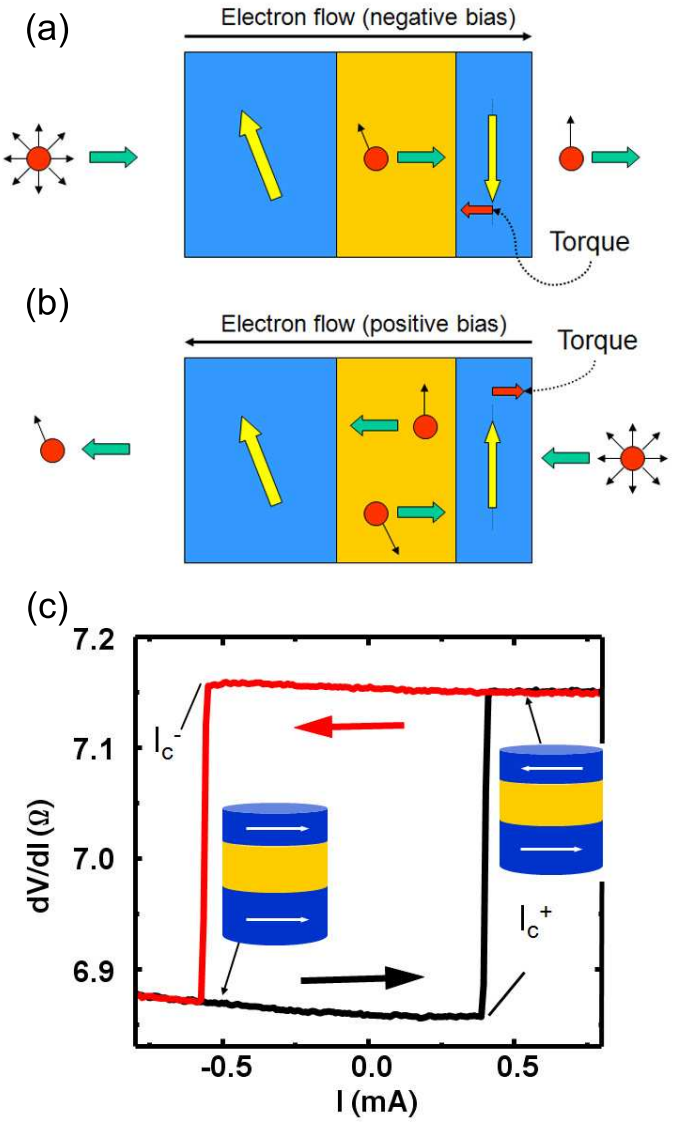

Figure 2.9: (a) For an antiparallel orientation between ferromagnets, electrons transmitted through the reference layer polarize the incident spin current with a component transverse to the free layer magnetization. Interactions at the spacer/free layer interface then exert a torque on the free layer which acts to reverse the magnet and induce a parallel orientation. (b) Reversal in an antiparallel configuration requires reversing the polarity of the current. Here, electrons transmit through the free layer and reflect off the reference layer with spin polarization antiparallel to the reference layer moment. The reflected electrons can then interact at the spacer/free layer interface and once again exert a torque on the free layer that acts to reverse the free layer into an antiparallel orientation. (c) dV/dI vs. I for a spin valve. Experimental results verify that reversing the polarity of the electric current allows reversal of the free layer in both directions.

through the reference layer and becomes polarized. The net spin polarization of the incident current is now antiparallel to the free layer so that interactions at the NM/FM interface impart a torque upon the free layer. For a parallel alignment of the moments (Fig. 2.9b), electrons flowing in the direction shown in (a) stabilize a parallel alignment. However, reversing the current so electrons flow through the free layer and scatter off the reference layer interface allows us to once again spin polarize the current antiparallel to the free layer moment, due to rotation of the reflected spins due to the band structure arguments discussed above, once again exciting the magnetization. Fig. 2.9c is a plot of resistance vs. DC current for a spin valve structure, where we observe complete magnetization reversal of the free layer by sweeping both negative and positive fields. Detection of reversal is achieved through the GMR effect, as we observe a high and low resistance state corresponding to an antiparallel and parallel alignment of the moments respectively.

The magnetization dynamics induced by electric currents through the spin transfer effect have numerous consequences on both basic magnetism research and commercial applications alike. For example, the development of spin torque FMR [27, 28] has led to greater understanding of intrinsic material damping parameters in patterned nanomagnets [29]. It also has been used to probe phenomena in magnetic tunnel junctions [30], furthering our understanding of bias effects and spin transfer interactions. On a more applied side, spin transfer may prove useful in both memory and communications applications, due to the various advantages these magnetic systems present over current technologies. In the next few sections I will discuss some of these technologies and the issues involved with them.

2.2 Hard Drive Read Heads

In 1956, IBM built the first magnetic hard disk drive featuring a total storage capacity of 5 MB at a recording density of 2 kbit in^{-2}. Advances in hard disk technology over the next 50+ years have led to the unprecedented growth of industries such as personal computers and the Internet by offering high density storage with exceptional performance and costs. Currently, the annual growth rate of storage density for these drives is $\sim$ 100% [31], and maintaining this trend motivates a wide range of research in basic physics and engineering. In this section, I will briefly describe the operational concept of a hard drive, and examine the evolution in technological advances that have driven the growth of storage density. I will also discuss the various issues limiting continued storage density growth and some strategies being investigated to avoid these issues.

A basic hard drive consists of three major components, the magnetic hard disks or platters containing the actual storage information, the read/write heads that interact with the hard disks, and the microelectronic controller that connects the computer's microprocessor to the hard drive. Fig. 2.10a shows a schematic of the hard drive, where the hard disks are connected to a spindle, allowing them to rotate at speeds up to 15,000 rpm. On these disks, the recording media is typically a single magnetic storage layer consisting of weakly coupled magnetic grains. One material currently used is CoPtCr doped with boron or tantalum, and is grown on top of a complex underlayer structure to promote proper crystallographic orientation, grain size, and grain distribution [31]. A thin carbon overcoat and a lubricant layer protect the media from oxidation and physical damage as a result of physical contact with the read/write head. These heads are attached to the end of actuator arms that move the head radially along the disk to address any spatial region

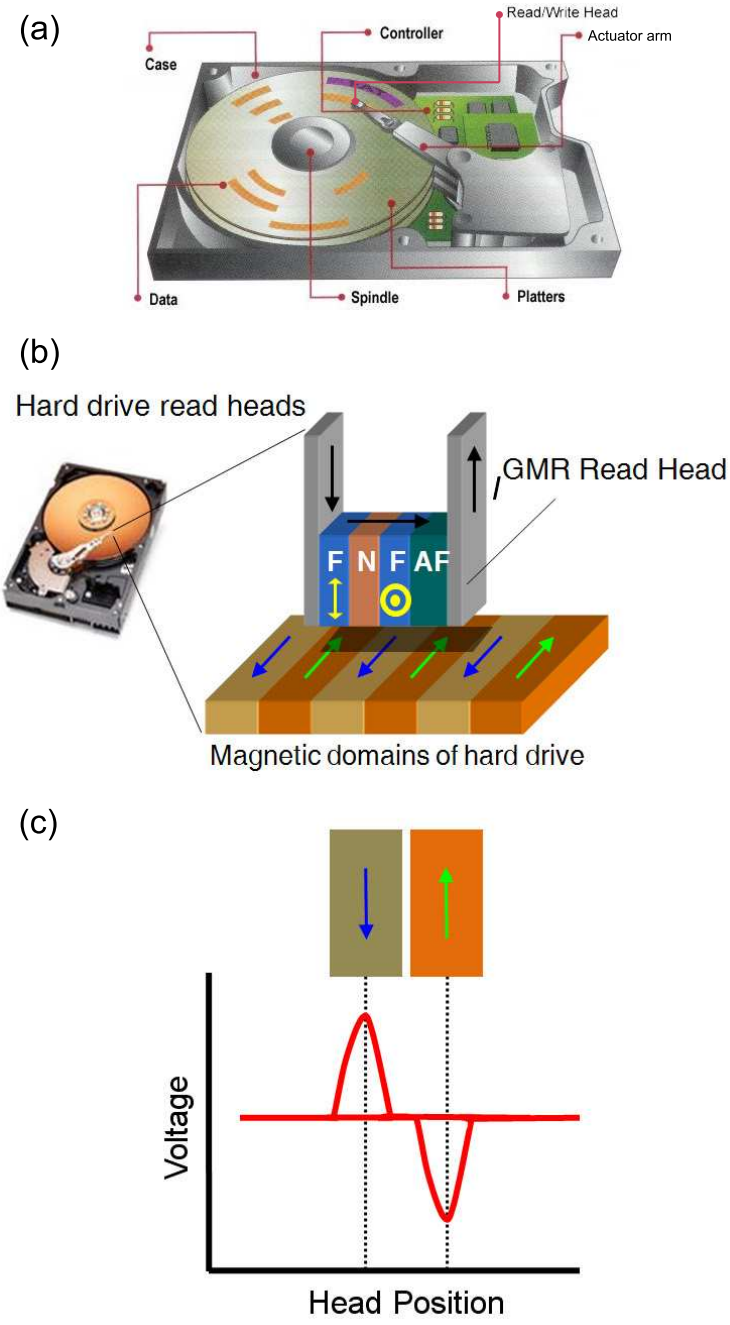

Figure 2.10: (a) Schematic of a computer hard drive. These consist of three main components, the hard disk which rotates on a spindle, the read/write head attached to the end of an actuator arm, and the microelectronic controller. (b) The head flies over the hard disk at a very small separation distance, and detects the magnetic fields originating from domains on the hard disk which comprise the bits encoding digital data. (c) Deflection of the read head free layer results in voltage spikes due to the GMR effect that are negative or positive depending on the domain orientation, allowing stored data to be read off the hard disk.

on the disk. Head-disk separations are typically on the order of nanometers and continue to shrink as storage densities. The heads themselves are composed of separate devices for detecting information (GMR or TMR read head) and writing information (usually incorporating some type of inductive coil to generate write fields).

Individual grains on the hard disk weakly interact to form domain regions or stripes, which are regarded as separate storage bit regions. In Fig. 2.10b, I show a GMR device as an example of the read head, where the head has been deposited with the reference layer exchanged pinned perpendicular to the free layer through the use of an antiferromagnet placed adjacent to the reference layer. As the disk spins below the head, dipole fields generated by these domain regions act to deflect the free layer magnetization either parallel or antiparallel to the reference layer, depending on the magnetization direction within the domain. By biasing the device with an electric current I, positive or negative voltage pulses (see Fig. 2.10c) are generated due to the GMR effect as the free layer magnetization deflects, which can then be converted into a digital signal for further processing. The write head operates in a similar manner, generating a magnetic field that interacts with the bit domains and reverses the domain magnetization orientation.

The evolution of the read/write head is an interesting case to examine, as it illustrates the symbiotic relationship between basic physics research in nanomagnetics and technology. Initial hard drives used a single inductive head performing both read and write functions, typically involving a ferrite core wrapped in a fine wire coil. Here, the dipole fields generated by the bit domains changed the flux through the coil as the head passed over them, creating a current which would then be detected. The polarity of this current determined the orientation of the

domain, and thus specified the information stored in the bit. Bit writing occurred by passing a current through the coil and using the resultant Oersted field to orient the bit domains, similar to the process used today. Unfortunately, generating magnetic fields large enough for reading and writing with these heads required both the head itself and the bit domains to be quite large, limiting the maximum storage density achievable to something on the order of Mbits in^{-2}.

Advances in thin film processing offered a solution to this problem, in the form of magnetoresistive heads involving the magnetotransport effects discussed at the beginning of this chapter. Micro- and nanofabrication techniques also allowed patterning of heads to progressively smaller dimensions, enabling smaller bit sizes and higher storage densities. The first of these heads involved anisotropic magnetoresistance (AMR), an effect by which the resistance of a single ferromagnetic layer changes in the presence of a magnetic field. Here, the probability of scattering off lattice electrons is different for conduction electrons moving parallel to the ferromagnet's magnetization than for conduction electrons traveling in a direction perpendicular to the magnetization. As the magnetic field of the bit rotates the magnetization, a change of resistance is detected, and detects the information stored on the bit. Typical magnetoresistances for these types of read head are below 1%, creating signal-to-noise (SNR) issues, especially as the head size scaled down. The discovery of the GMR effect, and its subsequent incorporation into these heads temporarily alleviated these issues by introducing similar magnetic performance with an order of magnitude larger magnetoresistive signal.

In 1995, Moodera et. al [32] discovered that magnetoresistance was also seen in ferromagnet/insulator/ferromagnet trilayer systems, where in this particular case they used CoFe/Al_2O_3/Co (or NiFe). This tunneling magnetoresistance (TMR) is

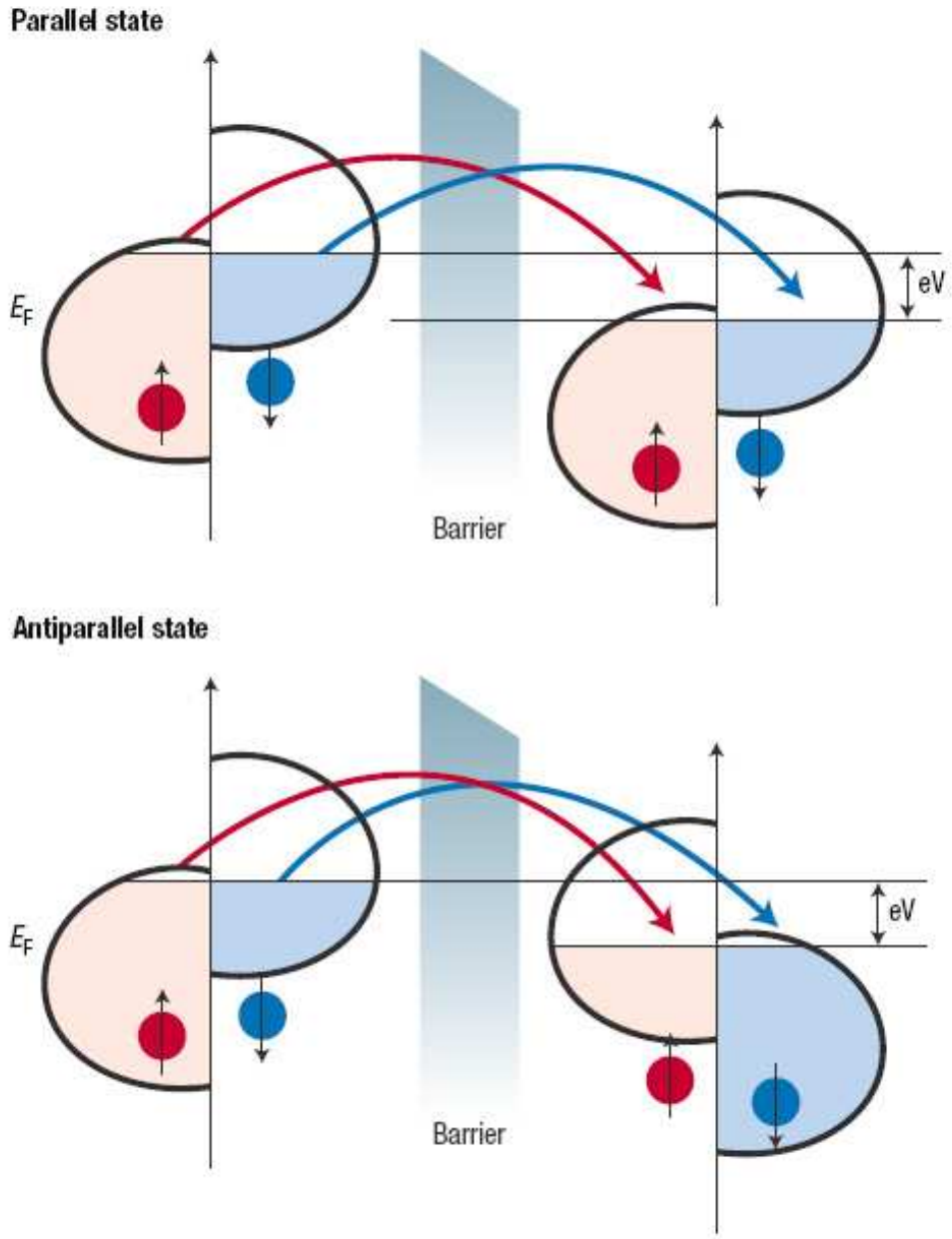

Figure 2.11: Schematic representation of the tunnel magnetoresistance in the case of two identical ferromagnetic metal layers separated by a non-magnetic amorphous insulating barrier such as Al_2O_3. Here, I assume the tunneling process conserves the spin. When electron states on each side of the barrier are spin-polarized, then electrons will more easily find free states to tunnel to when the magnetizations are parallel (top picture) than when they are antiparallel (bottom picture). Figure taken from [40]

attributed to the conduction electron polarization of the ferromagnetic electrodes, with the MR ratio given as [33]:

$$TMR\ \% \ = \frac{\Delta R}{R} = \frac{R_{AP} - R_P}{R_{AP}} = \frac{2P_1P_2}{1 - P_1P_2}, \tag{2.23}$$

where R_{AP} and R_P are the device resistance for antiparallel and parallel configurations of the electrode moments respectively and P_1 and P_2 are the polarizations for the two electrodes determined by spin polarization measurements, such as the Meservey-Tedrow technique [34]. A more simplistic explanation of this effect can be obtained by examining the band structure of the system, similar to what I have shown in describing GMR above. Fig. 2.11 shows an example of these systems for parallel and antiparallel alignments of the electrode moments. Here, biasing of the tunnel junction leads to a lowering of the Fermi energy for one electrode with respect to the other. In the parallel moment configuration, the number of electron states at the Fermi level are approximately equal in both electrodes for each spin orientation, and so there are sufficient available states for electrons to tunnel from the left electrode to the right electrode, assuming spin is conserved in the tunneling process. For an antiparallel alignment however, there are many fewer states in the right electrode for down spin tunneling electrons, decreasing the tunneling probability and increasing the antiparallel device resistance. TMR results in larger magnetoresistance percentages than obtained with GMR, and coupled with the large device resistance values expected due to the insulating barrier, these magnetic tunnel junction (MTJ) read heads offer much better SNR values than GMR heads, which has been instrumental in continued storage growth rates.

More recently, experiments with MgO tunnel junctions [35, 36] have exhibited extraordinarily large TMR percentages due to coherent tunneling of electrons within the MgO barrier, as indicated in Figs. 2.12a,b. Band structure calculations [37] of crystalline Fe/MgO/Fe trilayers (Fig. 2.12c) show that the Δ_1 sub-

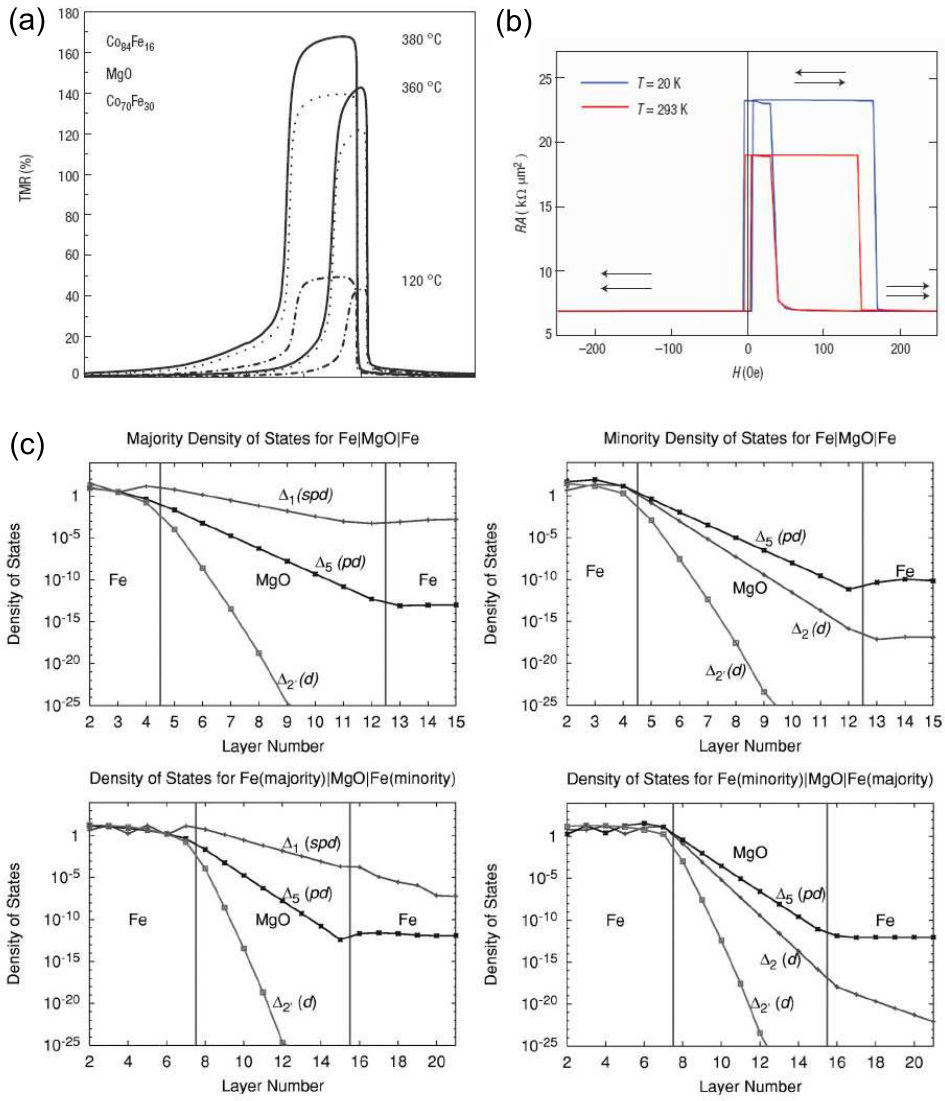

Figure 2.12: (a) Plot of TMR versus field for MTJ with 100 TaN / 250 IrMn/ 8 $Co_{84}Fe_{16}$/ 30 $Co_{70}Fe_{30}$/ 29 MgO/ 150 $Co_{84}Fe_{16}$/ 100 Mg with all thicknesses in $\mathring{A}$. These devices have been annealed to the different temperatures labeled. Figure taken from [35]. (b) Magnetoresistance curves (measured at a bias voltage of 10 mV) at $T = 293$ K and 20 K (MgO thickness $t_{MgO} = 2.3$ nm). The resistance-area product RA plotted here is the tunnel resistance for a 1×1 μm^2 area. Arrows indicate magnetization configurations of the top and bottom Fe electrodes. Figure taken from [36]. (c) Tunneling density of states (DOS) for $k_{\|} = 0$ for Fe(100)|8MgO|Fe(100). The four panels show the tunneling DOS for majority (upper left), minority (upper right), and antiparallel alignment of the moments in the two electrodes (lower panels). Additional Fe layers are included in the lower panels to show the TDOS variation in the Fe. Figure taken from [37].

band experiences minimal attenuation for majority carriers tunneling from the left electrode into the right electrode. Since the tunneling current is dominated by s electrons in this band, we expect electrons to have a large tunneling probability when the electrodes are in a parallel configuration. In the antiparallel case, the density of states for the Δ_1 band becomes more attenuated, as shown in the calculation for the Fe (majority)/MgO/Fe (minority), in turn causing the tunnel current to be more strongly attenuated. This fact, coupled with the lack of a Δ_1 for minority carriers, leads to a large increase in TMR. However, these effects only occur with the proper crystal structure and band symmetry, so that achieving large TMR values are strongly dependent on growth conditions and ferromagnetic electrode selection. MgO tunnel junctions are also being explored as bit elements for magnetic memory applications, due to their large TMR signals and the ability to tailor their resistances by changing the properties of the MgO barrier.

As storage densities continue to increase, both read head and media grain size must scale down to smaller and smaller dimensions, eventually approaching the superparamagnetic limit of both. One solution for the media could be to use materials with perpendicular anisotropy so that even for a small lateral area (x-y plane), the magnetization is stabilized in the z direction. Another such approach is called HAMR [31, 38], short for Heat Assisted Magnetic Recording, in which a large anisotropy material is used as the media. Here, the anisotropy is large enough that the magnetic field produced by the write head is insufficient to reverse the bit even for extremely small bit sizes. However, this strategy incorporates a laser to simultaneously heat the media while applying a field. Heating the media locally reduces its anisotropy until the applied field becomes sufficient to write the bit. Further research is required to incorporate this process into a commercial product, but these examples serve to illustrate the ample interest in developing

these systems.

Shrinking read head dimensions cause more problems than just the thermal stability of the nanomagnets. At smaller dimensions, spin transfer effects become more significant for the bias currents involved in the read process. Unlike the focus of this thesis, for these applications it is beneficial to increase the critical current to avoid spin transfer noise effects reducing SNR for the read head. This can be done by doping the ferromagnets with materials exhibiting large spin-orbit coupling, such as tantalum, and has been shown to be effective in increasing critical currents without significantly altering other magnetic properties [39]. For tunnel junctions, RC delay and Johnson noise will both increases as the MTJ size scales down. This constraint forces the RA product of the MTJ to scale down with device size, and will eventually lead back to the use of CPP GMR read heads. The eventual successor for future read head technologies may involve the use of semiconductor heterostructure Hall sensors, which would not require the use of any ferromagnets, thereby eliminating spin transfer and mag-noise. It is clear that this field still contains many interesting problems left to solve, and will continue to motivate nanomagnetic research for years to come.

2.3 Magnetic Random Access Memory

Recent demands for high performance computing and data storage have led to the development of several different memory technologies. One option that is of great interest is Magnetic Random Access Memory (MRAM), which is a technology relying on the integration of magnetic tunnel junction (MTJ) devices with Complementary Metal-Oxide-Semiconductor (CMOS) circuits. MRAM exhibits

reasonable performance in all desired memory attributes, such as nonvolatility, infinite endurance, and fast read/write times, making it competitive with current Si based memories. In this section, I will discuss two proposed memory architectures incorporating magnetic write strategies, one using magnetic fields that has currently been developed into a commercial product [1], and the second exploiting spin transfer effects.

2.3.1 Field Written Toggle MRAM

Spin valves and MTJs are ideal candidates for memory applications since binary information 0 and 1 can be recorded using the high and low magnetoresistance states of these devices. Fig. 2.13a shows the principle of magnetic solid state memory, in the basic "cross-point" architecture. In this architecture, the magnetic bit elements, usually MTJs for reasons that will be discussed later, are connected to the crossing points of two perpendicular arrays of parallel conducting lines (called "word" and "bit" lines). To write the state of a particular magnetic element, current pulses are sent down one line of each array, so that only at the crossing point of the wires is the resultant magnetic field large enough to orient the magnetization of the element. For reading, the resistance state between the two lines intersecting the addressed magnetic element is measured. This cross point architecture has the potential for providing extremely high densities, although there are issues that must still be addressed. In practice, the amplitude of the magnetoresistance signal remains to small for fast, reliable reading because of unwanted current paths other than the desired one. This results in a more complicated cell consisting of 1 MTJ and 1 CMOS transistor (1T/1MTJ), as is shown in Fig. 2.13b. These transistors are then used to further isolate the magnetic element to be addressed and effect

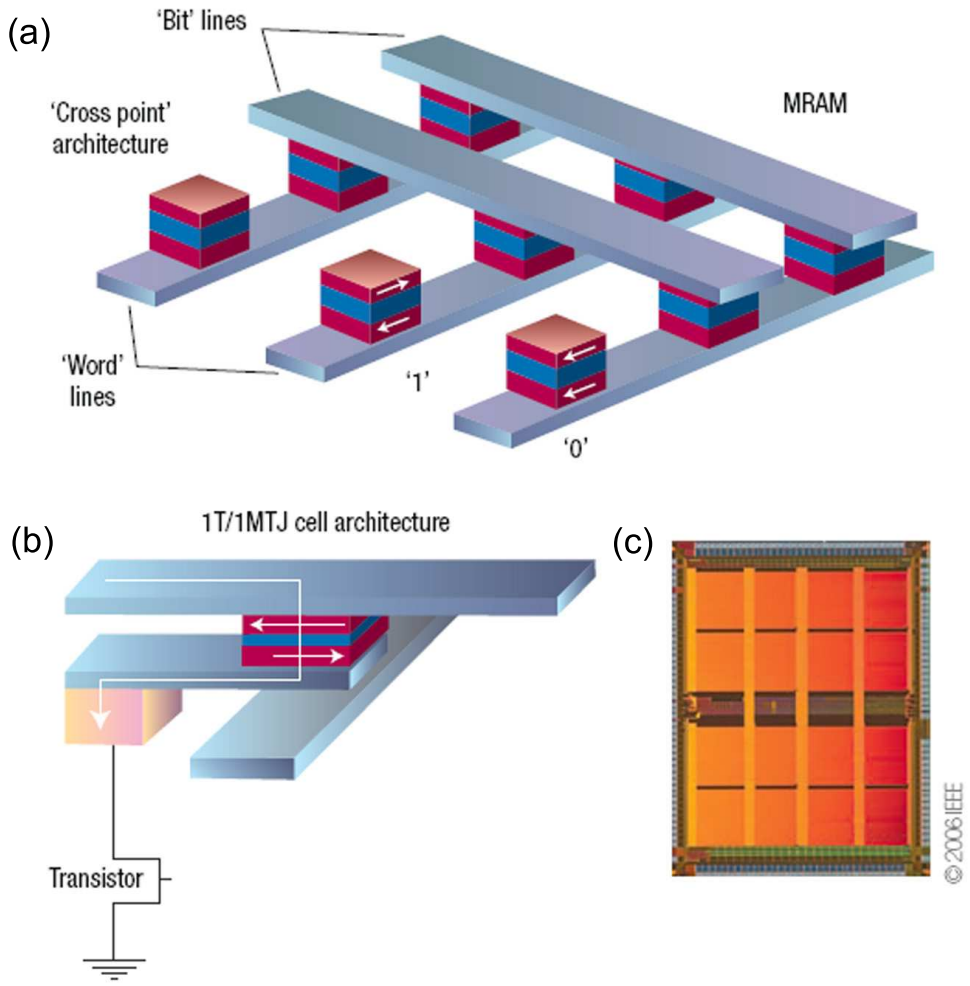

Figure 2.13: (a) Basic cross-point architecture. The binary information 0 and 1 is recorded on the two opposite orientations of the magnetization of the free layer of magnetic tunnel junctions (MTJ), which are connected to the crossing points of two perpendicular arrays of parallel conducting lines. For writing, current pulses are sent through one line of each array, and only at the crossing point of these lines is the resultant magnetic field high enough to orient the magnetization of the free layer. For reading, the resistance between the two lines connecting the addressed cell is measured. (b) To remove the unwanted current paths around the direct one through the MTJ cell addressed for reading, the usual MRAM cell architecture has one transistor per cell added, resulting in more complex 1T/1MTJ cell architecture such as the one represented here. (c) Photograph of the first MRAM product, a 4-Mbit stand-alone memory commercialized by Freescale in 2006. Figure taken from [40].

reliable reading of the bit state. A MTJ is more suited for this type of memory cell for impedance matching to the transistor, which are on the order of 1 kΩ. The commercial interest in this new memory technology is evident with several leading semiconductor companies developing demonstrator circuits and the recent release of a 4-Mbit stand-alone memory product [41] by Freescale Semiconductors in 2006, as shown in Fig. 2.13c.

Reliable memory performance requires excellent uniformity in device resistance, magnetoresistance, and switching field. Variation in resistance and magnetoresistance create read errors that corrupt the data stored in the memory. These issues require careful development of fabrication protocols to reproducibly process the magnetic elements. Variations in the switching fields from device to device are an even larger problem, leading to write errors such as "half-select", where the magnetic field from only one of the current carrying wires can switch some bits, also corrupting stored data. To address these variations, Freescale developed a toggle-switched approach [42] involving a synthetic antiferromagnet (SAF) free layer that is formed from two ferromagnetic layers separated by a thin nonmagnetic coupling spacer layer such as Ru (shown schematically in Fig. 2.14a). This strategy effectively eliminates half-select and strongly increases the write reliability as individual elements can no longer be reversed by the field of just one current carrying line, resulting in a wide operating region with a threshold onset for switching. Fig. 2.14b shows a schematic of the free layer, which is oriented at 45° to both current carrying lines. Fig. 2.14c shows the programming pulse sequence and the resultant magnetic behavior, where the arrows represent the magnetic moments of both free layer ferromagnets. In this example, the darker arrow is the layer that is adjacent to the tunnel barrier and is therefore the information storage layer that determines the resistance. To toggle the bit between states, the currents I_1 and I_2

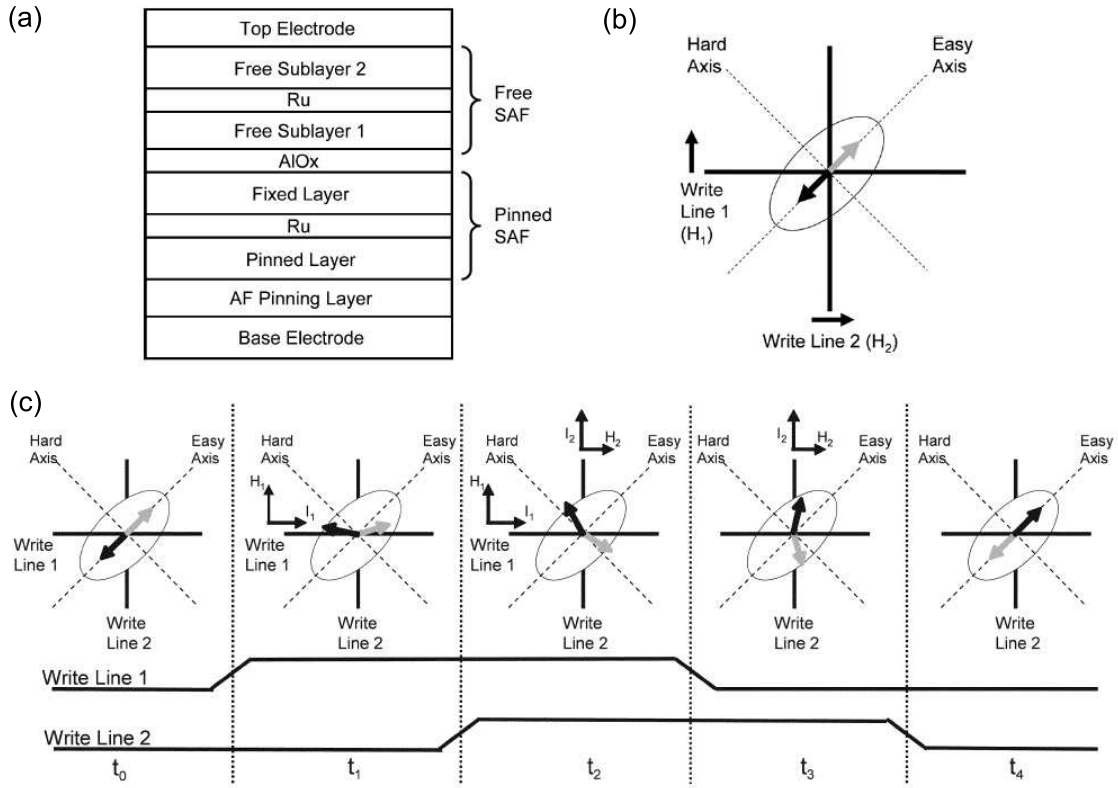

Figure 2.14: (a) Bit cell material stack showing the synthetic antiferromagnetic free layer. (b) Schematic of 45° orientation of the bit with respect to the programming current lines. (c) Schematic of the toggling operation of Savtchenko switching. Pulses are applied in a sequence designed to rotate the SAF 180° to the opposite resistance state. Figures taken from [41]

are pulsed with a phase relationship such that I_2 follows I_1. Due to the symmetry of the system, the bit can be toggled back to its original configuration with the same polarity pulse train. This approach has benefits in limiting the overall power consumption and the unipolar current allows the use of smaller transistors, thereby improving array efficiency.

There are many questions as to the future of this technology, mostly involving scaling down node sizes to increase potential storage density. First, even with a toggle based approach, as the nanomagnet size decreases and device density on chip increases, it will become harder to avoid half-select problems due to stray fields and reduced free layer coercivities. Second, the current carrying lines must be scaled down at the same rate as the magnetic bits, with their resistances going up as a result. Since the current required for generating the switching fields are quite large, on the order of 10 mA, this write scheme is expected to have problems with power dissipation and electromigration at higher densities. Clearly, an alternative writing scheme is required to continue the future growth of MRAM, which has opened the door for using spin transfer as a write scheme.

2.3.2 Current Written MRAM

Studies indicating that spin transfer switching is possible in MTJs [43, 44] have peaked interest in using spin transfer as a writing mechanism for memory applications (ST-MRAM). Several demonstration cells have been reported [45, 46] so far, and in Fig. 2.15 I show one of the proposed architectures [45]. Here, an extra line has been added (the "source" line) to the more traditional 1T/1MTJ field written MRAM architecture. On the write operation, a word line (WL) is selected to address a particular magnetic element, and positive voltage is applied

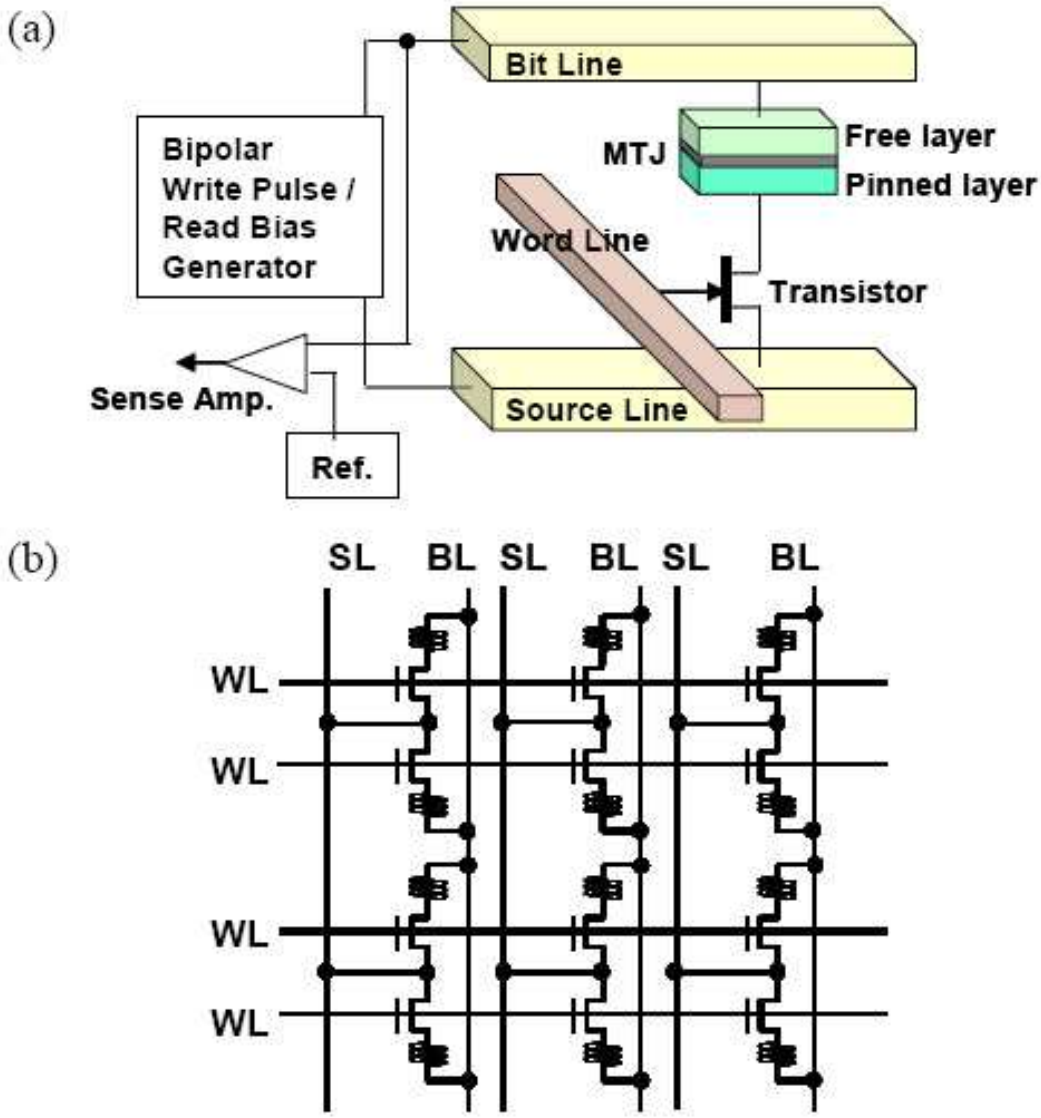

Figure 2.15: (a) A schematic memory cell image, and (b) cell array image. To control current direction, voltage is applied on a bit line (BL) or a source line (SL) on the write operation. Figure taken from [45]

on a bit line (BL) or a source line (SL) of a selected column. The magnetization direction of a switching layer is controlled by the current direction. On the read operation, a WL is selected, and voltage of -0.1 V is applied on a BL of a selected column. This architecture eliminates half-select problems entirely, since current is localized to the single magnetic bit being addressed, and the reversal currents required are for switching are typically smaller than those need for field switching, reducing power dissipation concerns. Although these demonstrations have yet to be developed into commercial products, they have shown the potential impact of spin transfer for these types of memory applications.

Several potential roadblocks still must to be addressed before successful commercialization of this technology can be implemented. The currents available for switching the state of the bits are limited to values accessible through the word transistor, typically on the order of 100-200 μA. Required switching current amplitudes for reversal in the nanosecond regime, which is the normal regime of operation, are much larger than seen using a DC current [25], and so particular care must be taken in designing the magnetic structure to operate within these parameters. In chapter 4, I address this issue in several different manners, the first involving the use of low saturation magnetization M_s nanomagnets for the free layer, which acts to reduce spin transfer critical currents. Incorporating these materials into MgO MTJs has so far yielded rather poor device performance, but current progress in the deposition of the these tunnel junctions with the low M_s electrode NiFeB have shown encouraging results with TMR on the order of 160% and RA products $\sim$ 10 $\Omega \cdot \mu m^2$ [47]. Another possible solution is discussed in chapter 5 considers the use of micromagnetic effects to enhance spin torque within the magnetic system, thereby reducing the required reversal current. These results are encouraging, and efforts are ongoing to identify and exploit these effects in

fabricated devices.

Finally, cycling currents through MTJs to continually write the bit states eventually leads to dielectric breakdown of the barriers, an effect known as barrier wearout. Engineering of the barrier layers can improve the robustness of these devices, however as the bits scale down to smaller sizes, it will become more and more difficult to prevent these breakdown effects. In Chapter 7, I discuss a concept for a three terminal device incorporating a spin valve and a MTJ sharing a common free layer. By doing so, we can have infinite endurance by writing through the spin valve part of the structure, while maintaining the benefits of a high magnetoresistance signal for reading by reading addressing the MTJ.

2.4 Spin-Torque RF Oscillators

Magnetic storage is not the only application proposed for the spin transfer systems discussed above, as magnetization oscillations excited by electric currents can generate RF voltages due to the GMR effect. These DC driven spin torque oscillators (STO) have the potential for applications in fields such as communications (cell phones), radar, and measurement (as reference oscillators) due to their scalability and ease in fabrication for on-chip requirements. From ferromagnetic resonance (FMR) calculations of small angle precession, the Kittel frequency of these oscillations are predicted to be [48, 49]:

$$f = \frac{\gamma}{2\pi}\sqrt{(H + H_{an} + H_d)(H + H_{an} + H_d + 4\pi M_{eff})}. \tag{2.24}$$

Here γ is the gyromagnetic ratio, H is the applied field, H_{an} accounts for a uniaxial easy axis anisotropy, H_d models the coupling from the fixed layer, and $4\pi M_s$ is the out of plane demagnetization field. For typical parameters associated with

ferromagnetic materials such as Co, Fe, NiFe, and CoFe, expected frequencies are on the order of GHz.

Early experimental results [49, 50] detected these oscillations by measuring the output RF voltage with a spectrum analyzer, as shown in Fig. 2.16. Measured frequencies are indeed on the order of GHz, and have been shown to vary with field in good agreement with Equation 1.24 [49]. In addition, the frequencies can also be tuned by varying the currents, as spin torque acts to excite the magnetization in two different manners, depending on the type of precessional orbit involved. For oscillations with the precession axis out of the plane of the film, increasing the current acts to speed up the orbital motion, so the oscillation frequency increases. When the precession axis is in-plane, the spin torque increases the precession angle and increases the orbital circumference, decreasing the frequency with increasing current. In this manner, these STO can be frequency tuned using either magnetic fields or currents.

The eventual use of these devices in real applications still requires substantial research into understanding the physics involved in exciting different macrospin and micromagnetic modes. In addition, for applications it is desired that the output signal have as narrow a linewidth as possible, with integrated powers greater than 1 μW. Currently, the development of MgO MTJs for ST-MRAM applications has provided scientists with devices capable of providing the necessary output powers, however these studies are still in their infancy. Linewidths down to 100 kHz have been observed in vortex oscillators [51, 52], but these devices also suffer from limited frequencies ($<$ 1 GHz) and small integrated powers. In chapter 6, I describe a micromagnetic configuration generated within a tapered spin valve nanopillar that is beneficial for use as a STO. This configuration produces RF sig-

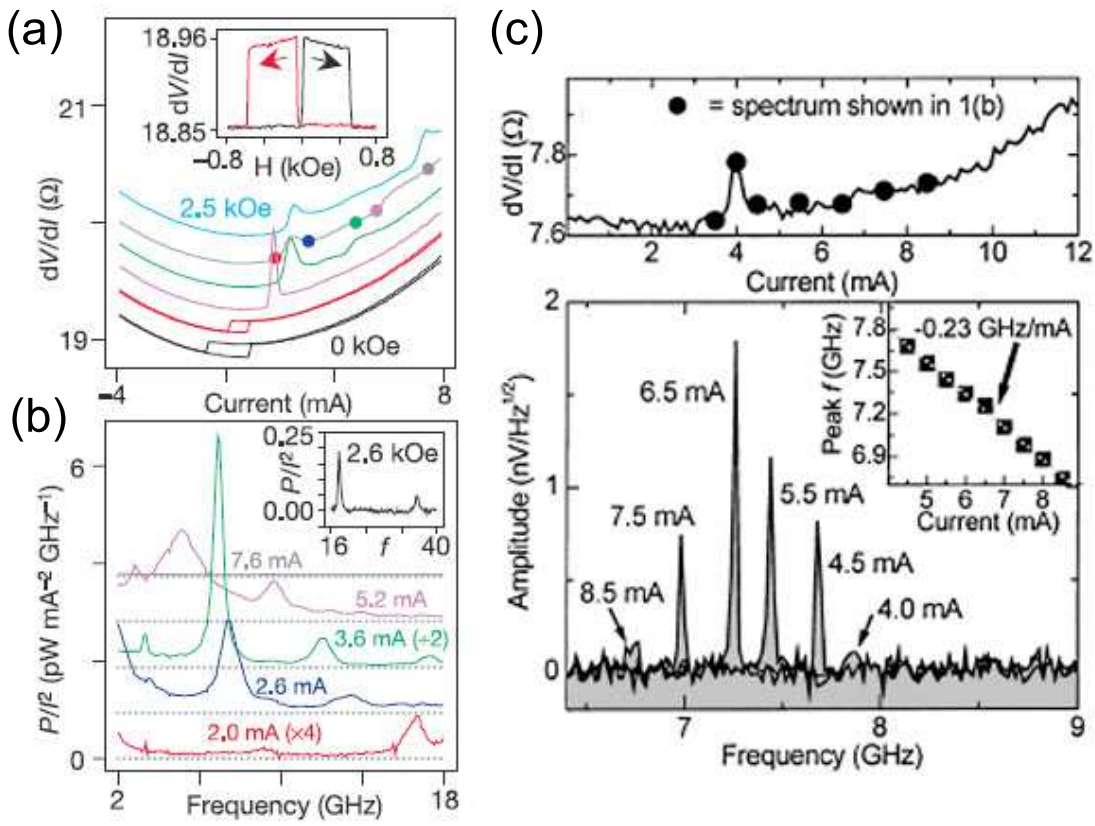

Figure 2.16: (a) Differential resistance versus current for magnetic fields between 0 (bottom) and 2.5 kOe (top) with 0.5 kOe steps and current sweeps in both directions. At $H = 0$, the switching currents are $I_c^+ = 0.88$ mA and $I_c^- = -0.71$ mA, and ΔR max$= 0.11\Omega$ between the P and AP states. Colored dots on the 2 kOe curve correspond to spectra shown in (b). Inset to (a), Magnetoresistance near $I = 0$. (b) Microwave spectra for $H = 2.0$ kOe, for I =2 mA (bottom), 2.6, 3.6, 5.2 and 7.6 mA (top). Inset to (b), Spectrum at $H = 2.6$ kOe and $I = 2.2$ mA, for which both f and $2f$ peaks are visible on the same scan. Figures (a) and (b) taken from [49] (c) $dV = dI$ vs I with $\mu_0 H = 0.1$ T. High frequency spectra taken at several different values of current through the device, corresponding to the symbols in the dV/dI scan. Variation of f with I (inset). Figure taken from [50].

nals in zero applied magnetic field, an useful characteristic for on-chip applications not observed in more macrospin like devices. Additionally, by applying small magnetic fields along the hard axis, the free and reference layers can be phase locked together, acting to both amplify the resultant signal to integrated powers on the order of hundreds of pW and stabilize the precession against thermal fluctuations, producing linewidths down to 2 MHz. These enhancements, which could be easily incorporated into MTJs could eventually yield the required STO properties for development into applications.

REFERENCES

[1] M. Durlam, D. Addie, J. Akerman, B. Butcher, P. Brown, J. Chan, M. DeHerrera, B. N. Engel, B. Feil, G. Grynkewich, J. Janesky, M. Johnson, K. Kyler, J. Molla, J. Martin, K. Nagel, J. Ren, N. D. Rizzo, T. Rodriguez, L. Savtchenko, J. Salter, J.M. Slaughter, K. Smith, J. J. Sun, M. Lien, K. Papworth, P. Shah, W. Qin, R. Williams, L. Wise, S. Tehrani, *IEEE IEDM*, 995 (2003).

[2] Slonczewski J.C., Current-driven excitation of magnetic multilayers, *J. Magn. Magn. Mater* **159**, L1 (1996).

[3] Berger L., Emission of spin waves by a magnetic multilayer traversed by a current, *Phys. Rev. B* **54**, 9353 (1996).

[4] Tsoi M., Jansen A.G., Bass J., Chiang W.-C., Seck M., Tsoi V., & Wyder P., Excitation of a Magnetic Multilayer by an Electric Current, *Phys. Rev. Lett.* **80**, 4281 (1998).

[5] Myers E.B., Ralph D.C., Katine J.A., Louie R.N., & Buhrman R.A., Current-induced switching of domains in magnetic multilayer devices, *Science* **285**, 867 (1999).

[6] Katine J.A, Albert F.J., Buhrman R.A., Myers E.B., & Ralph D.C., Current-driven magnetization reversal and spin-wave excitations in Co/Cu/Co pillars, *Phys. Rev. Lett.* **84**, 3149 (2000).

[7] Papaconstantopoulos D.A., *Handbook of the band structure of elemental solids*, Plenum Press (1986).

[8] Stiles M.D. & Zangwill A., Noncollinear spin transfer in Co/Cu/Co multilayers, *J. Appl. Phys.* **91**, 6812 (2002).

[9] Stiles M.D. & Zangwill A., Anatomy of a spin-transfer torque, *Phys. Rev. B* **66**, 014407 (2002).

[10] Stiles M.D., Spin-dependent interface transmission and reflection in magnetic multilayers, *J. Appl. Phys.* **79**, 5805 (1996).

[11] Upadhyay S.K., Louie R.N., & Buhrman R.A., Spin filtering by ultrathin ferromagnetic films, *Appl. Phys. Lett.* **74**, 3881 (1999).

[12] Baibich M.N., Broto J. M., Fert A., Van Dau F.N., Petroff F., Eitenne P., Creuzet G., Friederich A., & Chazelas J., Giant magnetoresistance of (001)Fe/(001)Cr magnetic superlattices, *Phys. Rev. Lett.* **61**, 2472 (1988).

[13] Binasch, G., Grünberg, P., Saurenbach, F. & Zinn, W., Enhanced magnetoresistance in layered magnetic structures with antiferromagnetic interlayer exchange, *Phys. Rev. B* **39**, 4828 (1989).

[14] Pratt. Jr. W.P., Lee S.F., Slaughter J.M., Loloee R., Schroeder P.A., & Bass J., Perpendicular giant magnetoresistances of ag/co multilayers , *Phys. Rev. Lett.* **66**, 3060 (1991).

[15] Valet T. & Fert A., Theory of the perpendicular magnetoresistance in magnetic multilayers, *Phys. Rev. B* **48**, 7099 (1993).

[16] Gilbert T.L., A phenomenological theory of damping in ferromagnetic materials, *IEEE Trans. Magn.* **40**, 3443 (2004).

[17] Schreiber F., Pflaum J., Frait Z., Muhge T., & Pelzl J., Gilbert damping and g-factor in Fe(x)Co(1-x) alloy films, *Solid State Comm.* **93**, 965 (1995).

[18] Tserkovnyak Y., Brataas A., & Bauer G.E.W., Enhanced Gilbert Damping in Thin Ferromagnetic Films, *Phys. Rev. Lett.* **88**, 117601 (2002).

[19] Tserkovnyak Y., Brataas A., & Bauer G.E.W., Dynamic stiffness of spin valves, *Phys. Rev. B* **67**, 140404 (2003).

[20] Heinrich B., Tserkovnyak Y., Woltersdorf G., Brataas A., Urban R., & Bauer G.E.W., Dynamic exchange coupling in magnetic bilayers, *Phys. Rev. Lett.* **90**, 187601 (2003).

[21] Emley N.C., Krivorotov I.N., Garcia A.G.F., Ozatay O., Sankey J.C., Ralph D.C., & Buhrman R.A., Time-resolved spin torque switching and enhanced damping in Py/Cu/Py spin-valve nanopillars, *Phys. Rev. Lett.* **96**, 247204 (2006).

[22] Ozatay O., Gowtham P.G, Tan K.W., Read J.C., Mkhoyan K.A., Thomas M.G., Fuchs G.D., Braganca P.M., Ryan E.M., Thadani K.V., Silcox J., Ralph D.C., & Buhrman R.A., Sidewall oxide effects on spin-torque- and magnetic-field-induced reversal characteristics of thin-film nanomagnets, *Nature Mater.*, in press (2008).

[23] Xiao J., Zangwill A., & Stiles M. D., Boltzmann test of Slonczewski's theory of spin-transfer torque, *Phys. Rev. B* **70**, 172405 (2004).

[24] Slonczewski J.C., Currents and torques in metallic magnetic multilayers, *J. Magn. Magn. Mater.* **247**, 324 (2002).

[25] Braganca P.M., Krivorotov I.N., Ozatay O., Garcia A.G.F., Emley N.C., Sankey J.C., Ralph D.C., & Buhrman R.A., Reducing the critical current for short-pulse spin-transfer switching of nanomagnets, *Appl. Phys. Lett.* **87**, 112507 (2005).

[26] Sun J.Z., Spin-current interaction with a monodomain magnetic body: A model study, *Phys. Rev. B* **62**, 570 (2000).

[27] Tulapurkar A.A., Suzuki Y., Fukushima A., Kubota H., Maehara H., Tsunekawa K., Djayaprawira D.D., Watanabe N., & Yuasa S., Spin-torque diode effect in magnetic tunnel junctions, *Nature* **438**, 339 (2005).

[28] Sankey J.C., Braganca P.M., Garcia A.G.F., Krivorotov I.N., Buhrman R.A., & Ralph D.C., Spin-transfer-driven ferromagnetic resonance of individual nanomagnets, *Phys. Rev. Lett.* **96**, 227601 (2006).

[29] Fuchs G.D., Sankey J.C., Pribiag V.S., Qian L., Braganca P.M., Garcia A.G.F., Ryan E.M., Li Z.P., Ozatay O., Ralph D.C., & Buhrman R.A., Spin-torque ferromagnetic resonance measurements of damping in nanomagnets, *Appl. Phys. Lett.* **91**, 062507 (2007).

[30] Sankey J.C., Cui Y.T., Sun J.Z., Slonczewski J.C., Buhrman R.A., & Ralph D.C., Measurement of the spin-transfer-torque vector in magnetic tunnel junctions, *Nature Phys.* **4**, 67 (2008).

[31] Moser A., Takano K., Margulies D.T., Albrecht M., Sonobe Y., Ikeda Y., Sun S., & Fullerton E.E, Magnetic recording: advancing into the future, *J. Phys. D: Appl. Phys.* **35**, R157 (2002).

[32] Moodera J.S., Kinder L.R., Wong T.M., & Meservey R., Large magnetoresistance at room temperature in ferromagnetic thin film tunnel junctions, *Phys. Rev. Lett.* **74**, 3273 (1995).

[33] Julliere M., Tunneling between ferromagnetic-films, *Phy. Lett. A* **54**, 225 (1975).

[34] Meservey R., Tedrow P.M., Spin-polarized electron-tunneling, *Phys. Rep.* **238**, 173 (1994).

[35] Parkin S.S.P., Kaiser C, Panchula A, Rice PM, Hughes B, Samant M, & Yang SH, Giant tunnelling magnetoresistance at room temperature with MgO (100) tunnel barriers, *Nat. Mater.* **3**, 862 (2004).

[36] Yuasa, S., Nagahama, T., Fukushima, A., Suzuki, Y. & Ando, K., Giant room-temperature magnetoresistance in single-crystal Fe/MgO/Fe magnetic tunnel junctions, *Nat. Mater.* **3**, 868 (2004).

[37] Butler W.H., Zhang X.-G., Schulthess T.C., & MacLaren J.M., Spin-dependent tunneling conductance of FezMgOzFe sandwiches, *Phys. Rev. B* textbf63, 054416 (2001).

[38] http://www.seagate.com/ww/v/index.jsp?locale=en-US&name=Seagate_Swings_%22HAMR%22_To_Increase_Disc_Drive_Densities_By_A_Factor_Of_100&vgnextoid=46e18adc5448d010VgnVCM100000dd04090aRCRD

[39] Ryan E.M., Ph.D. thesis, Cornell University (2008).

[40] Chappert C., Fert A., & Van Dau F.N., The emergence of spin electronics in data storage, *Nat. Mater.* **6**, 813 (2007).

[41] Engel B.N., Akerman J., Butcher B., Dave R.W., DeHerrera M., Durlam M., Grynkewich G., Janesky J., Pietambaram S.V., Rizzo N.D., Slaughter J.M., Smith K., Sun J.J., & Tehrani S., A 4-Mb toggle MRAM based on a novel bit and switching method, *IEEE Trans. Magn.* **41**, 132 (2005).

[42] Savtchenko L., Korkin A.A., Engel B.N., Rizzo N.D., Deherrera M.F., & Janes J.A., U.S. Patent No. 6,545,906 B1, April 8 (2003).

[43] Fuchs G.D., Emley N.C., Krivorotov I.N., Braganca P.M., Ryan E.M., Kiselev S.I., Sankey J.C., Ralph D.C., Buhrman R.A., & Katine J.A., Spin-transfer effects in nanoscale magnetic tunnel junctions, *Appl. Phys. Lett.* **85**, 1205 (2004).

[44] Huai Y.M., Albert F., Nguyen P., Pakala M., & Valet T., Observation of spin-transfer switching in deep submicron-sized and low-resistance magnetic tunnel junctions, *Appl. Phys. Lett.* **84**, 3118 (2004).

[45] Hosomi M., Yamagishi H., Yamamoto T., Bessho K., Higo Y., Yamane K.,

Yamada H., Shoji M., Hachino H., Fukumoto C., Nagao H., & Kano H., A novel nonvolatile memory with spin torque transfer magnetization switching:Spin-RAM, *IEDM Tech. Dig.*, 459 (2005).

[46] Kawahara T., Takemura R., Miura K., Hayakawa J., Ikeda S., Young Min Lee, Sasaki R., Goto Y., Ito K., Meguro T., Matsukura F., Takahashi H., Matsuoka H., & Ohno H., 2 Mb SPRAM (SPin-Transfer Torque RAM) with bit-by-bit bi-directional current write and parallelizing-direction current read, *ISSCC Dig. Tech. Papers*, 480 (2007).

[47] Read J.C., Ph.D. thesis, Cornell University (2008).

[48] Kittel C., *Introduction to Solid State Physics* 7th edn, 505 (John Wiley & Sons, New York, 1996).

[49] Kiselev S.I., Sankey J.C., Krivorotov I.N., Emley N.C., Schoelkopf R.J., Buhrman R.A., & Ralph D.C., Microwave oscillations of a nanomagnet driven by a spin-polarized current, *Nature* **425**, 380 (2003).

[50] Rippard W.H., Pufall M.R., Kaka S., Russek S.E., & Silva T.J., Direct-current induced dynamics in Co90Fe10/Ni80Fe20 point contacts , *Phys. Rev. Lett.* **92**, 027201 (2004).

[51] Pribiag V.S., Krivorotov I.N., Fuchs G.D., Braganca P.M., Ozatay O., Sankey J.C., Ralph D.C., & Buhrman R.A., Magnetic vortex oscillator driven by d.c. spin-polarized current, *Nat. Phys.* **3**, 498 (2007).

[52] Pufall M.R., Rippard W.H., Schneider M.L., & Russek S.E., Low-field current-hysteretic oscillations in spin-transfer nanocontacts, *Phys. Rev. B* **75**, 140404 (2007).

CHAPTER 3

FABRICATION

3.1 Introduction

The development of innovative magnetic nanostructures has driven extraordinary growth in the field of nanomagnetics, so in this chapter I will discuss the critical aspects of fabricating the devices discussed later in this dissertation. It is no coincidence that the field of spin transfer exploded with the development of magnetic nanopillars at Cornell [1], and since then interest in spintronics has motivated scientists and engineers to improve current nanofabrication techniques in an effort to upgrade present technologies and innovate future ones. Some of the happiest times in my graduate career involved countless hours spent investigating strategies for new magnetic devices at the Cornell Nanoscale Science and Technology Facility (CNF), spinning electron beam resists, etching oxide films, or characterizing structures using scanning electron microscopy. I have benefitted tremendously from the wealth of experience at Cornell University including the trained staff at CNF and my fellow members of the Buhrman group. In particular, I would like to thank Frank Albert, Nathan Emley, Ozhan Ozatay, and Andrei Garcia for guidance and/or assistance in all my fabrication projects. As I prepare for the next stage of my professional career in designing, processing, and characterizing spintronic devices, I hope that I have left the younger students a healthy interest in developing new devices, because without process development, nanomagnetics is doomed to stagnate.

As several previous students have already left very detailed descriptions of the nanopillar fabrication process currently used by the group [2, 3], this section will

focus on specific contributions I have made to upgrade the fabrication process. The majority of these contributions involve advancements in electron beam lithography (EBL) made necessary by our requirements for low spin transfer critical current spin valve devices and the limitations of our e-beam writer, which in this case is the Leica VB6 currently in use at the CNF. I will discuss electron proximity issues giving rise to pattern distortion, as well as strategies for pattern design and exposure that help minimize these effects. Directions for writing an e-beam exposure file will also be included to assist the reader in the complete e-beam patterning of any desired wafer level system.

The second part of this chapter deals with hydrogen silsesquioxane (HSQ), a spin-on glass developed by Dow Corning as a self-planarizing insulator that also has useful qualities as a negative tone e-beam resist. Here, I will show that the reduced electron sensitivity of HSQ is useful in patterning individual features with very small separation between them, a characteristic I exploited to fabricate closely spaced nanopillars. In addition, the properties of HSQ are very similar to SiO_2, making it an ideal insulating layer for nanopillars when treated properly, since the self-planarizing properties of the spin-on glass eliminate critical steps from the current nanopillar process, shortening the overall time required for fabricating devices. An added advantage may come from the smaller dielectric constant of HSQ compared to SiO_2, which would lower device capacitance and reduce shunting of RF signals, although this has yet to be shown. To conclude, I will outline a process using HSQ as both insulator and e-beam resist for nanopillar devices. Results from devices fabricated by this method indicate that device performance is as good as devices using PECVD silicon oxide.

A discussion of the design, fabrication, and measurement of a three-terminal

nanopillar concept I developed has been left for Chapter 7. This device represents the culmination of efforts from many people, all of whom I am greatly indebted to. I would especially like to thank Nathan Emley for motivating interest in this structure, my advisor Bob Buhrman for his input into the device design, and Jordan Katine for his input and for the actual fabrication of the devices.

3.2 Electron Beam Lithography (EBL)

3.2.1 Pattern Design

Patterning of critical submicron sized features is an integral aspect of nanomagnetics, from track widths of hard drive read/write heads [4], to tunnel junction sizes for integration with memory architectures [5]. As required storage densities increase in these technologies, optical lithography techniques will begin to lag behind in providing necessary feature sizes, making electron beam lithography (EBL) an attractive option for rapid prototyping and process development. EBL has also become an important tool for studying spin transfer phenomena, since nanometer scale features are required to ensure large enough current densities to provide sufficient angular momentum for exciting a nanomagnet. Initial experiments performed at Cornell [1, 6] involved elliptical devices estimated to be on the order of 60x130 nm^2, which were sufficient for verifying spin transfer as a valid magnetotransport effect. However, DC reversal currents for these devices were on the order of milliamps, unsuitable for use in practical applications. One method for reducing these currents involves significantly reducing the nanomagnet dimensions, a strategy requiring additional EBL development to pattern smaller shapes. Before

outlining the procedure for producing these small shapes, we must first explore the limiting mechanisms involved with EBL.

Several factors contribute to pattern distortion that become especially significant as device dimensions approach the minimum resolution of the e-beam tool, which is typically on the order of 4-5 nm. These include:

1) Electron proximity effects

2) Resist development and swelling

3) Electron beam voltage

4) Stability of the EBL tool

Here, the first two issues are specific to the particular e-beam resist exposed, while the second two are more general issues tied to the particular tool used for the exposure. Since CNF users are not allowed to vary the specs of the VB6 system or work with its hardware, I focused specifically on resist processing techniques. The resist chosen for this particular experiment was Poly(methyl methacrylate) (PMMA), a spin-on form of fiberglass. When exposed to high energy electrons, this polymer becomes broken into fragments, which can then be preferentially dissolved and removed in a developer solution. PMMA is an extremely versatile resist, with excellent adhesion to the multilayers used in our experiments, low film stress after spin on, and negligible swelling during development. It is also robust enough to survive through subsequent processing steps and is removed easily and controllably using a solvent such as acetone.

Electron proximity effects involve depositing energy into non-exposed resist regions due to electron scattering within the resist and underlying layers. By modeling the electron beam as a point source, this energy density can be described

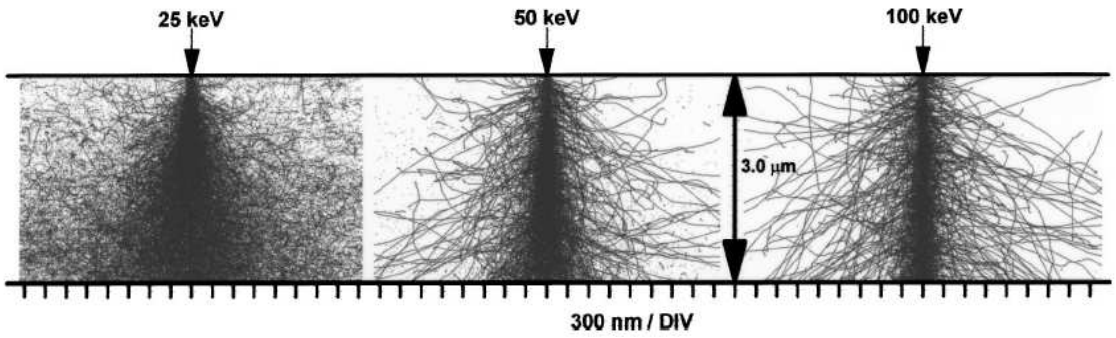

Figure 3.1: Monte Carlo simulations of electron scattering within a PMMA resist layer as a function of the electron beam voltage taken from [4]. As the beam voltage increases, the amount of forward scattering significantly decreases. Our VB6 tool operates at 100 kV, so we expect the majority of proximity effects to occur due to backscattered electrons, which changes critical doses for device exposure depending on the particular layer structure of the wafer. The simulations for 25, 50, and 100 kV use 6000, 15,000, and 30,000 electrons respectively.

using a double gaussian expression [7, 8]:

$$f(r) = \frac{1}{\pi(1+\eta)}\left[\frac{1}{\alpha^2}exp\left(\frac{-r^2}{a^2}\right) + \frac{\eta}{\beta^2}exp\left(\frac{-r^2}{\beta^2}\right)\right], \tag{3.1}$$

where r is the distance from the point of incidence, α, β are distances representing the scattering lengths for forward and backscattered electrons respectively, and η is the deposited energy ratio of backscattered to forward scattered electrons. For an EBL system operating at 100 kV, as is the case for the VB6, only backwards scattered electrons are expected to significantly contribute to proximity effects (see Fig. 3.1). Pattern exposure occurs by rastering the electron beam over the desired region of resist, which can be approximated as individual pixels each the width of the electron beam. The distributed energy within each pixel falls off with distance from the center, but at pattern edges, these contributions can sum up to contribute enough energy to expose the resist in regions not traced out by the electron beam. This can contribute to the pattern distortions shown in Fig 3.2, effects that become much more significant as the pattern size decreases. Several solutions for correcting these proximity effects have been proposed [7, 8] involving

the use of simulated energy distributions to break patterns into several smaller shapes that after exposure and development produce the original pattern. More recently, CAD programs for designing lithographic patterns such as PROXECCO [9, 10] have emerged using a similar strategy without the user needing to explicitly calculate energy distributions. As I did not have access to these programs during this project, I made educated guesses in designing non-elliptical shapes that would become approximately elliptical after development due to proximity effects. These include dumbbells, rectangles, and systems of squares with 10 and 20 nm spacing as shown in Fig. 3.3(a), (c), and (e). By relying on detailed characterization of different doses and development methods for these devices as described below, I was ultimately able to pattern approximately elliptical shapes with minimum dimensions shown in Fig. 3.3(b), (d), and (f).

The number of electrons required to impart sufficient energy into the resist to break the polymer apart is referred to as the critical electron dose, defined in units of $\mu C/cm^2$. Critical doses depend on the particular electron beam resist used and the development method involved in removing the exposed resist. This makes the development procedure chosen extremely important in successfully exposing small shapes. One developer that has proven effective in producing small pattern without distortion is LIGA, a mixture of 2-(2-butoxyethoxy) ethanol, morpholine (tetrahydro-1,4-oxazine), ethanolamine (aminoethanol), and water [11]. However, this solution is toxic, carcinogenic, and mutagenic, making its use extremely undesirable. Another strategy uses a solvent/non-solvent combination of methyl isobutyl ketone (MIBK) and isopropanol (IPA), where MIBK is a strong solvent for PMMA and IPA acts to dilute and weaken the developer. However, MIBK has been known to cause swelling in PMMA layers, sometimes leading to a pinching off of the resist at the top interface [4] (see Fig. 3.4), a catastrophic event if deposi-

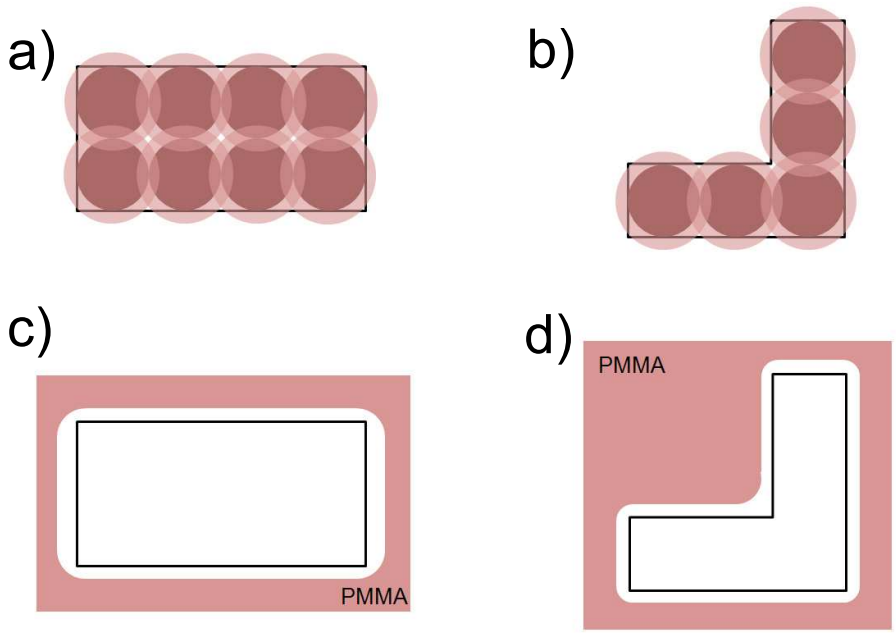

Figure 3.2: (a)-(b) Examples of electron energy distributed into resist during an exposure. Dark spots represent the actual electron beam with lighter halos represented energy imparted from backscattered electrons. When the energy in the halo regions is sufficient, distortions to the original patterns occur, as illustrated in (c)-(d), the final pattern in the resist after development. Proximity effects act to round off edges and increase the overall size of the pattern.

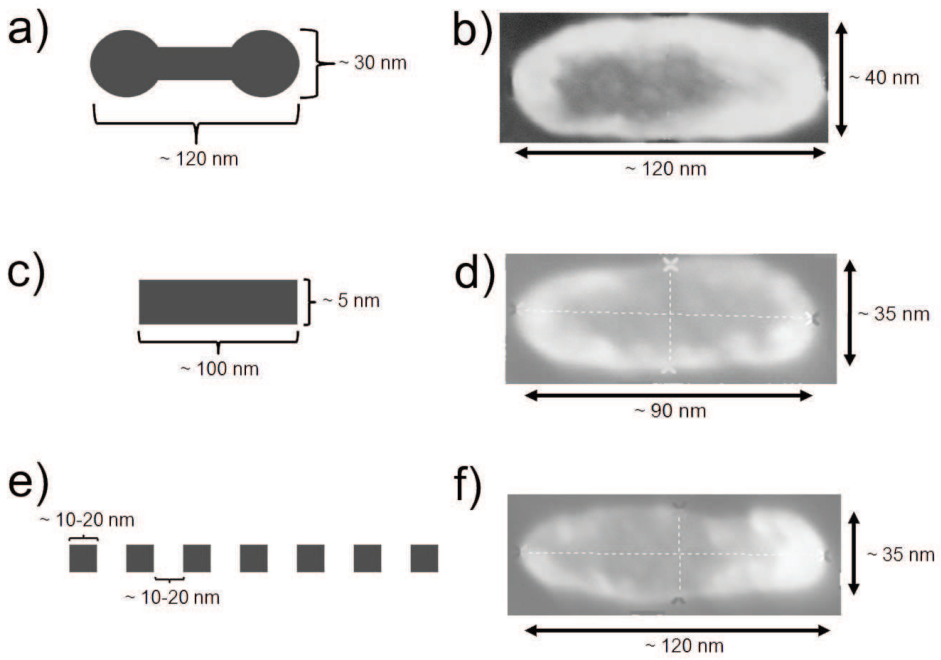

Figure 3.3: (a), (c), (e) Shapes exploiting proximity effects to produce small area patterns that are approximately elliptical. Different regions of each pattern can be assigned a different electron dose to assist in pattern distortion. For example, in the dumbbell shape (a), the circular ends can be defined as layer or datatype 1 in the CAD program used, while the rectangular region can be defined as layer or datatype 2. During pattern conversion, these regions are then associated with separate "clocks" that the VB6 uses to assign the time the beam dwells in a region of resist. (b), (d), (f) SEM micrographs of a Cr mask created by evaporation and liftoff after EBL for each shape. These results represent the optimal dimension for each shape and required extensive characterization to achieve. I note that even with all this work, dimensions for these patterns can fluctuate by 10-15 nm due to tool and processing fluctuations.

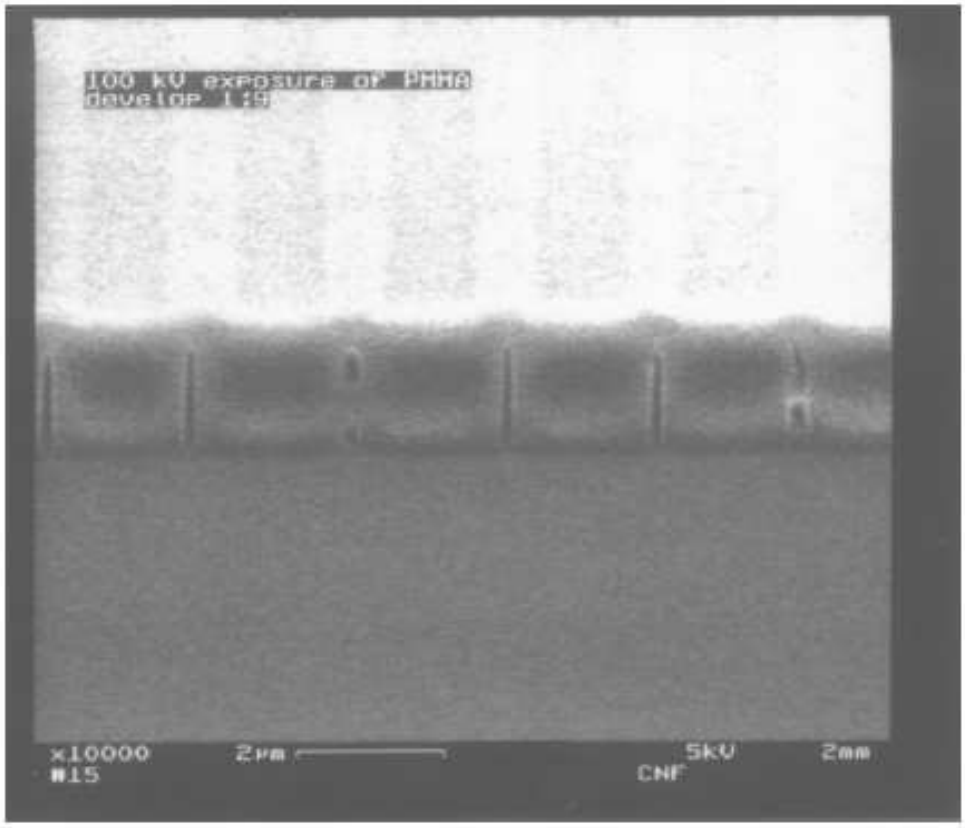

Figure 3.4: Swelling of PMMA with MIBK/IPA development, resulting in pinch off of the resist at the top of the layer. This effect significantly reduces the effectiveness of the exposure, especially if deposition and liftoff of another material is a subsequent step. Figure taken from [4]

tion and liftoff of another material is the next processing step, as it is in processing nanopillars. A final option is a solution of IPA/DI water, which is a surprising choice since neither water nor IPA are effective solvents of PMMA. However, this mixture acts as a co-solvent, with a solvent strength stronger than either of the individual components, a mechanism attributed to a modification of the alcohol molecule in the presence of water or alternatively to the interaction of water with the PMMA carbonyl group [12]. Combining this choice of developer with ultrasonic agitation assists PMMA removal in exposed regions, and has resulted in high resolution patterns in thin PMMA [13–15]. This is the strategy that I eventually settled upon for developing the devices discussed in later chapters.

One parameter I left unexplored is the temperature of the developer bath, which has been shown [4] to reduce resist sensitivity (i.e. more electron charge required for exposure) and increase pattern contrast as temperature decreases from room temperature to 0° C. An interesting experiment might be to explore if even smaller shapes could be patterned by cooling the developer bath.

As previously discussed, I chose patterns that take advantage of electron proximity effects to return approximately elliptical shapes after development. Before exposing wafers in our EBL tool, I had to create the FRE pattern files input by the VB6 into its pattern generator. A CAD program such as PED on the VAX Decterms available in CNF's computer room or LEDIT can be used to draw these patterns and generate a GDS file that then has to be converted into FRE format. Discretized areas of each pattern can be assigned different electron doses by means of "clocks" calculated by the VB6's pattern generator. A clock represents the amount of time the electron beam dwells on a certain region of resist, so as to deposit the requisite electron charge into the resist. Clock assignment is done in

the CAD program by assigning each region of the shape to a pattern "layer" or "datatype", as described in the caption of Fig. 3.3. If using PED, a GDS file must be created, which is done using the Dracula pattern converter found on the same Decterms as PED. The procedure for creating a FRE pattern file is as follows:

– Open the directory in which your PED library resides.

– At the prompt, type `symbgds` and enter.

– You will be prompted to enter your PED library name.

– You will then be prompted for your pattern file name as defined in PED.

– Press enter when asked for a reference library.

– You will then be prompted for a GDS filename, enter *filename*.gds.

– Press enter when prompted for text conversion factor.

– Press enter when asked for more options.

– Press enter when asked for output unit.

At this point, a GDS file will be input into the current directory.

If you use LEDIT or a similar CAD program, files can be directly output to GDS format for use in the next step. However, LEDIT does contain an option for directly designing elliptical patterns, although ellipses defined in alternative CAD programs (such as PED or autoCAD) can be edited, so some assistance may be required for using LEDIT.

Conversion of GDS files to FRE format makes use of the Computer Aided Transcription System (CATS) conversion suite installed on the CATS server at CNF. Contact someone on staff to obtain an account on this computer. Login can be made on any of the PC's in CNF's computer room through the use of the Hummingbird connection software. The procedure for using CATS is as follows:

– Log in to the CATS server and open the CATS directory.

– You must FTP the GDS files you want converted into this directory. This can only be done by connecting from the directory on CATS due to the firewalls placed on the CNF servers.

– When the GDS files to be converted are in the CATS directory, type `CATS`.

– CATS opens with 4 main windows, a terminal for typing commands, a window with a description of the type of file being converted to, a smaller window with options that can be selected, and a window for visually displaying the defined pattern. From the option window, select VB6 as the filetype. This should change the information window to VB6 file format and also change the options available in the option window.

– Type `readfile` *filename*`.gds` and hit enter.

– Type `input` *filename*`.gds` and hit enter. The pattern name should show up in the information window and also in the pattern visualization window.

– Type `datalayers`. Then type in the layers you want used in the conversion, especially if assigning more than one exposure clock.

– In the options window, click on *CFA by layer* or *CFA by datatype*, depending on how dose regions were defined in the CAD program. This option assigns different clocks (up to 32) to individual layers that have been defined in the CAD programs.

– Type `extent`. The field size (area of bounding box) will be displayed in μm.

– Type `do`. This discritizes the pattern into smaller polynomials which can be handled by the VB6 pattern generator. It outputs a .cflt file that must be used in the final step.

– Finally, type in `writefile` *filename*`.cflt`. The exact filename can be searched for in the CATS directory. You will be prompted to give a filename which should be *filename*`.fre`. An FRE file should now be available in the CATS file. FTP vb6b.cnf.cornell.edu from CATS to send the file to the VB6 for the next step.

At this point, you can check FRE files on the vb6b computer using the program `cview`.

3.2.2 Pattern Dose Testing

Designing and converting these pattern files is just one half of the challenge in exposing these small area devices. Meticulous characterization is also required to determine the critical electron doses necessary for reliably exposing a pattern with the smallest possible dimensions. These critical doses are dependent on several factors, such as the chemical sensitivity of the particular resist(s) used, the particular multilayer structure of the wafer underneath the resist, the stability of the particular ebeam tool used, and the particular developer chosen for the exposure. For my experiments, I chose a bilayer resist structure using two different molecular weights of PMMA. Here, higher sensitivity 495K molecular weight PMMA (4%) is the bottom layer, and lower sensitivity 950K molecular weight PMMA (2%) is the top layer, providing an undercut profile in the resist after development that is beneficial for subsequent liftoff steps.

The VB6 at CNF is a multiuser tool used for a variety of different processes, creating issues with beam calibration and electron current drift. Short of frequent maintenance on the tool, there are several methods for optimizing the performance of the tool prior to an exposure. One method I suggest is to always run the initialization programs, `hc1`, which initializes the 3" wafer stage, `foc` for focusing the electron beam, and `jobcal` for each wafer exposed. While executing these programs, there are various times where the electron beam is used as an SEM, rastering over an octagonal focus mark, which can be viewed on the LCD monitor provided at the tool. Although it takes additional time, if the focus mark appears

blurry after running these programs, I suggest running `foc` and `jobcal` again until the focus mark edges look sharp. Additional issues occur due to drift of the electron beam current, from which the frequency of a "clock" is calculated. Dose requirements for these small patterns increase sensitivity to even the smallest fluctuations in beam current, so a useful suggestion I make is to frequently remeasure the beam current using the Faraday cup located inside the tool. I will discuss the computer command controlling this action in the next section when I review the composition of an exposure file.

An interesting consequence of electron scattering during exposure is the dependence of required electron dose on the layer structure of the wafer, since interfaces dominate the backscattering behavior of the electrons within the films. This indicates that particular attention must be paid in characterizing critical doses every time the underlying multilayer stack has been significantly modified. To accomplish this, I have designed a test program targeted toward exposing a dose array of various pattern files. In an effort to replicate the exposure method used for patterning measurement wafers, I recommend exposing individual devices and defining an array through stage movements rather than using a pattern with multiple devices within a single exposure field. The file for running this test resides on the VB6 computer in `[vb.users.pfj.jobs]single_device_dosetest_bot.com`. A schematic of one isolated dose array is shown in Fig. 3.5. In this array, devices within the same row of a 5x30 array are exposed with the same electron dose, and the dose increases at an interval designated by the user moving down each column. Following exposure, the developer I chose was a solution of 7:3 IPA:DI water, which can be prepared using a graduated cylinder to measure out the proper ratio. A soak of $\sim$ 30-60 sec is followed by a 30-45 sec sonication to remove the exposed regions of resist.

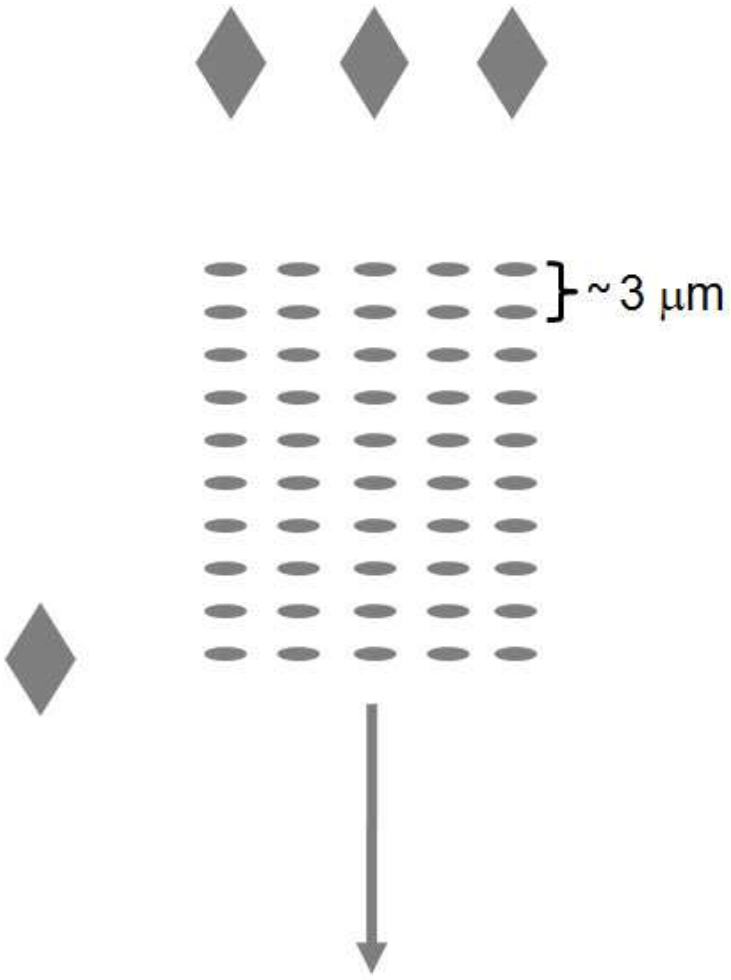

Figure 3.5: Dose exposure array for e-beam patterns. Each array is defined by individually exposing single ellipses and moving the wafer, the same exposure scheme used in measurement wafers. The default spacing between shapes is 3 μm, but can be chosen by the users. Micron sized diamond patterns are used as reference marks to both located the array in an SEM and to determine the row number, which corresponds to a particular electron dose.

Following chrome evaporation and lift off, the pattern will be transferred into the chrome, which can then be imaged using scanning electron microscopy. This allows the user to measure the exposed patterns and determine what dimensions are reasonably achievable. Micron-sized diamonds are placed adjacent to every tenth row of the array to determinate the particular row and dose of interest. At this point, the user has everything required to expose an actual measurement wafer.

3.2.3 Writing Exposure Files

In the following section, I will review a typical jobfile (COM) file I have used for fabricating nanopillar devices. These files are available on the VB6 computer in the `[vb.users.pfj.jobs]` directory. For additional descriptions of all the commands involved, I direct the reader to VB6 literature available in the `[vb.users.howto.userinfo]` directory, particularly the user manual `878275-2-7-VECTORBEAMOPERATORMANUAL.PDF` and command set `VECTORBEAMCOMMANDSETV04_14.HTML`. One final tool worth mentioning is `vbq`, an emulator for running virtual exposures. To use this program, type `@[vb.users.vbsym]vbq` in the directory containing your jobfile, and then type `@`*jobfilename*. The simulator will run through the jobfile program displaying any outputs associated with the program, but with the commands to the VB6 tool dummied out. Programming errors will be noted, which is extremely useful for debugging purposes.

`STANDARD_EXP_HF_16DEV_BOT.COM:`

```
$!  ALBERT-EXPOSE 16 PADS IN 9X9 5MM SPACED ARRAY
$!  HEIGHT SENSOR ON
```

```
$!  CENTERED WAFER.
$!  UNALIGNED.
$!
$   WS :== WRITE SYS$OUTPUT
$   WS ‘‘ ’’
$   WS ‘‘ ’’
$   WS ‘‘COM FILE WRITTEN BY NATHAN EMLEY - EDITED BY PAT BRAGANCA’’
$   WS ‘‘ ’’
$   WS ‘‘ ’’
$!
$   WAIT 00:00:05
```

The general format for a VB6 jobfile contains a $ header for each command line. Exclamation marks are used to comment out a line, as shown in the first four lines of this block, which describe the array defined by the stage moves. The command `WS :== WRITE SYS$OUTPUT` creates a logfile used as a debugging guide for system errors occurring during exposures. The command `ws`, or write screen, displays text contained in quotation marks. The final `Wait` command pauses the system for 5 sec before moving to the final lines of code.

```
$!============================
$! CALIBRATION
$!============================
$   SFAB                                ! FAB MODE, BEAM OFF
$   QSET CORR ON/ALL                    ! TURN ON ALL CORRECTIONS
$   QSET HEIGHT/REALTIME                ! SET REAL TIME HGT CORR.
$   QSET SORT NORMAL                    ! NORMAL PATTERN SORTING
```

```
$!
```

Two commands control the status of the electron beam in the tool, `SFAB` and `SSEM`. Using `SFAB` as shown above puts the system into fabrication mode, blanking the beam using an electromagnetic lens to make it is safe for the stage to move without the beam exposing the resist. When the stage reaches the desired position, the beam can then be turned on temporarily to expose a pattern, and then turned off for the next stage move. `SSEM` turns off beam blanking so the electron beam is used to image the wafer surface, similar to an SEM . Extensive imaging is not suggested as the PMMA is exposed at the same time. `QSET CORR ON/ALL` and `QSET HEIGHT/REALTIME` turn on realtime height and beam focusing corrections and their use is recommended to compensate for system fluctuations during exposure runs. `QSET SORT NORMAL` defines the method the pattern generator uses to input FRE files, with the default being normal.

```
$!============================
$! DOSE SET UP
$!============================
$!
$   QSET VRU 1
$   QSET RESIST 1000            !100 KV EXPOSURE
$   QSET BAND .6 5 /RELATIVE_DOSE
$   DOSE0 := 1.20
$   SDSE 0 ‘‘DOSE0’’ /REL
$   ACLK /BCM=FC
$   QDISPLAY CLOCKS
$!
```

This block describes the method used for defining electron doses. `QSET VRU 1` sets the virtual resist unit for the VB6, which defines the beam step size. In other words, if we consider a pattern broken into "pixels" each the size of the electron beam, a VRU of 2 causes the tool to expose every other pixel, 4 every fourth pixel, and so on. For patterns on the order of hundreds of microns, changing the VRU is advantageous, but for the dimensions I was dealing with, a VRU of 1 was optimal. `QSET RESIST 1000` defines a dose value (in μC/cm^2) to which all inferences of dose in the program are normalized to. For simplicity, I set it to 1000. `QSET BAND .6 5 /RELATIVE_DOSE` is an obsolete command according to the user manual, but as it doesn't affect things either way, I left it in. This command is used to tell the pattern generator the range of dose values you are planning on exposing during the course of running the jobfile. From these values, the pattern generator calculates the range of clock frequencies required, depending on the dose, the VRU, the beam current, and the beam size. `DOSE0 := 1.20` and `SDSE 0 ''DOSE0'' /REL` set the desired clock dose to 1200 μC/cm^2, as the relative dose value 1.2 is multiplied by 1000. Finally, the commands `ACLK /BCM=FC` and `QDISPLAY CLOCKS` tell the pattern generator to calculate clock frequencies and display them on the screen. Adding the option `/BCM=FC` to `ACLK` tells the VB6 to move the electron beam to the internal Faraday cup and measure the beam current before performing calculations. This method is preferred to the more common `ACLK /DOSE` command due to beam current drift during the exposure period.

```
$!  ================================
$!  COORDINATE TRANSFORMATION
$!  ================================
$!
```

```
$!                    BOTTOM CENTRE: 39.15 59.32
$!                    TOP CENTRE: 118 129
$  DWMO ABS /LOAD
$  SSPO ZERO 0 0
$!
$  SSPO MIDDLE 118 129
$!
$  DWCO CHIP /EXP=(ZERO) /OBS=(MIDDLE)
$  DWMO CHIP /LOAD
$  MVPO 0 0
$  CHGT /TAB=1 ! HEIGHT TABLE FOR BRIGHT CHROME.
$                SEEMS TO WORK FOR AU
$  DHGT
$!
```

The last and most important initialization process is defining the wafer coordinate system. Here, the commented top lines remind the user of the center coodinates of the two wafer positions on the 3" wafer stage. The command `DWMO ABS /LOAD` places the system in absolute coordinate mode, where the origin is the mark known as circle1 (refer to staff for location on stage). `SSPO ZERO 0 0` labels the origin "Zero", while `SSPO MIDDLE 118 129` labels the position 118, 129 (with units in mm) as "Middle". `DWCO CHIP /EXP=(ZERO) /OBS=(MIDDLE)` is the direct write coordinate system command, and defines a coordinate system "chip" where the "Middle" position becomes the origin. `DWMO CHIP /LOAD` loads this coordinate system so that we are now accurately placing patterns on the wafer, and `MVPO 0 0` moves the stage to the wafer center. Both `CHGT /TAB=1` and `DHGT` define value for height corrections to the beam focus.

```
$!  PATTERN 1 - DASHED LINES
$!  ================================
$!
$   SPAT [VB.USERS.BRAGANCA.SHAPES]line_dashed_spaced.fre
$!
$   WS ‘‘ ’’
$   WS ‘‘THIS IS THE FIRST PATTERN’’
$   WS ‘‘ ’’
$!
$   XOFFSET := -1.90
$   YOFFSET := -1.80
$   @9X9GRID_hf
$!
$   XOFFSET := -1.90
$   YOFFSET := -0.60
$   @9X9GRID_hf
$!
$   XOFFSET := -1.90
$   YOFFSET := 0.60
$   @9X9GRID_hf
$!
$   XOFFSET := -1.90
$   YOFFSET := 1.80
$   @9X9GRID_hf
..........
```

Finally, we have reached the point of actually exposing a pattern! The command `SPAT [VB.USERS.BRAGANCA.SHAPES]line_dashed_spaced.fre` loads the pattern file listed into the pattern generator, so that when the expose pattern command `EPAT` is given at the desired position, the beam traces out the pattern. `XOFFSET` and `YOFFSET` define offsets in the x and y coordinates (in mm) indicating where the patterns should be placed. `@9X9GRID_hf` calls on a separate COM file which contains the actual stage motion and exposure commands for placing elements within a 9x9 array. I will stop here and direct the reader to review `9X9GRID_hf.com` for more details. At this point, the reader should have a sufficient understanding of the commands involved in writing a COM file to finish reviewing the programs mentioned above.

3.3 Hydrogen Silsesquioxane (HSQ)

Hydrogen Silsesquioxane is spin-on glass originally commercialized by Dow Corning under the trade name FOX or Flowable OXide. It was originally intended as a self-planarizing spin-on material for use as an intermetallic dielectric targeted to reduce RC delay in semiconductor technologies, with very low defect density, excellent gap fill, and low dielectric constant. More recently, HSQ has been used as a negative tone resist for high resolution patterning in both e-beam [17, 18] and optical (< 157 nm wavelengths) [19] lithography. These studies indicate that HSQ has excellent resolution capabilities and mechanical strength after electron-beam exposure and development, making it an idea candidate for device processing, as the demand for critical device dimensions continues to shrink. In an effort to update the group's fabrication process, I have integrated this extremely versatile substance into our nanopillar process, as both an electron beam resist (following up the work described

in [2]) and as a self-planarizing insulating layer which eliminates the planarization steps associated with the current process.

3.3.1 Uses as an Insulating Dielectric

To understand the properties of HSQ, we must first examine the structure of the molecule itself. HSQ is composed of much the same atoms as silica (SiO_2), with 8 Si, 12 O, and 8 H atoms arranged in a cage-like structure (see Fig. 3.6). Each Si atom lies at the center of a tetragonal arrangement of 3 O and 1 H atom, with each O atom shared between two tetrahedra, linking them within the cage [21]. At sufficient annealing temperatures, the weaker Si-H bonds begin to break apart and the cage structure reforms into a network structure of Si-O bonds, giving annealed HSQ similar electrical and mechanical properties to silica [22, 23]. Typical processing parameters involve curing wafers spun with HSQ on a hot plate for one minute each at 150, 200, and 350 °C to bake off the resist, initiate Si-H bond dissociation, and flow the HSQ to improve planarization, respectively. These short cures are typically followed by a longer furnace anneal, at temperatures between 350-500 °C to ensure complete dissociation of Si-H bonds, however as I will discuss shortly, this has a drastic effect on the dielectric constant of the material.

The low k properties of these films depends on the three dimensional porous network structure formed as Si-H bonds begin to dissociate during curing (see Fig. 3.7). Here, the porous nature of HSQ causes its dielectric constant to be an average of the dielectric constant of air ($k \sim 1.00059$) and pure SiO_2 ($k \sim 4 - 5$). Increasing the furnace annealing temperature dissociates increasing larger amounts of Si-H bonds, causing the structure to rapidly approach a perfect SiO_2 lattice and eliminating pores within the material. This leads to an increase in material density,

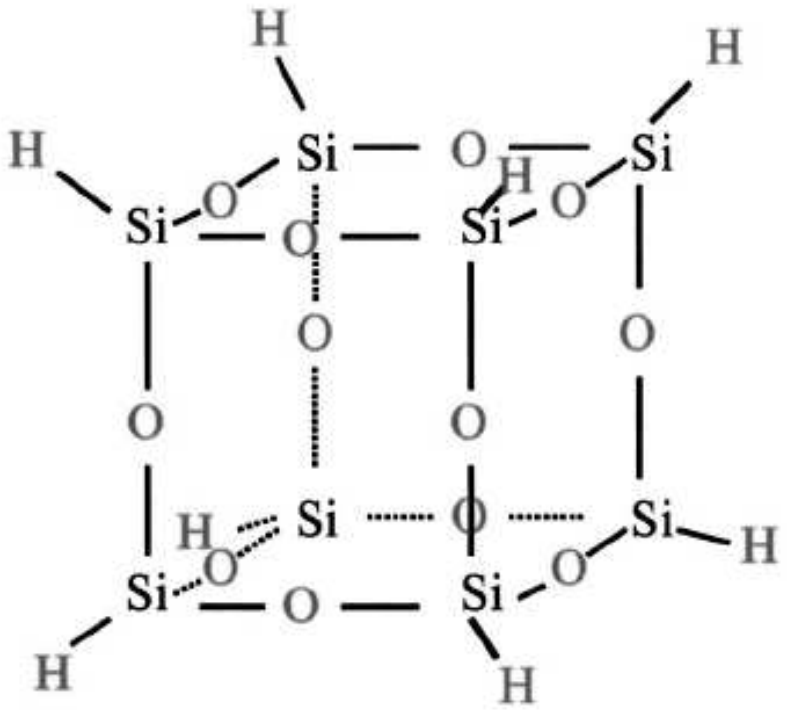

Figure 3.6: Cage structure of untreated HSQ. Treatment options include annealing, plasma oxidation, and electron beam exposure, all of which break the Si-H bond and lead to a reforming of the cage into a Si-O network structure. Figure taken from [20]

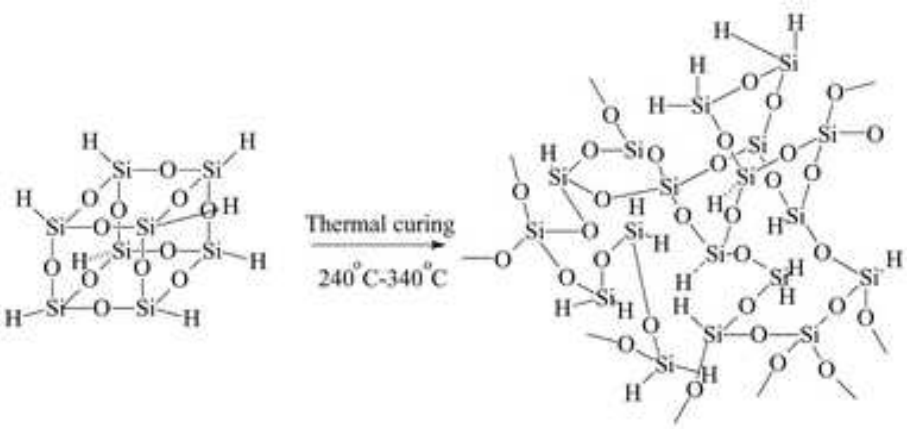

Figure 3.7: Example of realignment of HSQ from cage structure to network structure during annealing. Si-H are broken in the process, with the Si rebonding with O to reform the network. As temperature increases, more and more hydrogen bonds are broken, until a complete Si-O network lattice is formed, producing a insulating layer with the mechanical and electronic properties of conventional SiO_2. Figure taken from [24]

as verified by the decrease in HSQ film thickness with anneal temperature as shown in Fig. 3.8. Not surprisingly, the dielectric constant also increases from 2.7 to 3.8 within the same range of anneal temperatures, as the HSQ structure becomes more silica-like and pore density diminishes.

These properties, coupled with the self-planarizing properties of HSQ, make it an ideal replacement for the PECVD oxide currently used as the insulating layer for our nanopillars. I've used XR-1541, the Dow Corning HSQ follow-up to the venerable FOX brand, 22% in a solution of methyl isobutyl ketone (MIBK). This particular concentration produces a film thickness of $\sim$ 500 nm, 3-4X greater than feature sizes on the wafer, thereby ensuring planarization of the film above the nanopillar to within 10-15 nm. Thermal annealing at the temperatures mentioned above is not a realistic option for patterned nanopillars due to issues with Cu diffusion, so an alternative method of breaking the Si-H bonds is required to ensure required material properties and protect the film from subsequent processing

steps, specifically photolithography, which uses the same developer required for removing untreated HSQ. Luckily, exposing the film to an O_2 plasma, for example in an reactive ion etcher (RIE) tool, also acts to dissociate H atoms from the lattice and promote Si-O bonding. Plasma oxidation has been shown to increase the dielectric constant of HSQ [25, 26], however, these values remain lower than for PECVD deposited SiO_2, making HSQ a better choice as an insulator for RF measurements, such as DC current driven magnetization dynamics in magnetic nanopillars. A more complete description of this fabrication procedure is included at the conclusion of this chapter.

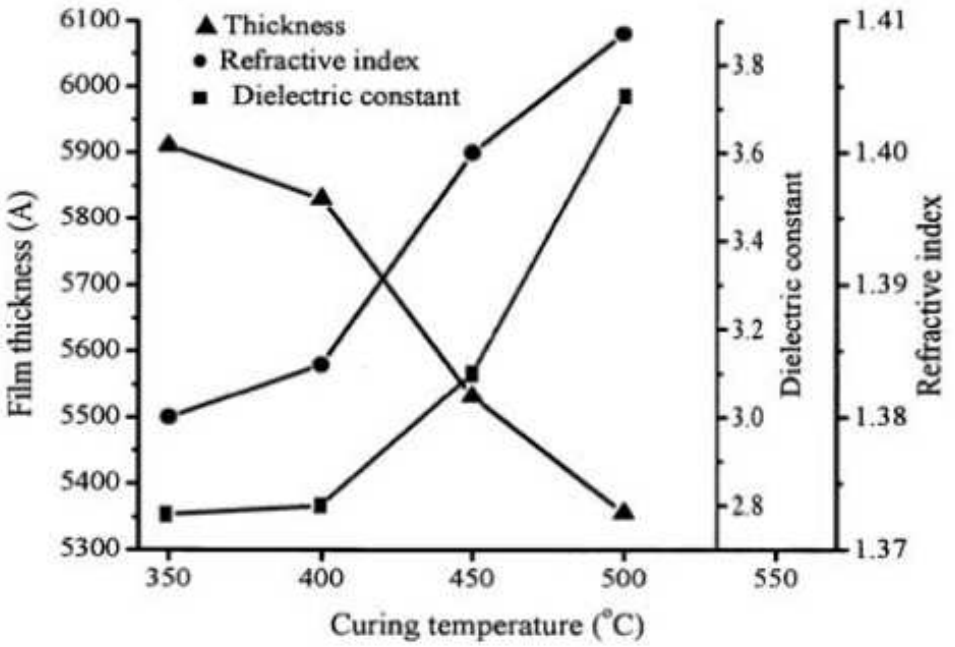

Figure 3.8: Various properties of HSQ as a function of anneal temperature taken from [25]. Annealing was performed by curing the spun on HSQ at 150, 200, and 300 °C each for one minute and then placing the wafer in an annealing oven for 1 hour at the temperatures plotted. The decrease in film thickness with anneal temperature indicates an increase in film density, corresponding to a changeover of the lattice from a cage to a network structure as shown in Fig. 3.7. This is accompanied by an increase in dielectric constant and refractive index as the porous nature of the HSQ is decreased by the lattice transition.

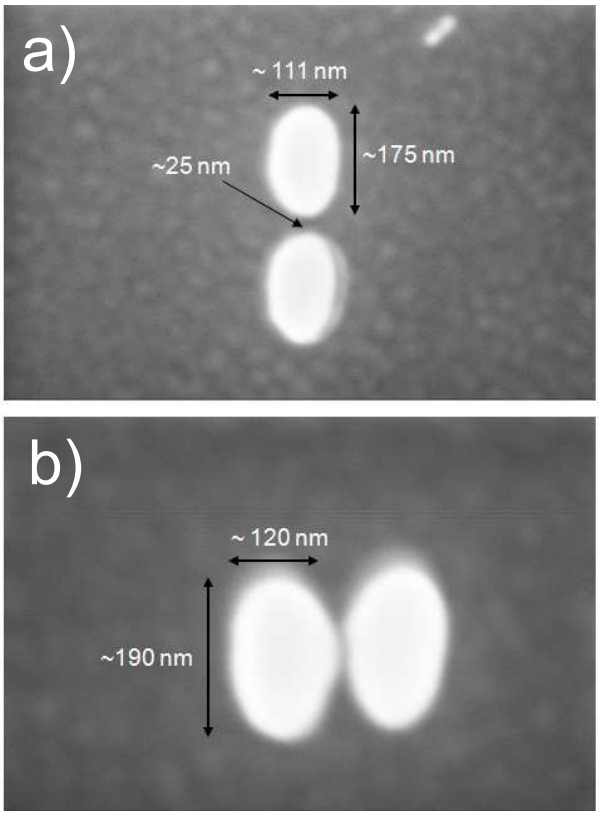

Figure 3.9: HSQ masks of coupled nanopillars. The experimental concept here was to fabricate adjacent nanopillars to try and phase lock current driven magnetization oscillations of the free layers through dipole field interactions. As the magnetic fields fall off rather quickly as a function of distance from the magnet, it was critical to pattern the pillars with as little separation as possible. The low electron beam sensitivity of HSQ makes it ideal for this application, although the doses required for small area patterns are extremely large, causing significant pattern distortion. Due to this fact, I chose to pattern larger elliptical patterns requiring a smaller dose. My result show distinct nanopillars can be patterned at separations approaching 20 nm either (a) head to tail or (b) side to side with relatively good results

3.3.2 Uses as an E-beam Resist

Bombardment of HSQ with high energy electrons can also break Si-H bonds in a manner similar to thermal annealing, making it an effective resist for EBL. Using a tetramethyl ammonium hydroxide (TMAH) based developer, such as the AZ 300 MIF developer currently in use at CNF, unexposed HSQ can be dissolved and removed. The sensitivity of HSQ is much lower than PMMA, making it an excellent choice for patterns spaced close together, where proximity effects can cause bleeding between patterns. Using the EBL characterization dose tests mentioned above, I was able to pattern devices as shown in Fig. 3.9 with spacings between nanopillars of less than 30 nm. Further details on using HSQ as an e-beam resist will be included in the following section outlining the use of HSQ for EBL and as the insulating dielectric.

3.4 Self-planarizing insulator HSQ nanopillar process

3.4.1 Fabrication Concept

A significant fraction of time spent in processing nanopillar wafers involves insulating the top and bottom electrodes of the nanopillar to ensure good electrical conduction through the nanopillar. At present, our process involves PECVD of SiO_2 as an insulator, requiring ion mill planarization of the oxide to ensure contact of the top electrode to the top of the nanopillar. Since HSQ is an insulating material spun onto a wafer, surface tension planarizes the HSQ film provided its thickness is substantially larger than the height of the nanopillar. Here, I outline a process for using HSQ as EBL resist and the insulating layer in fabricating

nanopillars, a choice reducing the amount of steps and time required for processing. Details for each step are included in the figure captions.

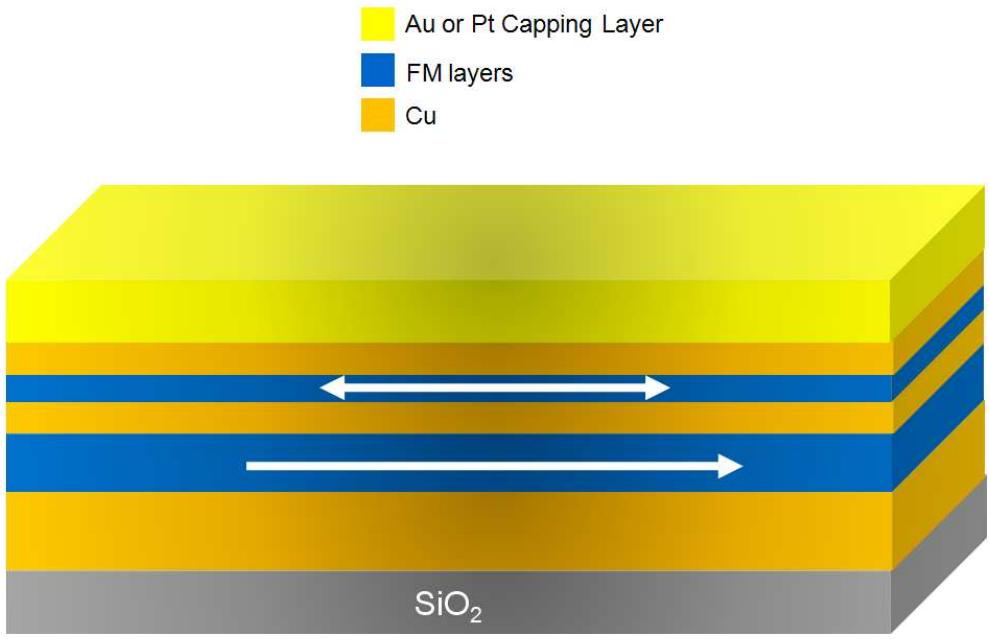

Figure 3.10: Sputter multilayers. Nanopillar fabrication begins by sputter deposition of the desired magnetic multilayers. For illustration purposes, I have shown a spin valve structure with a ferromagnet/Cu/ferromagnetic trilayer grown on a thick Cu layer and passivated with a Au or Pt capping layer.

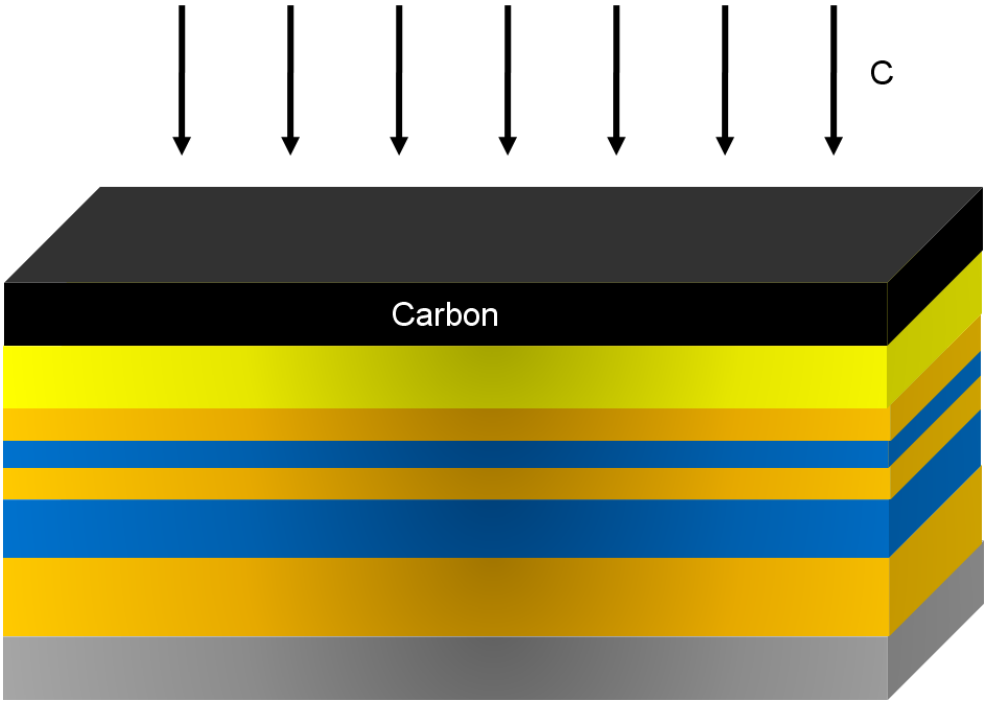

Figure 3.11: Carbon Evaporation. Strong adhesion of C to the surface of the multilayers requires a clean interface. I suggest baking wafers at 170°C on a hotplate for 10-15 minutes immediately before loading in the evaporator. Carbon evaporates by sublimation, so a constant evaporation rate is difficult to achieve. The proper rate is determined by using the crystal monitor to measure the amount of C deposited per minute. 18-25 $\AA$/s is a suitable rate for ensuring proper C adhesion, which is important for avoiding delamination during subsequent processing steps. The final C thickness should be 50-60 nm.

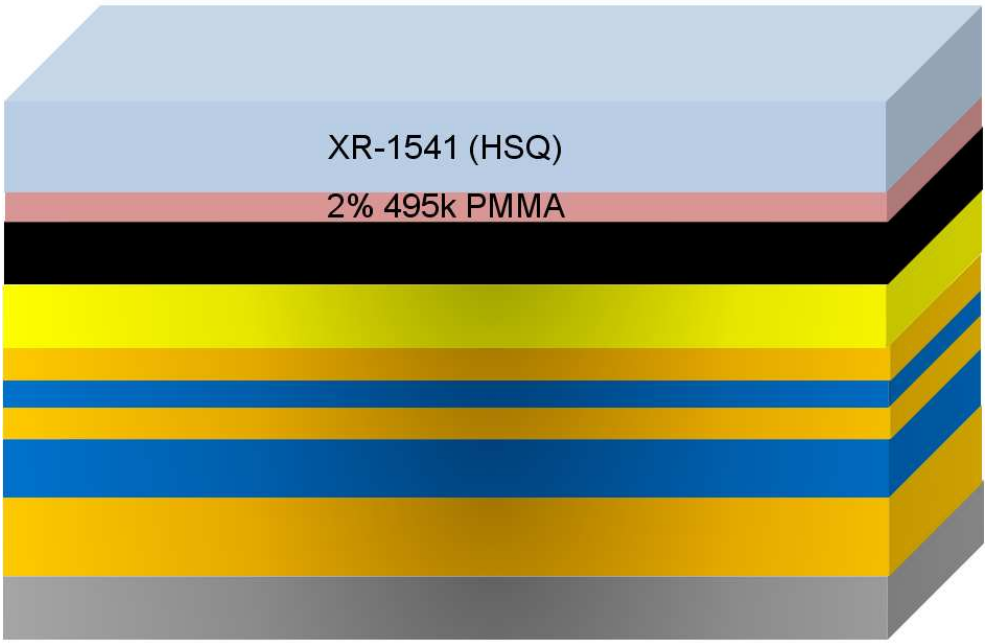

Figure 3.12: Spin on Ebeam resist. An HSQ ebeam procedure will be discussed here, however PMMA works just as well depending on the shapes required. Previous work [2] showed that PMMA is an excellent adhesion layer for XR-1541 (current brand of HSQ). I recommend spinning 495k 2% PMMA at 4000 rpm for one minute followed by a 15 minute bake on a 170°C hotplate, resulting in a PMMA thickness of 50 nm. Then spin 2% XR-1541 at 2000 rpm on top of the PMMA, followed by 2 minutes on the 170°C hotplate, resulting in an HSQ thickness of $\sim$ 130 nm.

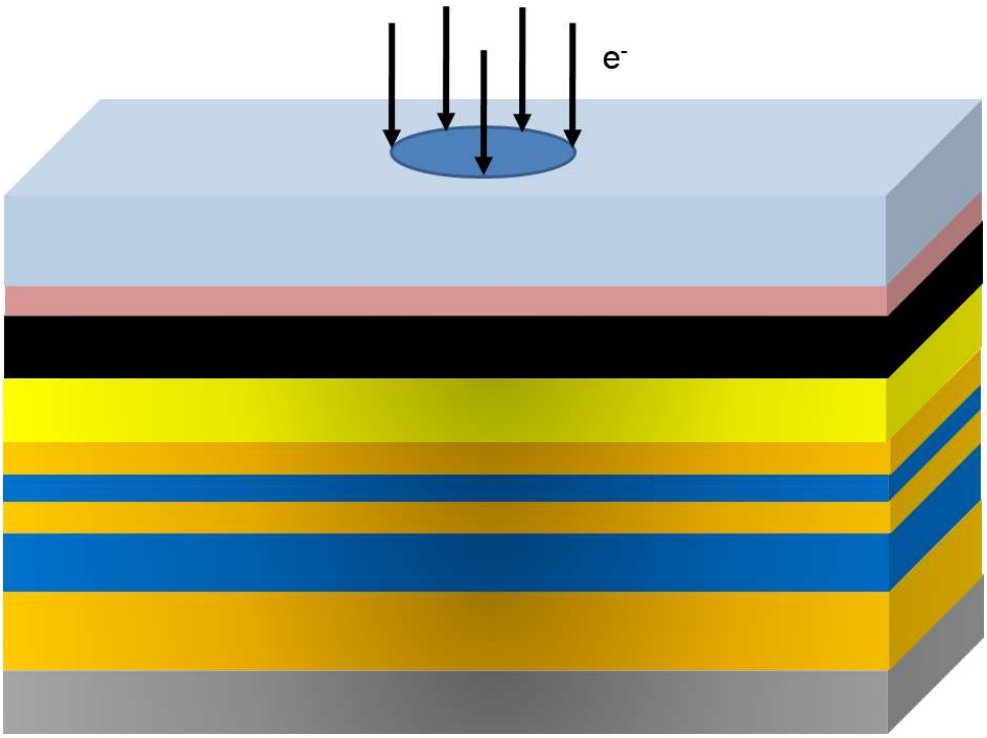

Figure 3.13: Electron beam lithography. After dose testing in a manner described in section 1.2.2, EBL is used to define the nanopillar profiles. For clean magnetic switching behavior, I recommend elliptical patterns, however for RF studies, elongated hexagons and circles are extremely useful as well.

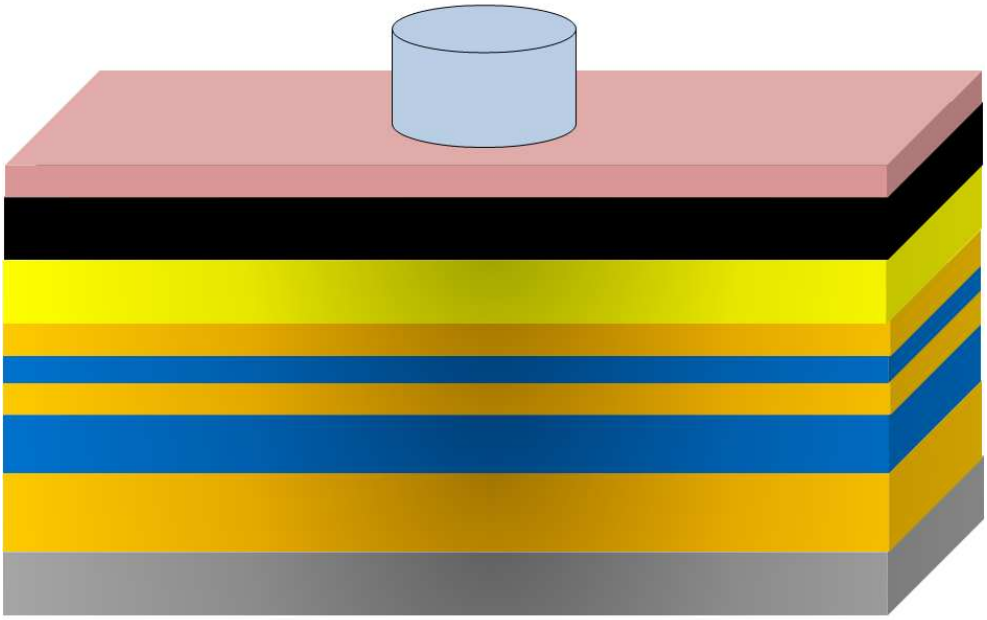

Figure 3.14: E-beam resist development. For HSQ resist, a 2 minute postbake on the 170°C hotplate assists in breaking H bonds and reformation from a cage to a network structure. At this point, unexposed HSQ is dissolved in a tetramethyl ammonium hydroxide (TMAH) based developer, such as AZ 300 MIF currently in use at CNF. It is important to use plastic dishware in developing HSQ, as the resist can chemically react with glassware. I recommend a 5-10 minute soak in 300 MIF with gentle agitation. Using an optical microscope, check for the larger features such as alignment marks, to verify that the lithography was effective.

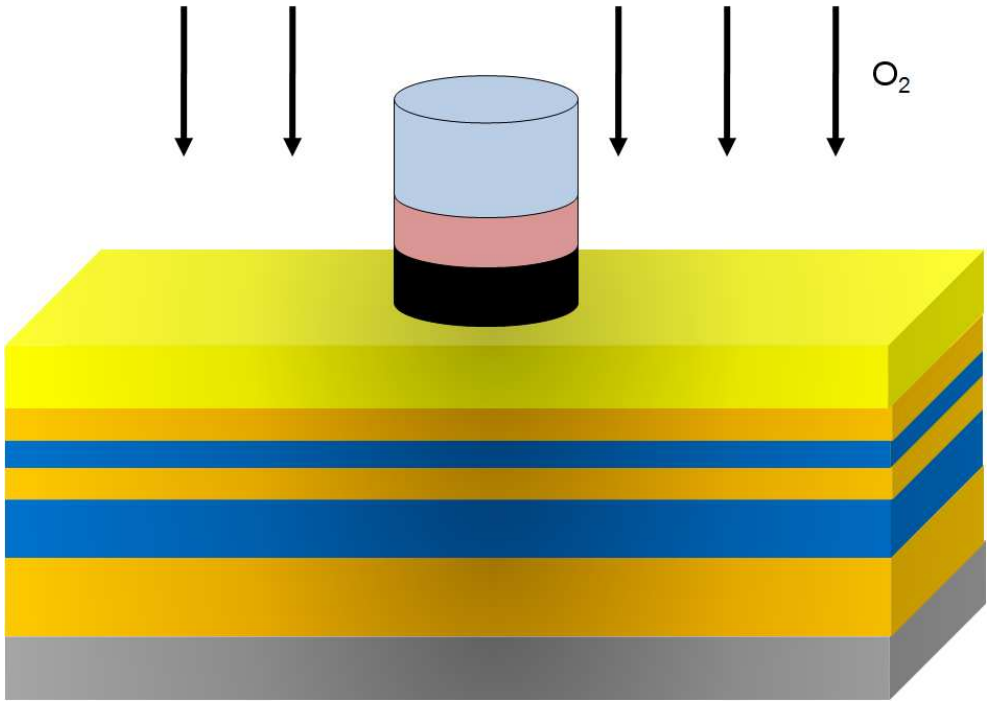

Figure 3.15: O_2 RIE to remove PMMA/Carbon. Using an reactive ion etcher, remove PMMA and carbon using an oxygen plasma, leaving patterned HSQ/Carbon as an ion mill mask. Either the PT-72 or the Oxford 80 etchers at CNF are suitable tools for accomplishing this step, however the required parameters are different for each tool. I recommend 150 W, 30 mTorr, and 30 sccm O_2 in the PT-72 and a higher power $\sim 200-250$ W for the Oxford. The plasma color should appear bright bluish-white while PMMA or Carbon is being etched and turn a dirty yellow-green color when the etching is complete. Wait $\sim 15-30$ after the plasma changes color before ending the etch. An additional benefit of the O_2 plasma is a strengthening of the HSQ as the plasma promotes formation of the network structure.

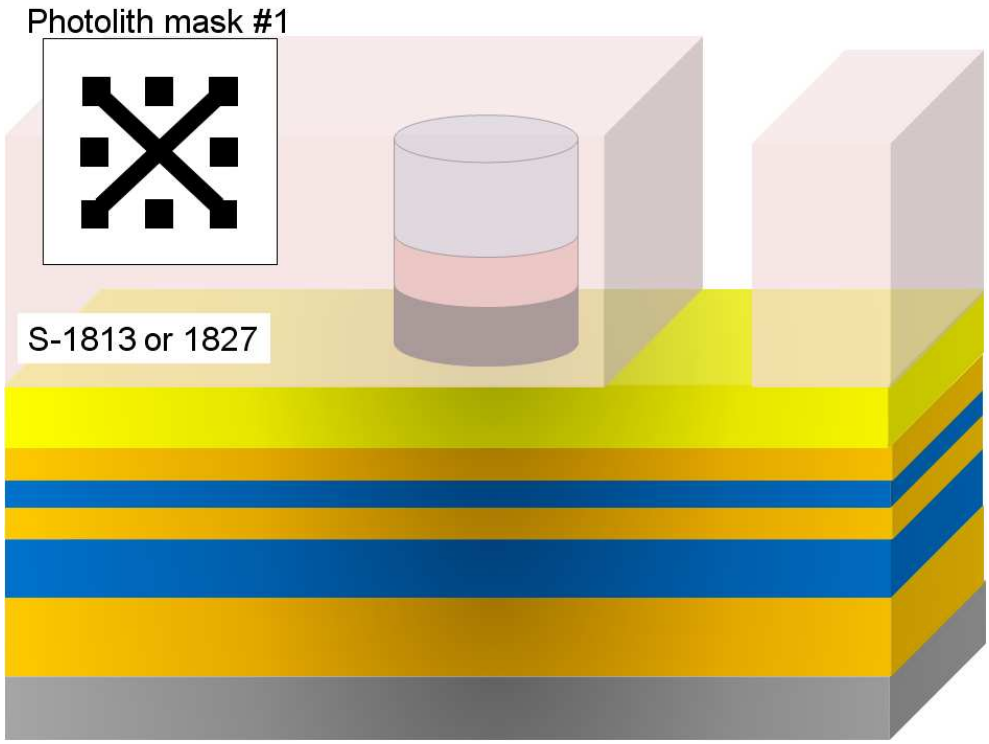

Figure 3.16: Photolithography 1 - "Define Leads". Spin on photoresist at 2000 rpm, either S1813 or 1827 can be used depending on the amount of material removed during ion milling. Bake 60 seconds on 115°C hotplate. Expose in 5X stepper using photolithography mask #1 "Define Leads". Develop for 65 sec in 300 MIF with gentle agitation. Remove and rinse with DI water. Finally, a descum using an 15-30 second O_2 plasma exposure will remove any trace amounts of photoresist remaining before further processing. This step masks off the bonding pads and bottom leads for each nanopillar device.

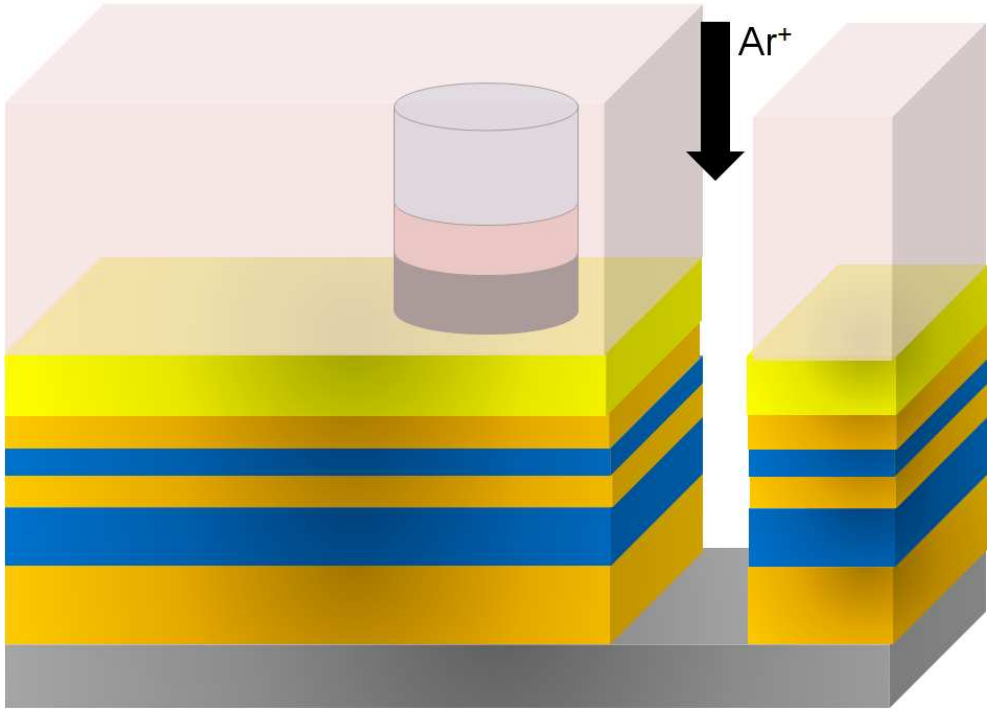

Figure 3.17: Ion mill to define bottom leads. Use the IBD in Clark Hall to ion mill the multilayers down to the thermally grown SiO_2 at the base of the wafer. Due to the length of this mill, it is critical that the stage is cooled to -10°C to avoid overheating and crosslinking of the photoresist, which makes it nearly impossible to strip resist off the wafer. Milling should be done with a 45° stage angle, 500 V beam voltage, 200 V accelerator voltage, and 60 mA. I do not include mill rates here as I suggest periodic mill rate calibrations to compensate for system fluctuations.

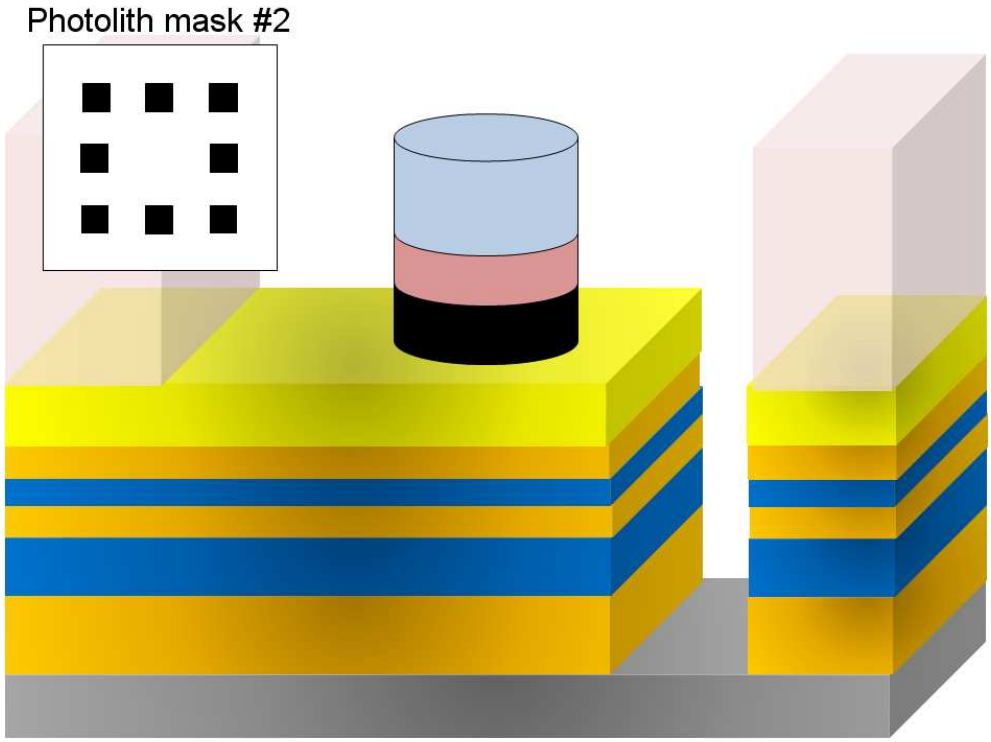

Figure 3.18: Photolithography 2 - "Define pillar". Strip photoresist from previous step by soaking in acetone for 15-30 minutes, transferring to a second acetone bath to sonicate for 20-30 sec, and finally soak in IPA for 1-2 minutes before rinsing with IPA and drying with N_2. Spin resist and use the 5X stepper to expose photolithography mask 2 "Define pillar". Develop and descum. This step protects the bonding pads, but exposes the C nanopillar mask and the leads for ion milling.

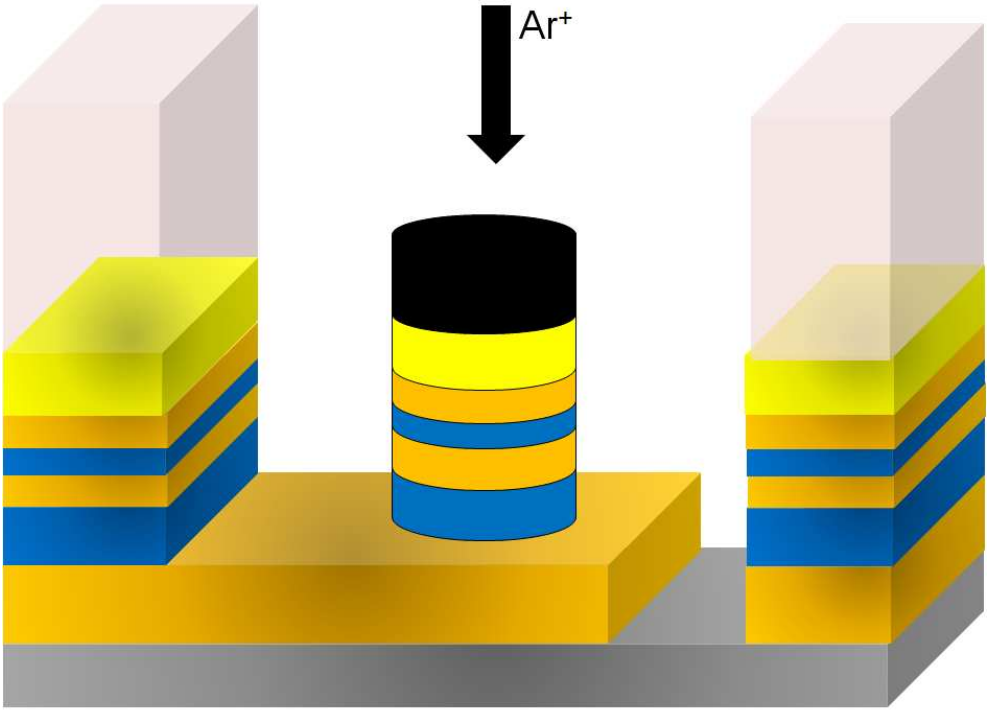

Figure 3.19: Ion mill to define nanopillar. Using the IBD with the stage cooled to -10°C and a 45° stage angle, ion mill to the Cu underlayer to define the nanopillar structure. Here, a 200 V beam voltage and 70 mA beam current improve mill uniformity across the wafer. Strip resist and then measure the etch depth using a profilometer.

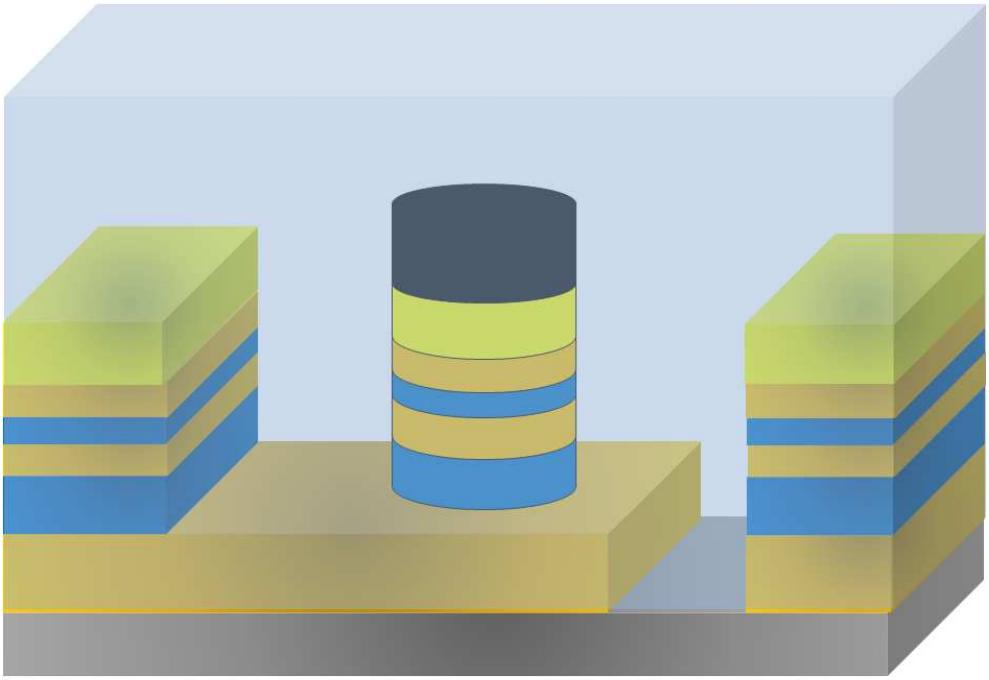

Figure 3.20: Spin on HSQ. IBD or evaporate a thin 5-10 nm SiO_2 adhesion layer for the next step. Spin on 22% or the current high concentration XR-1541 at $\sim$ 4000 rpm, which gives a film thickness $\sim$ 500 nm, a thickness that should be sufficient for maintaining planarization. Bake on 170°C hotplate for 2 min to evaporate solvent. To thin the oxide for easier processing in subsequent steps, use a CHF_3 or CF_4 plasma in the PT-72 to remove $\sim$ 200 nm (recipes available at etcher). Using the Filmetrics reflectometer, determine the approximate oxide thickness, which should be 250-300 nm thick.

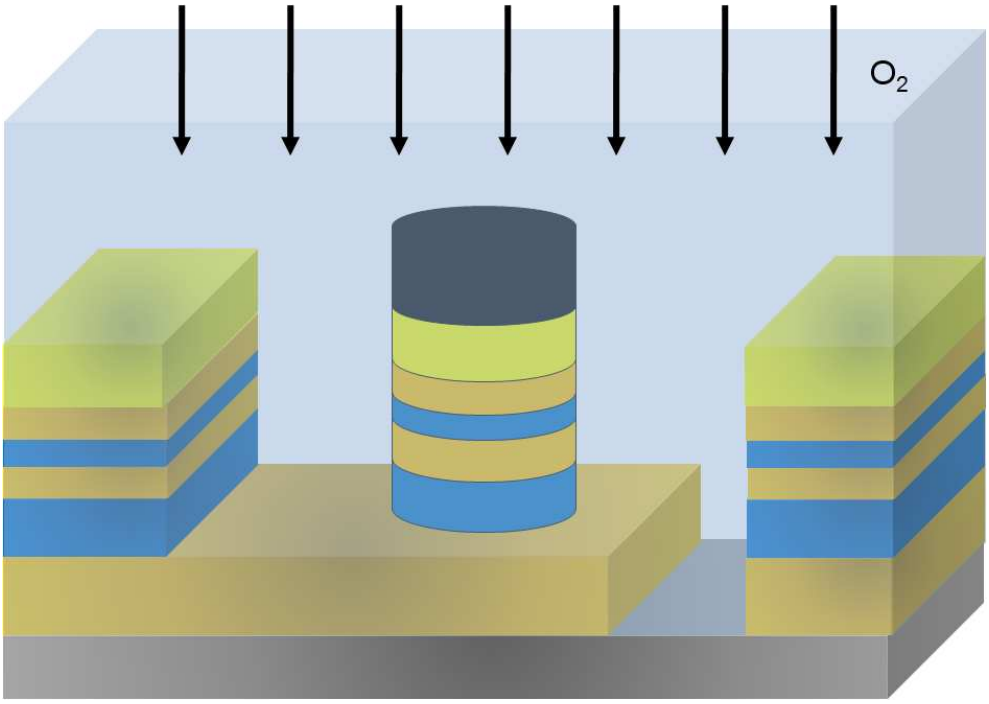

Figure 3.21: O_2 plasma exposure of HSQ. Expose the HSQ to an oxygen plasma in the PT-72 (80 W, 50 mTorr, 25 sccm of O_2) to promote network lattice formation. Unfortunately the mechanical strength of the film is relatively weak, so I suggest evaporating 50-60 nm of oxide to protect the HSQ from being scratched or damaged after O_2 treatment.

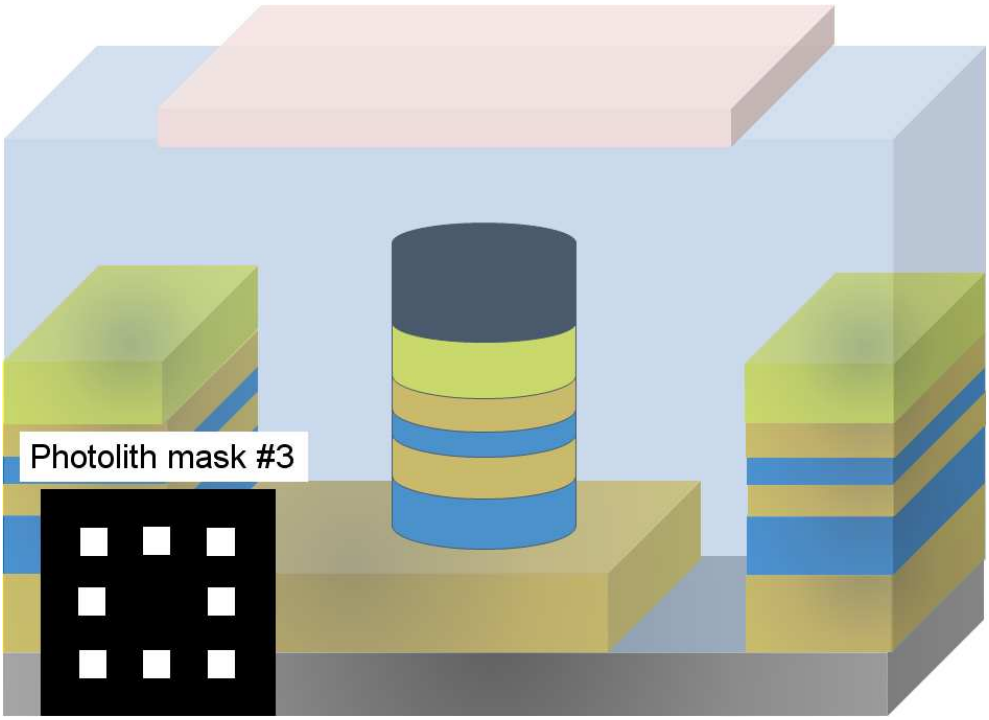

Figure 3.22: Photolithography 3 - "SiO_2 etch". Spin a P10 adhesion layer at 3000 rpm for 30 sec, then spin on photoresist. Expose mask 3 "SiO_2 etch" in 5X stepper, develop, and descum resist. This step opens windows in the photoresist so the oxide can be removed over the contact pads.

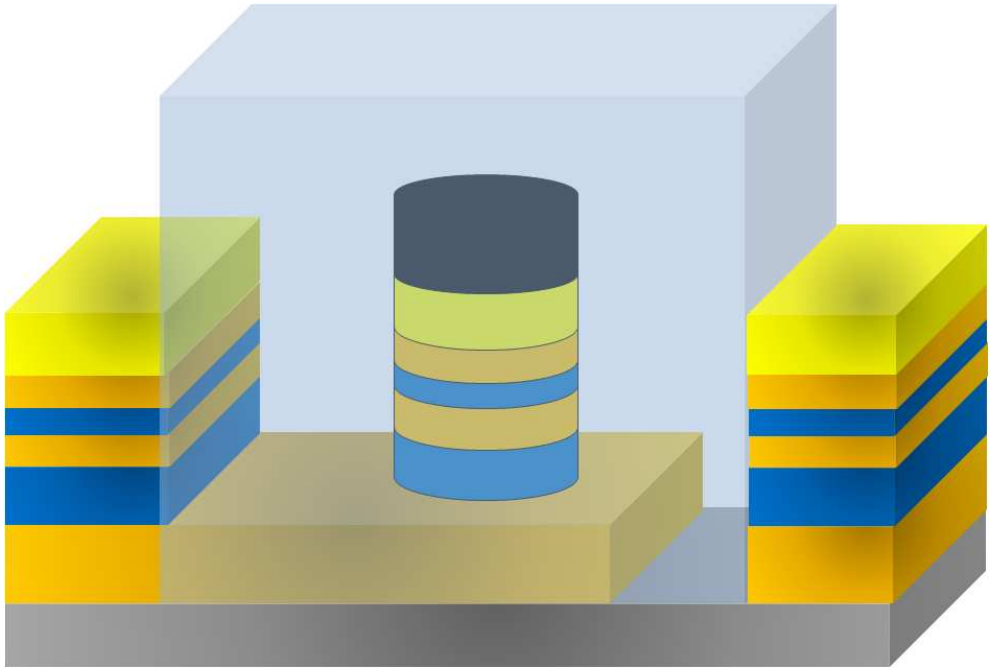

Figure 3.23: SiO_2 etch. Use either 6:1 Buffered Oxide Etch (BOE) or a CHF_3/O_2 RIE etch to remove oxide over bonding pads. If using BOE, time the etch to remove $\sim 1.5\times$ the oxide thickness measured in the Filmetrics. The RIE requires more time, but is inherently safer than dealing with HF. Be aware that etch times in RIE are approximate, and I suggest using the Filmetrics to check if the etch is complete. After stripping the resist, I suggest using the profilometer to measure the difference in height between the bonding pad and the oxide above the region containing the pillar. Due to spatial nonuniformities in ion mill rates, I suggest making a wafer map (i.e. measuring these depths on one device in many different die across the wafer). Knowing these depths will assist in contacting the top of the nanopillars.

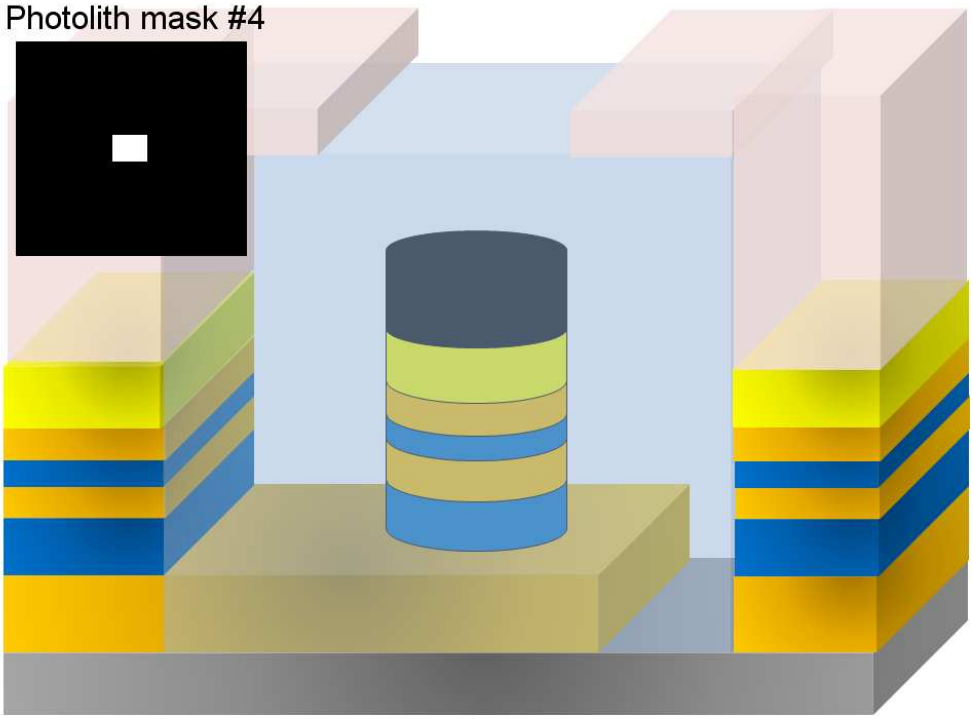

Figure 3.24: Photolithography 4 - "Etch SiO_2 above pillar". Spin P10/Photoresist bilayer, expose mask 5 "Etch SiO_2 above pillar" in 5X stepper, develop, and descum. This opens a small window above the nanopillar to thin the oxide above the pillar.

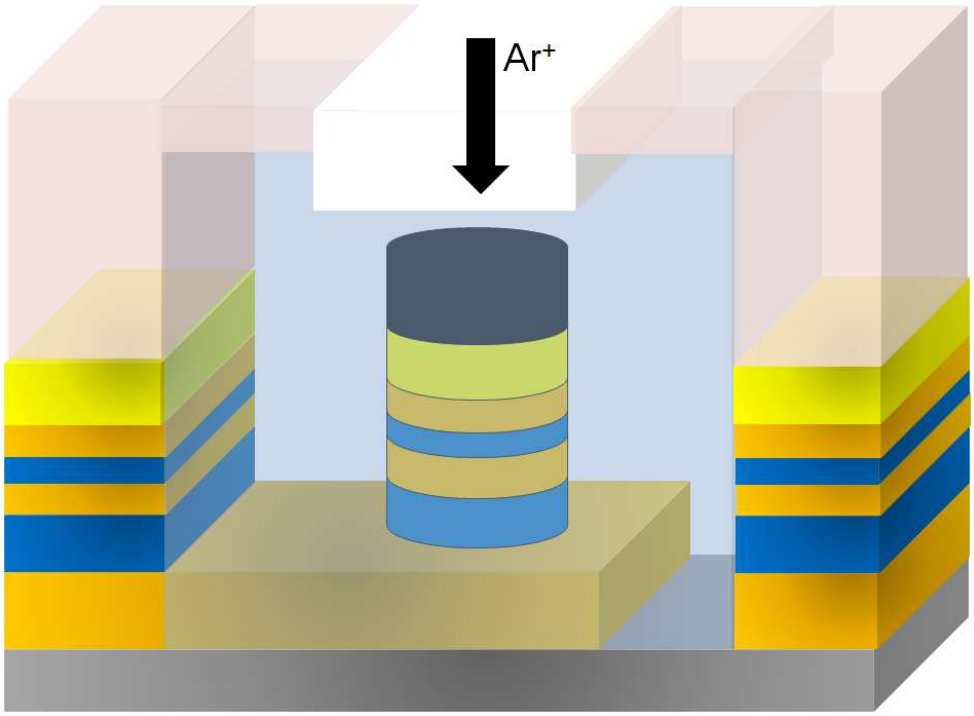

Figure 3.25: Thin oxide. Using the VEECO ion mill at CNF (you could also use the IBD), mill the oxide above the pillar until it is approximately 50 nm thick. The depths measured in step 14 are useful in determining the length of the mill. Mill with a stage angle of 25°, 500 V beam voltage, and 40 mA beam current. Strip resist after completion and repeat wafer map as before to check oxide height over pillar. This will be the targeted mill depth for the last step.

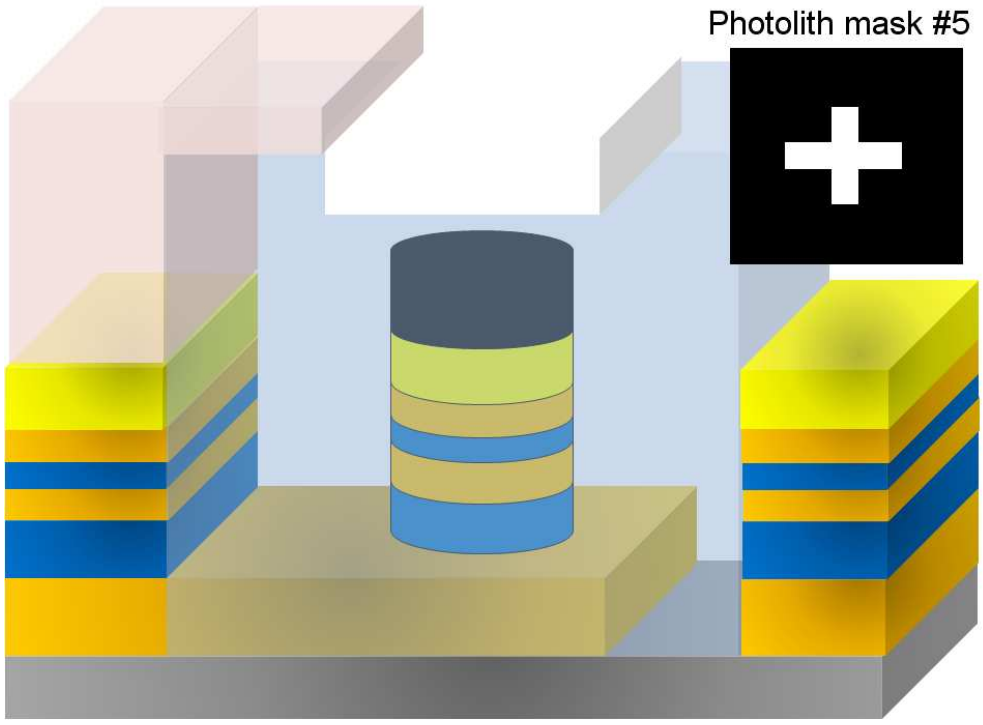

Figure 3.26: Photolithography 5 - "Top leads". Spin P10/photoresist bilayer, expose mask 6 "Top leads" in 5X stepper, develop, and descum. This step opens a cross shaped window to finish the mill to the top of the pillar and then deposit top leads which connect to the isolated contact pads surrounding the pillar. At this point, you can scribe the wafer into chips to process individually, or if the wafer map shows good uniformity, process the wafer as a whole.

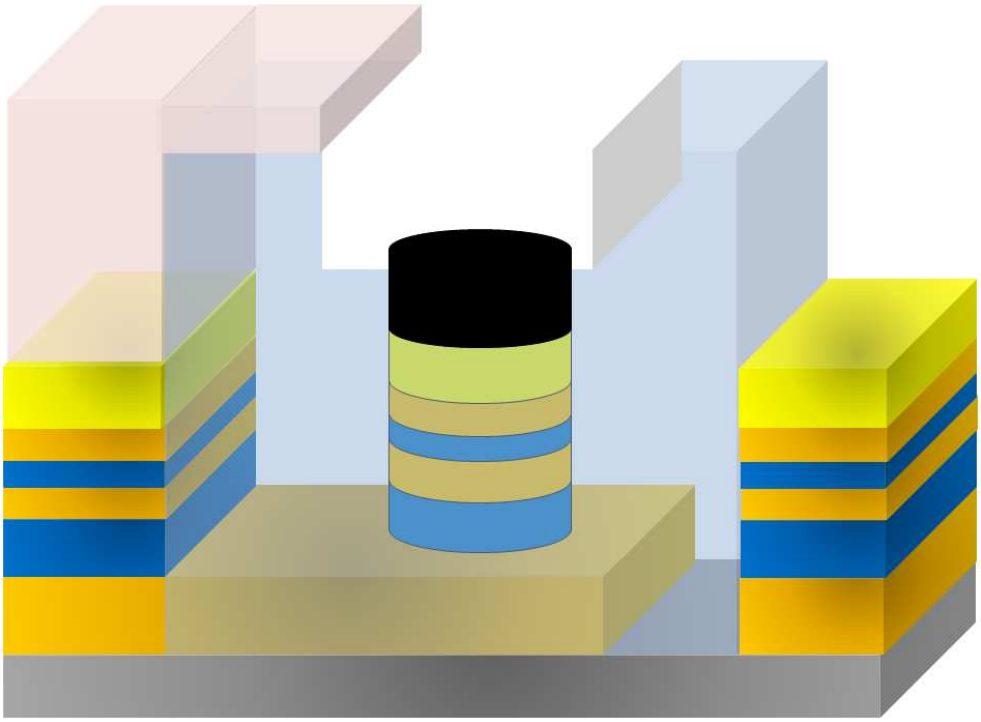

Figure 3.27: Ion mill to contact nanopillar. I suggest using the same mill system used in step 16 with the same parameters. Target the mill to stop 10 nm farther than the depth determined by profilometry to correct for small bumps in oxide height above the nanopillar.

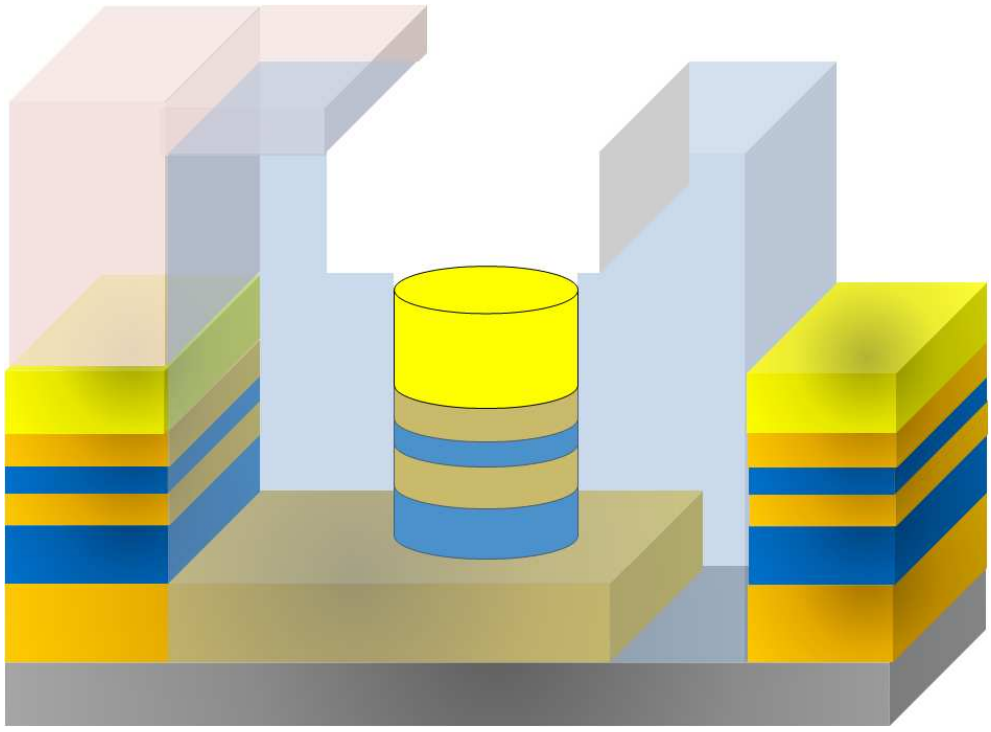

Figure 3.28: Clean top contact. Following ion milling, etch in O_2 plasma to remove PMMA/C residue remaining above capping layer of nanopillar. I recommend etching 3× longer than the etch in step 6, but no longer than 6 minutes, as O_2 etches photoresist.

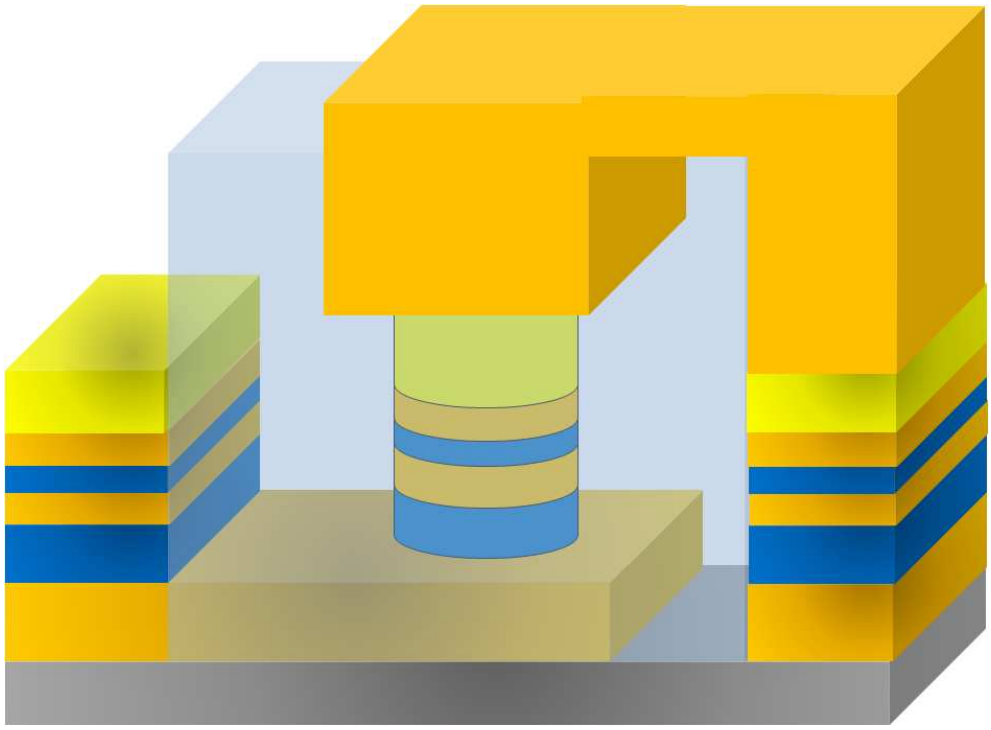

Figure 3.29: Top leads. Load chip or wafer into IBD. Perform a short ion mill face on (90° stage angle) for 7-15 sec to clean capping layer surface (no cooling, 500 V beam voltage, 60 mA beam current). Without breaking vacuum, rotate the stage to 160° and deposit 3000 $\mathring{A}$ Cu. Upon completion, remove chip/wafer and strip resist. At this point, the chip/wafer is ready to be electrically measured.

3.4.2 Experimental Results

The process outlined above was originally developed for a project attempting to phase lock [27, 28] the oscillating free layer moments of two nanopillars using dipolar field interactions. Since magnetic field strength decreases rapidly with distance away from the nanomagnet, I needed to position the nanopillars with the smallest possible separation between them. As I discussed in sec. 1.3.2, HSQ was an ideal resist for accomplishing this patterning, eventually resulting in separations of 20-30 nm between nanopillars (as shown in Fig. 3.9). Nanopillar fabrication involved using the process outlined in the previous sections, with HSQ as the insulating material, and a magnetic trilayer structure of 5 nm Py/8 nm Cu/20 nm Py. My original concerns with this strategy arose from the question of whether an HSQ layer was robust enough to survive processing on the back end of our fab. However, this insulating layer came out none the worse for the wear and functioned beautifully for my purposes, proving proof of concept for this process. Unfortunately, my coupled nanopillar idea suffered a worse fate, because without a means of addressing the individual nanopillars, there was no way to conclusively detect phase locking of the individual nanomagnets.

Device resistances are on the order of 1-10 Ω, similar to resistances of nanopillars processed with PECVD deposited SiO_2. This fact, coupled with a comparable ΔR to PECVD insulated pillars with similar dimensions indicate that HSQ is an effective insulator that can survive nanopillar processing, without concerns over sidewall shorting. Fig. 3.30(a) shows the minor loop of a single 150x250 nm^2 approximately elliptical nanopillar processed using the HSQ process. Here, issues with pattern distortion during EBL have reduced the aspect ratio of the device, resulting in a large area nanopillar with a small coercive field for the spin valve

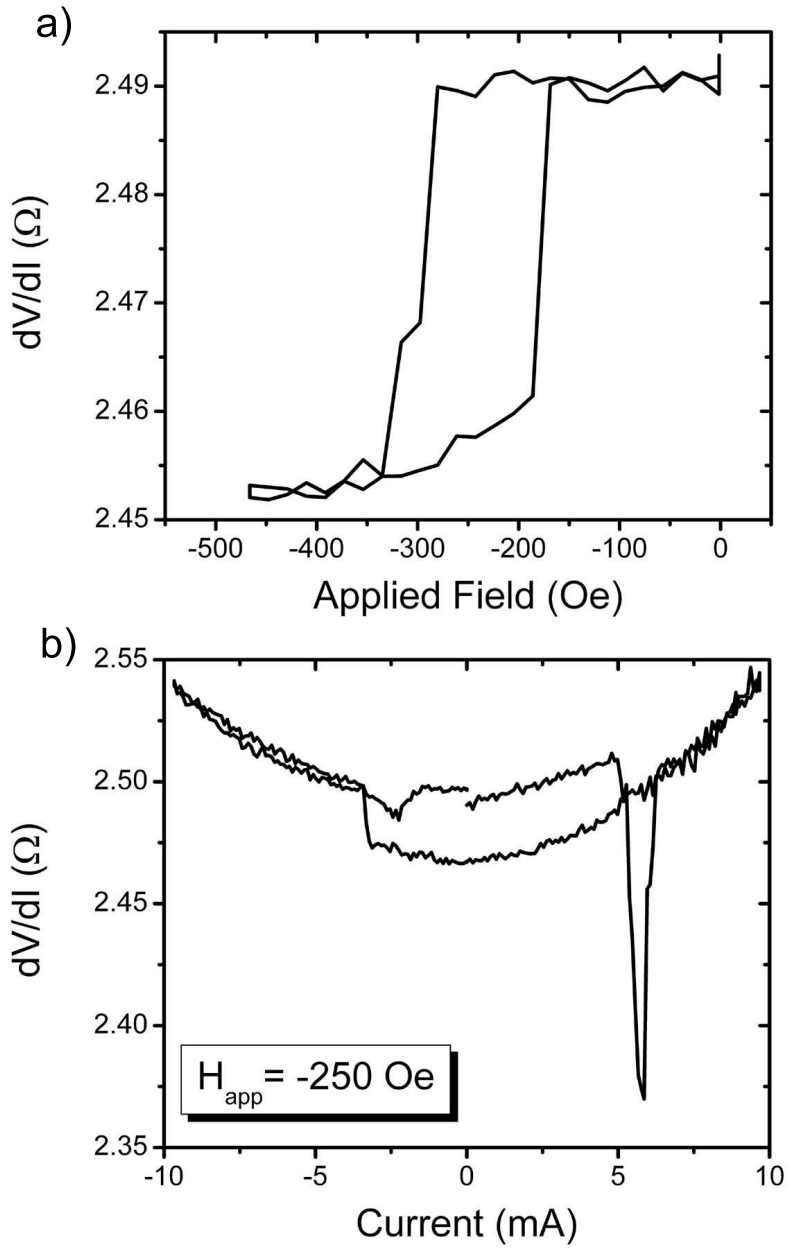

Figure 3.30: (a) Resistance vs. magnetic field for a single 150x250 nm^2 elliptical spin valve nanopillar processed as described above. Device resistance and magnetoresistance are comparable to devices fabricated with CVD deposited SiO_2 as the insulating dielectric, indicating that there is no drop off in device performance with the self-planarizing nanopillar process. (b) Resistance vs. current for same device in (a). The large critical currents are due to the relatively large device area patterned through the use of HSQ as an e-beam resist.

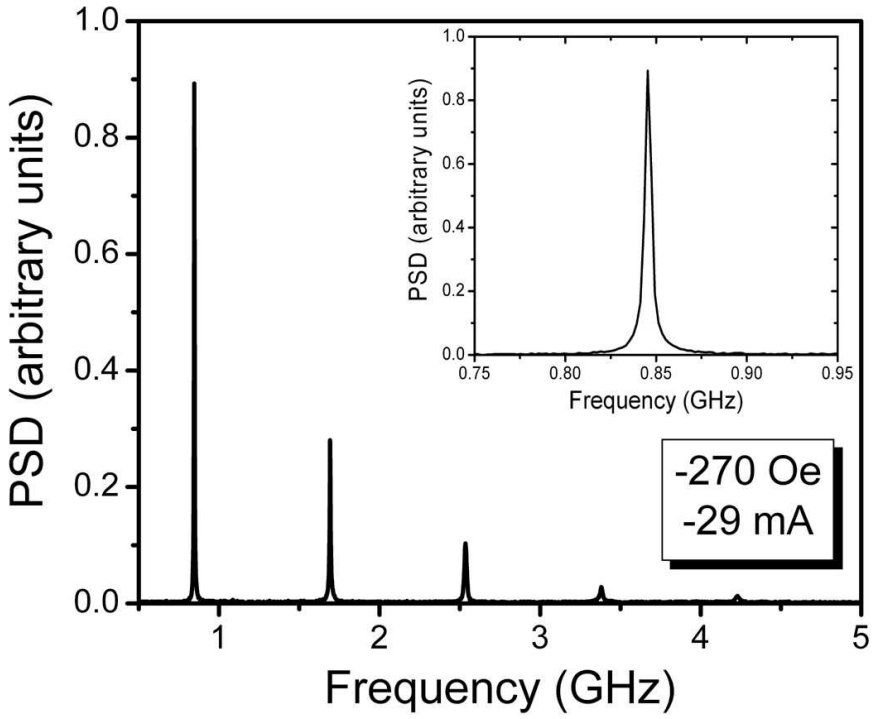

Figure 3.31: DC current driven GMR oscillations for device discussed in Fig. 3.30 taken at a field canceling the dipole field of the reference layer. Here, the small aspect ratio of the nanopillar, together with the large applied current generates a vortex state in the reference layer, similar to that in [29], resulting in a low frequency, narrow linewidth mode with harmonics up to n=5. These results indicate that HSQ should be suitable as an insulator for RF measurements, and possibly even better if the dielectric constant is lower than in SiO_2. (inset) Fundamental mode of oscillation, presenting characteristics of a vortex oscillator.

free layer. Fig. 3.30(b) shows a spin transfer scan for a typical device, where the large reversal currents are due to the large area of the device. Obviously device performance needs to be optimized, but several improvements can be made simply by improving the HSQ EBL, or by switching to an PMMA process.

To verify the RF properties of devices fabricated using this process, I measured DC current driven dynamics in the same device shown in Fig. 3.30. These results are shown in Fig. 3.31, where a magnetic field was applied to cancel out the dipole field of the reference layer and the device was biased at -29 mA. Due to the relatively low aspect ratio of the device and the large current applied, it is not surprising that a vortex state is formed within the reference layer, leading to peaks at low frequency with extremely narrow linewidths and large peak powers, results similar to those generated in nanopillars with thick reference layers [29] and point contacts [30]. These devices also display peaks up to the fifth harmonic, results similar to the local current injection of current through the use of a nanoconstriction placed within a nanopillar [31]. These results illustrate that HSQ fulfills fabrication and measurement requirements for spin transfer studies. As of the writing of this thesis, there is an effort to characterize the dielectric constant of HSQ processed as outlined above [32], which may prove insulating with HSQ to be an even better option for RF measurements than PECVD deposited SiO_2.

3.5 General Fabrication Tips

To conclude, I would like to offer several general suggestions/philosophies that have served me well in all my fabrication efforts.

1) Patience is the single most important quality for designing, developing, and executing fabrication processes. Remember, you can take the time to do it right the first time, or take the time later having to redo it.

2) Learn to enjoy the fabrication process and don't just treat it as an ends to a means.

3) Characterization is the key to fabrication. If you want to modify a process, test each step required. If you are not certain of a tool's operation, perform tests to check on its operation. Accurate and frequent calculations of deposition and etch rates help provide the level of precision required for success.

4) Use all of Cornell's resources to your advantage. That includes discussing issue/problems with coworkers and CNF staff members. Also, take the time to perform journal searches to research similar issues.

5) Keep your head up. During the course of your career in science and nanofabrication, there will be many instances where wafers or processes fail. Keep plugging away.

REFERENCES

[1] Katine J.A., Albert F.J., Buhrman R.A., Myers E.B., & Ralph D.C., Current-driven magnetization reversal and spin-wave excitations in Co/Cu/Co pillars, emphPhys. Rev. Lett. **84**, 3149 (2000).

[2] Emley N.C., Ph.D. thesis, Cornell University (2005).

[3] Albert, F.J, Ph.D. thesis, Cornell University (2002).

[4] Rooks M.J., Kratschmer E., Viswanathan R., Katine J., Fontana Jr. R.E, & MacDonald S.A., Low stress development of polymethylmethacrylate for high aspect ratio structures *J. Vac. Sci. Technol. B* **20**, 2937 (2002).

[5] Slaughter J.M., Dave R.W, DeHerrera M., Durlam M., Engel B.N., Janesky J., Rizzo N.D., & Tehrani S., Fundamentals of MRAM technology, *J. Supercon.* **19**, 19 (2002).

[6] Albert F.J., Katine J.A., Buhrman R.A., & Ralph D.C., Spin-polarized current switching of a Co thin film nanomagnet, *Appl. Phys. Lett.* **77**, 3809 (2000).

[7] Ea C.S. & Browna A.D., Incorporating a corner correction scheme into enhanced pattern area density proximity effect correction, *J. Vac. Sci. Technol. B* **19**, 1985 (2001).

[8] Osawa M., Takahashi K., Sato M., Arimoto H., Ogino K., Hoshino H., & Machida Y., Proximity effect correction using pattern shape modification and area density map for electron-beam projection lithography, *J. Vac. Sci. Technol. B* **19**, 2483 (2001).

[9] http://www.aiss.de/PROXECCO/PROXECCO.html

[10] The pattern conversion software CATS at CNF currently contains proximity correction software. I urge the reader to explore this option if small device dimensions are required, however, characterization similar to what I describe will still be required.

[11] Glashauser W., & Ghica G.-V., U.S.Patent No. 4,393,129

[12] Crowie J.M.G., Mohsin M.A., & McEwen I.J., *Polymer* **28**, 1569 (1987).

[13] Lavallee E., Beauvais J., & Beerens J., *J. Vac. Sci. Technol. B* **16**, 1255 (1998).

[14] Yasin S., Hasko D.G., & Ahmed H., *Appl. Phys. Lett.* **78**, 2760 (2001).

[15] Lee K.Y., Bucchignano J., Gelorme J., & Viswanathan R., *J. Vac. Sci. Technol. B* **15**, 2621 (1997).

[16] Fuchs G.D., Ph.D. thesis, Cornell University (2007).

[17] Henschel W., Georgiev Y.M., & Kurz H., Study of a high contrast process for hydrogen silsisquioxane as a negative tone electron beam resist, *J. Vac. Sci. Technol. B* **21**, 2018 (2003).

[18] Driskill-Smith A.A.G., Katine J.A., Druist D.P., Lee K.Y., Tiberio R.C., & Chiu A., Electron-beam lithography for the agnetic recording industry: fabrication of nanoscale (10 nm) thin-film read heads, *Microelectron. Eng.* **73-74**, 547 (2004).

[19] Peuker M., Lim M.H., Smith H.I., Morton R., van Langen-Suurling A.K., Romjin J., van der Drift E.W.J.M., & van Delft F.C.M.J.M., Hydrogen Silsesquioxane, a high-resolution negative tone resist, inverstigated for its applicability in photon-based lithographies, *Microelectron. Eng.* **61-62**, 803 (2002).

[20] van Delft F.C.M.J.M., Delay-time and aging effects on constrast and sensitivity of hydrogen silsesquioxane, *J. Vac. Sci. Technol. B* **20**, 2932 (2002).

[21] Dow Corning Corporation, Midland, Michigan 48686-0994, FO*x (R) Flowable Oxide Baseline Processing Overview.*

[22] Liou H.-C., & Pretzer J., Effect of curing temperture on the mechanical properties of hydrogen silsesquioxane thin films, *Thin Solid Films* **335**, 186 (1998).

[23] Belot V., Corrium R., Leclercq D., Mutin P.H., & Vioux A., Thermal Reactivity of Hydrogenosilsesquioxane Gels, *Chem. Mater.* **3**, 127 (1991).

[24] Yang C.-C. & Chen W.-C., The structures and properties of hydrogen silsesquioxane (HSQ) films produced by thermal curing, *J. Mater. Chem* **12**, 1138 (2002).

[25] Chen C.-T., & Chiou B.-S., The effects of surface-plasma treatment of thin-

film hydrogen silsesquioxane low k dielectric, *J. Mater. Sci. - Mater. Electron* **15**, 139 (2004).

[26] Liu P.T., Chang T.C., Sze S.M., Pan F.M., Mei Y.J., Wu W.F., Tsai M.S., Dai B.T., Chang C.Y., Shih F.Y., Huang H.D., The effects of plasma treatment for low dielectric constant hydrogen silsesquioxane (HSQ), *Thin Solid Films* **332**, 345 (1998).

[27] Kaka S., Pufall M.R., Rippard W.H., Silva T.J., Russek S.E., & Katine J.A., Mutual phase-locking of microwave spin torque nano-oscillators, *Nature* **437**, 389 (2005).

[28] Mancoff F.B., Rizzo N.D., Engel B.N., & Tehrani S., Phase-locking in double-point-contact spin-transfer devices, *Nature* **437**, 393 (2005).

[29] Pribiag V.S., Krivorotov I.N., Fuchs G.D., Braganca P.M., Ozatay O., Sankey J.C., Ralph D.C., & Buhrman R.A., Magnetic vortex oscillator driven by d.c. spin-polarized current, *Nat. Phys.* **3**, 498 (2007).

[30] Pufall M.R., Rippard W.H., Schneider M.L., & Russek S.E., Low-field current-hysteretic oscillations in spin-transfer nanocontacts, *Phys. Rev. B* **75**, 140404 (2007).

[31] Ozatay O., Emley N.C., Braganca P.M., Garcia A.G.F., Fuchs G.D., Krivorotov I.N., Buhrman R.A., & Ralph D.C., Spin transfer by nonuniform current injection into a nanomagnet, *Appl. Phys. Lett.* **88**, 202502 (2006).

[32] Tseng H., Ph.D. thesis, Cornell University (2012).

CHAPTER 4

HIGH-SPEED MAGNETIZATION REVERSAL IN LOW I_C NANOPILLAR SPIN VALVES

4.1 Introduction

Following the prediction [1, 2] and demonstration [3, 4] of the spin-transfer switching effect, the use of a spin-polarized current to reversibly switch the orientation of a thin film nanomagnet has been considered for future high speed, non-volatile nanoscale magnetic memory systems [5]. Several advances are needed to move this possibility closer to practical reality, with one being a reduction in the currents (I_c's) and the current densities (J_c's) required to exert sufficient spin torque for 1-10 ns-scale switching. Recent studies [6, 7] have demonstrated that spin transfer switching can occur on time scales as short as 100 ps, but this requires currents on the order of 10 mA. In contrast, switching currents on the order of 0.1-0.2 mA are required for making high-density memory circuits using minimum-area MOSFETs. Strategies for reducing I_c must be subject to the added constraint that the nanomagnet remains thermally stable, which means that devices must use nanomagnets with an energy barrier to reversal $U_A(T) \geq 1.0$ eV when operating at room temperature (RT), or an even larger barrier (> 1.3 eV) for an operating temperature of 100° C.

In this chapter, I will describe experiments exploring methods of reducing the spin-transfer critical current I_c for nanopillar spin valves using low saturation magnetization M_s nanomagnets. By patterning these materials into small area, large aspect ratio elliptical nanopillars, the effective magnetic volume of the free layer is reduced, decreasing I_c while maintaining the thermal stability of the nanomagnet

through shape anisotropy. DC and pulsed current experiments both indicate these strategies are effective, although further optimization is required to maximize the effects. In addition, I will describe macrospin simulations developed to explore the spin torque efficiency and phenomenological damping parameter of these magnets, which give some insight into the physical processes involved in magnetization reversal for these devices.

4.2 Advantages of Low M_s Nanomagnets

The theoretical prediction of spin transfer critical currents [1, 8] assuming the applied field and the polarization of the incident spin current are both in the plane of the films is:

$$I_c^{\pm} = \frac{\alpha}{\eta^{\pm}} \left(\frac{2e}{\hbar} \right) M_s V (H + H_k + 2\pi M_s), \tag{4.1}$$

where $I_c^{\pm}$ are the critical currents for the onset of magnetization dynamics, α is a phenomenological damping constant intrinsic to the chosen magnetic material, η is the spin torque efficiency parameter, e is the electron charge, V is the volume of the nanomagnet, and H, H_k, and $4\pi M_s$ are the applied, uniaxial shape anisotropy, and easy-plane anisotropy (demagnetization) fields respectively acting upon the nanomagnet. If the nanomagnet's demagnetization field $4\pi M_s \gg 2(H + H_k)$, this expression can be simplified as $I_c \propto \frac{M_s^2 V \alpha}{\eta^{\pm}}$, so it is clear that minimizing M_s, V, and α while maintaining strong spin torque efficiency is one pathway for reduced critical currents.

Requirements for data retention dictate that the magnetic state of the nanomagnet have a lifetime on the order of 10 years, which limits the extent to which both V and M_s can be reduced. The uniaxial nature of an elliptical nanomagnet

can be modeled with a double well potential, as shown in Fig 4.1(a), where the two well states represent the equilibrium states of the nanomagnet with the free layer moment oriented either parallel (P) or antiparallel (AP) to the reference layer along the semimajor axis. Here, an energy barrier U_A prevents thermal fluctuations kT from causing spontaneous hopping of the system from one state to the other, thereby reversing the orientation of the nanomagnet's moment. Assuming the anisotropy of the system occurs solely due to shape, $U_A \sim H_k M_s V/2$, so minimizing I_c without significantly reducing U_A below the threshold for stability (~ 1.3 eV) requires balancing the values of H_k, M_s, and V in such a manner as to simultaneously produce the smallest I_c with the largest U_A. Since H_k increases with film thickness, patterning the free layer nanomagnet into relatively thick, high aspect ratio ellipse should maximize H_k and promote thermal stability, allowing the use of a material with a small average M_s to achieve low reversal currents.

Transition metal ferromagnets such as Iron (Fe), Cobalt (Co), and Nickel (Ni), along with their various alloys are excellent candidates for nanomagnetic systems, not only for their relatively high Curie temperatures, but also because they can be sputter deposited effectively, making them compatible with industrial processing methods. Early GMR studies [9, 10] used superlattices of Fe and Cr grown by molecular beam epitaxy (MBE), where the thin Cr layers promoted antiferromagnetic coupling of the alternating Fe layers. More recent spin transfer experiments [3, 5] used sputter deposited Co/Cu/Co spin valves, where Cr was replaced by Cu to take advantage of the relatively long spin diffusion length of electrons in Cu, ensuring high spin polarization for the incident electric current. While these Co/Cu systems proved effective in studying spin transfer effects, they were hardly optimized with respect to device performance, requiring reversal currents between 1-10 mA for both DC [3, 5] and nanosecond width current pulses [6, 7] due to the

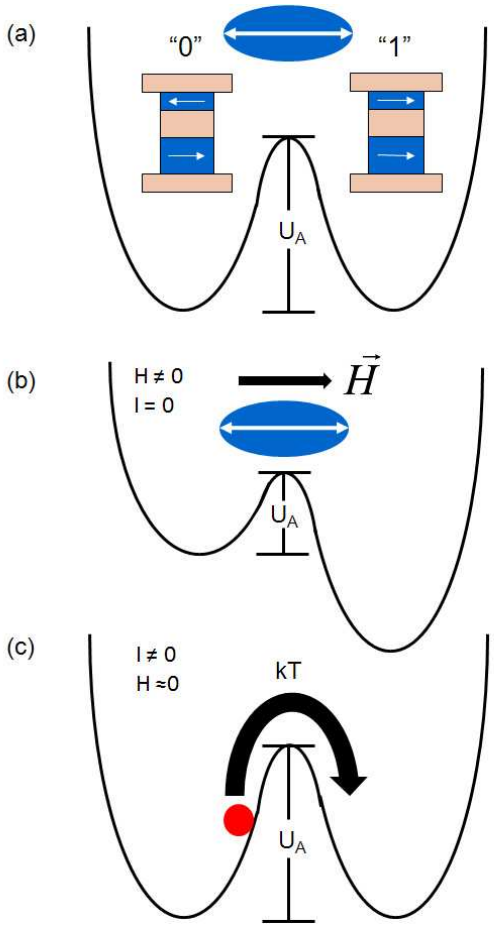

Figure 4.1: (a) Energy landscape for a nanomagnet with uniaxial anisotropy caused by its elliptical shape. The two energy wells represent the equilibrium states for the nanomagnet with its moment pointing either left or right along the semimajor axis and are separated by an energy barrier U_A. Due to the giant magnetoresistance (GMR) effect, these magnetization states correspond to different spin valve or magnetic tunnel junction resistances, which could represent the "0" and "1" binary states for magnetic memory applications. (b) An applied magnetic field opposite to the moment's orientation acts to increase the energy of the nanomagnet, until the point that $U_A \rightarrow 0$ and the system end up in the second well, resulting in magnetization reversal. (c) The application of electrical current increases the energy of the system, moving the state higher up the energy well, until it can hop over the barrier actuating magnetization reversal. As energy fluctuations kT become significant, thermal activation over the barrier drives reversal at smaller currents.

large $M_{s,Co}$. Alloys such as NiFe, or Permalloy (Py) as it is alternatively known, offer a low M_s choice for use as the nanomagnet, especially if it is Ni rich. $Ni_{81}Fe_{19}$ is a particularly useful composition since it has a relatively small $M_s = 560$ emu/cm^3 at room temperature (compared to $M_{s,Co} = 1420$ emu/cm^3 [3]) as determined by superconducting quantum interference magnetometry. This material also exhibits zero magnetocrystalline and magnetostrictive anisotropies, highly desirable properties when clean magnetic switching is necessary. As such, this material is ideally suited for this study in that it should exhibit low switching currents due to its small M_s, and the anisotropy field will depend solely on device shape, which can be tailored to enhance H_k and promote thermal stability.

4.3 Experiment

4.3.1 Device Configuration

I used electron beam lithography to pattern magnetic nanopillar structures with high-aspect-ratio (3:1) elliptical cross sections, employing proximity effect corrections described in Chapter 3 to obtain the desired shape from the exposed pattern. These patterns were ion etched into sputtered multilayer stacks of (all dimensions in nm) 2 Py/120 Cu/20 Py/12 Cu/X Py/2 Cu/30 Au, where Py is permalloy ($Ni_{81}Fe_{19}$) and the thickness X of the Py free layer was either 4.5 or 7 nm. A detailed description of this nanopillar process is given in Ref. [11]. Fig 4.2(a) shows a scanning electron microscope image of an approximately elliptical nanopillar having a 40 nm minor axis and a 3:1 aspect ratio, taken before deposition of the top electrode. Fig. 4.2(b) is a cross-sectional schematic of the device.

Three dimensional micromagnetic simulations (3-D OOMMF) [12] were used to predict the zero temperature anisotropy field of this particular device configuration. The program does this by discretizing the magnetic layers into individual cells and solving the Landau-Lifschitz-Gilbert (LLG) equation governing magnetization dynamics (ignoring spin torque interactions),

$$\frac{d\mathbf{M}}{dt} = |\overline{\gamma}|\mathbf{M} \times \mathbf{H}_{eff} - \frac{|\overline{\gamma}|\alpha}{M_s}\mathbf{M} \times (\mathbf{M} \times \mathbf{H}_{eff}), \tag{4.2}$$

within each individual cell, where $\mathbf{M}$ is an individual cell's magnetization, $\mathbf{H}_{eff}$ is the effective magnetic field consisting of a combination of applied, anisotropy, exchange, dipole, and demagnetization fields, α is the phenomenalogical Gilbert damping parameter, and $\overline{\gamma}$ is the Landau-Lifschitz gyromagnetic ratio, which is related to the Gilbert gyromagnetic ratio γ through the expression $\overline{\gamma} = \frac{\gamma}{(1+\alpha^2)}$ (see OOMMF user manual for details). For these simulations, $\overline{\gamma}$ was chosen to be 1.76×10^5 m/A·s and α=1 to bring the system to an energy minima quickly and minimize simulation time. A more extensive discussion of these simulations including spin torque interactions is included in Chapter 5. Using a 2 nm cubic cell size chosen for calculation convenience, a single 4 nm thick thin film of Py with a perfectly elliptical 40 × 120 nm^2 cross section is expected to have $H_k \approx 1100$ Oe. This result does not take into account the magnetic interactions between the free and reference layers of a spin valve due to the dipole fields generated by edge charges. Including this effect by simulating both the free and reference layers indicates that this interaction can be substantial, reducing $H_k \approx 900$ Oe. Deviations from a perfect ellipse also serve to reduce H_k, as shown by additional simulations of a complete nanopillar structure having the non-ideal shape shown in Fig 4.2(a), where $H_k = 785$ Oe for the free layer. In comparison, 4.2 K measurements of the free layer easy-axis coercive fields for devices with similar structure to the one in Fig 1a yield an average $H_c \approx 500$ Oe. We attribute the difference between the

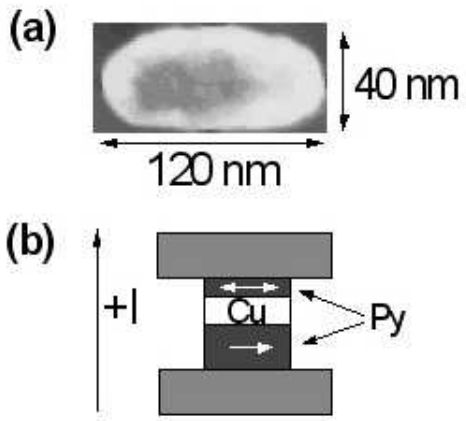

Figure 4.2: (a) (a) SEM image of nanopillars. Patterning with electron beam lithography produces reproducible approximate ellipses with 40x120 nm^2 dimensions. (b) Cross sectional schematic for nanopillar structure with convention for current direction.

measured H_c and the simulated H_k to the difference between the 4.2 K saturation magnetization of the simulated ideal Py material (M_s = 880 emu/cm^3) and that determined by SQUID magnetometry of a thin Py layer sandwiched between Cu films ($M_s = 645$ emu/cm^3), as well as to thin film roughness which was not modeled in the OOMMF simulation. Using the measured 4.2 K values we obtain U_A(4.2 K) $= M_s H_k V/2 \approx 1.7$ eV.

A typical magnetoresistance field scan of the free layer taken with the fixed layer magnetization orientation held fixed (minor loop) is shown in Fig. 4.3(a), and in Fig. 4.3(b) we show a spin-transfer scan for the same device exhibiting an order of magnitude smaller reversal currents than those achieved in Co/Cu spin valves. The minor loop was taken at T = 295 K for applied magnetic field excursions about the value that cancels out the average dipole field from the fixed layer and shows transitions that are thermally activated due to the finite value of $U_A(T)/k_BT$. Here $U_A(T)$ is smaller than $U_A(0)$ due to both the T dependence of M_s and H_K, and more importantly, non-ideal or non-macrospin pathways for

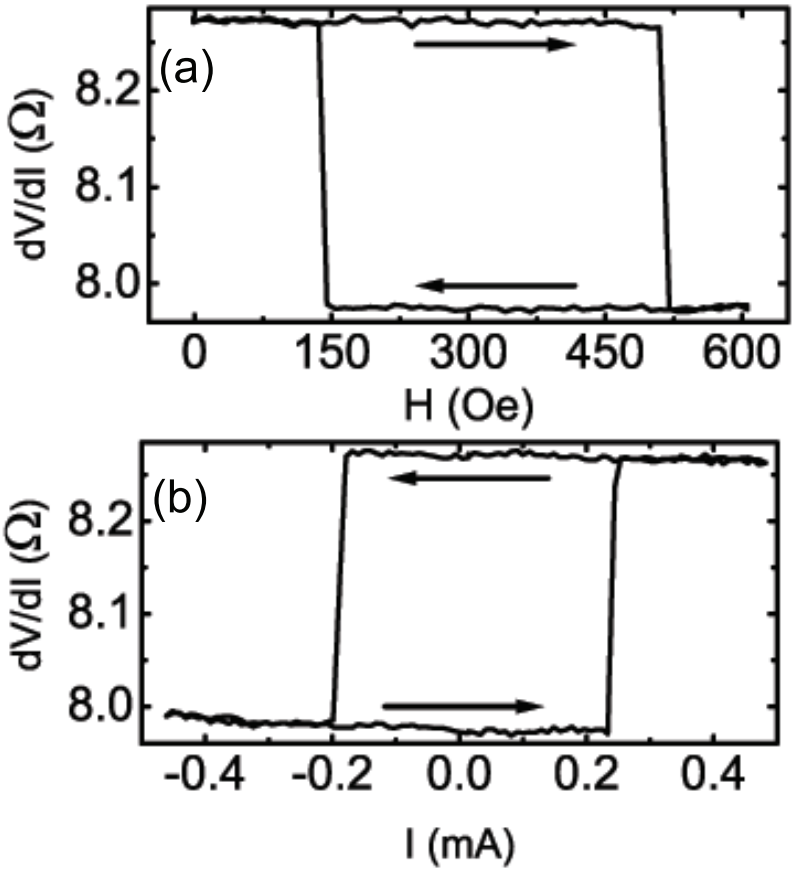

Figure 4.3: (a) Minor loop of free layer and (b) spin transfer curve, with convention for current shown in Fig. 4.2(b) for a typical device.

thermally activated reversal. The latter is generally modeled [13] by assuming a fictitious applied field H_e such that $U_A(T) = (M_s(T)H_k(T)V/2)(1 - H_e/H_k)^2$. Typically $H_e/H_k \leq 0.5$ for thin film nanomagnets [13, 14].

4.3.2 Thermally Activated Magnetization Reversal and Determination of $U_A(T)$

Spin-transfer magnetization excitations due to the application of an applied electric current can be described using the LLG equation including a term derived by Slonczewski to account for spin torque interactions. Here, the magnetization interacts with three different quantities, the effective magnetic field, which determines the potential energy landscape for the moment (Fig 1(a)-(b)), the damping, which acts as a mechanism for the moment to transfer energy to its environment, and of the course spin transfer, which acts as either a damping or "anti-damping" term depending on the polarity of the incident spin current. Excitations occur when this "anti-damping" spin transfer pumps energy into the magnet faster than the damping can remove it. However, this simple balance is valid only at zero temperature, which is not the case for the experiments discussed here, which were all performed at room temperature. At finite temperatures, the environment acts not only to absorb energy from the nanomagnet, but also to send energy kT back into the magnet in a stochastic, fluctuating manner. The dependance of magnetization reversal on these thermal fluctuations has long been the topic of numerous studies [15–17], as well as more recent studies investigating the role of thermal fluctuations on spin transfer induced magnetization reversal [18, 19].

To understand these interactions, we can consider a classical system with a

potential energy landscape U(x), where x are all possible states of the system. If this system has two stable equilibrium states, say by tailoring its shape so that it exhibits uniaxial anisotropy, it can be modeled as shown in Fig. 4.1(a), with two potential wells separated by a barrier U_A. Classical statistics states that for $T > 0$, the system will not remain in a state defined by these energy minima, but instead will fluctuate around the minima, with the probability of being found in a state with energy U being $P_{Boltzmann}(U) \propto e^{-U/kT}$. Therefore, there is a nonzero probability of finding the system at the top of the barrier, at which point it free to fall into the second energy well, resulting in a spontaneous reversal of its magnetic state. A more general expression for this transition probability [20] valid for a wide variety of physical and chemical processes can be derived from the differential equation

$$\frac{dP}{dt}(t) = -\frac{1}{\tau}P(t), \tag{4.3}$$

$$\tau = \tau_{0,switch}e^{(-U_A/k_bT)}, \tag{4.4}$$

where the attempt time prefactor $\tau_{0,switch}$ is determined by the microscopic details of the fluctuations within the potential well. When τ_0, U_A, and T are held constant, the transition probability simplifies to a simple exponential decay, where the probability of transmission between well states becomes less likely as the barrier height U_A increases. From these relationships, it is easy to see why U_A in these devices must be carefully considered, to prevent spontaneous switching between states by thermal excitations.

We can extend this discussion to the more specific case of magnetic reversal by considering the nanomagnet depicted in Fig. 4.1(a). Here, the two potential wells correspond to magnetization orientations pointing right or left along the major (easy) axis of the ellipse, with a barrier $U_A \sim H_k M_s V/2$. A magnetic field applied opposite to the magnetization direction will increase the energy of the magnet

(Fig 4.1(b)) and reduce the height of U_A. At T=0, reversal can occur only after $U_A(H) \rightarrow 0$. However, for finite temperatures, energy fluctuations due to thermal effects can promote activation over the barrier as $U_A(H)$ decreases, leading to reversal at lower applied fields. When the barrier height U_A is close to zero, it can be approximated by a power law [18, 19]:

$$U_A(H) = U_{A0}(1 - \frac{H}{H_{c0}})^{a_H}, \tag{4.5}$$

where H_{c0} is the $T = 0$ coercive field, U_{A0} is the barrier height at $H = 0$, and a_H is a scaling factor which is normally taken to be 2 or 3/2 [21]. We can similarly consider the effect of an applied current, which acts to increase the energy of the system towards U_A as shown in Fig. 4.1(c), lowering the effective barrier $U_A(I)$ the system sees. Here [19],

$$U_A(I) = U_{A0}(1 - \frac{I}{I_{c0}}). \tag{4.6}$$

where I_{c0} is the $T = 0$ critical current for exciting magnetization dynamics and U_{A0} is the barrier height at $I = 0$.

One useful way of determining values for U_{A0} and I_{c0} involves measuring the dispersion in reversal currents for a particular device. This method was first developed by Kurkijarvi [22], who considered thermal activation using a barrier of the form in Equation 4.6, but with I as a function of time, $I = \dot{I}t$, where $\dot{I}$ is the sweep rate. In this case, he derived the mean and standard deviation for any distribution of a critical parameter, such as switching currents, which to leading order becomes [18, 22, 23],

$$< I_c >= I_{c0}\left[1 - \frac{k_B T}{U_{A0}} ln\left[\frac{1}{\tau_0}\frac{k_B T}{U_{A0}}\frac{|I_{c0}|}{|\dot{I}|}\right]\right], \tag{4.7}$$

$$\sigma_{I_c} = |I_{c0}|\left(\frac{k_b T}{U_{A0}}\right), \tag{4.8}$$

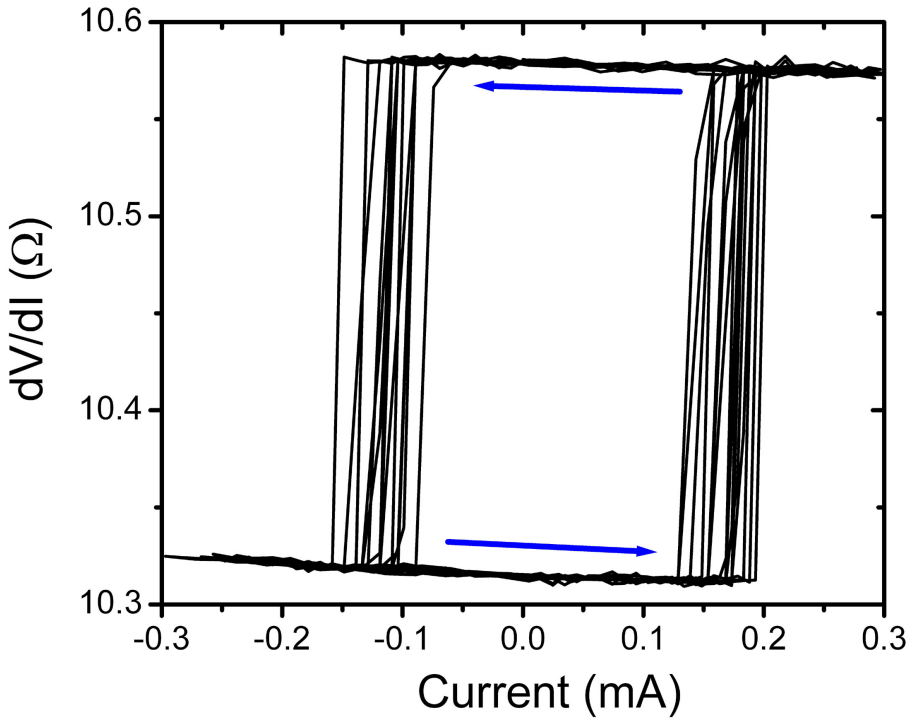

Figure 4.4: Multiple traces of resistance vs. current for a 4.5 nm thick Py free layer plotted on the same axes. Due to thermal activation processes, there is a spread of reversal currents whose mean and standard deviation are dependant on the energy barrier of the nanomagnet. By repeating this process at different current sweep rates $\dot{I}$, we can fit to Equation 4.7 as shown in Fig. 4.5.

where $\dot{I}$ is the current sweep rate. The distribution of switching currents for our system was determined by measuring 20 scans of current vs. resistance using standard ac lock-in techniques with a Wheatstone bridge for several different sweep rates. Setting the sweep rate was accomplished by varying the applied current step size for the sweep as well as the waiting time between steps. An example of the dispersion in switching currents is shown in Fig 4.4. In Fig. 4.5, we plot $\langle I_c \rangle$ for a 4.5 nm thick free layer as a function of $\dot{I}$ for transitions in which the free-layer moment is driven from parallel to the fixed-layer moment to antiparallel (P-AP) and vice versa (AP-P). Assuming a fluctuation attempt time $\tau_0 = 1$ ns [14],

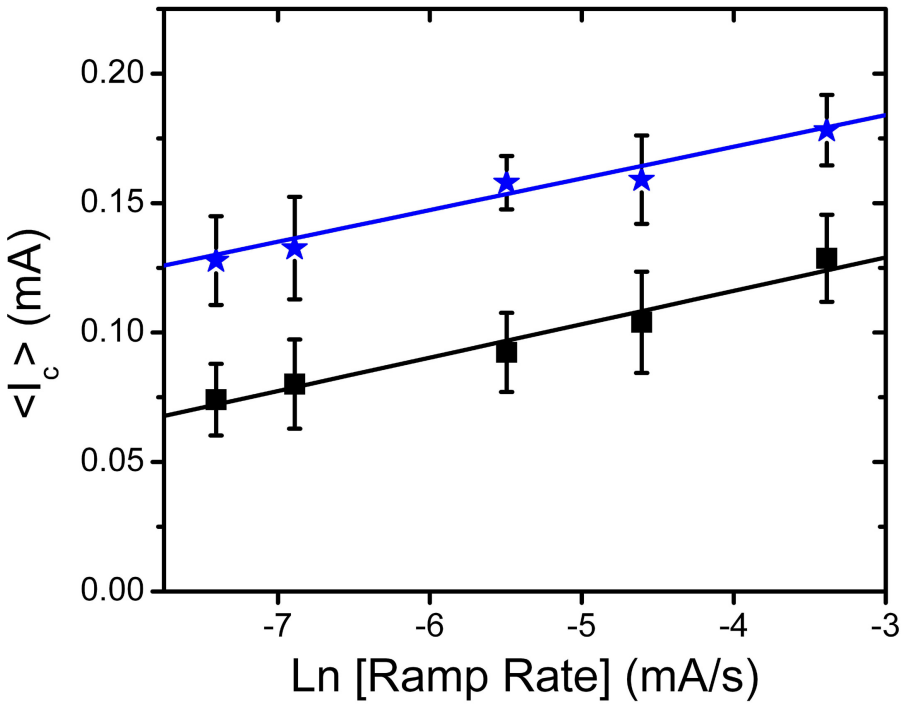

Figure 4.5: Average DC switching current vs. natural log of current ramp rate for a 4.5 nm thick Py free layer in the P-AP (★) and AP-P (■) switching directions. Error bars represent dispersion in switching current for 20 current sweeps at a given ramp rate, as shown in Fig. 4.4. Lines shown are least-squares fits using Equation 4.7

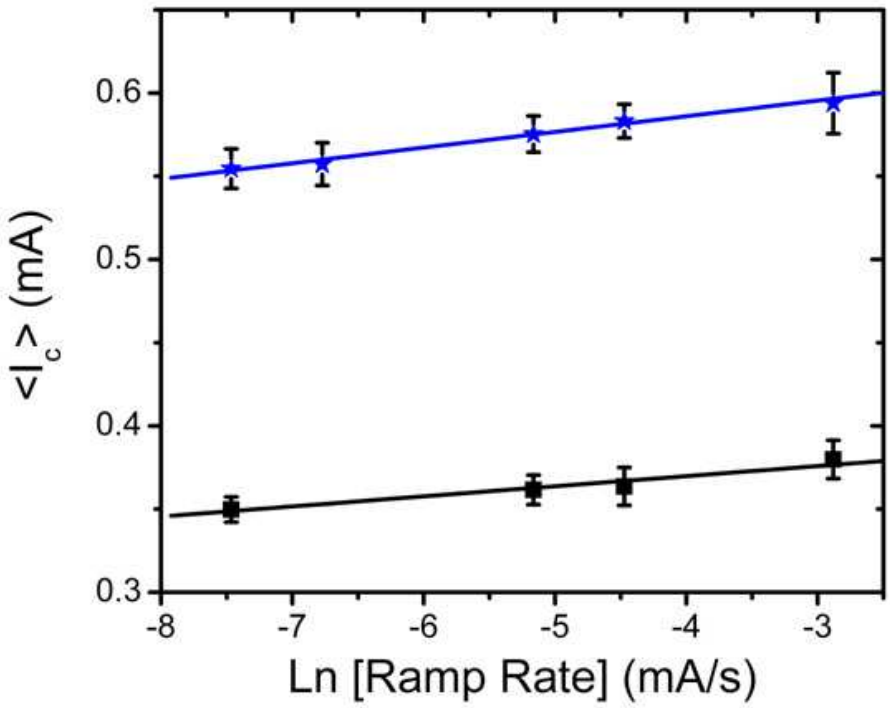

Figure 4.6: Average DC switching current vs. natural log of current ramp rate for a 7 nm thick Py free layer in the P-AP (★) and AP-P (■) switching directions. Error bars represent dispersion in switching current for 20 current sweeps at a given ramp rate, as shown in Fig. 4.4. Lines shown are least-squares fits using Equation 4.7

we obtain $U_{A,P-AP}(293K) = 0.85 \pm 0.03$ eV, $I_{c0,P-AP} = 0.42 \pm 0.03$ mA and $U_{A,AP-P}(293K) = 0.73 \pm 0.01$ eV, $I_{c0,AP-P} = 0.39 \pm 0.02$ mA. The difference in the two activation energies is qualitatively consistent with OOMMF simulations, which show that the dipole field from the fixed layer has a stronger perturbative effect on the free layer when it is in the AP state than when in the P state. Using the measured 293 K value of M_s (560 emu/cm^3), we would expect $U_{A0}(293K) =$ 1.3 eV, so the fitted values correspond to $H_e/H_k \approx 0.25$. Similar measurements for a 7 nm thick free layer sample (Fig. 4.6) yielded $U_{A,P-AP}(293K) = 2.12 \pm 0.1$ eV, $I_{c0,P-AP} = 0.77 \pm 0.01$ mA, and $U_{A,AP-P}(293K) = 1.92 \pm 0.24$ eV, $I_{c0,AP-P}$ $= 0.50 \pm 0.02$ mA, showing activation energies close to what would be expected from the difference in thickness between 4.5 and 7 nm. These results indicate that by optimizing the free layer thickness, we can maximize the benefits of these low M_s nanomagnets.

4.3.3 Pulsed Current Reversal Experiments

While I_{c0} is the minimum current for spin-torque switching in the absence of significant thermal activation, fast magnetization switching requires much larger currents. In the short-pulse regime, the switching time varies approximately as $\tau \sim 1/(I - I_{c0})$, with thermal effects resulting in a statistical distribution about this mean value [8, 13]. To perform these experiments, I used the circuit shown in Fig. 4.7, with a nanosecond width pulse generator connected to the capacitive port of a high frequency bias tee and both DC and low frequency AC current sources connected to the inductive port of the bias tee. The output of the bias tee was connected to a 20 GHz RF probe with a coplanar waveguide configuration, with the middle signal pin contacted to the top contact of the nanopillar and the

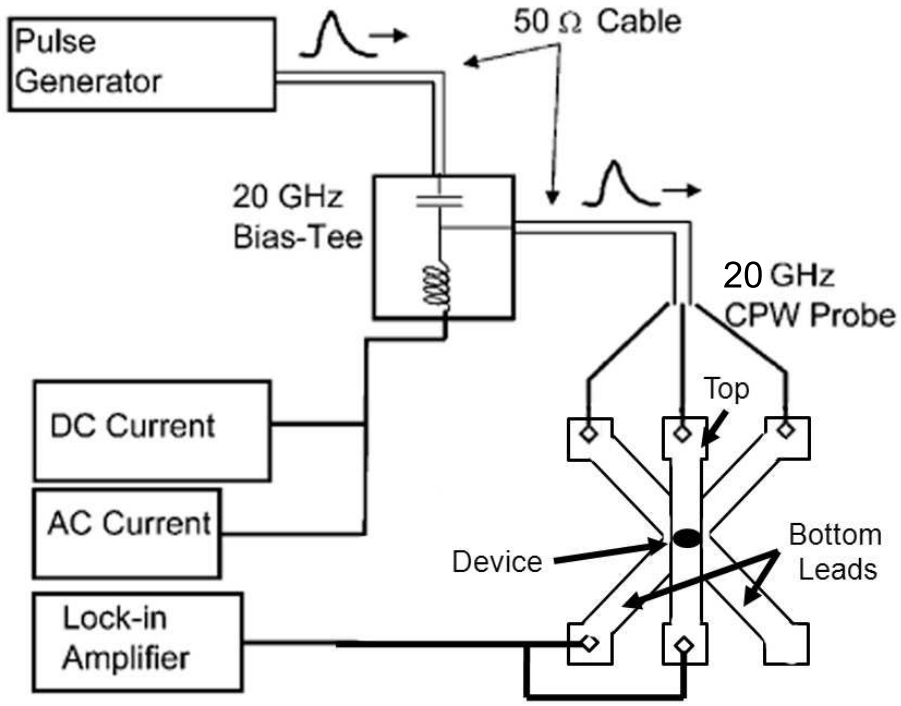

Figure 4.7: Circuit for pulsed current experiments. A pulse generator was connected to the capacitive port of a bias tee with DC and low frequency AC sources connected to the inductive port. After outputting a current pulse through the device, a lock-in amplifier also connected to the device allowed us to make a four point resistance measurement to determine if reversal occurred, which was indicated by a change in resistance. DC current was used to calibrate the system and to fill in points between the fixed attenuator settings of the pulse generator.

two grounding plane pins contacted to the bottom electrode. A DC probe is also contacted to the device to make standard 4 point resistance measurements using standard AC lock-in techniques. By pulsing the device at a fixed pulse width and current amplitude a hundred times and monitoring changes in resistance, we were able to obtain switching probabilities similar to those shown in Fig. 4.8, for AP-P reversal of a representative 4.5 nm Py free layer.

When dealing with RF signals, particular care must be taken in accounting for signal reflections due to impedance mismatches caused by components not being matched to 50 Ohms. This is especially true in these measurements, since we are using nanosecond pulses and the nanopillar devices are in the range of 1-10 Ohms, creating a large impedance mismatch. As such, I developed a calibration method for converting the voltage output by the pulse generator into the voltage (and therefore current) dropped across the device. Calibrating a particular device requires first fixing the pulse width and finding a voltage setting at which the switching probability is in the 40-70% range determined using a large amount of pulse attempt (> 500) to reduce errors introduced by the stochastic nature of the switching. The second step involves increasing the pulse generator attenuation setting by 1 decibel (dB) such that the current amplitude and switching probability decrease, and then continually adding a DC offset using the DC current generator until the switching probability matches the value at the previous attenuator setting. Starting from the relationship

$$attenuation(dB) = 20log\left[\frac{V_{out}}{V_{tot}}\right], \tag{4.9}$$

where V_{out} is the voltage output considering the attenuator setting used and V_{tot} is the maximum voltage output by the generator (this expression also holds for the current across the device). After performing some calculations, the current output for an n dB attenuator setting is found to be related to the $n+1$ attenuator setting

by the relationship $I_{ndB} = 1.122 I_{n+1dB}$. Returning to the experimental results, the DC offset required to balance the switching probability can be considered the difference in current between these two attenuator settings, so that

$$I_{ndB} - I_{n+1dB} = \Delta I \tag{4.10}$$

$$I_{n+1dB} = \frac{\Delta I}{.122}. \tag{4.11}$$

This gives us the calibrated current amplitude at the n+1 attenuator setting, thereby allowing us to map the current amplitude for any attenuator value since $I_{ndB} = 1.122 I_{n+1dB}$. For the samples measured in this study, I found that the calibration doesn't change much for different pulse amplitudes, however other students have mentioned calibration deviations at different pulse widths, so I suggest redoing this calibration for at least the largest and smallest pulse widths considered to verify that the calibration values don't vary.

In Fig. 4.8, I show results for negative (AP-P) current-pulse switching for a 4.5 nm free layer device. The current amplitude required to obtain 100% switching probability is $\sim$ 0.4 mA for a 100 ns pulse, and increases as the pulse width decreases, a general trend in all devices measured. An interesting phenomena is the large increase in current amplitude $I >$ 4-5 I_{c0} required to obtain a high probability of switching with shorter ($\sim$ 1 ns) pulses. We attribute this to the existence of two different reversal regimes, with thermally activated spin transfer reversal dominating at longer pulse widths down to $\sim$ 10 ns and spin torque driven reversal dominating at shorter pulse lengths. In the spin torque driven regime, the pulse width approaches the magnetization precession period, requiring significantly larger currents to drive the oscillations fast enough to facilitate reversal before termination of the pulse. An interesting consequence of this is that I_{c0} determined through the slow ramp rate experiments described in the previous section do not

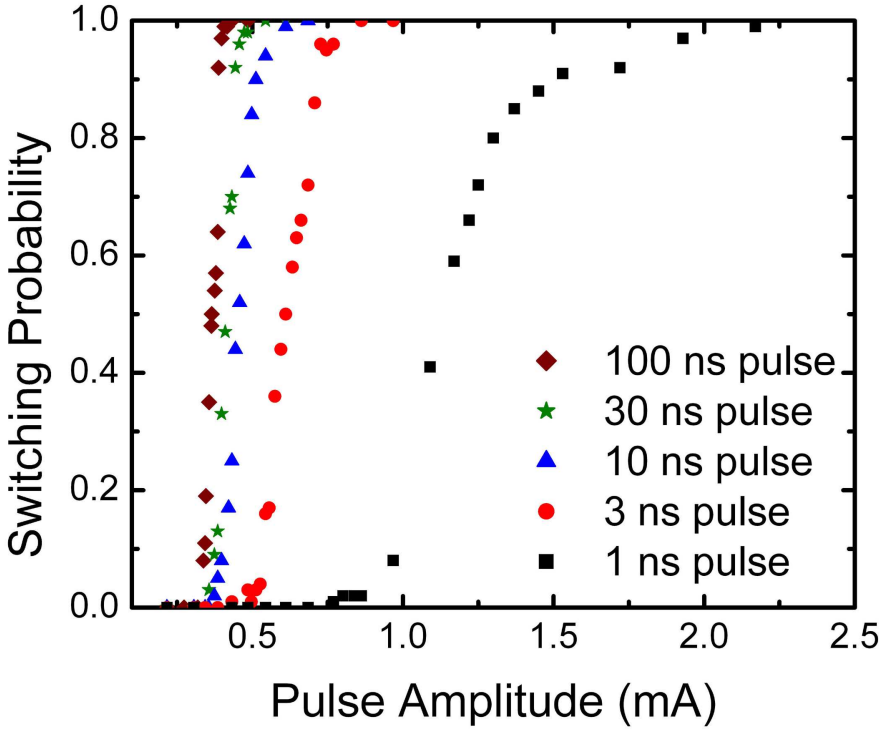

Figure 4.8: Switching probability vs. current amplitude for several different pulse widths. Reversal probability between 0 and 1 occur due to the stochastic nature of thermally assisted magnetization reversal. Current amplitudes for 100% reversal at 1 ns are $\sim 4 - 5I_{c0}$, indicating that extrapolations from slow DC ramp rate measurements do not accurately reflect required switching current amplitudes for fast switching. As the pulse width decreases, the mechanism for reversal shifts from thermally assisted reversal to spin torque driven reversal, where the current must significantly increase to ensure a rapid precession of the magnetization to the switching point prior to termination of the current pulse.

accurately predict reversal currents for ns switching, an incorrect strategy used in many recent spin valve and magnetic tunnel junction experiments to estimate fast reversal currents.

4.4 Macrospin Simulations

To gain some further insight into the details of spin transfer reversal in these systems, I used the Landau-Lifshitz-Gilbert (LLG) equation macrospin model of the nanomagnet, as modified to include the spin-torque effect [1, 13], to simulate the distribution of short-pulse switching probabilities. This equation can be written as:

$$\begin{aligned} \frac{d\overrightarrow{M}}{dt} &= \gamma\overrightarrow{M} \times (\overrightarrow{H}_{eff} + \overrightarrow{H}_{lang}) - \gamma\alpha\overrightarrow{M} \times (\overrightarrow{M} \times (\overrightarrow{H}_{eff} + \overrightarrow{H}_{lang})) \\ &- \frac{I\gamma\hbar g(\theta)}{2eM_sVsin(\theta)}\overrightarrow{M} \times (\overrightarrow{M}_{fixed} \times \overrightarrow{M}), \end{aligned}$$

where γ is the gyromagnetic ratio, I is the electric current, e is the electron charge, and H_{eff} is the sum of contributions from the anisotropy, applied, and demagnetization fields. Temperature effects were included in two different ways, one involving H_{lang}, which is a random Langevin field simulating temperature effects, with components determined using a gaussian distribution with zero mean and standard deviation $\sqrt{2\alpha k_B T/\gamma M_s V\Delta t}$ [13, 24], where α is the Gilbert damping parameter, k_B is the Boltzmann constant, γ is the gyromagnetic ratio, M_s and V are the magnetization and volume of the free layer, and Δt is the integration time step of the simulation. The second temperature effect involves fluctuations of the free layer magnetization about its easy axis equilibrium position due to thermal fluctuations kT producing a random offset angle θ_0 for each reversal attempt with components determined using a gaussian distribution with zero mean and standard deviation

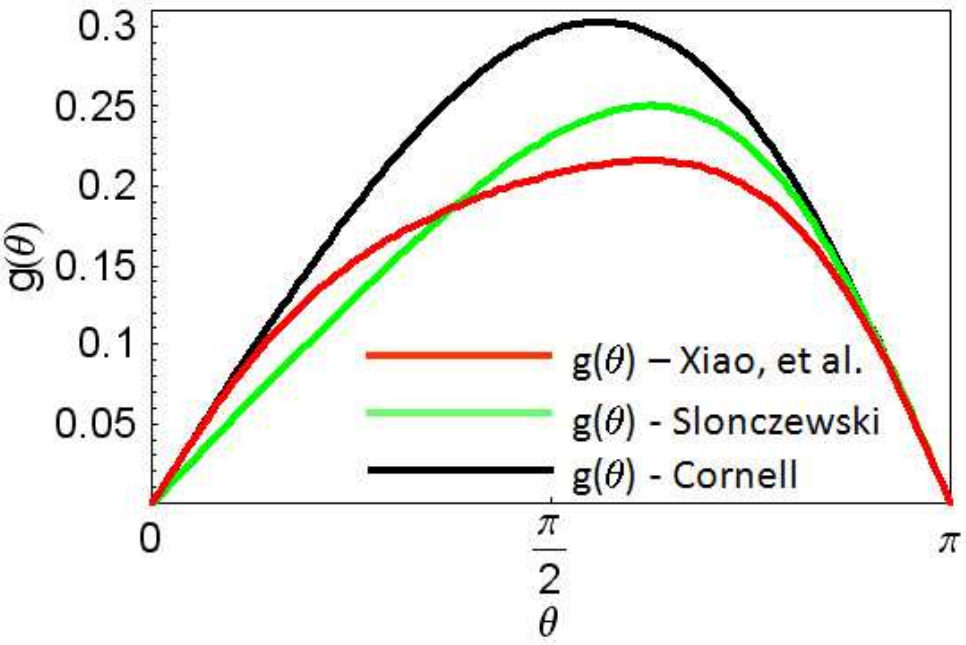

Figure 4.9: $g(\theta)$ as predicted by three different spin transfer models. Macrospin fits to our results using these models show Slonczewski's form captures the proper amplitude but not the symmetry of the switching currents. Xiao's form does just the opposite, allowing us to fit the current symmetry, but not the amplitude if a realistic value for the spin polarization created using Py is used. Our solution was to use a more simplified expression $g(\theta) = Asin(\theta)/(1 + Bcos(\theta))$ with fit parameters A and B describing the spin torque amplitude and symmetry respectively.

$\sqrt{kT/2U_{A0}}$. This angle θ_0 determines the initial misalignment between the free and reference layers, from which the initial strength of the spin torque is calculated. These temperature effects model the stochastic nature of free layer magnetization reversal, leading to switching probabilities between 0 and 1 at finite temperatures.

The function $g(\theta)$ characterizes the strength of the spin torque exerted on the free-layer nanomagnet as a function of the angle θ between its moment and that of the fixed layer. In choosing the form of this expression, I considered several spin transfer theories, including ones by Slonczewski [1] and Xiao *et. al* [25] which are

plotted in Fig. 4.9. The Slonczewski for of $g(\theta)$ is:

$$g(\theta) = [-4 + (1+P)^3(3 + cos(\theta))/4P^{3/2}]^{-1}, \tag{4.12}$$

where P is the spin polarization of the current incident on the free layer. I found Equation 4.12 ineffective in fitting our results as the relatively large polarization values required to model the reversal currents seen in our devices creates a large asymmetry in spin torque between 0 and 180° misalignments of the two nanomagnets, indicated by the significant differences in slopes around those theta values for the curve shown in Fig. 4.9. As our reversal currents are relatively symmetric (see Figures 4.10-4.11), this expression fails to capture the behavior of our system. Xiao finds $g(\theta)$ to be:

$$g(\theta) \approx \frac{P\Lambda^2 sin\theta}{(\Lambda^2+1) + (\Lambda^2-1)cos\theta}, \tag{4.13}$$

where P is the spin polarization and Λ is a spin torque asymmetry parameter which can be tuned to match the symmetry of our reversal currents. However, use of this expression with a reasonable value of $P = 0.37$ for Py [26] returns much larger switching currents than seen experimentally. Therefore, we chose to use a simplified expression for $g(\theta)$ incorporating aspects of the two previous expressions

$$g(\theta) = Asin(\theta)/(1 + Bcos(\theta)), \tag{4.14}$$

where A and B are constant fit parameters representing the amplitude and asymmetry of the spin torque respectively. This simplified $g(\theta)$ was useful in examining some fundamental properties of the free layer magnetization reversal.

The strength of the switching torque is determined by slopes $|dg(\theta)/d\theta| = g_0^{'}$ or $g_\pi^{'}$ at the mean starting angles (0 for P - AP, π for AP - P), where we assume $g_0^{'} = A/(1+B)$ and $g_\pi^{'} = A/(1-B)$. In simulating the data, we use the activation energies for magnetic reversal obtained from the slow ramp rate measurements to

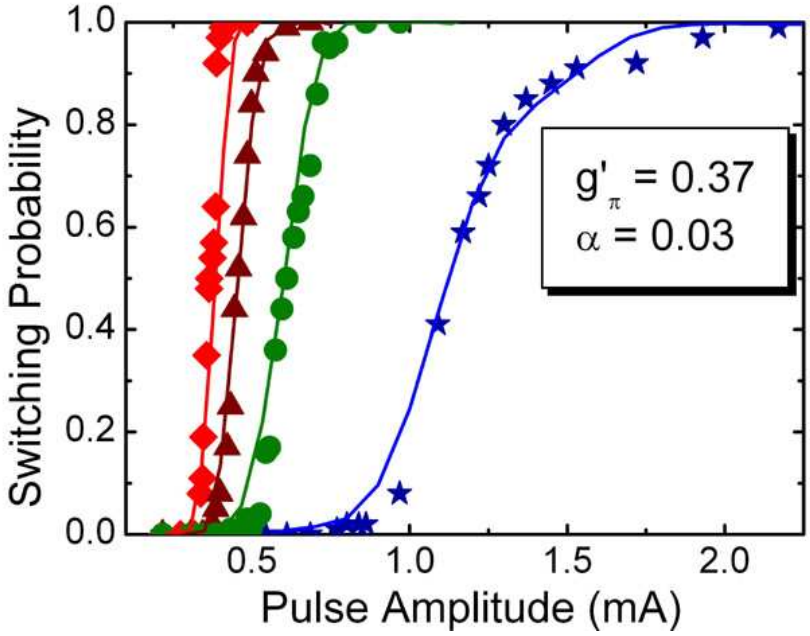

Figure 4.10: Switching probabilities vs. pulse amplitude and single domain simulation fits for AP-P transition in a 4.5 nm Py free layer. Pulse widths for each curve from left to right are 100 ns (♦), 10 ns (▲), 3 ns (●), and 1 ns (⋆).

determine the thermal distribution of the angle θ_0 at the initiation of the pulse. We then vary $g_0^{'}$, $g_\pi^{'}$, and the Gilbert damping parameter α to obtain fits to the data. Results of the best-fit simulations are also shown in Figures 4.10-4.11. All three parameters affect the magnitude of current necessary for switching, but α has different consequences than $g_0^{'}$ and $g_\pi^{'}$ on how the switching probabilities depend on the pulse width, since the influence of H_{lang}, which depends on α, changes from smaller ($\sim$ 1 ns) to larger ($\sim$ 100 ns) time scales. Thus, there is a unique combination of $g_0^{'}$, $g_\pi^{'}$, and α that gives the best agreement with the entire set of measured probability distributions from 1-100 ns.

From our fits, we generally find that $g_0^{'} \sim 0.25 - 0.3$ and $g_\pi^{'} \approx 1 - 1.3 g_0^{'}$. Several theoretical predictions for $g(\theta)$ have been proposed recently based on different treatments of the effects of non-equilibrium spin populations in the elec-

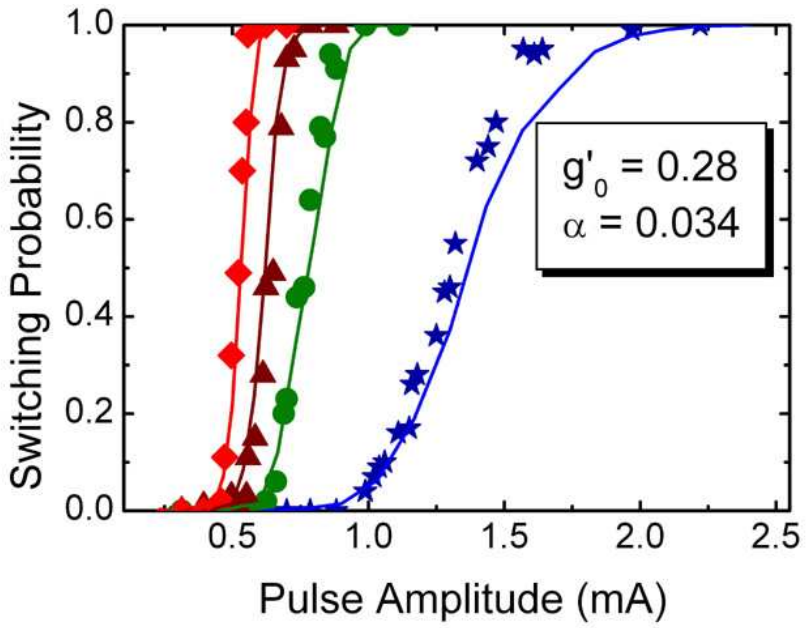

Figure 4.11: Switching probabilities vs. pulse amplitude and single domain simulation fits for P-AP transition in a 4.5 nm Py free layer. Pulse widths for each curve from left to right are 100 ns (♦), 10 ns (▲), 3 ns (●), and 1 ns (⋆).

trodes [25, 27–29]. Our finding that $g_0^{'} \approx g_\pi^{'}$ is in conflict with the prediction that $g_0^{'} \ll g_\pi^{'}$ within some of these models [25, 28]. Perhaps this is due to the fact that Py has a short spin-relaxation length [30], comparable to our free-layer widths, which should act to reduce non-equilibrium electrode effects. As shown in the next chapter, micromagnetic magnetization configurations may also play a role. The near symmetry of $g_0^{'}$ and $g_\pi^{'}$ reflects that the magnitudes of measured critical currents are surprisingly similar for P-AP and AP-P switching, which is advantageous for practical memory devices. Our fits also yield values for the phenomenological damping parameter, $\alpha \approx 0.03$, which is comparable to recent reports [31], but is $\sim 4\times$ the damping in bulk Py. Unlike recent spin torque ferromagnetic resonance (ST-FMR) experiments [37] of small angle magnetization dynamics in Py nanomagnets which measure damping values closer to bulk values (~ 0.01), these experiments involve a different regime of dynamics with large amplitude oscilla-

tions leading up to the reversal event. In this regime, it appears that the effective damping acting on the free layer is increased, as extracted from our macrospin fits. Additional enhancement of the damping could be caused by non-equilibrium "spin pumping" effects [32, 34], interactions of the precessing free layer with the fixed layer, and/or spin relaxation arising from defects generated in the nanopillar fabrication process.

4.5 Summary

To fully explore the advantages of low M_s ferromagnets, I also fabricated nanopillar devices with a free layer consisting of a PyCu alloy. This built upon work performed by Andrei Garcia [35] to introduce a diamagnetic material, like Cu, into permalloy to provide us with an even lower saturation magnetization ferromagnet for spin transfer studies. Introducing Cu into the alloy reduced the saturation magnetization by roughly a factor of two, to $\sim$ 260 emu/cm^3 at 295 K. Devices with this material as the free layer exhibited small ΔR and superparamagnetic behavior at room temperature due to the smaller M_s of the magnet, making them unsuitable for reversal experiments. In an effort to improve on these results, I introduced a thin CoFe (6 $\mathring{A}$) layer between the Cu spacer and the PyCu, which due to the high interfacial polarizing properties of the material acted to enhance spin polarization and improve the magnetic properties of the free layer. By the simple process of adding this interfacial layer, ΔR was increased by a factor of 2-3, while the free layers began exhibiting ferromagnetic behavior, although this required the use of a larger free layer volume (5.5 $\times$ 60 $\times$ 180 nm^3 ellipses) to maintain free layer thermal stability. $\langle M_s \rangle$ = 360 emu/cm^3 at 293 K for this CoFe (0.6 nm)/$Py_{65}Cu_{35}$ (5.5 nm) composite free layer, retaining a lower value than in

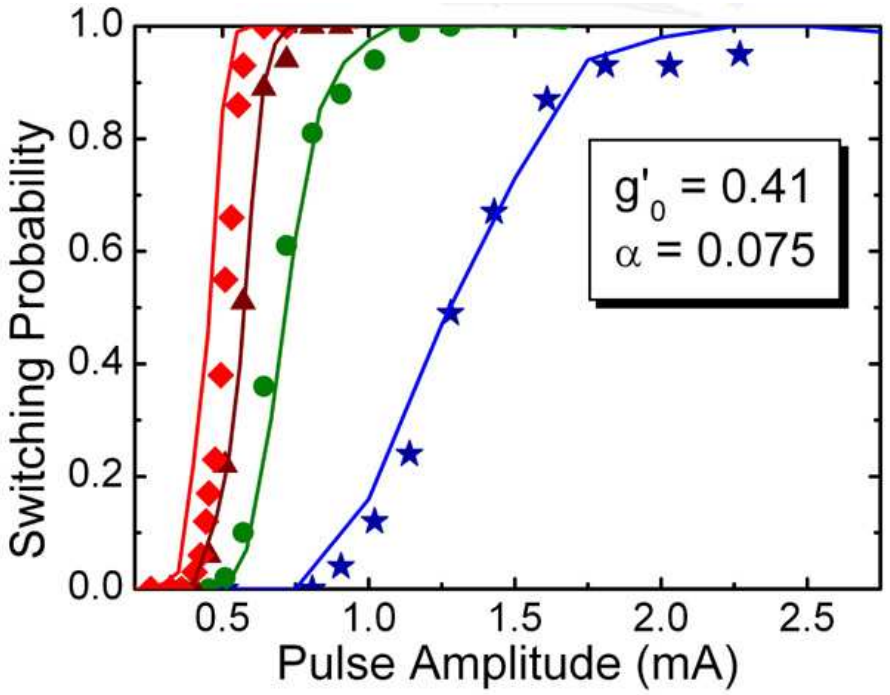

Figure 4.12: Switching probabilities vs. pulse amplitude and simulations (solid lines) for AP-P switching of a 0.6 nm CoFe/5.5 nm PyCu free layer measured at 295 K. Pulse widths for each curve from left to right are 100 ns (♦), 10 ns (▲), 3 ns (●), and 1 ns (⋆).

the pure Py material used in the experiments described above. Pulse-switching results for one such device are shown in Fig. 4.12 along with model fits. The torque parameters for this device, $g_0^{'} = g_\pi^{'} = 0.41$, are somewhat larger than is typical for the pure Py devices, indicating that the use of a thin, high M_s cladding layer could be successful in enhancing interfacial spin polarization without significant alteration of material parameters such as M_s. However, the damping is also much larger, $\alpha \approx 0.075$, due either to spin pumping effects (which scale as $1/M_s$) or impurities introduced in the free layer during cosputtering of Py and Cu. This increased damping combined with the larger free layer volume required for thermal stability reduces the overall advantage of the smaller M_s for this alloy, so that significantly smaller values of I_c are not achieved.

In summary, we have fabricated high aspect ratio, thermally stable nanopillar spin valves that require comparatively low currents for the short-pulse spin-torque switching of the Py and PyCu free layers. Current amplitudes of approximately 4-5 I_{c0}, where I_{c0} is the $T = 0$ critical current determined by slow-ramp-rate measurements, are required to ensure switching with 1 ns pulses. Fits to the pulse data using the LLG model indicate a high damping parameter $\alpha \approx 0.03$, and that the spin-torque function $g(\theta)$ is more symmetric than expected theoretically, with initial slopes $g_0^{'} \approx g_\pi^{'} \approx 0.2 - 0.3$. Devices with PyCu-alloy free layers have an even higher $\alpha \approx 0.075$ and require larger area patterns to maintain thermal stability, indicating that the maximum benefit for room temperature switching is achieved using pure Py. Further reductions in I_{c0} will require increases in $g_0^{'}$ and $g_\pi^{'}$, and/or decreases in α. Additional methods of increasing switching speed for a fixed pulsed current amplitude include introducing a nonzero equilibrium angle between the free and fixed layers [18, 31], or fabricating devices with two fixed layers, one on either side of the free layer [36, 37]. An enhancement in H_k would

result from eliminating the dipole field on the free layer through use of a properly designed synthetic antiferromagnetic fixed layer.

REFERENCES

[1] Slonczewski J.C, Current-driven excitation of magnetic multilayers, *J. Magn. Magn. Mater* **159**, L1 (1996).

[2] Berger L, Emission of spin waves by a magnetic multilayer traversed by a current, *Phys. Rev. B* **54**, 9395 (1996).

[3] Katine J.A, Albert F.J., Buhrman R.A., Myers E.B., & Ralph D.C., Current-driven magnetization reversal and spin-wave excitations in Co/Cu/Co pillars, *Phys. Rev. Lett.* **84**, 3149 (2000).

[4] Myers E.B., Ralph D.C., Katine J.A., Louie R.N., & Buhrman R.A., Current-induced switching of domains in magnetic multilayer devices, *Science* **285**, 867 (1999).

[5] Albert F.J., Emley N.C., Myers E.B., Ralph D.C., & Buhrman R.A., Quantitative study of magnetization reversal by spin-polarized current in magnetic multilayer nanopillars, *Phys. Rev. Lett* **89**, 226802 (2002).

[6] Kaka S., Pufall M.R., Rippard W.H., Silva T.J., Russek S.E., Katine J.A., & Carey M., Spin transfer switching of spin valve nanopillars using nanosecond pulsed currents, *J. Magn. Magn. Mater.* **286**, 375 (2005).

[7] Devolder T., Tulapurkar A., Yagami K., Crozat P., Chappert C., Fukushima A., & Suzuki Y., Ultra-fast magnetization reversal in magnetic nano-pillars by spin-polarized current, *J. Magn. Magn. Mater.* **286**, 77 (2005).

[8] Sun J.Z., Spin-current interaction with a monodomain magnetic body: A model study, *Phys. Rev. B* **62**, 570 (2000).

[9] Baibich M.N., Broto J. M., Fert A., Van Dau F.N., Petroff F., Eitenne P., Creuzet G., Friederich A., & Chazelas J., Giant magnetoresistance of (001)Fe/(001)Cr magnetic superlattices, *Phys. Rev. Lett.* **61**, 2472 (1988).

[10] Binasch, G., Grünberg, P., Saurenbach, F. & Zinn, W., Enhanced magnetoresistance in layered magnetic structures with antiferromagnetic interlayer exchange, *Phys. Rev. B* **39**, 4828 (1989).

[11] Emley N.C., Ph.D. thesis, Cornell University (2005).

[12] Donahue M.J, & Porter D.G., *OOMMF User's Guide, Version 1.0*, *Technical Report No.* NISTIR 6376 (National Institute of Standards and Technology, Gaithersburg, MD, 1999).

[13] Koch R.H., Katine J.A, & Sun J.Z., Time-resolved reversal of spin-transfer switching in a nanomagnet, *Phys. Rev. Lett.* **92**, 088302 (2004).

[14] Krivorotov I.N., Emley N.C., Garcia A.G.F., Sankey J.C., Kiselev S.I., Ralph D.C., & Buhrman R.A., Temperature dependence of spin-transfer-induced switching of nanomagnets, *Phys. Rev. Lett* **93**, 166603 (2004).

[15] Neel L., *Ann. Geophys.* **5**, 99 (1949).

[16] Brown W.F., Thermal fluctuations of a single-domain particle, *Phys. Rev.* **130**, 1677 (1963).

[17] Wernsdorfer W., Classical and quantum magnetization reversal studied in nanometer-sized particles and clusters, *Adv. Chem. Phys.* **118**, 99 (2001).

[18] Myers E.B., Albert F.J., Sankey J.C., Bonet E., Buhrman R.A, & Ralph D.C., Thermally activated magnetic reversal induced by a spin-polarized current, *Phys. Rev. Lett* **89**, 196801 (2002).

[19] Myers E.B., Ph.D. thesis, Cornell University (2002).

[20] Arrenhius S., ber die Reaktionsgeschwindigkeit bei der Inversion von Rohrzucker durch Suren, *S. Phys. Chem.* (Leipzig) **4**, 226 (1889).

[21] Victora R.H., Predicted time-dependance of the switching field for magnetic materials, *Phys. Rev. Lett* **63**, 457 (1989).

[22] Kurkijarvi, J., Intrisic fluctuations in a superconducting ring closed with a josephson junction, *Phys. Rev. B* **6**, 832 (1972).

[23] Garg A., Escape-field distribution for escape from a metastable potential well subject to a steadily increasing bias field, *Phys. Rev. B* **51**, 15592 (1995).

[24] Sankey J.C., Krivorotov I.N., Kiselev S.I., Braganca P.M., Emley N.C., Buhrman R.A., & Ralph D.C., Mechanisms limiting the coherence time of spontaneous magnetic oscillations driven by dc spin-polarized currents, *Phys. Rev. B* **72**, 224427 (2005).

[25] Xiao J., Zangwill A., & Stiles M. D., Boltzmann test of Slonczewski's theory of spin-transfer torque, *Phys. Rev. B* **70**, 172405 (2004).

[26] Soulen R.J., Byers J.M., Osofsky M.S., Nadgorny B., Ambrose T., Cheng S.F., Broussard P.R., Tanaka C.T., Nowak J., Moodera J.S., Barry A., Coey J.M.D., Measuring the spin polarization of a metal with a superconducting point contact, *Science* **282**, 85 (1998).

[27] Manschot J., Brataas A., & Bauer G.E.W., Reducing the critical switching current in nanoscale spin valves, *Appl. Phys. Lett.* **85**, 3250 (2004).

[28] Slonczewski J.C., Currents and torques in metallic magnetic multilayers, *J. Magn. Magn. Mater.* **247**, 324 (2002).

[29] Kovalev A.A., Brataas A., & Bauer G. E. W., Spin transfer in diffusive ferromagnet-normal metal systems with spin-flip scattering, *Phys. Rev. B* **66**, 224424 (2002).

[30] Steenwyk S.D., Hsu S.Y., Loloee R., Bass J., & Pratt W.P., Perpendicular-current exchange-biased spin-valve evidence for a short spin-diffusion length in permalloy, *J. Magn. Magn. Mater.* **170**, L1 (1997).

[31] Krivorotov I.N., Emley N.C., Sankey J.C., Kiselev S.I., Ralph D.C., & Buhrman R.A., Time-domain measurements of nanomagnet dynamics driven by spin-transfer torques, *Science* **307**, 228 (2005).

[32] Tserkovnyak Y., Brataas A., & Bauer G.E.W., Dynamic stiffness of spin valves, *Phys. Rev. B* **67**, 140404 (2003).

[33] Fuchs G.D., Sankey J.C., Pribiag V.S., Qian L., Braganca P.M., Garcia A.G.F., Ryan E.M., Li Z.-P., Ozatay O., Ralph D.C., & Buhrman R.A., Spin-torque ferromagnetic resonance measurements of damping in nanomagnets, *Appl. Phys. Lett.* **91**, 062507 (2007).

[34] Heinrich B., Tserkovnyak Y., Woltersdorf G., Brataas A., Urban R., & Bauer G.E.W., Dynamic exchange coupling in magnetic bilayers, *Phys. Rev. Lett.* **90**, 187601 (2003).

[35] Private communication with Andrei Garcia. The PyCu alloy mentioned was deposited using cosputtering of Py with Cu.

[36] Berger L., Multilayer configuration for experiments of spin precession induced by a dc current, *J. Appl. Phys.* **93**, 7693 (2003).

[37] Fuchs G.D., Krivorotov I.N., Braganca P.M., Emley N.C., Garcia A.G.F., Ralph D.C., & Buhrman R.A., Adjustable spin torque in magnetic tunnel junctions with two fixed layers, *Appl. Phys. Lett.* **86**, 152509 (2005).

CHAPTER 5

ENHANCEMENT IN SPIN-TORQUE EFFICIENCY BY NONUNIFORM SPIN CURRENT GENERATED WITHIN A TAPERED NANOPILLAR SPIN VALVE

5.1 Introduction

The ability of a spin-polarized current pulse to rapidly reverse the orientation of a thin film nanomagnet through the transfer of spin angular momentum has been studied extensively due to possible uses in high performance magnetic random-access memory (MRAM). However, the realization of spin torque (ST) MRAM requires that the current level for reliable and fast writing be low enough to be compatible with both scaled complementary metal-oxide-semiconductor (CMOS) transistors and high-performance magnetic tunnel junctions (MTJs) employed as MRAM elements [1–3]. Additional requirements for data retention demand that the nanomagnet have a strong enough combination of anisotropy field H_K and magnetic moment $\mathbf{m}$ so that there is a sufficient energy barrier U_A opposing random thermal reversal of the nanomagnet orientation [4, 5]. This poses a significant challenge, since the current for ST reversal also scales with $\mathbf{m}$, making the current (density) levels for fast (< 3 ns) ST writing quite high, > 1 mA ($> 10^7$ A/cm^2), in experiments to date [6–8].

Several methods have been examined to reduce the ST reversal current I_s. One approach is to increase the spin polarization P of the incident current, but this effect begins to saturate [9, 10] once $P > 66\%$. At that point, the angular momentum transferred per electron with polarization transverse to $\mathbf{m}$ becomes very close to the ideal limit, neglecting spin accumulation effects that can occur in

spin valve structures [11–13]. Combining this approach with two reference layers bracketing the free layer can further reduce I_s by up to a factor of two [14, 15], but this still may not be sufficient to realize high speed nonvolatile ST-MRAM. Other strategies involve more complicated structures, such as injecting a highly localized spin-polarized current by use of a nanoconstriction [16], or using ferromagnetic multilayers where the reference and free layers are polarized out of plane [17] due to intrinsic perpendicular anisotropy. Although these approaches can reduce I_s, they require advances in magnetic materials or complicated fabrication processes such that their practicality has yet to be fully demonstrated.

Here we discuss simulations and experimental results demonstrating an alternative means of substantially enhancing the efficiency of spin-polarized currents driving the fast reversal of thin film nanomagnets, in a way that does not require materials development or multiple nanolithography steps. This approach integrates the strategy proposed in Chapter 4 using ferromagnetic material with a comparatively low saturation magnetization density M_s and high spin filtering properties, such as $Ni_{81}Fe_{19}$ alloy (Py), together with a device geometry utilizing a comparatively thick reference layer with tapered sidewalls. As a consequence of this geometry, the spin current generated by the reference layer is not uniformly polarized in the plane of the film, but instead has a component with substantial out-of-plane polarization (OPP) maximized near the ends of the major axis of the device. Micromagnetic simulations (MMS), as discussed below, predict a substantially reduced threshold current required for magnetic reversal, and a significant enhancement in the rate at which the reversal time decreases with current above this threshold. These simulations are supported by experimental ST pulse-switching results obtained from spin-valve nanopillar device structures designed and fabricated to enhance the OPP component of the current flowing between the

reference and free layers. Our study indicates that tuning the geometry of a ST device to obtain a spatially non-uniform OPP current component is an enabling technique for the realization of ST-MRAM with reliable nanosecond writing at low current-pulse amplitudes.

5.2 Spin-Torque Reversal

The basics of nanomagnet reversal by spin transfer in metallic multilayers are well established [9, 18]. When a spin current generated by electrons passing through or reflecting from a ferromagnetic reference layer impinges on a nanomagnet, the component of the spin current transverse to the local moment of the nanomagnet is transferred to it with an efficiency that depends on the nanomagnet's spin filtering properties. If both the polarization of the incident spin current and the easy axis of the nanomagnet are in the plane of the film, the predominant average effect of the spin transfer is, depending upon the direction of current flow, to exert either an extra damping or "anti-damping" torque on the nanomagnet. In the latter case, when $I = I_c$ the spin torque initiates oscillations of the free layer magnetization. When the switching current I_s is reached, the oscillations have grown in amplitude sufficiently that the nanomagnet moment develops a net component opposite to its original easy-axis orientation, at which point the spin torque causes the nanomagnet to settle rapidly into a quiescent magnetically-reversed state.

I_c can be estimated analytically by modeling the nanomagnet as uniformly polarized and by employing the standard Landau-Lifschitz-Gilbert-Slonczewski (LLGS) equation to describe the behavior of this "macrospin". When both the reference and free layers have their equilibrium moments fully in plane we have

[9, 19–21],

$$I_c^{\pm} = \frac{\alpha}{\eta^{\pm}} \left(\frac{2e}{\hbar} \right) M_s V \left[H_{eff} + 2\pi M_{eff} \right], \tag{5.1}$$

Here $I_c^{\pm}$ is the critical current for the onset of dynamics when the reference and free layers are nearly parallel/anti-parallel, α is the Gilbert damping parameter, e is the electron charge, M_s is the saturation magnetization of the free layer, V the free layer volume, H_{eff} the effective field acting on the free layer, $4\pi M_{eff}$ is its effective demagnetization field (typically $4\pi M_{eff} >> H_{eff}$), and $\eta^{\pm}$ is the spin torque efficiency parameter, which varies with the alignment angle θ between the free and reference magnets. To the extent that the macrospin model approximates the true critical current for ST reversal of a nanomagnet, the pathway for reducing switching currents is clear; maximize η, and minimize α, M_s, and V. However, the constraint of thermal stability, which is typically taken as requiring $U_A = M_s H_k V/2 \geq 40kT$, where T is the device operating temperature, and materials constraints determining damping (≥ 0.01 for conventional MRAM materials), provide limited flexibility for optimization. One strategy, since H_k scales with both M_s of the nanomagnet and its thickness, is to use a thicker free layer composed of a lower M_s material to maintain U_A, thereby lowering I_c through a reduction in the demagnetization field $4\pi M_{eff}$ (assuming high spin torque efficiency is maintained).

A different approach for ST switching is to use a spin current polarized entirely perpendicular to the plane of the in-plane magnetized free layer [22, 23]. In this case, the predominate effect of the spin torque is to directly force the free layer magnetization out of plane. When this effect becomes large enough relative to H_k, the nanomagnet begins to precess freely about the large out-of-plane demagnetization field. Macrospin modeling [21] predicts this onset to be at

$$I_c^{\perp} = \frac{M_s V}{\eta(\theta = \pi/2)} \left(\frac{2e}{\hbar} \right) \left[\frac{H_k}{2} \right]. \tag{5.2}$$

Reversing the spin torque after a 90° rotation of the free layer and then terminating it at the 180° point could result in very rapid reversal ($\sim$ 100 ps), but this requires both precise timing of the current pulse and higher amplitudes than spin currents polarized in-plane, since typically $H_k > \alpha(2\pi M_{eff})$.

Here, I demonstrate that a significant benefit in nanosecond reversal can be achieved with a combination of both in-plane and out-of-plane polarized spin currents. By employing the macrospin approximation, it is straightforward to obtain a qualitative understanding of this effect using simulations, although to our knowledge such a combination has not been previously discussed. This involves solving the LLGS equation for a single magnetic layer with a uniform moment, where the spin-torque term used was of the form in ref. 6, with a value of $\Lambda = 1$ for the torque asymmetry parameter to directly compare to the micromagnetic simulations discussed below. Typical material parameters were used for Py: the damping constant $\alpha = 0.014$ [24], the $T = 0$ saturation magnetization of the free layer $M_s = 650$ emu/cm^3 (determined by superconducting quantum interference device magnetometry measurements), easy axis anisotropy field $H_k = 150$ Oe, and spin polarization [25] $P = 0.37$. These simulations show that the reversal rate of a 5 nm thick, 45x125 nm^2 elliptical Py nanomagnet will be substantially enhanced if, e.g., the spin current ($P = 37\%$) has its polarization 10° out of plane, in comparison to the case of an equal current that is fully in-plane polarized (IPP). This enhancement, which does not require a precisely timed pulse, occurs because the OPP component accelerates the rate at which the macrospin moment spirals out of the plane (Fig 5.1) and is somewhat similar in nature to the benefit of an applied, in-plane hard-axis magnetic field applied simultaneously with an IPP current [26]. This enhancement grows with the OPP in the macrospin model, but when the out-of-plane torque finally becomes large enough to overcome H_k, the effect transitions

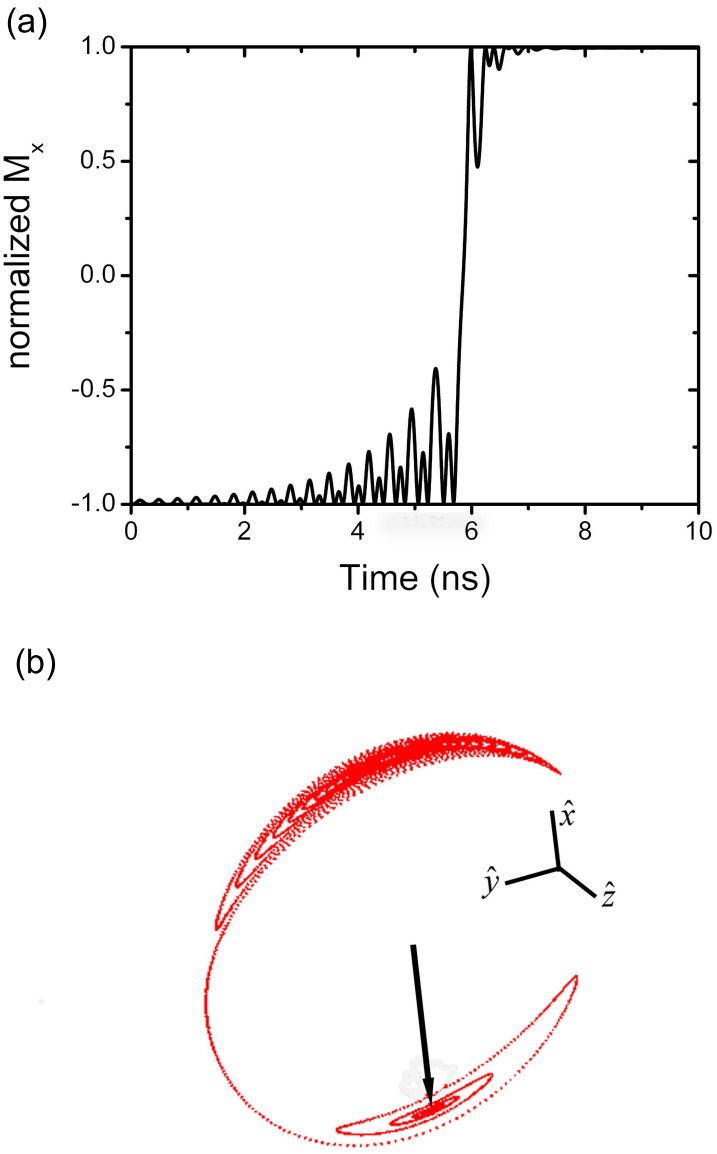

Figure 5.1: (a) Normalized M_x vs. time for a macrospin nanomagnet excited by a -2 mA current polarized 10° out of plane. The out of plane polarization accelerates the rate at which the amplitude of the magnetization oscillations grows, resulting in faster reversal than with in-plane polarization only. (b) Three dimensional representation of the magnetization trajectory for the simulation in (a).

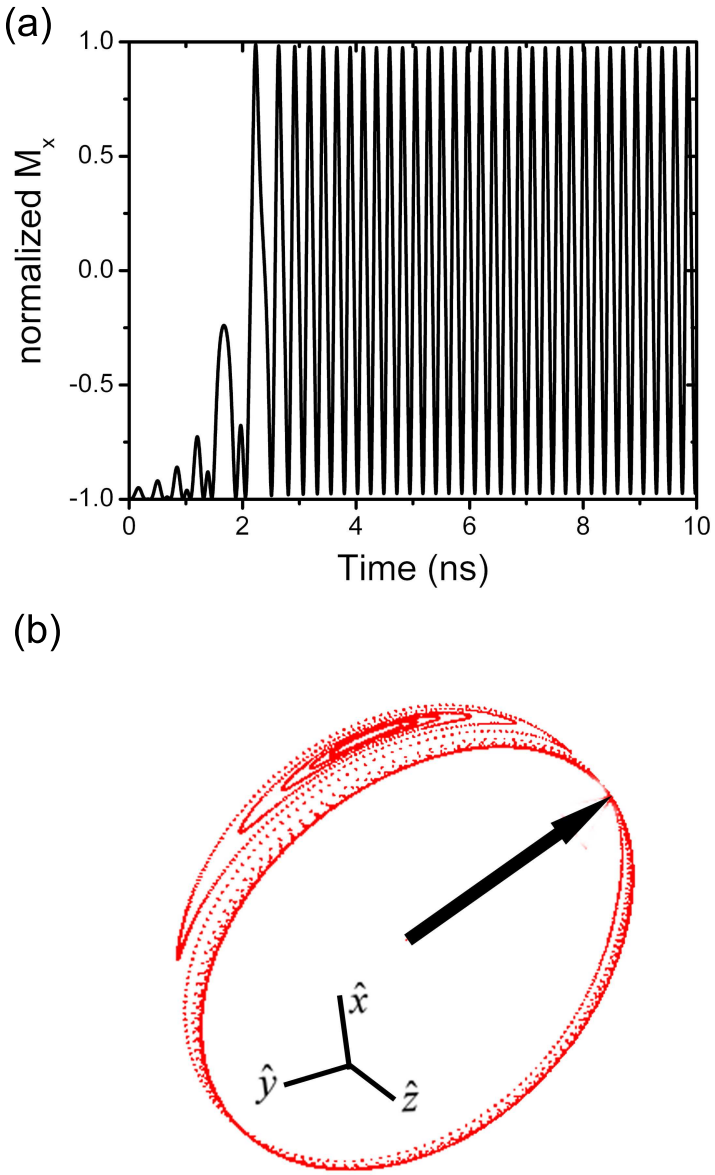

Figure 5.2: (a) Normalized M_x vs. time for a macrospin nanomagnet excited by a -3 mA current polarized 10° out of plane. Even with a small out of plane component, large enough current amplitudes pull the magnetization out of plane far enough to drive the magnetization into a persistent precessional mode oscillating around the demagnetization field. (b) Three dimensional representation of the magnetization trajectory for the simulation in (a), illustrating magnetization oscillation with the precession axis out of plane ($\hat{z}$ axis).

from one assisting the IPP reversal mechanism to one where the OPP current dominates, resulting in continuous precession about the demagnetization field for as long as the current is applied (Fig. 5.2). We show below that when the micromagnetic behavior of nanopillar devices and of spatially non-uniform spin currents are considered, this detrimental effect can be minimized and a small OPP component can have an even greater positive effect on short pulse ST reversal than indicated by the macrospin model.

5.3 Micromagnetic Simulations of Spin-Torque Reversal

While macrospin modeling provides qualitative understanding, micromagnetic simulations (MMS) give better insight into the detailed reversal behavior of nanomagnetic structures [27]. These micromagnetic simulations [28] incorporate the LLGS equation (not including a field-like torque term) at $T = 0$ with the same spin torque and material parameters as used in the macrospin simulations, with the exchange constant $A = 1.3 \times 10^{-6}$ erg cm^{-1}, and the volume discretized into 2.5 nm cubes for computational purposes. Static ($I = 0$) simulations of a spin valve structure are used to determine both the field required to cancel out the average dipole field exerted on the free layer by edge charges on the reference layer for the two layer structures, and to calculate the initial micromagnetic state of the free and reference layers at the dipole field. To avoid an initial state with collinear magnetic moments in the two layers, we induce an initial in-plane misalignment (10°) by calculating the configuration with a magnetic field along the in-plane hard axis of the ellipse. This field is turned off simultaneously with the application of the current pulse for $I = 0$ simulations. Dynamic ($I \neq 0$) simulations include effects from magnetic interactions between the two layers and the Oersted field due to I. Spin torque is

exerted upon both layers, with the local spin polarization of the current incident upon a layer being dependent on the local magnetization vector of the second ferromagnet, i.e. the current flow was assumed to be one-dimensional [11–13]. We treat spins classically and use the simplifying assumption that spins transmit the parallel component and reflect the antiparallel component of the local magnetization perfectly, depending on the direction the electrons traverse. This assumption requires us to use a value of $\Lambda = 1$ for the asymmetry parameter [11] to avoid false enhancement in spin torque in one reversal direction over the other. This choice, which neglects the spin accumulation effects that are expected to be present in spin valve structures, still allows for qualitative comparison of the reversal time between different device configurations.

We first consider an elliptical disk of finite thickness that has a spatially non-uniform demagnetization tensor (unlike an ellipsoid of rotation), such that the demagnetization field $4\pi M_{eff}$ decreases significantly from the center to the ends of the major axis of the disk. When properly considered by MMS, this lowers the local critical current density J_c for the onset of ST excited magnetization oscillations near the ends. Zero T simulations including the Slonczewski ST term [11, 28] (ST-MMS) reveal that, for currents slightly above I_s, ST-driven oscillations grow faster at the ends of the ellipse, resulting in a reversal process that is considerably different from uniform macrospin precession. This is indicated in Fig. 5.3, which shows the simulated micromagnetic evolution of a single 5 nm thick Py elliptical disk with 45 nm x 125 nm^2 cross-sectional dimensions. At time $t = 0$ ns, the average magnetization ($\hat{m}_{free}$) is simulated with its initial condition being initially at 170° to the polarization of the incident current ($\hat{m}_p$), which is uniform and in plane along the long axis of the ellipse (see inset Fig. 5.4). Spin torque excites magnetization oscillations that evolve over time. Unlike the macrospin picture,

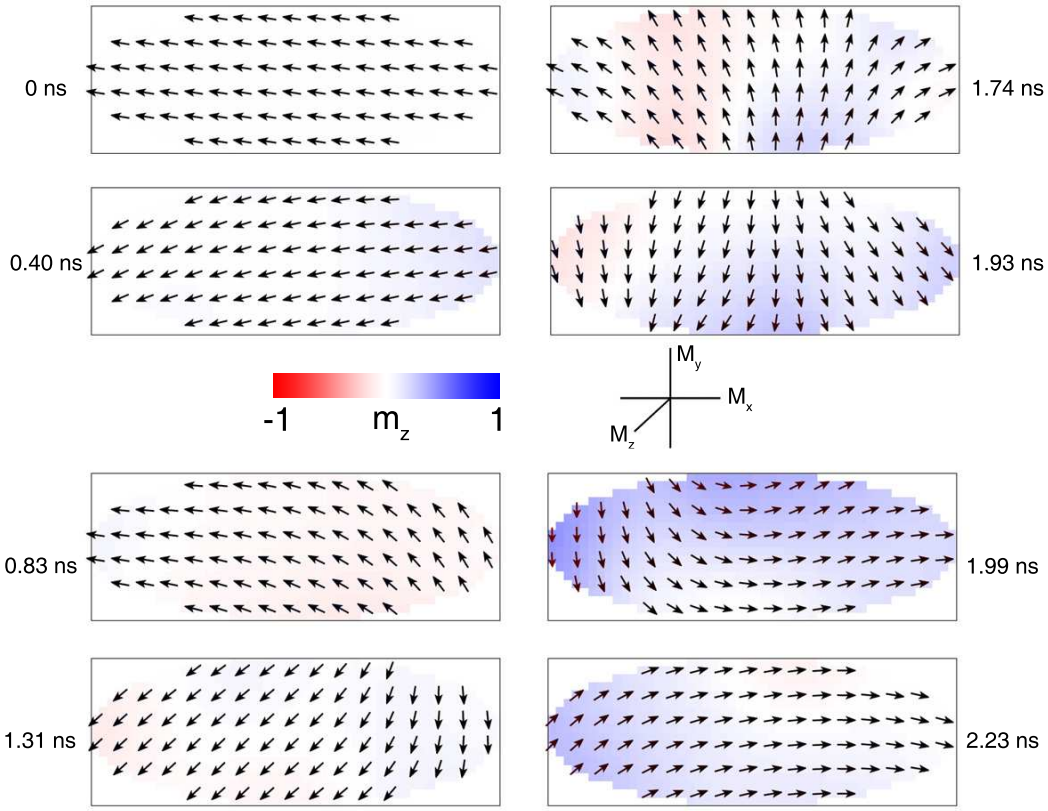

Figure 5.3: Frames of a $T = 0$ micromagnetic simulation at several points in time during the dynamic evolution its moment. Here, we model a single 5 nm thick, 45x125 nm^2 elliptical nanomagnet with $I = 1.5$ mA, using material parameters for Py. The arrows in each frame represent the local in-plane (x-y plane) magnetization of the nanomagnet, while the color scale represents the local out-of-plane (z-axis) magnetization component. These simulations illustrate the importance the edge magnetization oscillations have on reversal behavior, growing in amplitude much more rapidly than the center of the magnet, and eventually dragging the interior along due to exchange interactions. Thus the magnetization does not precess at all uniformly in this reversal process.

which relies on a gradually building oscillation of the assumed uniform and rigid magnetization of the nanomagnet, we see significant magnetization oscillations begin at the edges, since the demagnetization field of the magnet is $\sim 30\%$ smaller there. This manifests as a larger displacement away from the x-axis at the edges of the ellipse for the times between 0 and 1.31 ns. At $t = 1.74$ ns, the amplitude of the magnetization oscillations brings the magnetization approximately 90° in plane from its initial position, however, the magnetization cannot reverse due to competition from the left and right ends of magnet. Another half precession is required ($t = 1.93$ ns) to reach a state where the magnetization can fully reverse, at $t = 1.99$ ns.

In Fig. 5.4, we plot the reversal rate for such a nanomagnet as determined by ST-MMS for a range of currents, assuming that the polarization of the incident electrons is in-plane and uniform across the nanomagnet's surface. In comparison to macrospin simulation employing the same material parameters and spin-transfer efficiency η the micromagnetic calculation predicts a reduced critical current and a switching rate at larger current increased by approximately a factor of 2. The result of macrospin simulation for the case where the incident spin current is polarized 10° out-of-plane is also shown for comparison. While the macrospin simulation indicates that an out-of-plane polarization is effective in enhancing ST reversal in the shorter pulse regime, the micromagnetic details indicate faster reversal over the entire range of pulse widths that we have simulated. ST-MMS does indicate that the ST enhancement due to the micromagnetics of a thick, low M_s free layer is slightly lower when a typical fully-patterned, spin-valve nanopillar device structure is modeled. Then, if the reference layer is assumed to be uniformly magnetized in-plane, ST-MMS predicts switching rates as shown in Fig. 5.7, with the difference compared to Fig. 5.4 being attributed to the effect of the non-uniform component

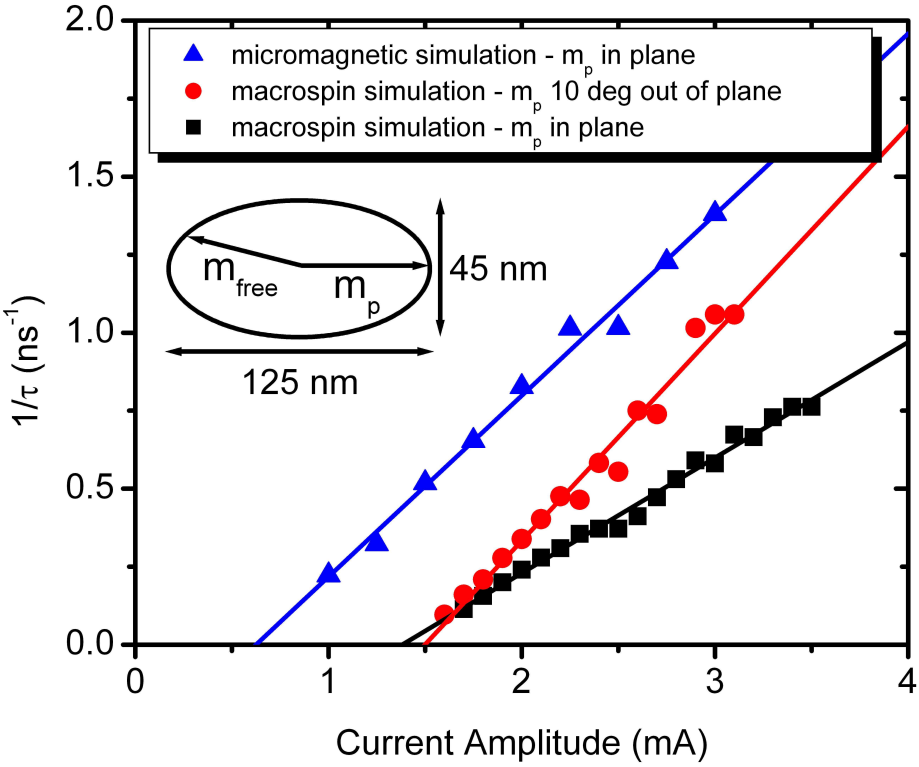

Figure 5.4: Comparison of reversal times τ for the elliptical nanomagnet discussed in Fig. 5.3 treated both as a macrospin and micromagnetically. From the macrospin simulations, we find that a spin current polarization ($\hat{m}_p$) oriented 10° out of the plane of the film can substantially enhance the magnetization reversal rates, especially for time scales on the order of 1 ns, as compared to the in-plane polarization case. The large additional enhancement in reversal rate for the micromagnetic simulations indicate that the incoherent reversal mechanism shown in Fig 5.3 is more efficient than coherent T=0 macrospin reversal. The lines are least squares fit through the simulation results.

of the dipole field from the reference layer in suppressing magnetization oscillations at the ends of the free layer. This detrimental effect of the dipole field can be largely countered by choosing the reference layer geometry and material so as to generate a spatially non-uniform spin current with a significant OPP component. Such a spin current can be obtained by using a relatively thick ($\sim$ 20 nm) low-M_s reference layer, so that demagnetization effects result in an out-of-plane magnetization component at the ends of the major axis of a patterned ellipse. This effect is enhanced by tapering the edges of the reference layer, which can be accomplished via directional ion beam milling during nanopillar patterning. A cross-sectional view of the $I = 0$ equilibrium state of this Py-Cu-Py spin valve structure modeled with MMS is shown in Fig. 5.5(a). For this structure, the magnetization cants $\sim 20^\circ$ out of plane at the ends of the interface adjacent to the free layer, and gradually transitions to fully-in-plane near the center. Our ST-MMS calculations for magnetic reversal in this geometry include the interactions between the free and reference layers, both magnetically and by using the reference layer magnetization to determine the local current polarization acting upon the free layer, starting in the misaligned state shown in Fig. 5.5(b). The simulations show that the OPP component initiates large magnetization oscillations at the ends of the free layer more rapidly than with the use of a uniform IPP current for the same initial starting state, accelerating the reversal process even though the average oscillation amplitudes grow at about the same rate (see Fig. 5.6). This characteristic of excitation with a non-uniformly polarized current is different than for macrospin reversal, ultimately enhancing reversal in these inverted nanopillars. For reversal times in the 1-3 ns range (see Fig. 5.7), this enhancement is especially significant since this is the timescale over which a reduction in I_s is required for applications. Our simulations do indicate that the variation of the reversal rate with bias cur-

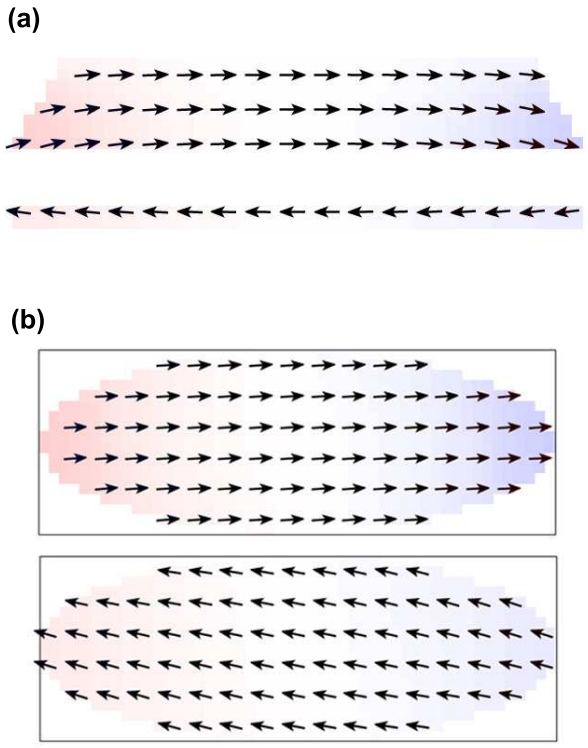

Figure 5.5: (a) T=0 equilibrium state of a two-layer structure with a tapered reference layer above the free layer, as calculated with MMS. (b) Misaligned ($\sim$ 10°) state of the adjacent reference and free layer interfaces calculated by MMS assuming the tapered device geometry and the existence of a 200 Oe in-plane hard-axis magnetic field. This misaligned state is used as the initial configuration for the dynamic simulations, to avoid artifacts associated with a nearly collinear initial state. For the configuration in (b), the magnetization near the edges of the reference layer curls significantly out of plane, which generates current with a partial OPP component and enhances the magnetization oscillations at the edges of the free layer.

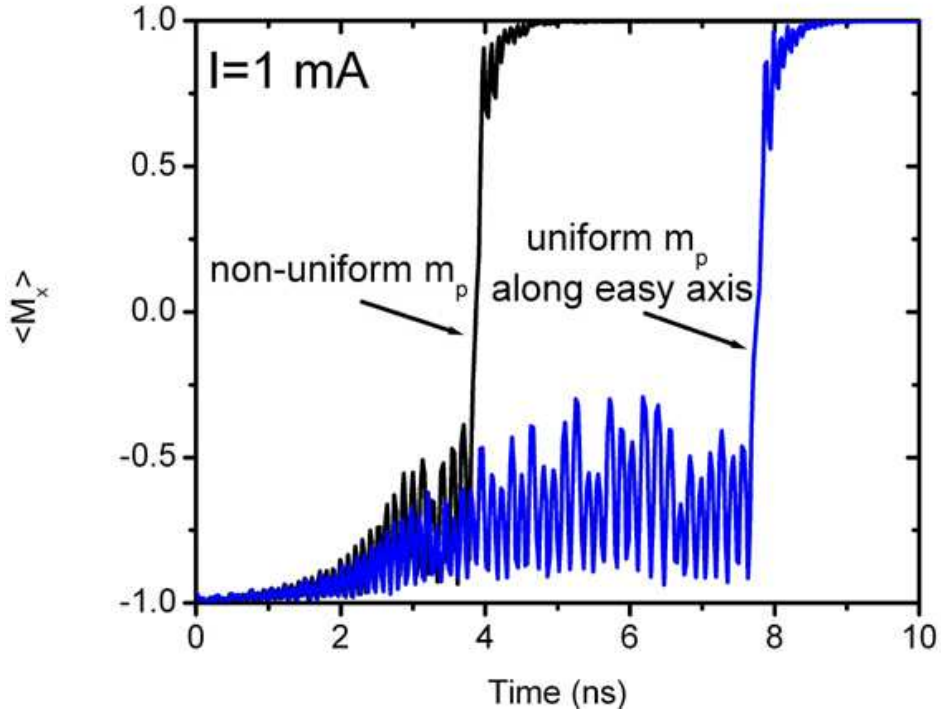

Figure 5.6: Micromagnetic simulations comparing spin transfer reversal excited by current polarized by a tapered reference layer (causing a spatially non-uniform polarization with a component polarized out of the plane) and current with spatially uniform polarization in plane, a condition similar to the macrospin simulation shown in Fig. 5.4. A partial OPP component enhances the magnetization oscillations at the edges of the free layer. The amplitude of these oscillations grows quickly with the assistance of this non-uniform polarization, leading to a significantly faster reversal than with a uniform in plane polarization along the easy axis, as seen in this graph, which shows the evolution of the average free-layer M_x with time at 1 mA. Because the reversal process starts at the ends of the major axis of the free layer and then spreads to involve the entire nanostructure through the exchange interaction, the amplitude of M_x does not grow monotonically until the reversal point as it does in the macrospin model.

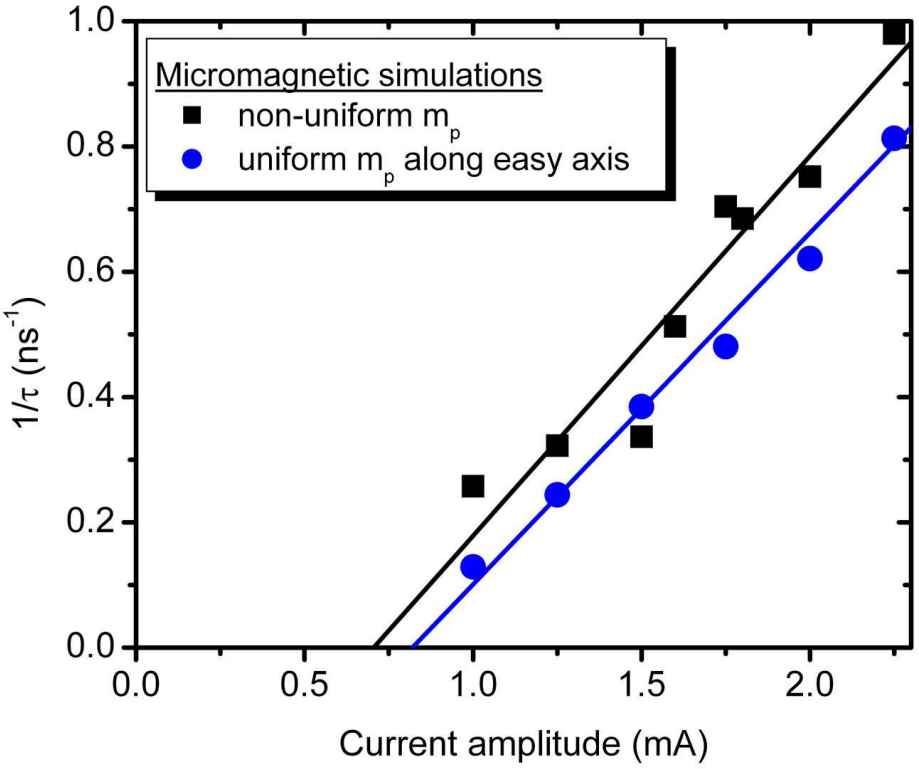

Figure 5.7: The rates for $AP \rightarrow P$ reversal predicted by ST-MMS for the spatially non-uniform OPP case are enhanced compared to the results assuming a uniform, in-plane fixed-layer magnetization along the easy axis. The lines are least-square fits through the ST-MMS results, which deviate from linear behavior due to the incoherent nature of the reversal.

rent in the micromagnetic results may not be as regular as predicted by macrospin modeling, as at certain bias currents the oscillations originating at the two ends can, due to the different directions of the OPP, momentarily oppose each other and slow down the transition to the reversed state. However, experimental results, as discussed in part below, suggest that thermal effects may reduce these interactions, and overall the effect of micromagnetic structure is to significantly enhance reversal efficiency.

5.4 Experimental Demonstration of Spin-Torque Enhancement

We confirmed these beneficial micromagnetic effects with experiments on Py-Cu-Py spin-valve nanopillar devices fabricated from thin film multilayers deposited in two different configurations. In the first, or "standard" case, the multilayer was deposited in the following sequence: 120 Cu/20 Py/12 Cu/5.5 Py/2Cu/30 Pt, where Py is $Ni_{81}Fe_{19}$ and the thicknesses are in nm. For the "inverted" case, the multilayer stack was 120 Cu/4.5 Py/12 Cu/20 Py/2Cu/30 Pt, placing the reference layer of the patterned nanopillars above the free layer rather than below it. The nominal lateral dimensions of the elliptical nanopillar structures were 50 x 130 nm^2, but sidewall tapering of the device during ion milling results in inverted samples having both larger free layers and reference layers with a substantial out-of-plane magnetization component on the side adjacent to free layer (as in Fig. 5.5(a)).

For comparison to MMS, we performed room temperature measurements to determine ST reversal probabilities as a function of current amplitude over a range of pulse widths (1-100 ns), all of which have a significant distribution due to ther-

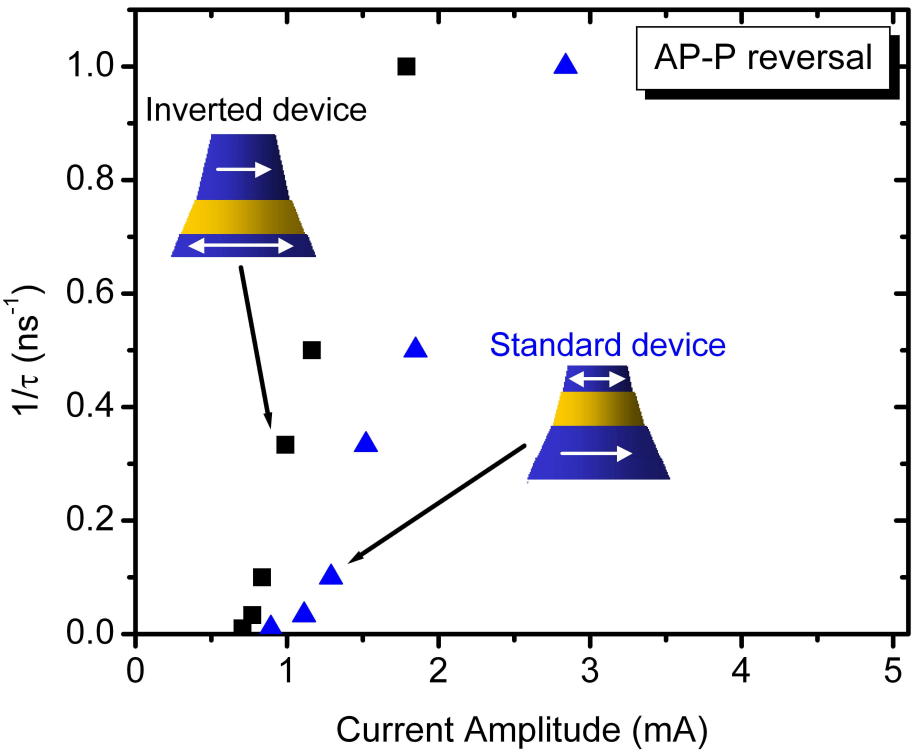

Figure 5.8: $AP \rightarrow P$ reversal rate vs. current for two different device structures, with the reference layer either above (inverted device) or below (standard device) the free layer. In both cases, the sidewalls were tapered during the ion milling required for nanopillar definition. The standard-structure free layer is 5.5 nm thick with a nominal 50 x 130 nm^2 elliptical area, while the inverted-structure free layer is 4.5 nm thick with an area $\sim$ 1.5 that of standard structure. We measured reversal probability for current pulses between 1-100 ns long, and for a given pulse length we define the reversal current as the value which first achieves reversal 95% of the time. A large enhancement occurs for the inverted structure, despite the larger free layer volume.

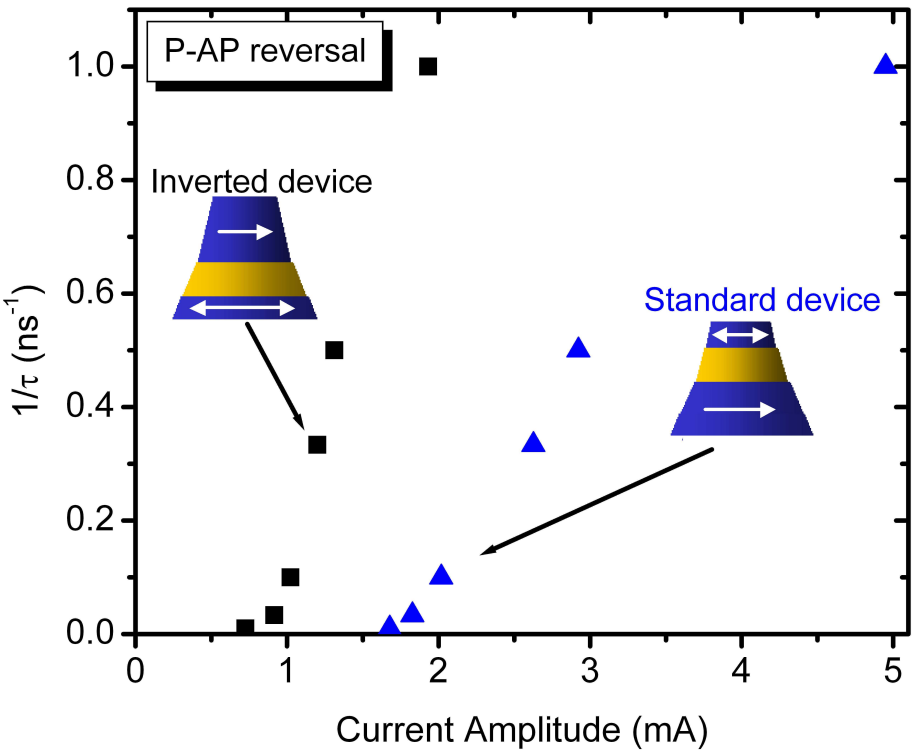

Figure 5.9: $P \rightarrow AP$ reversal rate vs. current for two different device structures, with the reference layer either above (inverted device) or below (standard device) the free layer. In both cases, the sidewalls were tapered during the ion milling required for nanopillar definition. The standard-structure free layer is 5.5 nm thick with a nominal 50 x 130 nm^2 elliptical area, while the inverted-structure free layer is 4.5 nm thick with an area $\sim$ 1.5 that of standard structure. We measured reversal probability for current pulses between 1-100 ns long, and for a given pulse length we define the reversal current as the value which first achieves reversal 95% of the time. A large enhancement occurs for the inverted structure, despite the larger free layer volume.

mal fluctuations [6, 29]. Figures 5.8 and 5.9 plot the pulse current amplitudes I_s required to provide 95% reversal probability as a function of pulse width for a representative device of each configuration type, for the two cases where the free layer of both device configurations is reversed from a state antiparallel to the reference layer to one parallel (AP→P), and vice versa (P→AP). Similar results were seen in 4-5 devices each of standard and inverted configurations. As predicted by ST-MMS (cf Fig. 5.4), the variation of the short-pulse reversal rate with I for standard devices is indeed considerably more rapid than predicted by the macrospin model when applied for the case of $P \sim 0.37$ and free layer dimensions of the standard devices. Even more notably, and also in qualitative accord with ST-MMS, the inverted devices exhibit considerably lower switching currents, and a stronger variation with current amplitude, than the standard devices, despite a free-layer volume estimated to be ~ 1.2 times larger.

One final point to note is that we find that the asymmetry ratio of switching currents, I_c^+/I_c^-, is considerably less in the inverted vs. the standard devices, ~ 1.2 vs. ~ 1.6, and in both cases considerably less than predicted by one-dimensional spin transport analysis [11–13]. We attribute this to the reduction, by the non-uniform magnetization of the reference layer, of the spin accumulation effects that would otherwise enhance η^- but not η^+. This negative effect on η^- is outweighed by the overall increase in ST efficiency by OPP.

5.5 Tapered Nanopillar with Two Reference Layers

To obtain the optimum enhancement, we propose to combine the benefits of the out-of-plane spin polarization with a second magnetic reference layer using the

three-magnetic-layer device structure shown in Fig. 5.10. The two thick outer reference layers are anti-parallel to each other, and the sides of the top reference layer are tapered to promote out-of-plane magnetization. The free layer is a 5 nm Py elliptical disk with lateral dimensions of 45 x 125 nm^2 and the reference layers are Py as well. Fig. 5.11 shows the MMS predictions for switching rates for two variations of this structure. In one case, the spin polarization for each layer is taken to be 37%, as should approximately be the case for such a metallic spin valve structure. Since this structure would not exhibit a significant magnetoresistance signal, the second case assumes a tunnel junction between the free layer and the top reference layer with a tunneling spin current polarization of 66%, which results in a near ideal spin torque efficiency of $\eta = 0.92$ [30]. The simulations indicate that the free layer nanomagnet is thermally stable, $U_A \sim 1.75$ eV, and in comparison to the MMS result for a simple inverted spin-valve, the three-magnetic-layer devices switch at the same rate at $\sim 2\times$ lower current. An even simpler approach would be to eliminate the taper, and employ a nanopillar structure with thick, low Ms reference layers and straight sidewalls. Here, the dipole fields originating from edge charges on the two reference layers would have the same effect as tapering the sidewalls, promoting out-of-plane magnetization at the ends of both low-Ms reference layers. This design does not require an ion mill process for tapering, and MMS show that the reversal is only slightly slower than the tapered device in this case, $\sim 5 - 10\%$ (not shown).

5.6 Consequences and Conclusions

More extensive $T > 0$ MMS analysis and experimental studies will be required to fully quantify and optimize these micromagnetic enhancement effects, but clearly

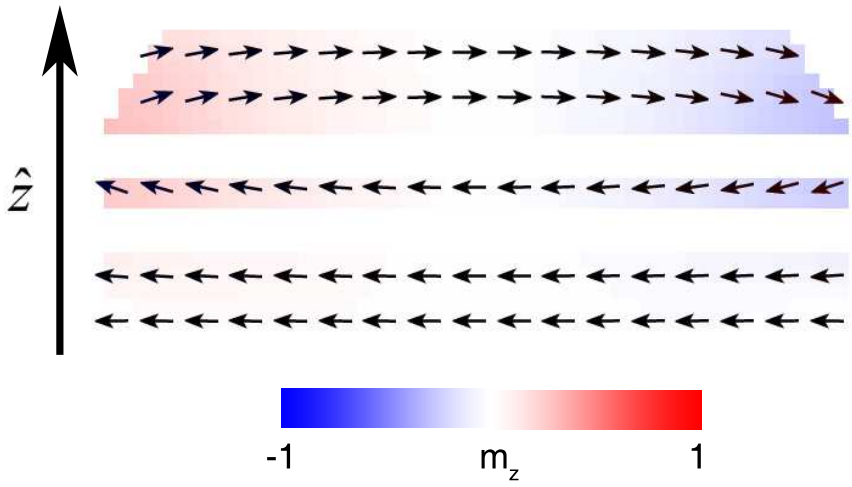

Figure 5.10: Schematic of the equilibrium state (T=0) of a device with two reference layers sandwiching the free layer. Tapering the top of the structure couples the advantage of spin-torque enhancement through micromagnetic effects with added torque from the second reference layer. The spacers can be either non-magnetic metals such as Cu, or if higher polarization is required, insulating layers, such as AlOx or MgO. The two reference layer thicknesses can also be chosen to eliminate the dipolar field acting upon the free layer.

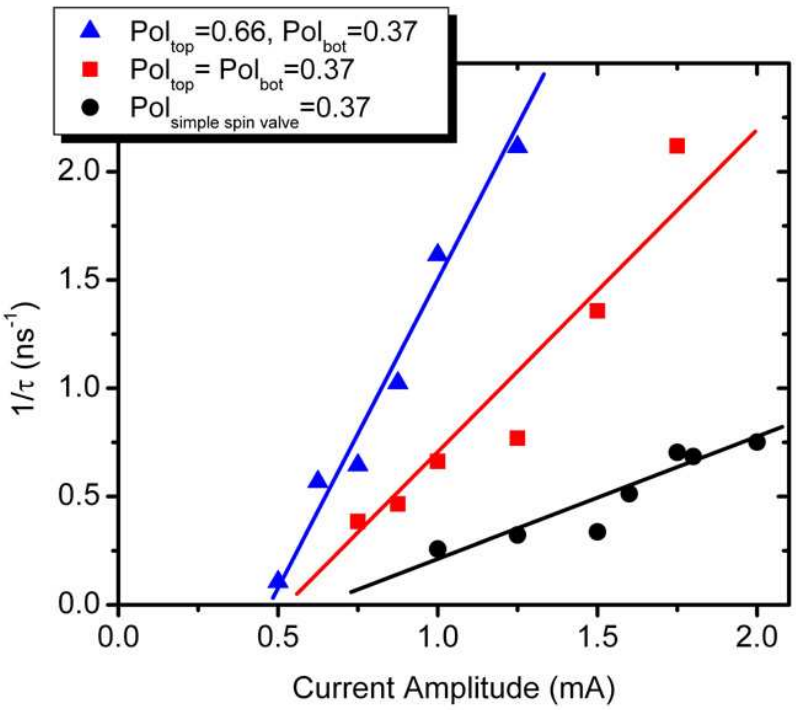

Figure 5.11: T=0 MMS of 2 structures, the first with both spacers being metallic ($P = 0.37$ for both reference layers), and the second with the top spacer assumed to be a tunnel barrier ($P_1 = 0.37$, $P_2 = 0.66$). A misaligned state ($\sim 10 - 15°$) is generated for the free layer with both reference layers along the easy axis in a separate simulation by adding a hard axis field. Similar results for the simple spin valve structure ($P = 0.37$) shown in Fig. 5.5 are included for comparison. The reversal currents predicted are promising for the development of devices with the parameters necessary for ST-MRAM. The lines shown are guides to the eye.

they can be quite significant. We have shown that non-uniform pathways for magnetization reversal can lead to much faster switching in spin valve systems. By using relatively simple fabrication techniques, we can induce magnetization configurations in both magnetic layers that take advantage of these non-uniform reversal mechanisms to obtain more efficient reversal. Future development of this approach for MRAM applications would require the use of magnetic tunnel junctions, where these effects could be easily incorporated. We note that a voltage-dependent field-like contribution to the spin torque that has been found to be significant in tunnel junctions [30] should also augment the OPP effect due to the micromagnetics of this proposed structure, leading to an even more efficient ST reversal process. Although it is quite likely that the combination of several techniques for the enhancement of spin-torque reversal will be required to finally achieve the low switching current values necessary for MRAM applications, we expect that the enhancement in the spin-torque reversal that can be achieved by the micromagnetic mechanisms discussed here will play an important role in the final spin torque device implementation.

5.7 Review of OOMMF Simulation Code

The following section reviews a typical spin transfer OOMMF script used for running the simulations described in both this chapter and the next. Descriptions of commands and the command structure in italics are included for each section of code.

Defining constants

```
set pi [expr 4*atan(1.0)]
```

```
set mu0 [expr 4*$pi*1e-7]
set xlim 125e-9      Sets x dimension (in meters) of magnet
set ylim 45e-9       Sets y dimension of magnet
set hfixed 20e-9     Sets thickness of fixed layer
set hspacer 12.5e-9  Sets thickness of spacer layer
set hfree 5e-9       Sets thickness of free layer
set zlim [expr {$hfixed+$hspacer+$hfree}]  Sets z dimension of system
set theta [expr $pi*30/180]     Sets sidewall taper angle if desired
set cellx 2.5e-9     These next three parameters define the size of the
set celly 2.5e-9     individual cells that the magnets will be discretized into
set cellz 2.5e-9
set AvalFree 13e-12     Exchange constant for free layer - value for Py
set AvalFixed 13e-12    Exchange constant for fixed layer
set alphaval 0.014      Damping constant for Py free layer
set MsvalFree 650e3     M_s of free layer in A/m - value for Py at 4.2K
set MsvalFixed 650e3    M_s of fixed layer
set total_current 1e-3     Applied current in amps, always input + polarity
set total_current_oersted 1e-3     Value with proper polarity
set current_density [expr {$total_current/($pi/4*($xlim)*($ylim))}]
set Polarization 0.37     Sets spin polarization - value for Py
set Lambda 1.0     Sets asymmetry parameter lambda
set fieldFile filename.ohf      Define oersted field file
Parameter Happ 0.250     Applied field in kOe
set Happ [expr {$Happ*1e6/(4*$pi)}]     Convert field to A/m
Parameter Happ_angle 0     Direction of applied field, in degrees
set Happ_angle [expr {$Happ_angle*$pi/180.}]  Convert angle to radians
```

Defining the Atlas

```
Specify Oxs_ScriptAtlas:EllipticalAtlas ‘‘
  xrange { 0 $xlim }
  yrange { 0 $ylim }
  zrange { 0 $zlim }
  regions {free spacer fixed }
  script {Elliptical $hfixed $hspacer $hfree $xlim $ylim $zlim $theta}
’’

Specify Oxs_RectangularMesh:mesh ‘‘
  cellsize {$cellx $celly $cellz}
  atlas :EllipticalAtlas
’’
```

Atlases define the spatial coordinates of the system simulated. Here, we define an atlas named *EllipticalAtlas* using a script *Elliptical* defined at the end of the program. The spatial limits of the system are defined using in the `xrange`, `yrange`, and `zrange` lines. Three regions are defined, corresponding to the free, spacer, and fixed layers, so that parameter values can independently be defined for each layer. Calculations are carried out by breaking each region into individual cells, each of which can have a different solution to the LLGS equation. In this example, we have chosen a rectangular mesh to apply to *EllipticalAtlas*. For this simulation, the system will be broken into 2.5 nm cubes.

Defining the Effective Fields

```
Specify Oxs_Exchange6Ngbr:Py ‘‘
 atlas :EllipticalAtlas
 default_A $AvalFixed
  A {
    spacer spacer 0
    spacer free 0
    spacer fixed 0
    free free $AvalFree
  }
’’

# Applied field
Specify Oxs_FixedZeeman:Happ [subst {
 field {[expr {cos($Happ_angle)}] [expr {sin($Happ_angle)}] 0.0}
  multiplier $Happ
}]

#Demag field
Specify Oxs_Demag {}

# Oersted field
Specify Oxs_FixedZeeman:oerstedField ‘‘
  field { Oxs_FileVectorField {
      xrange { 0 $xlim }
      yrange { 0 $ylim }
      zrange { 0 $zlim }
```

```
    file $fieldFile
  }}
 multiplier $total_current_oersted
''
```

This block defines the various magnetic fields involved in the spin valve system. `Specify Oxs_Exchange6Ngbr` defines the exchange field of the system by considering the exchange interactions of a chosen cell with its 6 nearest neighbor cells. The exchange constant within each layer, as well as between adjacent layers must be implicitly defined here, or the exchange fields will be calculated incorrectly. In the example, cells in the free or fixed layer regions are assigned values determined in the parameter block, while the spacer region is assigned to have no exchange interactions, within the layer itself or with either magnet.

The applied field is set using the `Specify Oxs_FixedZeeman` command, which defines a spatially uniform, time independent magnetic field. All vector fields are defined by a magnitude and directions, which are defined by the field angles and the multiplier value. If consideration of the demagnetization fields are desired, `Specify Oxs_Demag {}` alerts the program to consider those fields in the calculations. Finally, Oersted fields are included, using a vector field file calculated with an external program. I suggest using a program like Mathematica to calculate this field, or at least using already calculated files to approximate your system. The results of this file should be for a 1 mA current value, so that the results can be multiplied by the simulated current.

Defining the Evolver

`#Evolver`

```
Specify Oxs_SpinXferEvolve:evolve ‘‘
  alpha $alphaval     damping constant
  start_dm 0.01     starting dm
  mp {1 0 0}     starting plarization direction
  propagate_mp 1
  J_direction +z     current direction
  J [expr {$current_density}]     current density
  P { Oxs_ScriptScalarField {
       atlas :EllipticalAtlas
       script {PolBoth $Polarization $hfixed $hspacer $hfree $zlim}
  }}
  Lambda $Lambda     torque asymmetry parameter
’’
```

The evolver is the LLGS solver for OOMMF. For spin torque simulations, we must use `Oxs_SpinXferEvolve`. This evolver has several values that must be defined, as labeled above. `Propegate_mp` is an option initially developed at NIST and perfected by Vlad Pribiag, and has been one of the most important enhancements to the code, in that it allows for the local spin polarization to be defined by the local moments of the ferromagnets at any point in time. Here, the command uses a boolean input, with 0 turning the option off (i.e. spatially and time independent polarization defined by m_p) and 1 turning the option on. `P` assigns a script to define the regions where the local polarization is determined, an option which is especially useful in imparting torque at the interface only, since the torque is normalized to the z cell (mesh) dimension.

Defining the Time Driver

```
#Time driver
Specify Oxs_TimeDriver [subst {
 basename EllipticalSV_$xlim$ylim$hfixed$hspacer$hfree     output filename
 evolver evolve
 stopping_time 10e-9     total simulation time (s)
 mesh :mesh
 stage_count 1
 stage_iteration_limit 0
 total_iteration_limit 0

 Ms  { Oxs_AtlasScalarField {
     atlas :EllipticalAtlas
     default_value 0
     values {
        free $MsvalFree
        fixed $MsvalFixed
     }
 }}
 m0 { Oxs_FileVectorField {
     file filename.omf
     multiplier 1
     atlas :EllipticalAtlas
 }}
}]
```

The time driver calculates the LLGS over the time interval defined using the evolver defined in the previous block. In this block, the user defines the length of the simulation in seconds and the output filenames. The initial state of the nanomagnets are defined in this block, with the saturation magnetization M_s determining the magnitude of the moment and $m0$ determining the local magnetization direction of each nanomagnet. Here, M_s is defined for each spatial region of the system, with the local magnetization direction defined by an external file calculated using OOMMF to determine the equilbrium magnetization of the magnets for the magnetic field being considered.

Define Scripts

```
proc Elliptical { hfixed hspacer hfree xlim ylim zlim theta x y z }
  {  set xrad [expr 2*($x-[expr {$z-.46667}]*[expr {tan($theta)}]*
             $zlim/$xlim)*$xlim/($xlim-2*[expr {$z-.46667}]*$zlim*
             [expr {tan($theta)}])-1]
    set yrad [expr 2*($y-[expr {$z-.46667}]*[expr {tan($theta)}]*
             $zlim/$ylim)*$ylim/($ylim-2*[expr {$z-.46667}]*$zlim*
             [expr {tan($theta)}])-1]
    set xrad2 [expr 2.*$x - 1. ]
    set yrad2 [expr 2*$y - 1]
    set test [expr $xrad*$xrad+$yrad*$yrad]
    set test2 [expr $xrad2*$xrad2+$yrad2*$yrad2]
    set a [expr $z*[expr {tan($theta)}]*$zlim]
    set b [expr ($xlim-$a)/$xlim]
    set c [expr ($ylim-$a)/$ylim]
    if {$test>1 && $z>=[expr {($hfree+$hspacer)/$zlim}]
```

```
        && $z<1 } {return 0}
    if {$test2<1 && $z>0 && $z<=[expr {$hfree/$zlim}] } {return 1}
    if {$test2<1 && $z>[expr {$hfree/$zlim}] &&
        $z<[expr {($hfree+$hspacer)/$zlim}] } {return 2}
    if {$z>=[expr {($hfree+$hspacer)/$zlim}] && $z<1 } {return 3}
    return 0
}

proc PolBoth { Polarization hfixed hspacer hfree zlim x y z } {
    set hz [expr {0.5*tan($theta_compliment)}]
    if { [expr {$hz-1}] <= 0}  {return 0}
    set ratio [expr {($hz-$z)/$hz}]
    set indicator [expr {4*(pow((($x-0.5)/$ratio),2) +
        pow((($y-0.5)/$ratio),2))}]
    if { $indicator > 1 } {return 0}
    if { $z>=[expr {($hfree-2.5e-9)/$zlim}] &&
        $z<=[expr {$hfree/$zlim}] } {return [expr {$Polarization}]}
    if { $z>[expr {$hfree/$zlim}] &&
        $z<[expr {($hfree+$hspacer)/$zlim}]} {return 0}
    if { $z>=[expr {($hfree+$hspacer)/$zlim}] &&
        $z<=[expr {($hfree+$hspacer+2.5e-9)/$zlim}]}
        {return [expr {$Polarization}]}    return 0
}
```

The script *Elliptical* uses the equation for an ellipse normalized to the x and y limits of the system to define the elliptical regions for each layer. The return com-

mands, returns the regions defined in the atlas section (1, 2, 3 correspond to the free, spacer, and fixed layers respectively). *Polboth* defines the regions where spn polarization must be calculated. Here, the interfaces of the two magnets adjacent to one another are assigned to have the polarization calculated while the remainder of the system has no polarization, and therefore no spin torque exerted

In concluding, there are many different options for setting up the magnetic system simulated that have not been discussed here, but this script illustrates the basic concepts of OOMMF. If different options are required, I suggest reviewing the OOMMF user manual available in the doc/userguide directory of the OOMMF folder. Good luck and happy simulating!

REFERENCES

[1] Diao Z.T., Pakala M., Panchula A., Ding Y.F., Apalkov D., Wang L.C., Chen E., & Huai Y.M., Spin-transfer switching in MgO-based magnetic tunnel junctions, *J. Appl. Phys.* **99**, 08G510 (2006).

[2] Diao Z.T., Li Z.J., Wang S.Y., Ding Y.F., Panchula A., Chen E., Wang L.C., & Huai Y.M., Spin-transfer torque switching in magnetic tunnel junctions and spin-transfer torque random access memory, *J. Phys.: Condens. Matter* **19**, 165209 (2007).

[3] Chappert C., Fert A., & van Dau F.N., The emergence of spin electronics in data storage, *Nat. Mater.* **6**, 813 (2007).

[4] Slaughter J.M., Dave R.W, DeHerrera M., Durlam M., Engel B.N., Janesky J., Rizzo N.D., & Tehrani S., Fundamentals of MRAM technology, *J. Supercon.* **19**, 19 (2002).

[5] Rizzo N.D., DeHerrera M., Janesky J., Engel B., Slaughter J., & Tehrani S., Thermally activated magnetization reversal in submicron magnetic tunnel junctions for magnetoresistive random access memory, *Appl. Phys. Lett.* **80**, 2335 (2002).

[6] Braganca P.M., Krivorotov I.N., Ozatay O., Garcia A.G.F., Emley N.C., Sankey J.C., Ralph D.C., & Buhrman R.A., Reducing the critical current for short-pulse spin-transfer switching of nanomagnets, *Appl. Phys. Lett.* **87**, 112507 (2005).

[7] Kaka S., Pufall M.R., Rippard W.H., Silva T.J., Russek S.E., Katine J.A., & Carey M., Spin transfer switching of spin valve nanopillars using nanosecond pulsed currents, *J. Magn. Magn. Mater.* **286**, 375 (2005).

[8] Devolder T., Tulapurkar A., Yagami K., Crozat P., Chappert C., Fukushima A., & Suzuki Y., Ultra-fast magnetization reversal in magnetic nano-pillars by spin-polarized current, *J. Magn. Magn. Mater.* **286**, 77 (2005).

[9] Slonczewski J.C., Current-driven excitation of magnetic multilayers, *J. Magn. Magn. Mater.* **159**, L1 (1996).

[10] Slonczewski J.C., Currents, torques, and polarization factors in magnetic tunnel junctions, *Phys. Rev. B* **71**, 024411 (2005).

[11] Xiao J., Zangwill A., & Stiles M. D., Boltzmann test of Slonczewski's theory of spin-transfer torque, *Phys. Rev. B* **70**, 172405 (2004).

[12] Slonczewski J.C., Currents and torques in metallic magnetic multilayers, *J. Magn. Magn. Mater.* **247**, 324 (2002).

[13] Kovalev A.A., Brataas A., & Bauer G. E. W., Spin transfer in diffusive ferromagnet-normal metal systems with spin-flip scattering, *Phys. Rev. B* **66**, 224424 (2002).

[14] Berger L., Multilayer configuration for experiments of spin precession induced by a dc current, *J. Appl. Phys.* **93**, 7693 (2003).

[15] Fuchs G.D., Krivorotov I.N., Braganca P.M., Emley N.C., Garcia A.G.F., Ralph D.C., & Buhrman R.A., Adjustable spin torque in magnetic tunnel junctions with two fixed layers, *Appl. Phys. Lett.* **86**, 152509 (2005).

[16] Ozatay O., Emley N.C., Braganca P.M., Garcia A.G.F., Fuchs G.D., Krivorotov I.N., Buhrman R.A., & Ralph D.C., Spin transfer by nonuniform current injection into a nanomagnet, *Appl. Phys. Lett.* **88**, 202502 (2006).

[17] Mangin S., Ravelosona D., Katine J.A., Carey M.J., Terris B.D., & Fullerton E.E., Current-induced magnetization reversal in nanopillars with perpendicular anisotropy, *Nat. Mater.* **5**, 210 (2006).

[18] Berger L., Emission of spin waves by a magnetic multilayer traversed by a current, *Phys. Rev. B* **54**, 9353 (1996).

[19] Katine J.A., Albert F.J., Buhrman R.A., Myers E.B., & Ralph D.C., Current-driven magnetization reversal and spin-wave excitations in Co/Cu/Co pillars, emphPhys. Rev. Lett. **84**, 3149 (2000).

[20] Sun J.Z., Spin-current interaction with a monodomain magnetic body: A model study, *Phys. Rev. B* **62**, 570 (2000).

[21] Lee K.J., Redon O., & Dieny B., Analytical investigation of spin-transfer dynamics using a perpendicular-to-plane polarizer, *Appl. Phys. Lett.* **86**, 022505 (2005).

[22] Kent A.D., Ozylimaz B., & del Barco E., Spin-transfer-induced precessional magnetization reversal, *Appl. Phys. Lett.* **84**, 3897 (2004).

[23] Redon O., Dieny B., & Rodmacq B., *US Patent No.* 6,532,164 B2 (March 10, 2003).

[24] Pribiag V.S., Krivorotov I.N., Fuchs G.D., Braganca P.M., Ozatay O., Sankey J.C., Ralph D.C., & Buhrman R.A., Magnetic vortex oscillator driven by d.c. spin-polarized current, *Nat. Phys.* **3**, 498 (2007).

[25] Soulen R.J., Byers J.M., Osofsky M.S., Nadgorny B., Ambrose T., Cheng S.F., Broussard P.R., Tanaka C.T., Nowak J., Moodera J.S., Barry A., Coey J.M.D., Measuring the spin polarization of a metal with a superconducting point contact, *Science* **282**, 85 (1998).

[26] Devolder T., Crozat P., Kim J.V., Chappert C., Ito K., Katine J.A., & Carey M.J., Magnetization switching by spin torque using subnanosecond current pulses assisted by hard axis magnetic fields, *Appl. Phys. Lett.* **88**, 152502 (2006).

[27] Carpentieri M., Consolo G., Azzerboni B., Torres L., & Cardelli E., Spin-transfer torque switching in magnetic multilayers, *IEEE Trans. Magn.* **43**, 1677 (2007).

[28] Donohue M.J. & Porter D.G., *OOMMF Users Guide, Version 1.0, Technical Report No. NISTIR 6376* (National Institute of Standards and Technology, Gaithersburg, MD, 1999).

[29] Emley N.C., Krivorotov I.N., Ozatay O., Garcia A.G.F., Sankey J.C., Ralph D.C., & Buhrman R.A., Time-resolved spin-torque switching and enhanced damping in Permalloy/Cu/Permalloy spin-valve nanopillars, *Phys. Rev. Lett.* **96**, 247204 (2006).

[30] Sankey J.C., Cui Y.-T., Buhrman R.A., Ralph D.C., Sun J.Z., & Slonczewski J.C., Measurement of the spin-transfer-torque vector in magnetic tunnel junctions , *Nat. Mater.* **4**, 67 (2008).

CHAPTER 6

CONSEQUENCES OF MICROMAGNETIC CONFIGURATIONS GENERATED WITHIN TAPERED NANOPILLARS ON MAGNETIZATION DYNAMICS

6.1 Introduction

With the prediction that a spin-polarized current could excite dynamics within a thin nanomagnet [1, 2] through an exchange of spin angular momentum, possibilities for a new generation of spintronic devices have risen. These include magnetic random access memory elements utilizing a spin-torque writing mechanism, and microwave and millimeter wave nano-oscillators, where the giant magnetoresistance (GMR) effect converts steady state magnetic excitations into RF voltages. Several different approaches have been employed for these spin-torque oscillator (STO) studies, including mechanical point contacts [3], nanoconstrictions [4] to extended magnetic multilayer films, and fully patterned nanopillar spin valves [5, 6]. While such studies clearly demonstrate that high frequency responses caused by coherent magnetization oscillations can be obtained from such nanomagnetic structures, a stumbling block for practical applications is the large applied magnetic field that is typically required to stabilize the magnetic structure and ensure persistent dynamics. More recently, two new approaches have been employed that have enabled STOs to operate at low magnetic fields. In the first case, the use of two different magnetic materials with different spin scattering properties has resulted in spin accumulation effects in a spin valve structure that enable persistent oscillations of the free layer magnetization in zero or low field, but so far this approach has yielded very broad linewidths and low microwave powers [7]. In the other

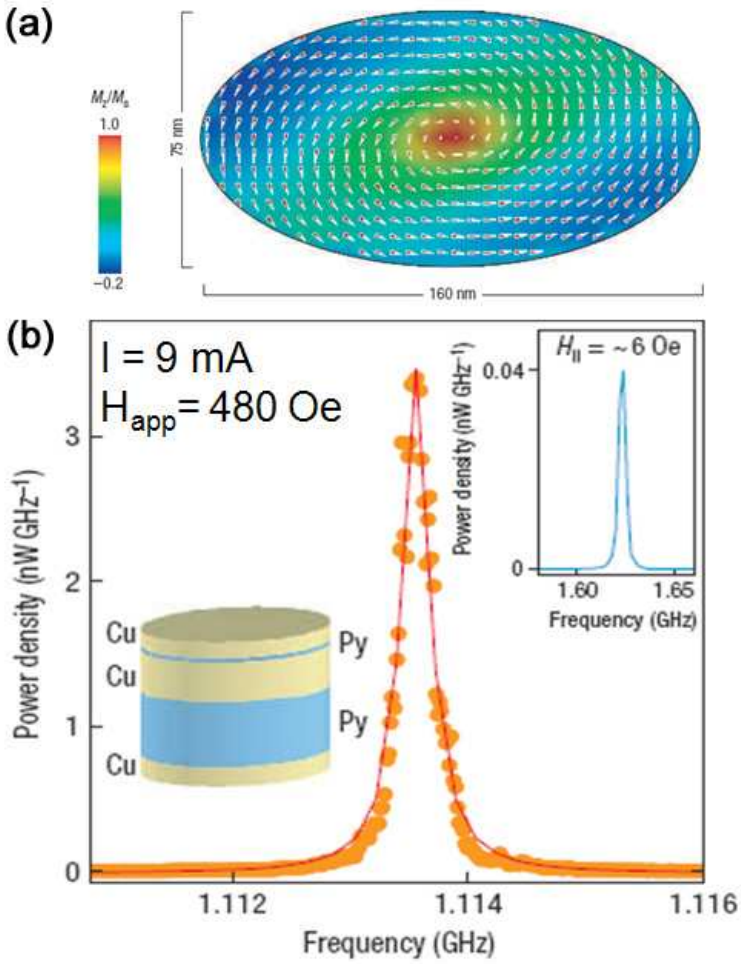

Figure 6.1: (a) A micromagnetic vortex configuration is generated in a thick ($\sim$ 60 nm) Py reference layer as it minimizes the magnetostatic energy of the system. This is confirmed by this micromagnetic simulation, where the color scale indicates the magnitude of the out of plane magnetization component. The region in red indicates the core of the vortex, where there the magnetization is entirely out of the plane of the magnet. (b) DC driven oscillations of the vortex core result in a relatively sharp microwave peak with $\Delta f = 2.8{\times}10^2$ kHz and $f/\Delta f = 4.0 \times 10^3$ for H_c = 480 Oe and I = 9.0 mA. The continuous line is a lorentzian fit to the data. Figures taken from [8].

approach, a spin-polarized current has been employed to excite a spatially nonuniform magnetization configuration, a magnetic vortex, into persistent gyroscopic oscillation [8, 9]. This can result in oscillations with extremely narrow linewidths as shown in Fig. 6.1, but only at relatively low frequencies $\sim$ 1 GHz, since the vortex precessional frequency is generally much lower than spin wave frequencies.

In this chapter, I will demonstrate, by experiment and micromagnetic simulation, another approach by which large, steady-state magnetization oscillations can be excited at low and zero magnetic fields by spin-transfer torque using a spin valve structure that has been fabricated to have distinctly non-uniformly magnetized elements. This is accomplished by tapering the sidewalls of the structure and placing the thinner "free" layer beneath the thicker "reference" layer, as was discussed in the previous chapter. This results in a net out-of-plane magnetization component in both layers. When biased with a sufficiently large current, correlated spin wave oscillations occur in the two layers that result in giant magnetoresistance microwave oscillations at considerably higher frequencies than obtained with any of the previous zero-field spin torque oscillator studies. I will also discuss a mechanism of phase locking these free and reference layer oscillations using a small magnetic field biased along the hard axis of the nanomagnets, resulting in RF voltage spectra with large integrated power and linewidths approaching those seen in vortex oscillators.

6.2 Effect of Micromagnetic Structure on Easy Axis Dynamics

Our devices consist of sputter deposited multilayer stacks of 120 Cu/4.5 Py/12 Cu/20 Py/2 Cu/30 Pt, where Py is $Ni_{81}Fe_{19}$ and thicknesses are in nm. For clarity, in this section I will refer to the ferromagnetic layers as thin and thick, as opposed to the free and reference layers, because dynamics are excited mostly in the thicker reference layer of this structure for easy axis fields. Electron beam lithography and ion milling were used to pattern nominally 40 x 120 nm^2 elliptical nanopillars, with contact to the nanopillars made through photolithography. The ion mill angle was chosen to produce a tapered profile of the nanopillar sidewall, which we estimate to be roughly 30° off normal. Fig. 6.2a shows a schematic of the device with the $T = 0$ equilibrium micromagnetic state at zero field, calculated using micromagnetic simulations [10] whose details are discussed below. Here, the local magnetization at the edges of the nanomagnets curls out of the plane of the film along the direction of the dipole fields generated by the thin and thick layers. This occurs because the demagnetization field is spatially nonuniform for a thin elliptical magnetic element, with the field strength decreasing away from the center, making the magnetization there more susceptible to being pulled out of plane by the dipole fields. Using low M_s materials and a tapered profile serves to enhance this effect, thereby creating a magnetization state with an out of plane component localized at the edges of the ellipse.

In the standard case of a spin valve with a more spatially uniform magnetization oriented in-plane, observations of magnetization oscillations occur only for certain device orientations. This normally requires stabilizing the spin valve against magnetization reversal by biasing it with a large magnetic field, which aligns the thin

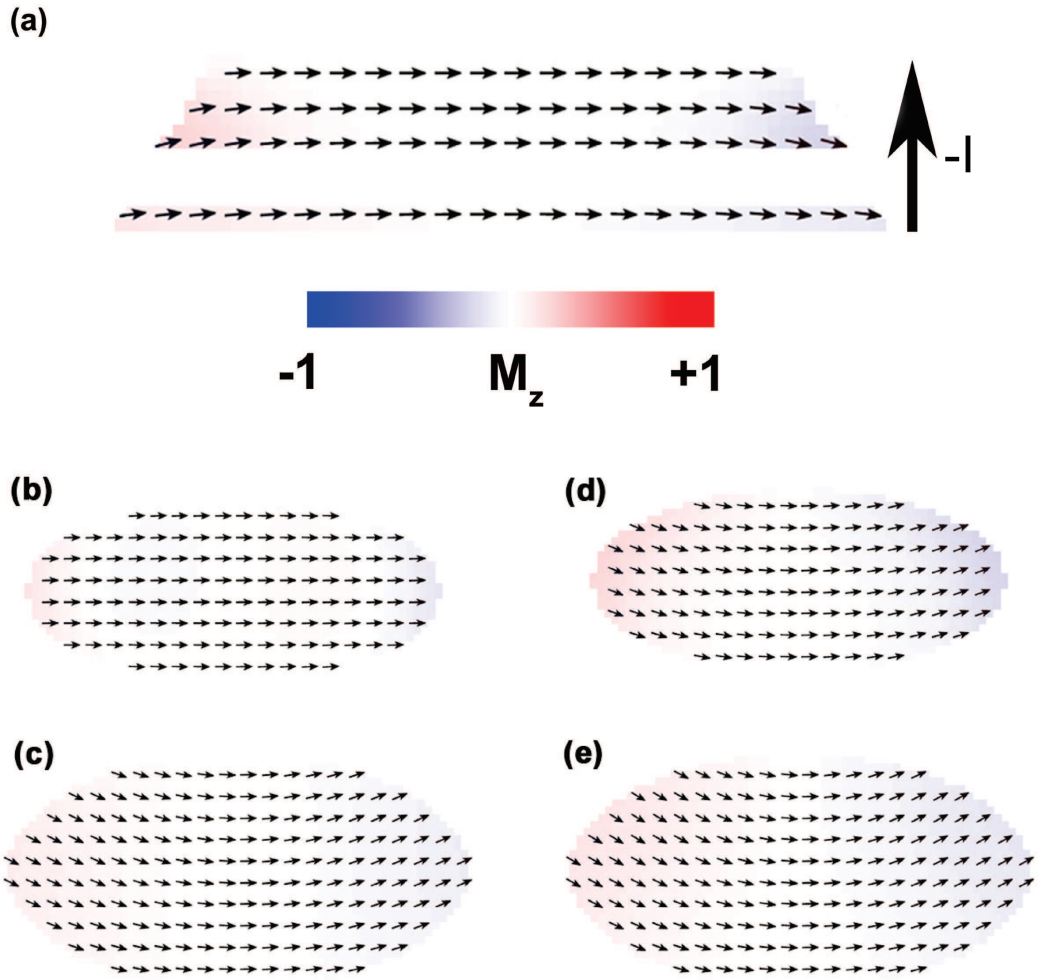

Figure 6.2: (a) Schematic of the equilibrium state of an inverted nanopillar spin valve with tapered sidewalls as calculated with micromagnetic simulations. Spin transfer simulations with -3 mA and zero applied field indicate that the reference layer begins precessing immediately following application of the current, forcing sympathetic oscillations in the free layer. (b-e) Simulated micromagnetic cross section of the reference and free layers respectively at the beginning (b,c) and midpoint (d,e) of the magnetization oscillations.

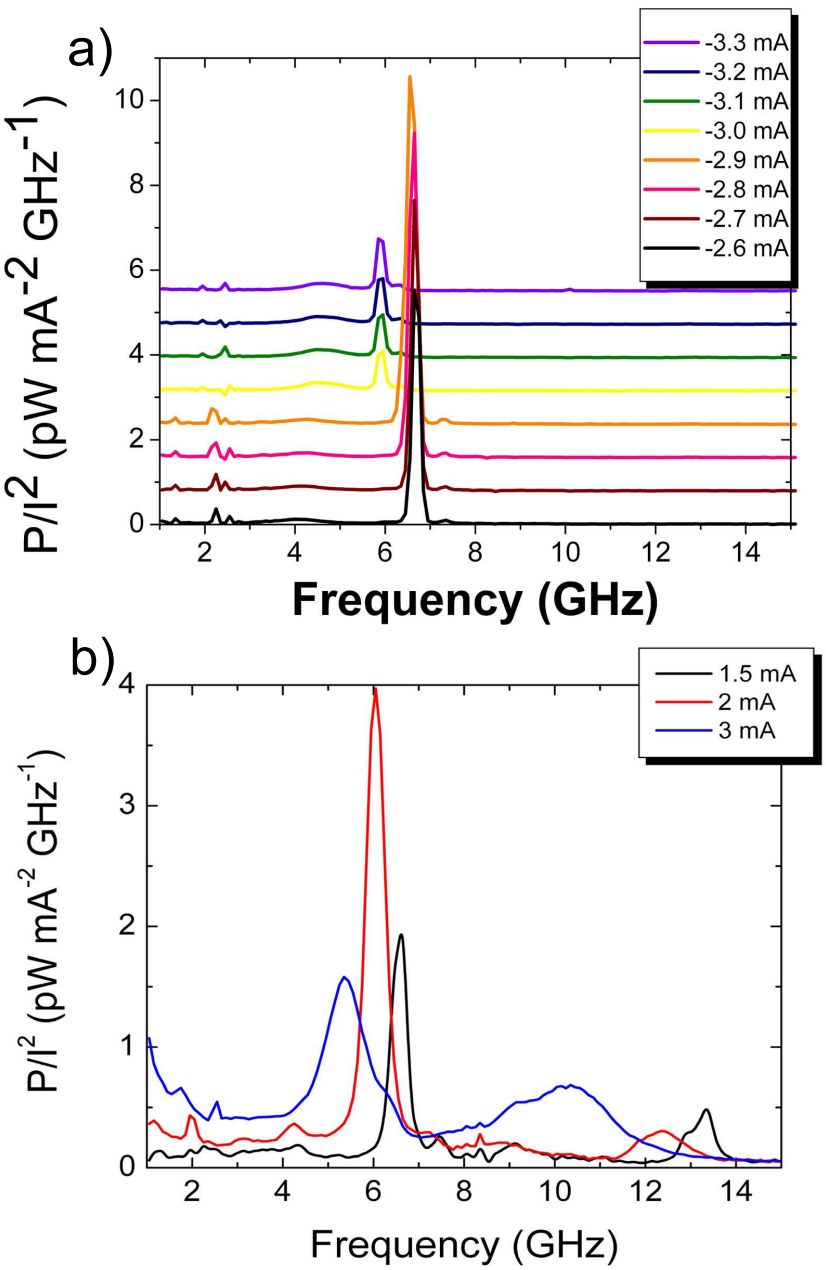

Figure 6.3: DC current driven spectra excited in an inverted nanopillar with tapered sidewalls for (a) negative and (b) positive current polarities. Small negative currents act to orient the layers into a parallel alignment, after which increasingly larger current magnitudes excite the thicker ferromagnet in the manner shown in Fig. 6.2. Positive currents excite strong magnetization oscillations in both layers, resulting in the layers alternating between antiparallel and parallel orientations as determined by micromagnetic simulations. These oscillations become extremely incoherent, resulting in broad peaks with low frequency tails, signals that are insufficient for practical applications. For this reason, I will focus on dynamics excited at negative current polarities.

layer parallel (P) with respect to the thick layer, as opposed to antiparallel (AP). Additionally, the critical current for the onset of dynamics I_c is [1, 11] :

$$I_c = (\frac{2e}{\hbar})\frac{\alpha}{\eta}M_s V[2\pi M_{eff} + H_{eff}], \tag{6.1}$$

where α is the Gilbert damping parameter, e is the electron charge, M_s is the saturation magnetization of the nanomagnet, V the volume of the nanomagnet, H_{eff} the effective field acting on the nanomagnet, $4\pi M_{eff}$ is its effective demagnetization field, and η is the spin torque efficiency parameter. Since the demagnetization field of a thin film nanomagnet is typically quite large (> 0.7 Tesla), rather large currents are required to excite spin-transfer oscillations.

In contrast, the micromagnetic configuration shown in Fig. 6.2a provides two significant enhancements over a more traditional configuration. First, I_c is reduced locally at the edges of both magnetic layers due to the smaller demagnetization field occurring there. This makes it easier to excite magnetization oscillations on the edges, which can then spread to a more significant portion of the nanomagnet through exchange interactions [12]. More importantly, the local spin current incident upon the edges of either nanomagnet will have a component spin polarized partially out of plane, which was shown in Chapter 5 to enhance the effect of spin torque acting on the free layer, thus lowering the current amplitudes required for fast nanosecond magnetization reversal. For spin valve configurations where the current does not serve to excite reversal, these spatially nonuniform spin currents still act to pull the local moments on the edges of the ferromagnets further out of plane, allowing the magnetization to oscillate around the local demagnetization field [13–15]. Oscillations in the thin and thick magnetic layers become coupled through both magnetic interactions between the dipole fields as well as the spin currents incident on the nanomagnets. These micromagnetic properties serve to excite dynamics regardless of the orientation of the spin valve (AP or P) with

relatively low currents $\sim \pm 2$ mA (indicated by the corresponding spectra in Fig. 6.3), even in the absence of a magnetic field.

Fig. 6.4a shows the results of a $T = 0$ micromagnetic simulation including spin torque for the structure in Fig. 6.2a at zero applied field and -3 mA. Here, $M_s = 560$ emu/cm^3, corresponding to the room temperature M_s of Py as determined by superconducting quantum interference device magnetometry measurements, and the local spin polarization incident on one nanomagnet is determined by the local magnetization of the adjacent nanomagnet interface. Further details of these simulations can be found in Ref. [12] or Chapter 5 of this dissertation. For negative currents, the spin torque acts to stabilize the thin layer, while driving the thick layer away from its equilibrium state. An initial response is seen in the thick layer, with the oscillation period corresponding to a frequency of $\sim$5.6 GHz, as shown in Fig. 6.4b. Following a ring up of its magnetization, the thin layer also begins oscillating coherently with approximately the same frequency as the reference layer, but with much smaller amplitude. Looking into the plane of the film, the thin layer maintains a "C" state with some small displacement, as seen in Fig. 6.2c and 6.2e, presumably from interactions with the Oersted field generated by the applied current, while the reference layer alternates between a more uniform magnetization state along the semimajor axis of the ellipse and a "C" state (Fig. 6.2b and 6.2d). This explains the 1:1 correlation between the measured GMR oscillations and the magnetization oscillations seen in the simulations, differing from 2:1 expected from a small angle oscillation in the uniform magnetization picture [6]. Simulations for positive currents also show excitations, but in that direction the current acts to destabilize the thin layer, creating one or more nonuniform modes within that layer. For the remainder of this chapter, we will focus on dynamics excited in the negative current region, where excitations in the thicker Py layer

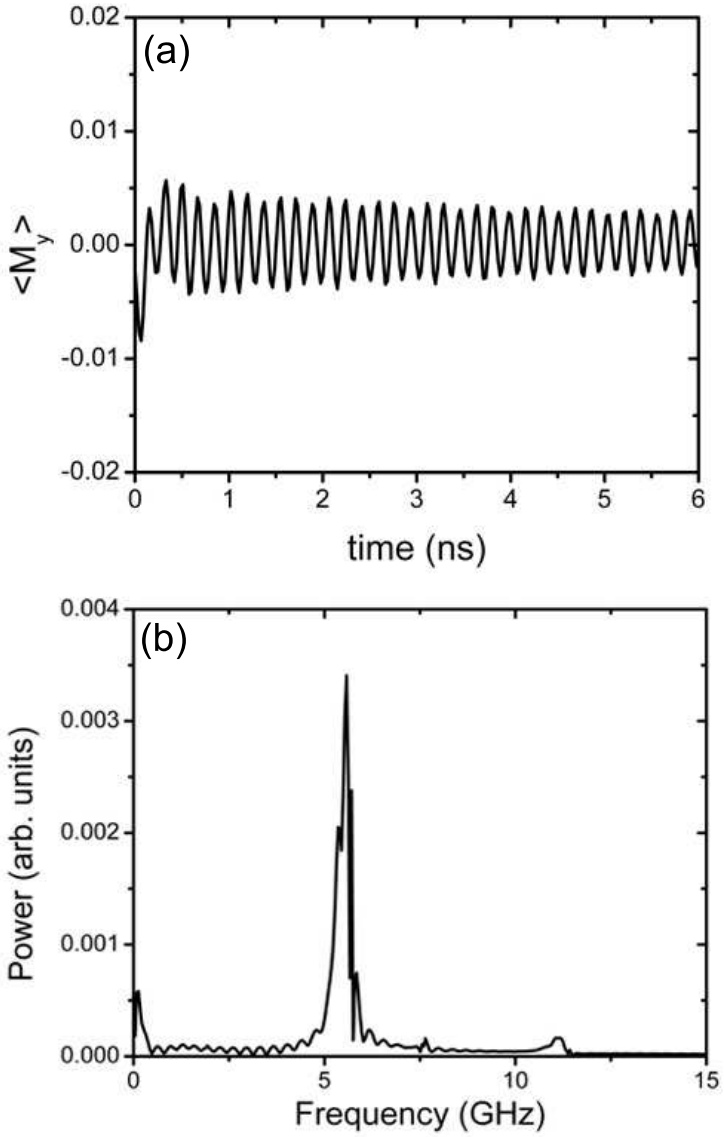

Figure 6.4: (a) Spatially averaged value of M_y vs. time for an inverted nanopillar at -3 mA and zero applied field as calculated using $T = 0$ micromagnetic simulations. (b) Fourier transform of the results shown in (a). The dynamics excited in this structure occur at 5.6 GHz, accurately predicting one of the modes seen in the experimental results (see Fig. 6.5)

lead to more coherent dynamics, as seen in comparing Fig. 6.3a and b.

In Fig. 6.5a, we see a typical field coercive loop at zero current bias for the thin layer in a device similar to the one shown in Fig. 6.3, where the loop is offset from zero due to the dipole field of the thick layer. Fig. 6.5b shows the GMR response measured with a spectrum analyzer for a DC current of -2.9 mA, over various fields throughout the coercive loop. At zero field, where only the antiparallel state is accessible, we see a reference layer mode excited at 6.5 GHz. Increasing the field into the hysteretic region promotes a parallel configuration of the ferromagnets for a -2.9 mA current, resulting in large amplitude peaks between 5.3-5.5 GHz with a minimum linewidth of $\sim$ 50 MHz. Here, we attribute these two modes to differences in the size of the precessional orbit determined by the orientation of the applied magnetic field along or opposite to the thick layer's magnetization, as shown in Fig. 6.6. Micromagnetic simulations predict a mode at 5.6 GHz (Fig. 6.4) for zero applied field and 6.5 GHz for applied fields parallel to the thick layer's magnetization, in reasonable agreement with our experimental results, although the field regimes for the two modes are reversed. For now, the reasons for this discrepancy are not well understood, but the experimental results give us some indication of possible explanations. One characteristic of the devices not seen in the simulations is a propensity at finite applied fields for the reference layer precession axis to be reoriented 180° to its initial position at the beginning of a scan (which is parallel to the positive field direction) after the applied current becomes large enough to excite the ferromagnet. As the excited reference mode is dependent on the relative orientation of the applied field with respect to the reference layer as described above, this deviation in the behavior of the device from the simulation results is extremely significant. For example, in the case of dynamics excited at the dipole field, the reference layer actually becomes oriented

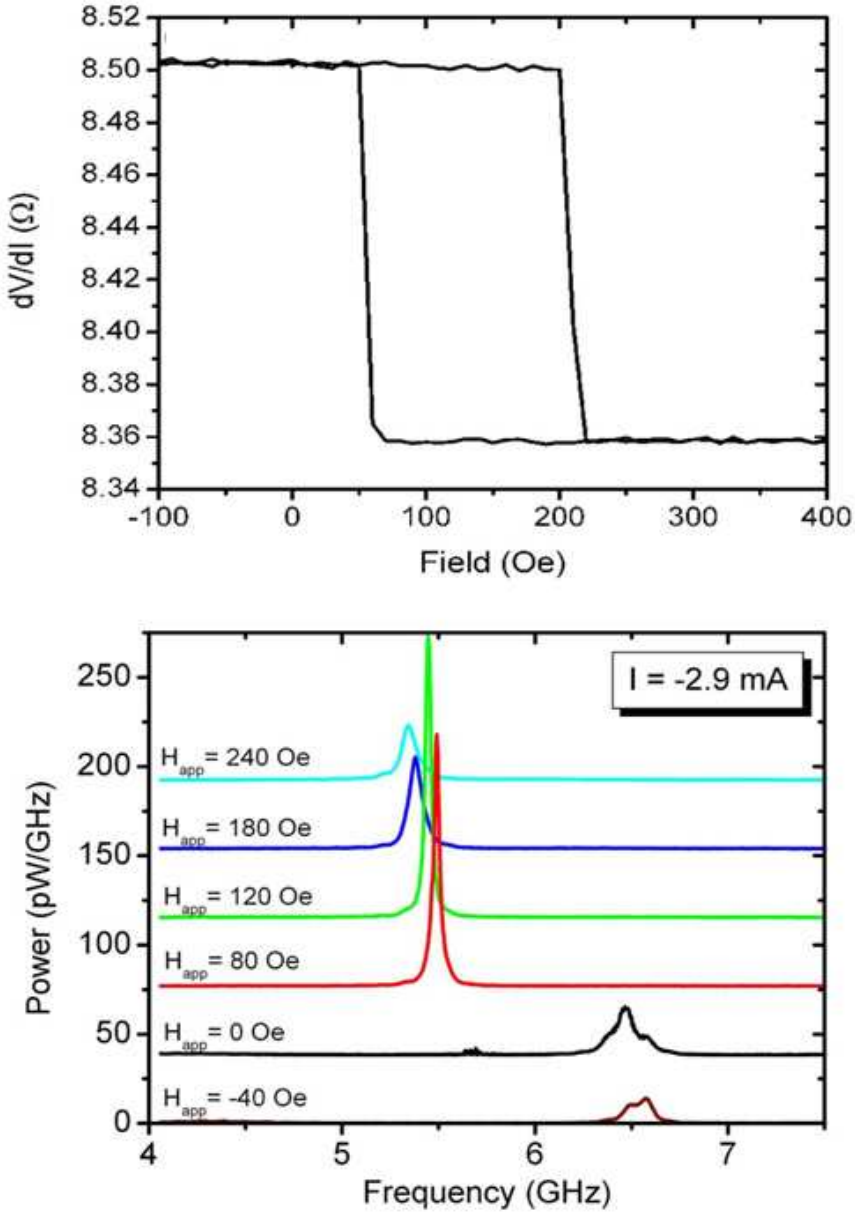

Figure 6.5: (a) Coercive field of the free layer. The hysteresis loop is offset from zero field due to the dipole interaction between the free and reference layers (b) RF spectra measured at zero field and several points along the hysteretic field region of the free layer. Oscillations occur throughout this field region, as predicted by the micromagnetic simulations shown in Fig. 6.2.

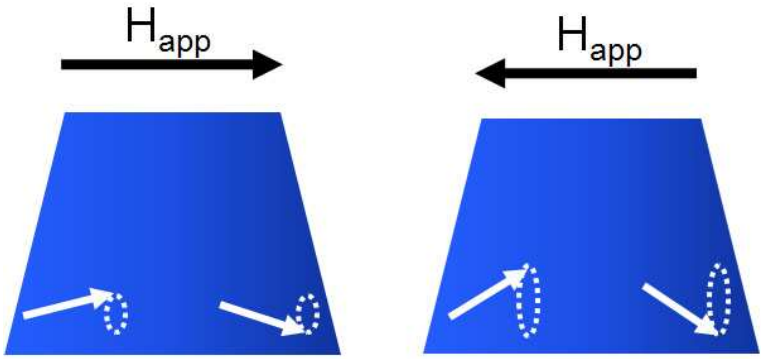

Figure 6.6: Two modes can be excited in the thicker layer of inverted nanopillars depending on the orientation of the effective magnetic field with respect to the thick layer's magnetization. Field parallel to the magnetization stabilizes the oscillation, while field antiparallel drives the magnetization into a larger precession orbit and a lower precession frequency, resulting in the two modes observed in the experimental results. These modes are in agreement with micromagnetic simulations which predict modes at 5.6 (see Fig. 6.4) and 6.5 GHz (for an applied field canceling the dipole field). For certain field and current values, the system can hop between the two modes as shown in Fig. 6.7.

opposite the field, and so it is not unexpected to see the lower frequency mode excited. At zero field, the effective field on the reference layer (i.e. the dipole field of the free layer) is parallel to the reference layer, and although similar to the simulation case, this field may be larger than predicted by the simulations due to shape nonidealities, resulting in the higher frequency mode. Regardless, these micromagnetic simulations have allowed us to accurately map out the reference layer modes capable of being excited in these devices. Other small deviations in simulated frequencies may be due to nonidealities in device shape, or small local variations in magnetization due to defects. Figures 6.7-6.8 show the RF response of the same device measured in Fig. 6.5 as a function of current at both zero applied field and 120 Oe, which is the field required to cancel out the average dipole field generated by the reference layer. These show a redshift in peak frequency with increasing current, indicative of large-angle precession, which is consistent with

our simulation results.

In conclusion, I have presented a method of preparing a magnetic nanopillar structure by means of an angled ion milling scheme, which produces a spatially nonuniform micromagnetic state in both magnetic layers of the device. This configuration induces an out of plane magnetization component at the edges of the magnetic layers, which can precess coherently by exerting a spin torque on the magnets through the injection of an electric current, even in the absence of an external magnetic field, as we verify in both micromagnetic simulations and experimental results. Excitations occur regardless of the orientation of the layers with respect to one another, however the number of modes and their peak linewidths depend on whether magnetization oscillations are excited in the reference layer (negative polarities) or both layers (positive polarities) simultaneously. Further enhancements in the taper angle, as well as varying the saturation magnetization of the nanomagnets, may help to increase the oscillation frequency by tuning both the out of plane magnetization and demagnetization fields at the edges of the nanomagnets. In addition, these enhancements do not require spin accumulation effects as in Ref. [7], and require relatively small currents, making them promising for adaptation into magnetic tunnel junction (MTJ) oscillators for applications requiring much larger RF output. These results illustrate the effect that the micromagnetic configuration can have on magnetization dynamics in magnetic nanostructures, indicating that identifying additional configurations could be beneficial to incorporating further enhancements for magnetization dynamics and reversal.

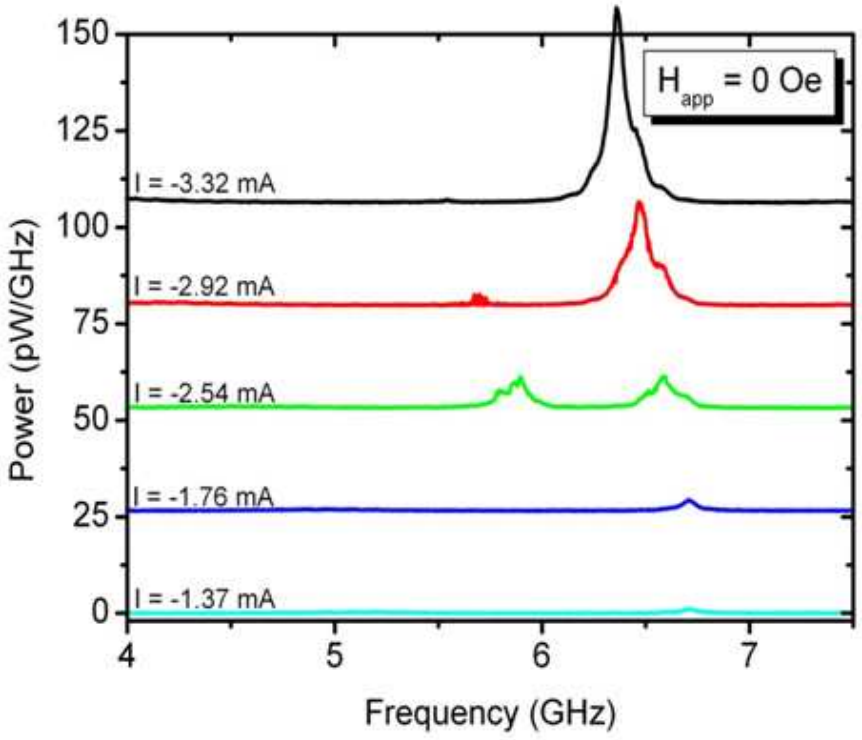

Figure 6.7: RF response of tapered devices at various currents for zero applied field. Oscillations occur at relatively low currents and fields due to the out of plane magnetization curling at the edges of the nanomagnets.

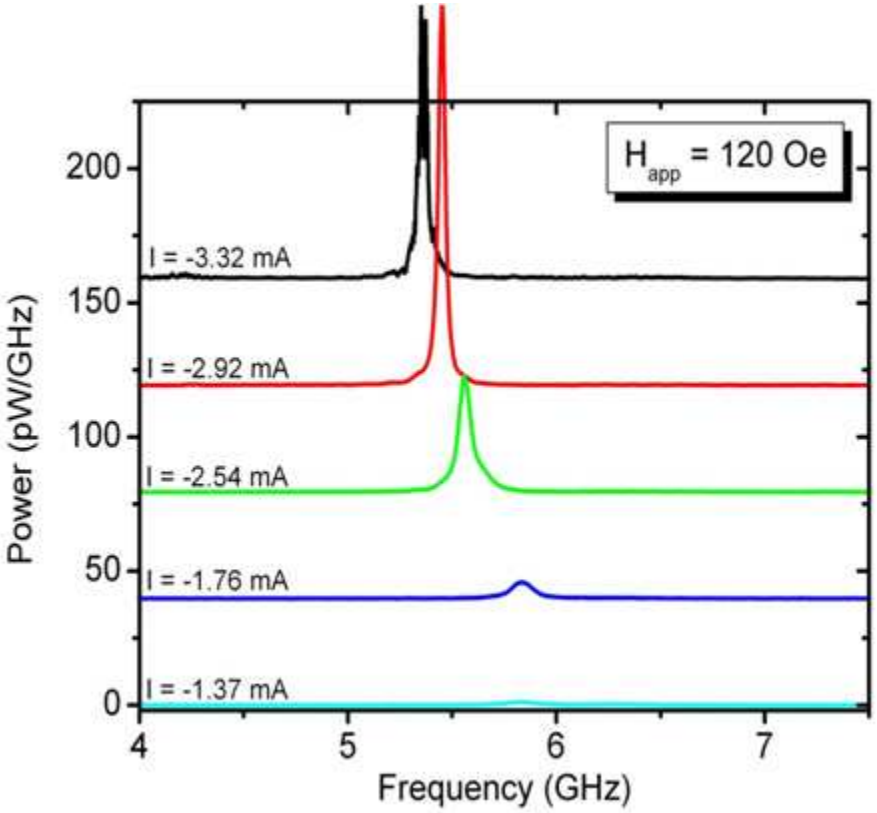

Figure 6.8: RF response of tapered devices at various currents biased at a field along the easy axis canceling the dipole field exerted by the reference layer on the free layer. Oscillations occur at relatively low currents and fields due to the out of plane magnetization curling at the edges of the nanomagnets.

6.3 Effect of Micromagnetic Structure on Hard Axis Dynamics

The results in the previous section have shown that an inverted spin valve nanopillar device with tapered sidewalls has the ability to excite both the thin free layer and thick reference layer of the spin valve into persistent precessional modes due to (1) out of plane curling of the local magnetization at the edges of both ferromagnets and (2) the nonuniform spin currents generated as a result of this curling. Although these results are promising for zero field applications, an overall increase in integrated power and decrease in the resultant linewidths is required for integration into commercial systems. By applying a small magnetic field along the hard axis of the device, I have observed a significantly different microwave response then with field along the easy axis. Fig. 6.9 shows this response in one such device, which I will refer to as device 1. Here, the RF signal is characterized by extremely narrow linewidths on the order of 1-10 MHz, which are the lowest measured values at room temperature that I am aware of for STO other than vortex oscillators. Unlike vortex oscillators however, these devices are not limited to frequencies ~ 1 GHz, and they exhibit integrated powers up to an order of magnitude larger, ranging from 100-300 pW depending on the current and field parameters.

A recent study [16] using untapered spin-valve nanopillars in the standard configuration with an exchange biased reference layer has shown that the linewidth of the microwave signals produced by these spin-torque driven magnetization oscillations varies as a function of the angle the applied field makes with the easy axis of the device, becoming minimized with field applied along the hard axis. This decrease in linewidths is attributed to the excitation of very large angle ($\sim 180^{\circ}$), coherent magnetization oscillations in the free layer with field biased in the hard

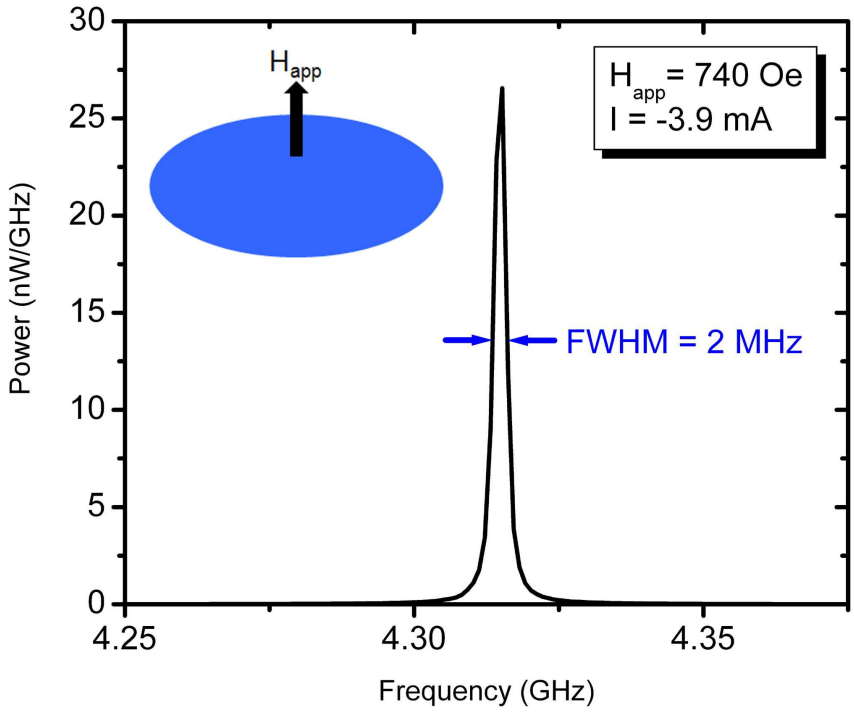

Figure 6.9: RF spectra of an inverted nanopillar with a 740 Oe field applied along the hard axis of the magnet and -3.9 mA current. This sample, which I will refer to as device 1, exhibited the smallest linewidth seen in these devices (2 MHz), with similar devices having linewidths on the order of 10 MHz. The integrated power for this device is also quite large $\sim$ 100 pW. In these devices, there is a critical field at which the linewidth decreases and the integrated power increases, and persists for roughly 300-400 Oe beyond the critical field. This field dependence will be discussed in more detail below.

axis direction, as oppose to mostly incoherent oscillations at field angles closer to the easy axis of the device. The reduction in linewidth can be understood by considering the thermal mechanisms responsible for line broadening in these systems, as was first explored by Sankey et. al [17]. By modeling thermal fluctuations as a randomly varying field with a Gaussian distribution, we can examine the effect these fluctuations have on linewidth due to deviations caused along or transverse to the magnetization's precession orbit. Deviations along the orbit either speed up or slow down the precession, and from the time needed for this random-walk process to dephase, the contribution to the FWHM is estimated to be:

$$\Delta f_a \approx \frac{4\pi\gamma\alpha k_B T}{M_s V D} n^2, \tag{6.2}$$

where α is the Gilbert damping parameter, k_B is Boltzmanns constant, α is the gyromagnetic ratio, M_s and V are the magnetization and volume of the free layer, D is the length of the precession trajectory on the unit sphere, and n is the value of the harmonic the peak represents. Fluctuations transverse to the precession orbit cause small deviations in the precession angle θ such that they will produce a spread around $\langle\theta\rangle$. If the frequency depends significantly on θ this will then introduce a further broadening of the linewidth:

$$\Delta f_b = n\frac{df}{d\theta}|_{\langle\theta\rangle}\Delta\theta, \tag{6.3}$$

where $\frac{df}{d\theta} \approx \frac{df}{dI}$ as the magnitude of the spin torque helps to determine the precession angle of the magnetization. From these two expressions, it is clear that a large, spatially coherent precessional orbit will be less susceptible to thermal line broadening as the effect of thermal fluctuations are minimized in that case.

Several important distinctions must be made between the results in [16] and those discussed in this section for inverted nanopillars. First, the fields used in [16] were larger than those used in my experiments by approximately a factor of 2.

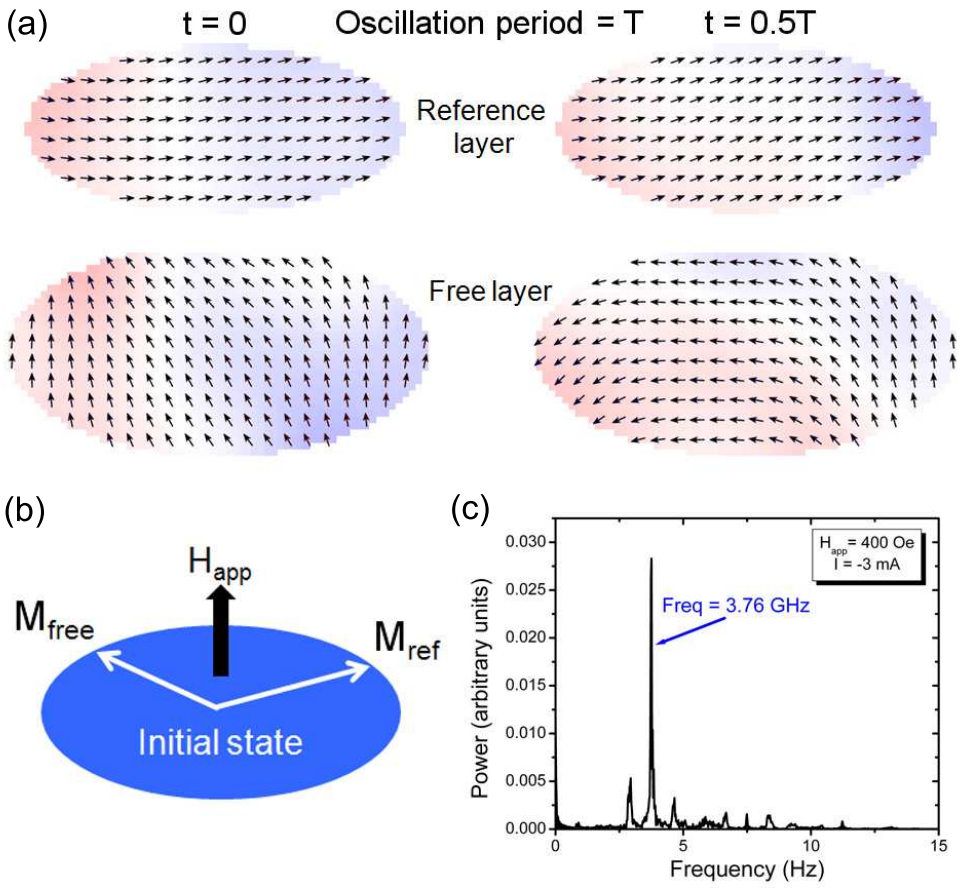

Figure 6.10: (a) Micromagnetic cross section of the free and reference layers at the beginning and midpoint of magnetization oscillations excited using a -3 mA current and 400 Oe hard axis field. The free layer magnetization on average oscillates between the easy axis and the hard axis, a large displacement that generates the large integrated power seen in the experimental results and plays a role in the narrow linewidths. Small oscillations also occur in the reference layer, which can phase lock with the free layer oscillations. (b) Hard axis fields pull the free and reference layers away from the easy axis, resulting in the skewed state shown. This large initial misalignment of the magnetizations strongly enhances the spin torque acting upon both layers. (c) Fourier transform of the simulation in (a) give an oscillation frequency of 3.76 GHz, in good agreement with our experimental results.

Micromagnetic simulations of the device described here at these fields (400-500 Oe) (Fig. 6.10a) predict a $\sim$90° oscillation of the free layer magnetization as opposed to 180° as shown in [16]. Even with a smaller precessional orbit, the linewidths in these devices are two orders of magnitude smaller than the values reported in [16], indicating that there are additional mechanisms contributing to the extremely coherent nature of dynamics in these inverted structures. Second, the polarity of the current required to excite the dynamics in the inverted structures discussed here is the opposite of that required in [16]. This particular current polarity acts to excite not only the free layer, but the reference layer as well due to its curled micromagnetic state, an important characteristic for achieving these narrow linewidths as will be discussed below.

To explore the additional mechanisms involved in further stabilizing these inverted nanopillars against thermal linewidth broadening, I used micromagnetic simulations with the field now biased along the hard axis, resulting in the initial skewed magnetization state shown in Fig 6.10b. As previously mentioned, these simulations predict a large $\sim$90° oscillation of the magnetization. Fig. 6.10a shows the magnetization state at the interfaces of the free and reference layers adjacent to one another at the beginning and midpoint of an oscillation period. The large integrated powers measured in these devices are due to the significant fraction of the GMR signal obtained through this large amplitude oscillation. Fourier transforms of these simulation results for -3 mA and 400 Oe (shown in Fig. 6.10c) indicate a strong signal present at $\sim$ 3.76 GHz. This simulated frequency is in relatively good agreement with our measured devices, including the one plotted in Fig. 6.11a, which I will refer to as device 2. A comparison of an inverted and a standard device excited under the same hard axis field and current bias conditions is shown in Fig. 6.11. Here, a marked difference exists in both linewidth (9 MHz

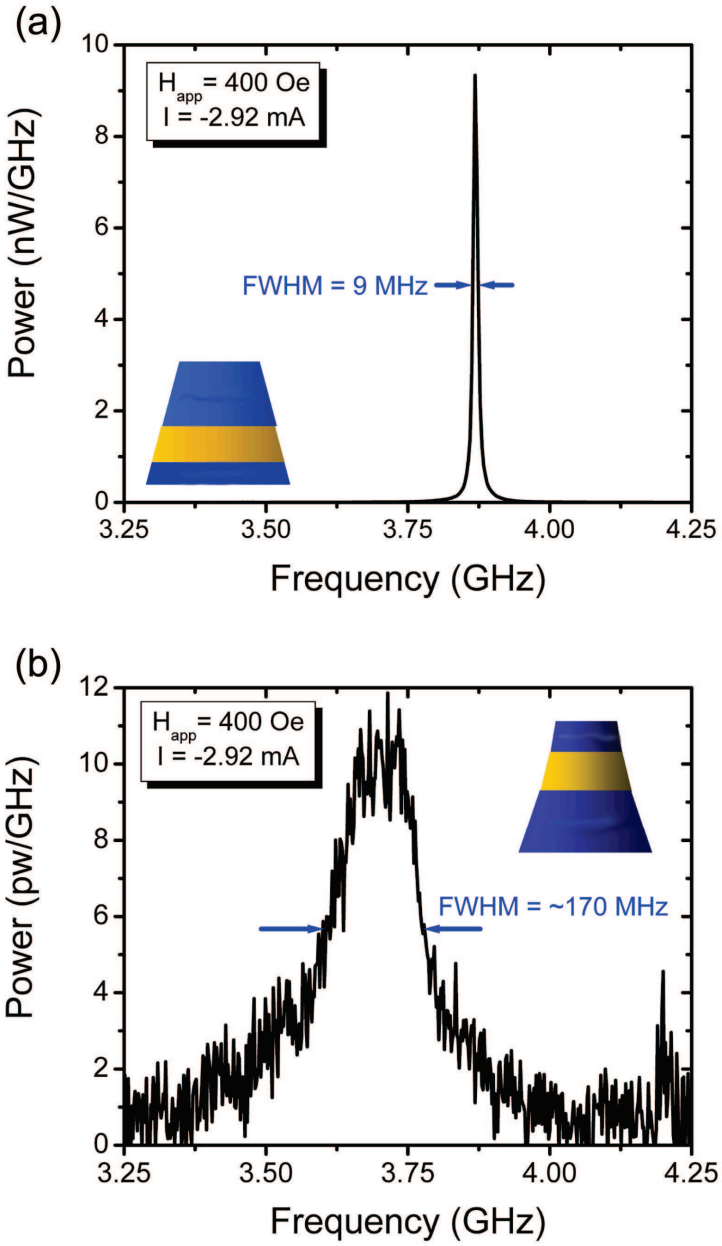

Figure 6.11: (a) RF spectra at -2.92 mA and 400 Oe hard axis field of an inverted nanopillar device similar to the one shown in Fig. 6.9, which will be referred to as device 2. The linewidth of this device is 9 MHz and the integrated power is 136 pW. (b) RF spectra of a standard device at the same field and current as the inverted device in (a). The dynamics of this device are much less coherent than in the inverted device, with a linewidth of 170 MHz and integrated power of 5 pW.

to 170 MHz) and integrated powers (136 pW to 5 pW) between the inverted and standard devices.

Fig. 6.12 plots the frequency and the full width at half max (FWHM) of the measured RF spectra as a function of magnetic field and electric current. In both sets of data, we see regions where the frequency varies weakly with field and current, simultaneously resulting in a significant drop in linewidth. This behavior is reminiscent of phase locking phenomena observed in point contacts spaced close to one another [18, 19], where spin waves generated under the contact regions constructively interfere when their frequencies become equal. Focusing on the field dependence, we see several different regions of behavior, starting at low field where the FWHM is fairly large. As the field increases, it reaches a phase locked state at approximately 520 Oe, at which $\frac{df}{dH}$ decreases and the linewidth drops sharply. At about 1000 Oe, there is a change in the frequency of the excited mode, bringing the device out of the locked state. Further increasing the field up to 2000 Oe brings the device through several different frequency modes. In the small linewidth regime, the the free layer oscillations must lock to oscillations of the reference layer, most likely mediated through spin currents. This makes the curled reference layer magnetization state caused by the tapered sidewalls of the nanopillar even more significant as the excitation of both layers is critical.

Phase locking these ferromagnetic excitations requires that the frequencies of the free and reference layer modes be equal, or in the case of parametric amplification as I will discuss later, the reference layer frequency must be twice that of the free layer. In our specific case, we can examine the relative frequencies involved in these inverted nanopillars using Kittel formulism (i.e. assuming a uniform magnetization) [20]. This FMR calculation assumes that both the field and magnetization

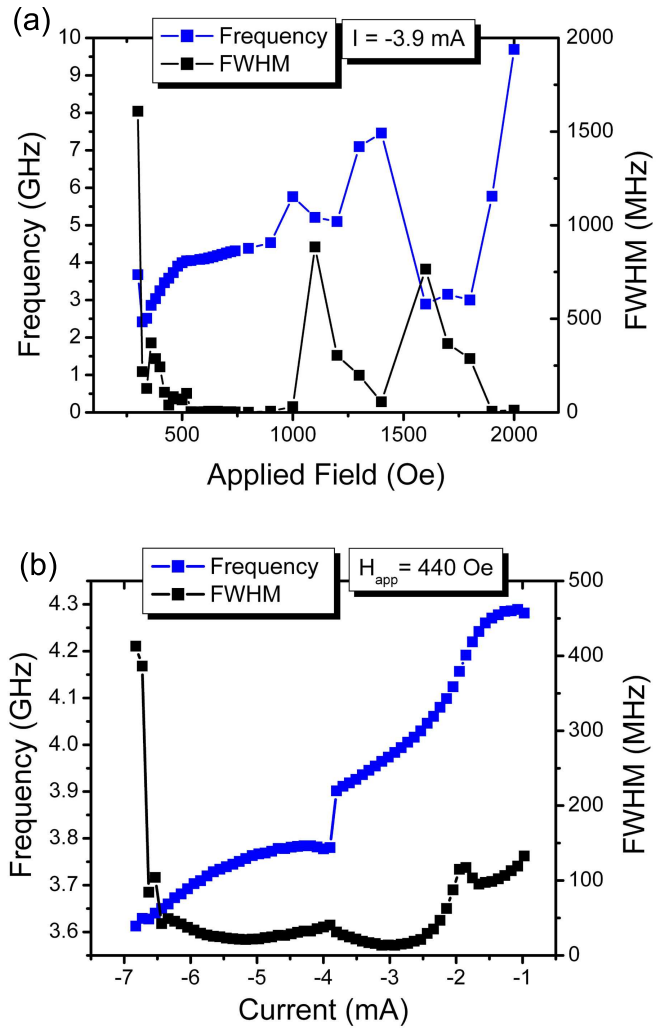

Figure 6.12: (a) Field dependence of frequency and linewidth as a function of applied hard axis field for device 1. For small fields, the frequency changes quite rapidly as the field increases, with a decrease in linewidth. At $\sim$ 520 Oe, the oscillations in both magnetic layers phase lock, causing the frequency dependence on field to decrease and the linewidth to drop to the order of 10 MHZ. For larger fields, several different modes are excited depending on the magnitude of the field, causing the linewidth to vary over the entire field range. (b) Dependence of mode frequency and linewidth on current bias for device 2. the behavior here also implies phase locking occurring in this device, where small linewidths are accompanied by a small variation of frequency with current. For increasing current, a mode expulsion occurs at ~ -4 mA followed by a quick locking back to the new frequency and then a transition to a more spatially incoherent mode at currents > 6.5 mA

of a ferromagnet point along the $\hat{z}$ axis. The effective internal magnetic fields exerted on the ferromagnet can then be expressed as:

$$B_x^i = -N_x M_x \ ; \ B_y^i = -N_y M_y \ ; \ B_z^i = B_0 - N_z M_z, \tag{6.4}$$

where B_0 is the applied field, and M_i and N_i are the magnetization components and demagnetization factors respectively in the x, y, and z directions. Substituting these values into the formula for Larmor precession, $\frac{d\vec{M}}{dt} = \gamma \vec{M} \times \vec{B}$, where $B = B_0 \hat{z}$ give the expressions:

$$\frac{dM_x}{dt} = \gamma[B_0 + (N_y - N_z)M_z]M_y, \tag{6.5}$$

$$\frac{dM_y}{dt} = -\gamma[B_0 + (N_x - N_z)M_z]M_x, \tag{6.6}$$

where γ is the gyromagnetic ratio. To first order, we may set $\frac{dM_z}{dt} = 0$ and $M_z = M$ (as previously mentioned, this calculation assumes the magnetization points in the $\hat{z}$ direction). Steady state solutions $\mathrm{e}^{-i\omega t}$ exist only if:

$$\begin{vmatrix} i\omega & \gamma[B_0 + (N_y - N_z)]M \\ -\gamma[B_0 + (N_x - N_z)]M & i\omega \end{vmatrix} = 0$$

such that $\omega_0^2 = \gamma^2[B_0 + (N_y - N_z)M][B_0 + (N_x - N_z)M]$

Using these equations is simple for field and magnetization in plane along the easy axis and out of plane, but not trivial for examining dynamics excited with an in-plane hard axis field. For our case, there are a few problems in using the above formulated equations without considering the system carefully. First, the direction as well as the amplitude of the effective magnetic field acting on the ferromagnets is important, especially due to the assumptions made in deriving the formulas. Second, as the applied hard axis field increases, the magnetization continuously rotates into the hard axis, so that the magnetization only points in the same direction as the field for large hard axis fields. Because of this, an analytical

solution valid for all field and magnetization directions is extremely difficult to derive. As an alternative, I have calculated the expected frequencies at small magnetic fields with the magnetization along the easy axis and with a large hard axis field orienting the magnetization along the hard axis. The frequencies can then be roughly extrapolated to get a sense of their dependence on the hard axis magnetic field. Using a chart of demagnetization factors for general ellipsoids [21] and the dimensions of 5 nm x 80 nm x 160 nm and 20 nm x 40 nm x 120 nm for the free and reference layers of the tapered inverted nanopillar, I find:

$$\omega_{0,free}^2 = \gamma^2[B_0 + (0.04(4\pi))M][B_0 + (0.9(4\pi))M] \ (B_0 \ll 0) \tag{6.7}$$

$$\omega_{0,free}^2 = \gamma^2[B_0 - (0.04(4\pi))M][B_0 + (0.86(4\pi))M] \ (B_0 \gg 0) \tag{6.8}$$

$$\omega_{0,ref}^2 = \gamma^2[B_0 + (0.26(4\pi))M][B_0 + (0.58(4\pi))M] \ (B_0 \ll 0) \tag{6.9}$$

$$\omega_{0,ref}^2 = \gamma^2[B_0 - (0.26(4\pi))M][B_0 + (0.32(4\pi))M] \ (B_0 \gg 0) \tag{6.10}$$

Here, $B_0 \ll 0$ just means a very small hard axis field that doesn't appreciably rotate the ferromagnet's moment away from the easy axis, and $B_0 \gg 0$ means a large enough hard axis field to rotate the magnetization substantially. These expression verify that at some field value the frequencies of the layers have to cross, since the reference layer frequency is higher than the free layer's frequency at low field and lower at high field. This shows that a nanopillar can be specifically designed in terms of shape to force the natural FMR frequencies of the two layer into values suitable for phase locking at a specific field value.

In Fig. 6.13, I show mode frequency, FWHM, and integrated power as a function of field angle away from the device hard axis, where a positive angle is defined as creating an easy axis field component parallel to the reference layer magnetization. Here, we find that the device performance is maximized for small angles around the hard axis. There is a sharp increase in linewidth and decrease in power

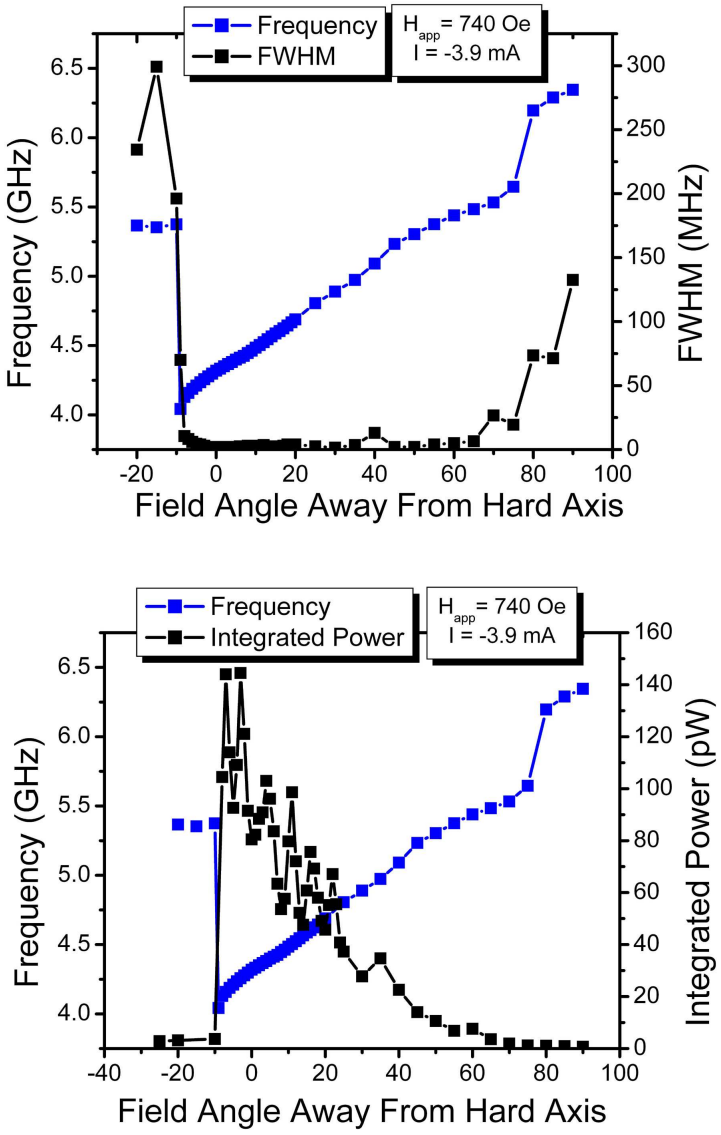

Figure 6.13: (a) Dependence of frequency and FWHM on field angle from the hard axis for device 1. Rotating the field to negative angles induces an easy axis field component oriented opposite to the reference layer magnetization that can reverse the reference layer and break the phase locking. For positive angles, the phase locking persists up to large angles but eventually breaks leading to an increase in the linewidth. This particular device exhibits locking over a larger range of field angles than any other device, but the behavior is qualitatively similar for all inverted samples. (b) Integrated power as a function of field angle for device 1. The maximum power occurs around 0 degrees, and tails off with increasing angle, indicating that the displacement of the magnetization oscillations decreases with increasing angle.

as the angle goes negative, which we attribute to a reversal of the reference layer, driving the frequencies of the two layers out of the locking regime. For positive angles, the locking phenomena persists over a larger range of of field angle as the mutual frequencies of the free and reference layers stay in the locking regime. Other devices exhibited rejection of this phase locked state at much lower angles away from the hard axis, although the qualitative behavior shown in Fig. 6.13a is the same for all the inverted devices examined. The integrated power falling off as a function of positive field angle indicates the precession angle of the magnetic excitations decreases with field angle, reducing the GMR signal and the total power.

As of the writing of this thesis, we are still exploring possible mechanisms for the phase locking between the ferromagnetic layers in this system. One method we use involves running micromagnetic simulations biased at several magnetic fields to explore the evolution of the magnetic excitations in both ferromagnetic layers. The results are shown in Figures 6.14-6.16, where I have taken Fourier transforms of the transverse component of magnetization M_z vs. time for the free layer and the interface of the reference layer. Although these simulations are taken at zero temperature, we find that the spectra exhibit finite linewidths because the oscillations are not entirely spatially coherent. At -3 mA and 200 Oe, the free layer oscillations result in a broad FMR peak centered around 3.25 GHz with what appears to be two satellite peaks corresponding to a modulation of a lower frequency signal, which appears to be a spin wave traveling laterally between the two ends of the ellipse. In comparison, the reference layer shows a broad peak centered at 6 GHz (the natural FMR frequency of the reference layer) with a corresponding peaks at the same frequencies as the free layer, indicating the reference layer is sympathetically excited by the spin current polarized by the free

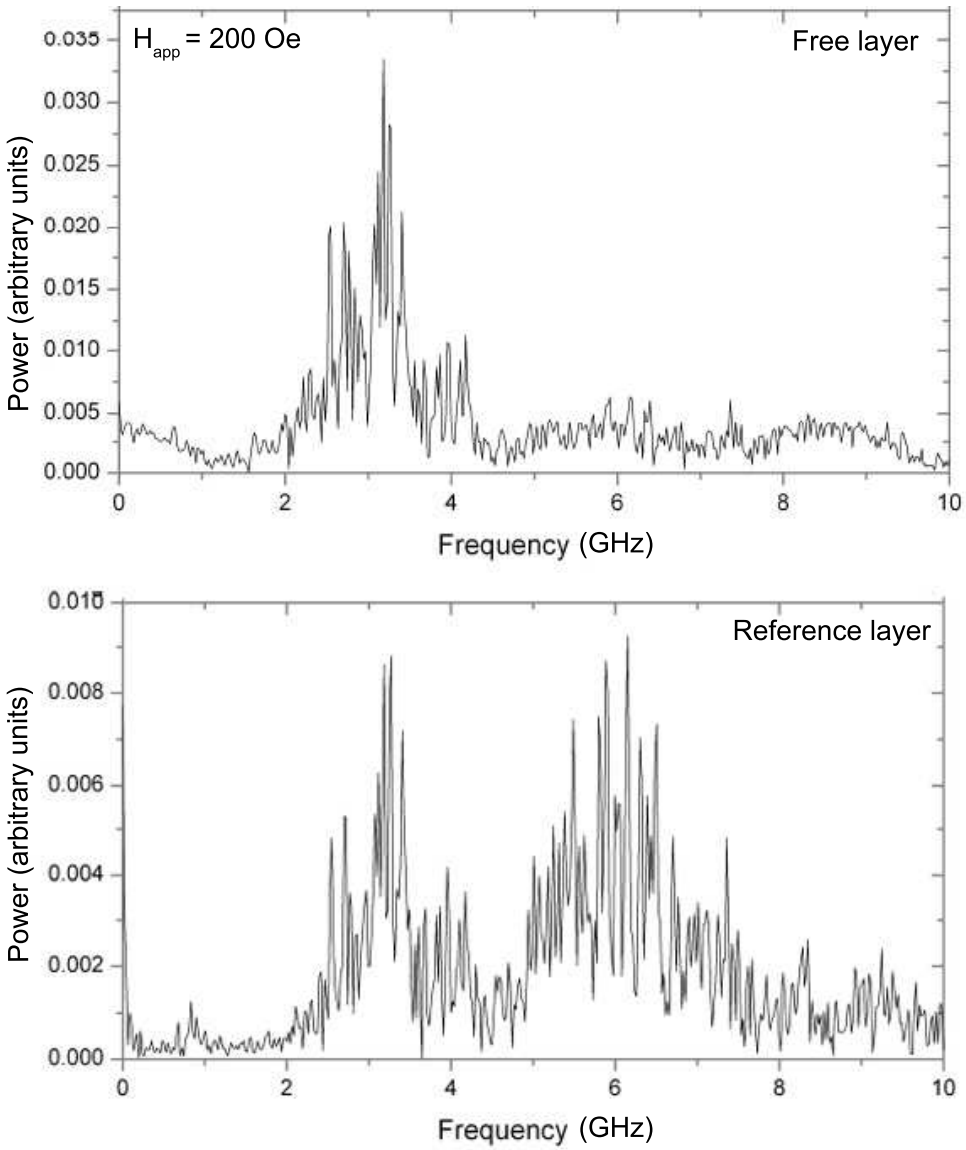

Figure 6.14: Fourier transform of the transverse component of magnetization M_z of a micromagnetic simulation at -3 mA and 200 Oe. Here, the spectra of the free layer and the interface (first 5 nm) of the reference layer are plotted separately. The FMR frequency is ~ 3.25 Ghz for the free layer and ~ 6 GHz for the reference layer, with relatively large linewidths. There are two small satellite peaks on either side of the free layer mode, indicating the modulation of a low frequency spin wave mode with the FMR mode. This mode involves a spin wave traveling back and forth between the ends of the free layer. Free layer peaks appearing in the reference layer spectra illustrates feedback occurring between the free and reference layer.

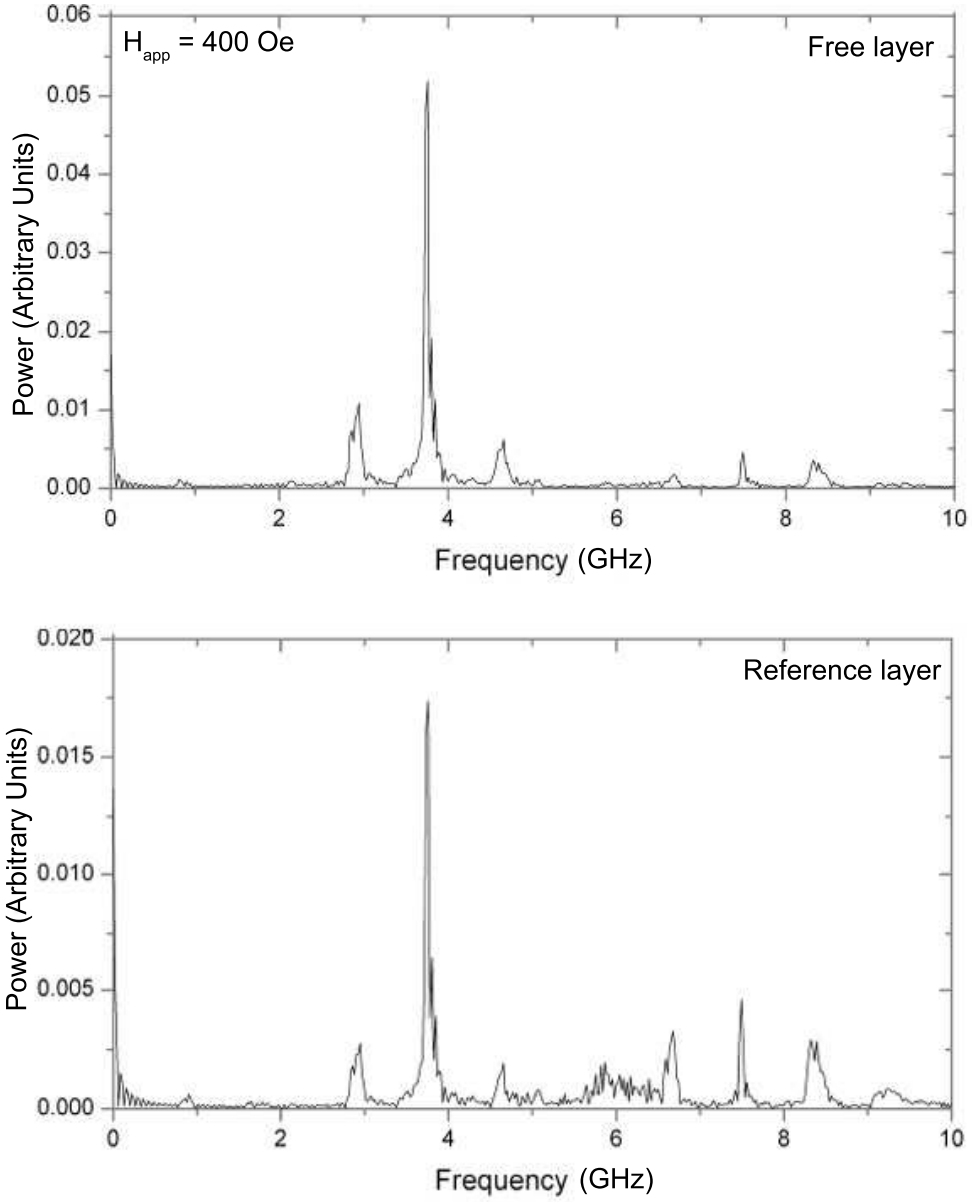

Figure 6.15: Fourier transform of the transverse component of magnetization M_z of a micromagnetic simulation at -3 mA and 400 Oe. Here, the spectra of the free layer and the interface (first 5 nm) of the reference layer are plotted separately. The linewidth of the free layer mode is much more narrow than at 200 Oe as phase locking occurs between the two ferromagnetic layers, possibly mediated by a resonance between one of the modulated modes at 3 GHz and the 6 GHz mode in the reference layer. This resonance condition is satisfied for parametric oscillators, as is discuss in the text.

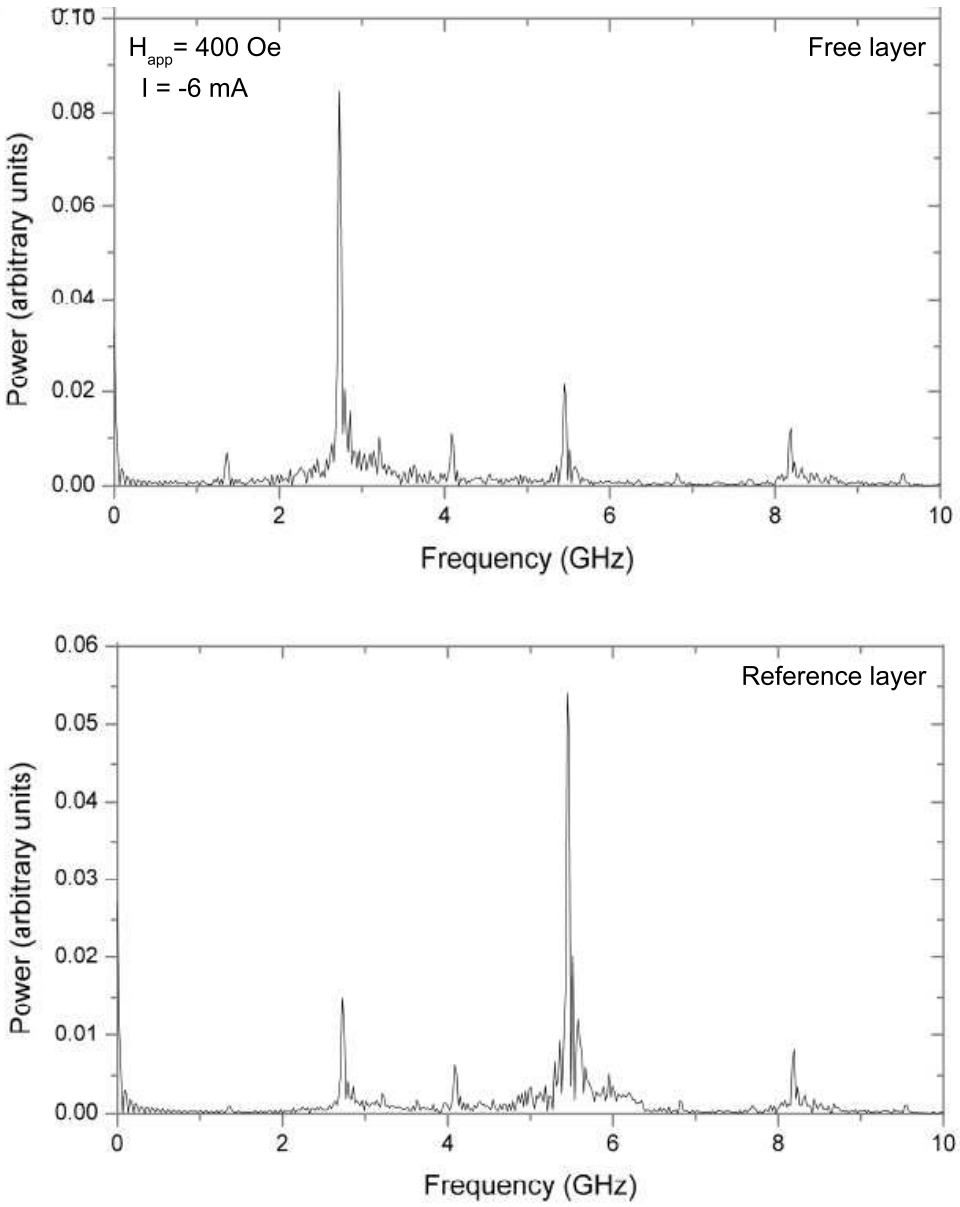

Figure 6.16: Fourier transform of the transverse component of magnetization M_z of a micromagnetic simulation at -6 mA and 400 Oe. Here, the spectra of the free layer and the interface (first 5 nm) of the reference layer are plotted separately. Increasing the current at this field brings the FMR frequency of the reference layer closer to a value twice that of the free layer FMR frequency without requiring the modulated spin wave mode.

layer. Increasing the field to 400 Oe, the amplitude of the oscillations increases dramatically, and the linewidths dramatically decrease, indicating the layers have locked together at this point. The natural frequency of the reference layer is still on the order of 6 GHz, but now one of the modulated peaks occurs at a frequency of 3 GHz, which enables a resonant phenomena known as parametric amplification that I will describe shortly. By looking at the transform of the simulation results for a -6 mA current at 400 Oe (Fig. 6.16), this relationship in frequencies is even clearer, with the fundamental frequency of the reference layer driving the free layer oscillations and the second harmonic of the free layer mutually driving the reference layer in a feedback loop that produces a very pure RF signal. It is also possible that the spin wave mode modulated with the magnetization oscillation helps mediate the phase locking of the ferromagnetic layers.

This system can be considered a parametric oscillator [22], which is defined as a simple harmonic oscillator whose parameters (resonant frequency and/or damping) vary in time in some well defined way. To understand resonant phenomena in these systems, I begin with the 1D equation of motion for this type of oscillator:

$$\frac{d^2x}{dt} + \beta(t)\frac{dx}{dt} + \omega^2(t)x = 0, \tag{6.11}$$

where the damping and resonant frequency β and ω depend only on time and not on the state of the oscillator. We can use this formula to define a STO, where the spin current incident on the free layer has a RF polarization that varies periodically in time due to the reference layer oscillations. This change in polarization makes the spin torque acting on the free layer to vary in time, which can be thought of as causing the effective damping (spin torque + Gilbert damping torque in the LLG equation) to vary in time. The resonant frequency may or may not vary in time as well, but that is not important in the context of this derivation. Solving the parametric oscillator equation involves making a change of variables so that

$q(t) = e^{D(t)}x(t)$, where $D(t) = \frac{1}{2}\int^t d\tau\ \beta(t)$. After this change of variables, the damping term drops out and the equation of motion becomes:

$$\frac{d^2q}{dt} + \Omega^2(t)q = 0, \tag{6.12}$$

$$\Omega^2(t) = \omega^2(t) - \frac{1}{2}\left(\frac{d\beta}{dt}\right) - \frac{1}{4}\beta^2. \tag{6.13}$$

assuming any time dependence in β or ω can be treated as a small perturbation, which is the case in the inverted devices as the reference layer oscillation amplitude is small, we can write the transformed frequency $\Omega^2(t)$ as:

$$\Omega^2(t) = \omega_n^2[1 + f(t)], \tag{6.14}$$

where ω_n is the natural frequency of the damping harmonic oscillator and $f(t)$ is the time dependent part of the transformed frequency. Now, the equation of motion can be written as

$$\frac{d^2q}{dt} + \omega_n^2 q = -\omega_n^2 f(t)q, \tag{6.15}$$

which represents a simple harmonic oscillator being driven by a signal $-\omega_n^2 f(t)q(t)$ that is proportional to its response q. Assume $q(t) = Acos\omega_p t$ and that the pumping term $f(t) = f_0 sin\omega t$. The product $f(t)q(t)$ can be written using trigonometric identities as

$$\frac{f_0}{2}A(sin(\omega - \omega_p)t + sin(\omega + \omega_p)t). \tag{6.16}$$

The condition for resonance is that the driving force frequency be equal to the natural frequency of the oscillator, so from this result, it is clear that a driving force with a frequency twice the natural frequency of the parametric oscillator will cause phase locking of the oscillator, as seen in the hard axis dynamics of the inverted nanopillars. Because of this, these inverted nanopillars have two important characteristics that the standard devices do not, first that the reference

layer is easily excited by spin torque along with the free layer, and second, these excitations appear to have a frequency relationship such that a feedback loop is established with phase locking between the oscillating ferromagnets.

Analysis of these results is still ongoing, but the discussion here clearly illustrates the effect that interactions between simultaneously excited free and reference layer magnetization oscillations can have on spin torque driven dynamics. Application of a hard axis field drives large angle oscillations in the free layer that can phase lock with reference layer oscillations, resulting in an RF response with large integrated powers and narrow linewidths. From our calculations of the FMR frequencies of the individual layers, we see that the shape and saturation magnetization of the magnets can be specifically chosen to produce the correct range of spin wave frequencies to promote phase locking. Even more promising is the fact that these structural and material improvements could be easily incorporated into magnetic tunnel junctions with ultrathin tunnel barriers, where the power could be increase by 5-6 orders of magnitude due to the much larger magnetoresistance value while minimizing the linewidth of the signal through phase locking of the free and reference layers. These effects are promising for the eventual realization of on-chip STO for a variety of applications.

REFERENCES

[1] Slonczewski J.C., Current-driven excitation of magnetic multilayers, *J. Magn. Magn. Mater.* **159**, L1 (1996).

[2] Berger L., Emission of spin waves by a magnetic multilayer traversed by a current, *Phys. Rev. B* **54**, 9353 (1996).

[3] Tsoi M., Jansen A.G., Bass J., Chiang W.-C., Seck M., Tsoi V., & Wyder P., Excitation of a Magnetic Multilayer by an Electric Current, *Phys. Rev. Lett.* **80**, 4281 (1998).

[4] Rippard W.H., Pufall M.R., Kaka S., Russek S.E., & Silva T.J., Direct-current induced dynamics in Co90Fe10/Ni80Fe20 point contacts , *Phys. Rev. Lett.* **92**, 027201 (2004).

[5] Katine J.A, Albert F.J., Buhrman R.A., Myers E.B., & Ralph D.C., Current-driven magnetization reversal and spin-wave excitations in Co/Cu/Co pillars, *Phys. Rev. Lett.* **84**, 3149 (2000).

[6] Kiselev S.I., Sankey J.C., Krivorotov I.N., Emley N.C., Schoelkopf R.J., Buhrman R.A., & Ralph D.C., Microwave oscillations of a nanomagnet driven by a spin-polarized current, *Nature* **425**, 380 (2003).

[7] Boulle O., Cros V., Grollier J., Pereira L.G., Deranlot C., Petroff F., Faini G., Barnas J., & Fert A., Shaped angular dependence of the spin-transfer torque and microwave generation without magnetic field, *Nature Phys.* **3**, 492 (2007).

[8] Pribiag V.S., Krivorotov I.N., Fuchs G.D., Braganca P.M., Ozatay O., Sankey J.C., Ralph D.C., & Buhrman R.A., Magnetic vortex oscillator driven by d.c. spin-polarized current, *Nat. Phys.* **3**, 498 (2007).

[9] Pufall M.R., Rippard W.H., Schneider M.L., & Russek S.E., Low-field current-hysteretic oscillations in spin-transfer nanocontacts, *Phys. Rev. B* **75**, 140404 (2007).

[10] Donohue M.J. & Porter D.G., *OOMMF Users Guide, Version 1.0, Technical Report No. NISTIR 6376* (National Institute of Standards and Technology, Gaithersburg, MD, 1999).

[11] Sun J.Z., Spin-current interaction with a monodomain magnetic body: A model study, *Phys. Rev. B* **62**, 570 (2000).

[12] Braganca P.M., Ozatay O., Garcia A.G.F., Lee O.J., Ralph D.C., & Buhrman R.A., Enhancement in spin-torque efficiency by nonuniform spin current generated within a tapered nanopillar spin valve, *Phys. Rev. B* **77**, 144423 (2008).

[13] Lee K.J., Redon O., & Dieny B., Analytical investigation of spin-transfer dynamics using a perpendicular-to-plane polarizer, *Appl. Phys. Lett.* **86**, 022505 (2005).

[14] Kent A.D., Ozylimaz B., & del Barco E., Spin-transfer-induced precessional magnetization reversal, *Appl. Phys. Lett.* **84**, 3897 (2004).

[15] Redon O., Dieny B., & Rodmacq B., *US Patent No.* 6,532,164 B2 (March 10, 2003).

[16] Thadani K.V., Finocchio G., Li Z.-P., Ozatay O., Sankey J.C., Krivorotov I.N., Cui Y.-T., Buhrman R.A., & Ralph D. C., Strong linewidth variation for spin-torque nano-oscillators as a function of in-plane magnetic field angle, Submitted to *Phys. Rev. B* (2008).

[17] Sankey J.C., Krivorotov I.N., Kiselev S.I., Braganca P.M., Emley N.C., Buhrman R.A., & Ralph D.C., Mechanisms limiting the coherence time of spontaneous magnetic oscillations driven by dc spin-polarized currents, *Phys. Rev. B* **72**, 224427 (2005).

[18] Mancoff F.B., Rizzo N.D., Engel B.N., & Tehrani S., Phase-locking in double-point-contact spin-transfer devices, *Nature* **437**, 393 (2005).

[19] Kaka S., Pufall M.R., Rippard W.H., Silva T.J., Russek S.E., Katine J.A., Mutual phase-locking of microwave spin torque nano-oscillators, *Nature* **437**, 389 (2005).

[20] Kittel C., *Introduction to Solid State Physics* 7th edn, 505 (John Wiley & Sons, New York, 1996).

[21] Osborn J.A., Demagnetizing factors of the general ellipsoid, *Phys. Rev.* **67**, 351 (1945).

[22] en.wikipedia.org/wiki/Parametric_oscillator

CHAPTER 7

THREE-TERMINAL NANOPILLAR

7.1 Introduction

Recent demands for high performance computing and data storage have led to the production or development of several different memory technologies. One option that is of great interest is Magnetic Random Access Memory (MRAM), which is a technology relying on the integration of magnetic tunnel junction (MTJ) devices with Complementary Metal-Oxide-Semiconductor (CMOS) circuits. MRAM exhibits reasonable performance in all desired memory attributes as shown in Table 1, making it competitive with current Si based memories, each of which has at least one significant shortcoming. As such, MRAM could potentially be an universal memory technology [1] eliminating the higher complexities and costs currently associated of building systems with multiple memory technologies in order to satisfy system requirements. Current advances in MTJ fabrication and memory cell design have led to the commercial release of 4 Mb MRAM chips [2], which have the potential to be the starting point for a burgeoning new technology.

This MRAM product utilizes a "cross-point" architecture, by which two perpendicular sets of conductive lines above and below the MTJs (the "bit" and "word" lines respectively) form a grid, with the MTJs situated at each overlap of the wires. Current carried down these wires generates Oersted fields, which interact with the lower coercivity "free" magnetic layer of the MTJ and can initiate a reversal of the layer's moment. In this scheme, the magnetic properties of the MTJs are tailored to require an Oersted field contribution from both lines, effectively addressing the single magnetic element located at the intersection between the bit and word lines.

Table 7.1: Comparison of current memory technologies

	SRAM	DRAM	FLASH	MRAM
read	Fast	Moderate	Fast	Moderate-Fast
write	Fast	Moderate	**Slow**	Moderate-Fast
nonvolatile	**No**	**No**	Yes	Yes
endurance	Unlimited	Unlimited	**Limited**	Unlimited
cell size	**Large**	Small	Small	Small

These Oersted fields are a nondestructive means of writing the MTJs, ensuring infinite write endurance.

For this particular writing scheme, tight tolerances are placed on the acceptable uniformity of magnetic properties for each individual element [1] to avoid so-called "half-select" problems, where elements not directly under a cross point are reversed erroneously due to abnormally small coercive fields. Alternatively, the use of spin transfer currents flowing through the elements themselves would eliminate half-select issues owing to the smaller amplitude of current required for spin transfer reversal vs. Oersted field generation and the localized nature of the write current. Although this method relaxes the requirement on coercive field uniformity, it ultimately replaces one engineering issue with another. Spin transfer reversal in MTJ's requires ultra-thin barriers [3, 4] such that the resistance-area (RA) product of the device is small enough to allow sufficient current density to actuate reversal. Fabrication of these devices in itself is a nontrivial undertaking, but even more importantly, the strain of high reversal current densities passing through these thin barriers will eventually lead to wear out of the device, reducing the overall write endurance of ST-MRAM.

A solution to this problem was initially proposed by Slonczewski in his original patent on spin transfer [5, 6] and later pursued by a fellow coworker of mine in the Buhrman group, Nathan Emley [7]. Since spin transfer in all metallic spin valve (SV) systems involves a transfer of angular momentum at the free layer's interface through spin-dependant scattering of spin polarized electrons, Slonczewski proposed a device where spin polarized electrons could ballistically impinge on the interface of the magnet and then conduct away through some other channel. This method of spin transfer is referred to as *reflection mode*, whereas the more common method referenced in this dissertation involving electrons flowing through the free layer is called *transmission mode*. As the electrons don't penetrate much into the free layer in reflection mode, a tunnel barrier opposite the nanomagnet would see very little current, thus protecting it against wear out and once again providing infinite write endurance for the device. Fig. 7.1 [7] illustrates this device concept, involving a MTJ and a metallic spin valve (SV) coupled through a common ferromagnetic (FM) layer acting as the free layer for both devices. As the structure requires a top, middle, and bottom electrode for operation, it was dubbed the "three-terminal nanopillar". DC current applied between the bottom and middle electrode is polarized by the bottom ferromagnetic layer, either by transmission through (electron flow from bottom to middle electrode) or reflection off (electron flow from middle to bottom electrode) the polarizer. These electrons impart angular momentum at the interface before leaving out the middle electrode. Because the current does not pass through the barrier, restrictions on the barrier RA product are removed as well as concerns about wearout, making this device an ideal candidate for MRAM or other spintronic devices.

The ultimate outcome of this experiment [7] resulted in partially functioning devices, as the MTJ component did not exhibit magnetic behavior, presumably

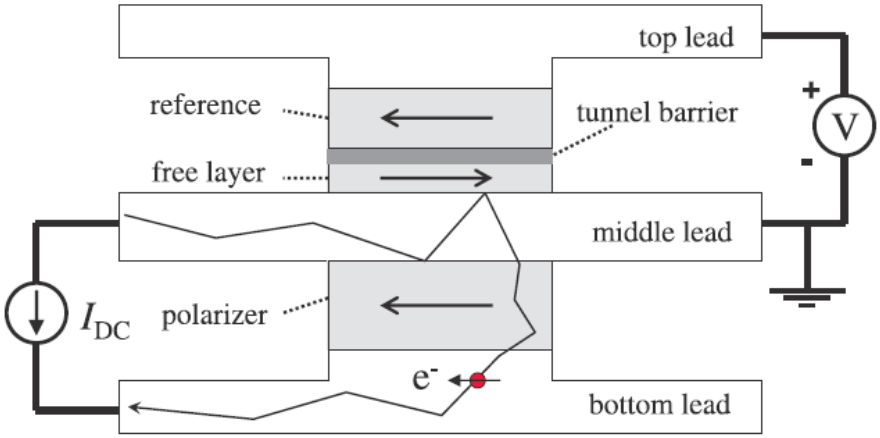

Figure 7.1: The 3-terminal device as described in [6] and show here in its simplest form (taken from Ref. [7]), consists of a bottom polarizing layer separated from a MTJ by a plane of non-magnetic metal, which is labeled the middle lead. The geometry is such that the spin-polarized electrons emanating from, or scattering off of the polarizer/middle lead interface may strike the free layer and transfer their spin angular momentum to the free layer. Although the electrons provide the spin torque, they do not propagate through the MTJ but instead conduct either out the middle lead or through the polarizer to the bottom lead, depending on the direction of current flow. The idea is that all spin-torque-induced excitations possible in 2-terminal devices in transmission mode spin transfer should likewise be possible in reflection mode spin transfer like that exhibited by the 3-terminal nanopillar. However, studies in lateral spin valves [8] have shown that the currents required for reflection mode reversal are extremely large, making practical implementation difficult for these devices.

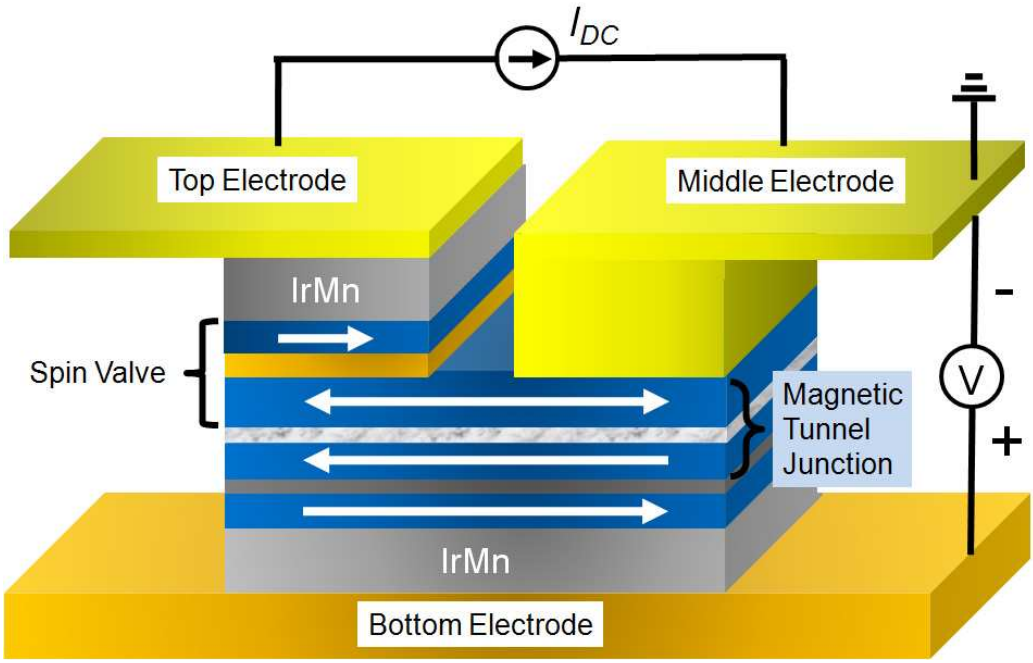

Figure 7.2: 3-terminal device concept modified from original reflection mode concept. In this design, all the magnetic multilayers are deposited in the initial stage of fabrication, and aligned EBL and ion milling is performed to controllably etch a middle electrode into the ferromagnetic free layer shared by the spin valve and tunnel junction components of the device. Electrons flowing between the middle and top electrodes can reverse the free layer through transmission mode spin-torque interactions. By biasing the MTJ between the middle and bottom electrodes, the orientation of the free layer's moment can be read out through tunneling magnetoresistance effects. This strategy is compatible with modern microelectronic fabrication techniques and could be an enabling structure for developing high performance MRAM memory cells.

through sidewall shorting issues arising during device fabrication. Despite this disappointing outcome, the experience of designing and fabricating these devices provided us with extremely valuable experience for making a second attempt. Experiments in lateral spin valves [8] considering spin accumulation in nanowires [see Fig. 7.3] have indicated that reflection mode reversal requires extremely large currents, creating concerns on whether free layer reversal can be actuated to orientations both parallel and antiparallel to the reference layer. With this in mind, I have chosen to modify Nathan's original concept to utilize transmission mode as the write process. In addition, the fabrication procedure has been modified to allow both the MTJ and the SV components to be deposited simultaneously, with subtractive steps following to define the bottom, middle, and top electrodes. The completed device is shown in Fig. 7.2, and overall follows a similar read/write procedure as in the reflection mode device, with the exception that the current flows through the free layer as opposed to the spacer as in Nathan's device. This results in an interesting reversal process involving the nucleation and propagation of a domain wall due to nonuniform current injection. In the following sections, I will highlight the procedure for fabricating this device, display the results for read/write experiments on these devices, and explore this novel reversal mechanism.

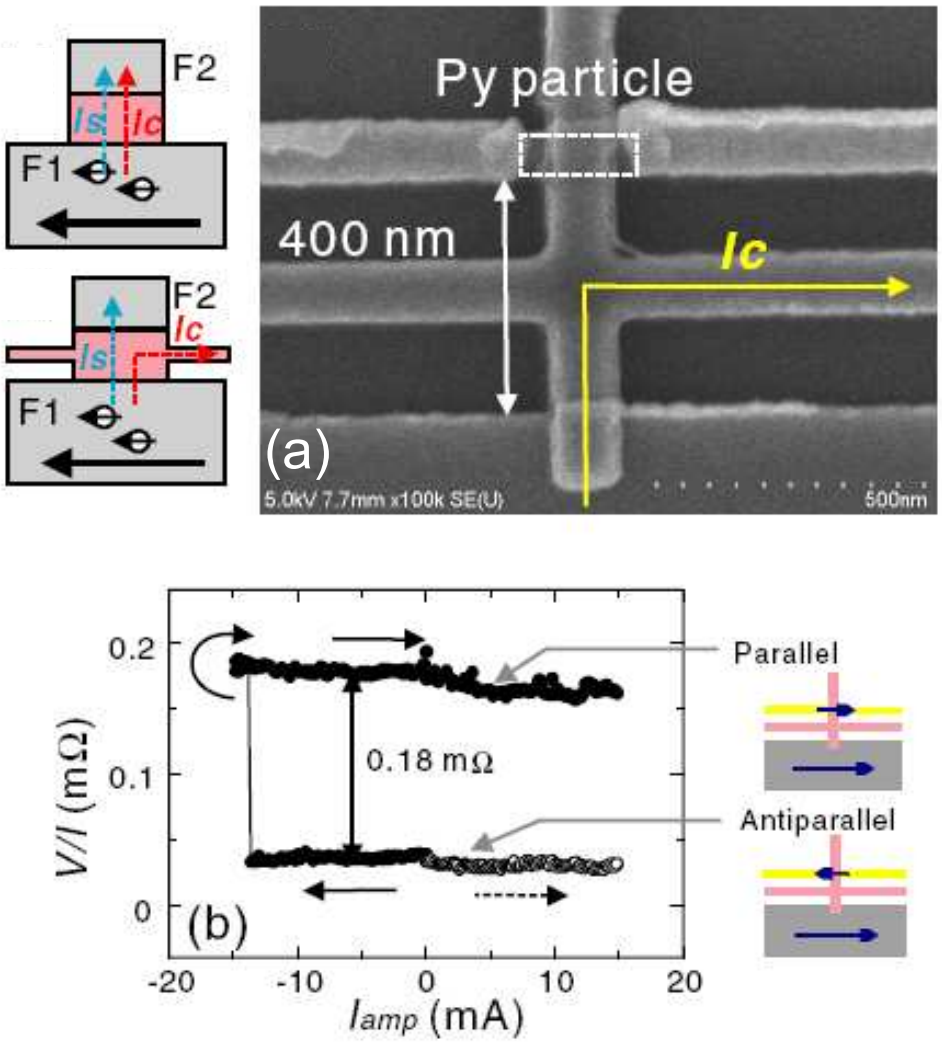

Figure 7.3: (a) Lateral spin valve structure for studying spin accumulation and reflection mode spin transfer reversal effects (from Ref. [8]). Cartoons illustrate two different device configurations, one (top left) with the magnetic particle [F2] isolated from the current passing laterally through FM1, and another (bottom left) with an electrode contacted to FM2, similar to the device concept in Fig. 1. In either geometry, the electric current flow is assumed to flow away from FM2 (as shown in SEM image), so that spin torque effects can only occur due to spin reflections. (b) Resistance vs. current for lateral spin valve device. Reflected spins can reverse the moment of FM2 from an orientation antiparallel to the moment of FM1 to one parallel (AP-P), however the current required, ~ 15 mA, is more than an order of magnitude larger than reversal by transmission mode. Additionally, the device fails before sufficient current to reverse P-AP can be injected, making transmission mode a more appealing write mechanism for a 3-terminal device.

7.2 Fabrication Concept

In discussing the process for fabricating these devices I would be remiss in not acknowledging two individuals without who this project would not have succeeded. Nathan Emley was my graduate student mentor, and he was an extraordinary inspiration for ingenuity in nanofabrication. He accepted the original challenge in designing and fabricating three terminal devices, using a multitiered additive process to define the all-important middle electrode [7]. Unfortunately, sidewall shorting issues derailed the performance of this structure. His herculean effort in designing and fabricating these devices provided valuable knowledge to me in this second round of design and fabrication. The second individual I would like to thank is Jordan Katine of Hitachi Global Storage Technologies (HGST), who provided both his time and HGST facilities turn my concept into real devices. Without Jordan's expertise, this project would never have gotten off the ground.

The steps below outline a subtractive nanofabrication process to define both the middle and top electrodes within a nanopillar structure. Success of this process depends on first defining the nanopillar and insulating its sidewalls in a self-aligned manner, similar to the process presented in [7]. As such, I begin my description of this process assuming the definition and insulation of the nanopillar has already been achieved. From this point on, the details of each individual process step will be expanded upon in the figure captions.

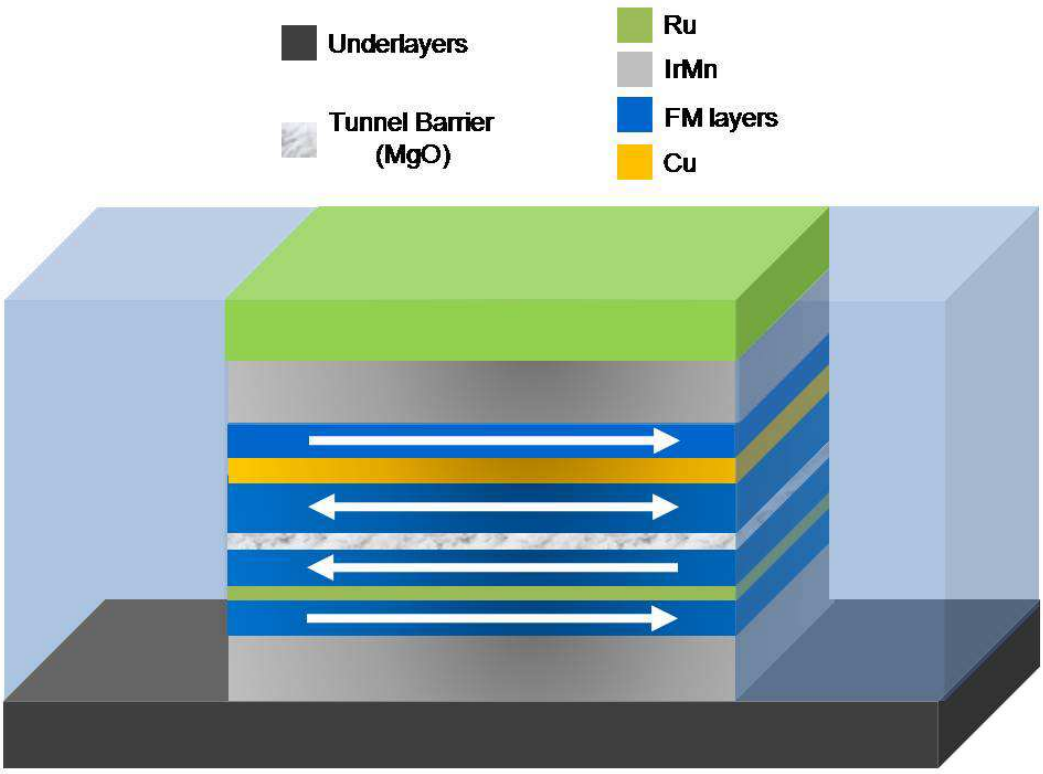

Figure 7.4: The fabrication process begins by sputter depositing a multilayer stack. For the devices built by Jordan, we used a stack of 70 IrMn/25 CoFe/8 Ru/25 CoFeB/MgO/5 CoFe/60 NiFe/10 CoFe/30 Cu/25 CoFe/60 IrMn /60 Ru where all thicknesses are in $\mathring{A}$. The bottom IrMn/CoFe/Ru/CoFeB layers form a synthetic antiferromagnet (SAF) that acts to provide both strong pinning for the bottom reference layer (RL1) and to promote the growth of the ultrathin MgO barrier, resulting in a barrier RA product of $\sim 3\Omega \cdot \mu m^2$. CoFe/NiFe was chosen for the bilayer free layer material as previous studies [9, 10] on ferromagnets with low saturation magnetization M_s have shown substantial reductions in the current required for spin torque reversal, although we have found that this choice, coupled with the low RA barrier, results in a device with low TMR. The top CoFe reference layer (RL2) was stabilized by exchange bias with the top IrMn layer in the direction antiparallel to RL1. Electron beam lithography (EBL) and ion milling were then used to pattern elliptical nanopillars similar to those shown in Fig. 1a, and standard photolithography was used to pattern the bottom electrode. A self-aligned process [11] insulated the nanopillar sidewalls with Al_2O_3 while allowing for contacting to the top of a device.

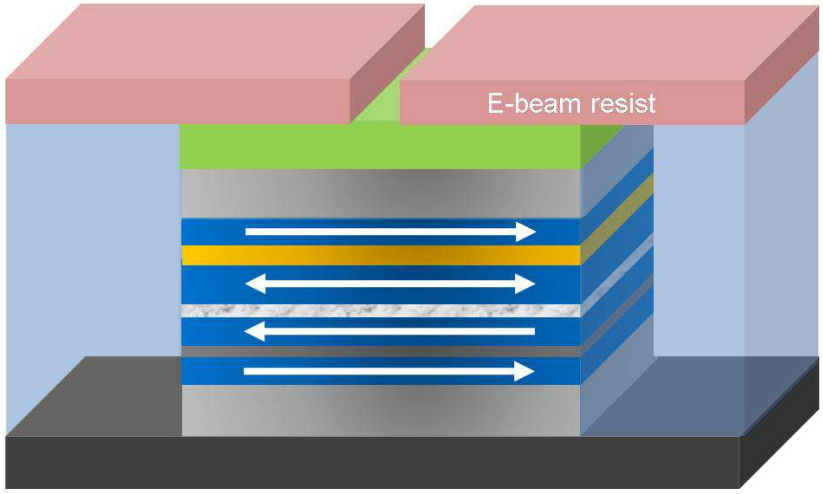

Figure 7.5: Aligned EBL using a positive tone resist such as PMMA to define an isolation trench between the left and right sides of the nanopillar. This exposure defines a $\sim$ 40 nm wide rectangle placed at the halfway point of the ellipse, perpendicular to its semimajor axis.

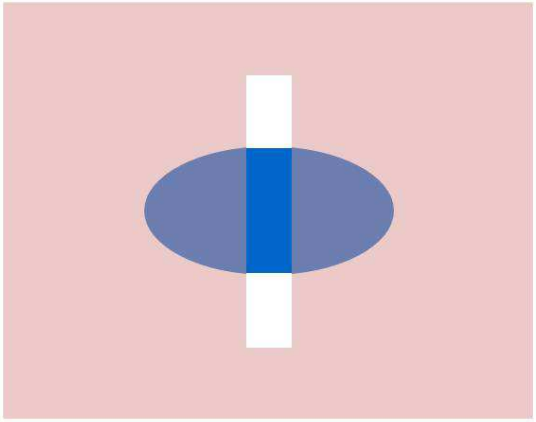

Figure 7.6: Top down view of aligned EBL step 1. A rectangular pattern is exposed to separate the right and left sides of the nanopillar

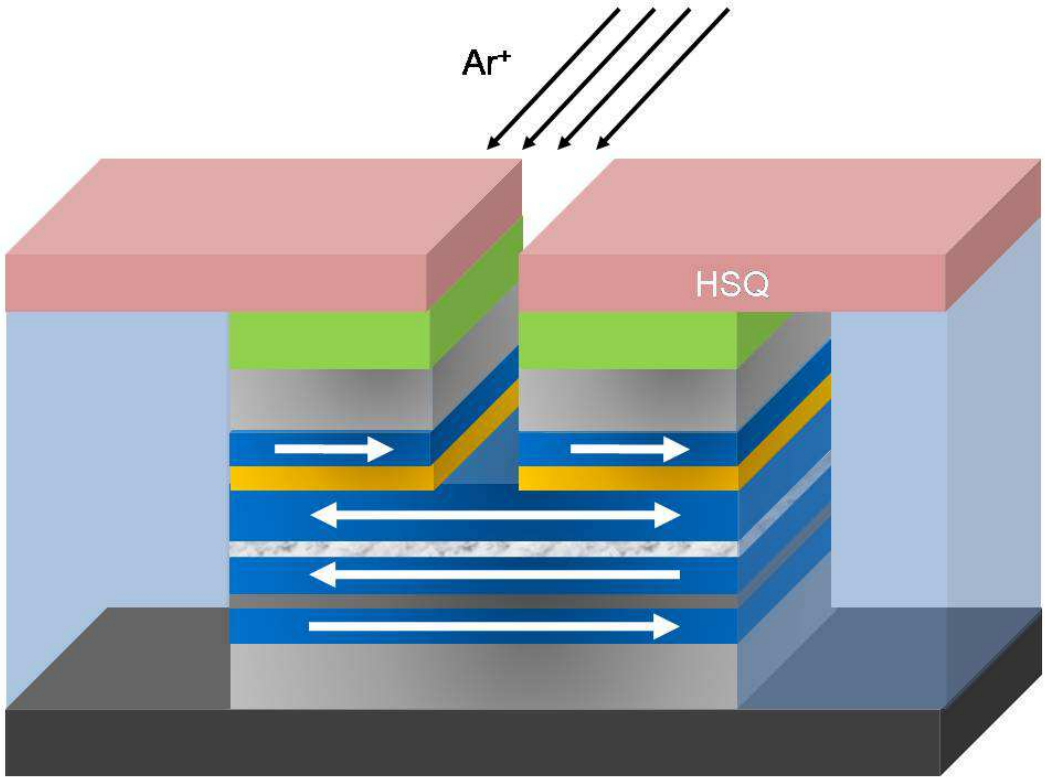

Figure 7.7: Ion mill isolation trench into nanopillar. Here, the ion milling was terminated when the free layer was reached, as determined by secondary ion mass spectroscopy. This step isolates the two nanopillar sides to avoid shorting between the middle and top electrode in subsequent fabrication steps.

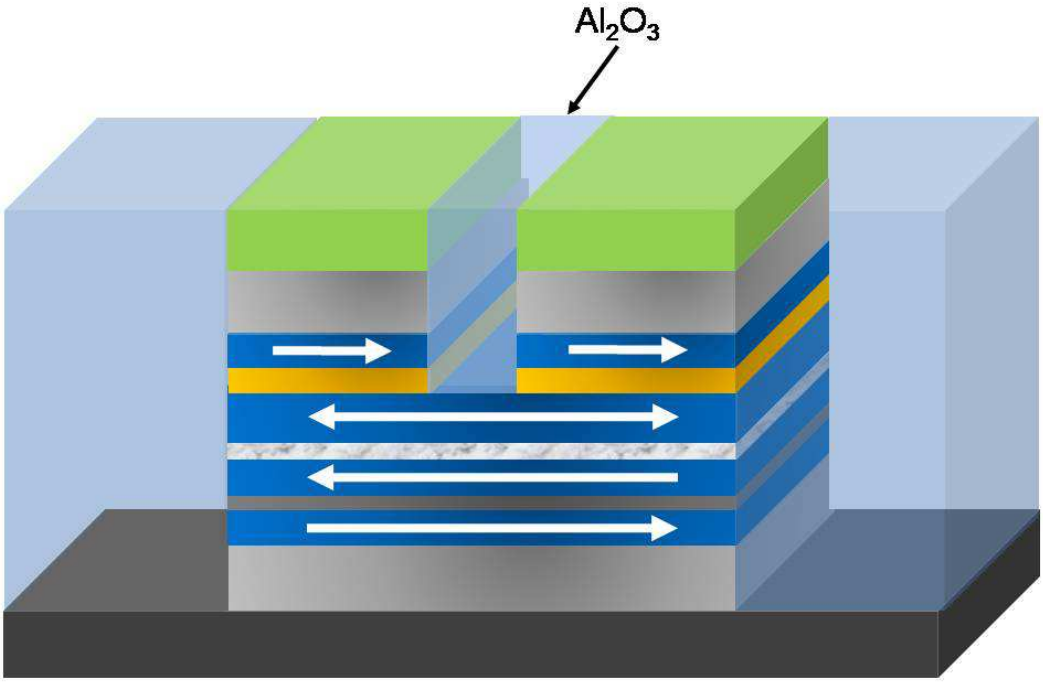

Figure 7.8: Alumina refill of isolation trench. In this step, we deposit an amount of Al_2O_3 equal to the etch depth of the previous step. Subsequent lift-off of the e-beam resist leaves the trench refilled with alumina, with the right an left ends of the device exposed.

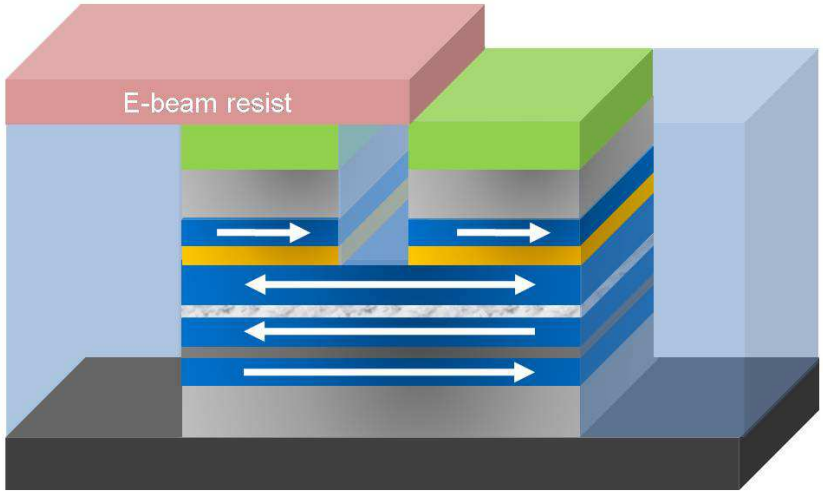

Figure 7.9: Aligned e-beam 2 to define the middle electrode. Here, we use EBL to open up the resist above the right edge of the nanopillar, exposing the right half for subsequent ion milling steps.

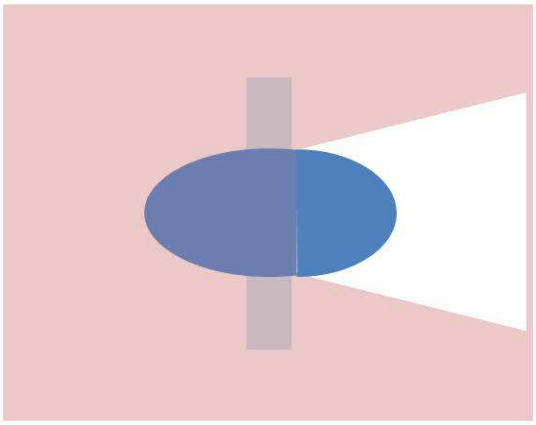

Figure 7.10: Top down view of second aligned e-beam step. Resist is opened up above right half of ellipse.

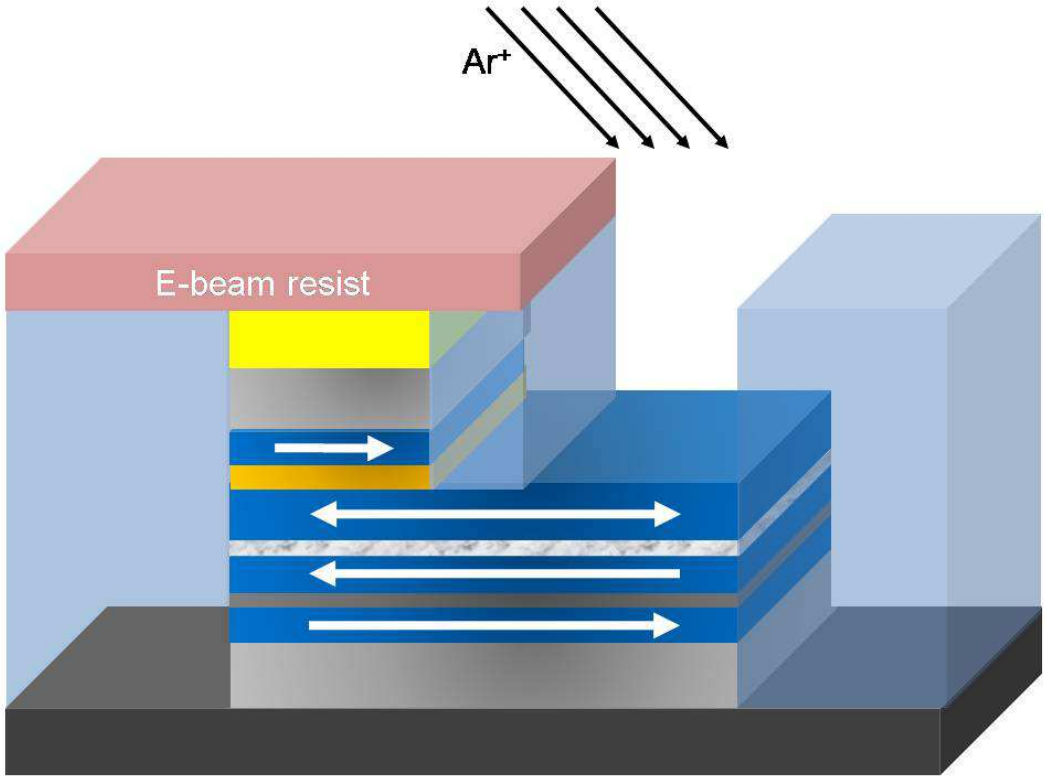

Figure 7.11: Ion mill to define middle contact. Here, the ion milling was terminated when the free layer was reached, allowing current to flow across the free layer. As this step requires an extreme level of mill precision, the use of SIMS characterization here is critical. TEM cross-sections of these devices shown later in this chapter indicate a high level of accuracy in this mill step, indicating contacting of the middle electrode to any layer of the deposited stack should be possible. This level of accuracy may open the door for additional device structures utilizing this configuration.

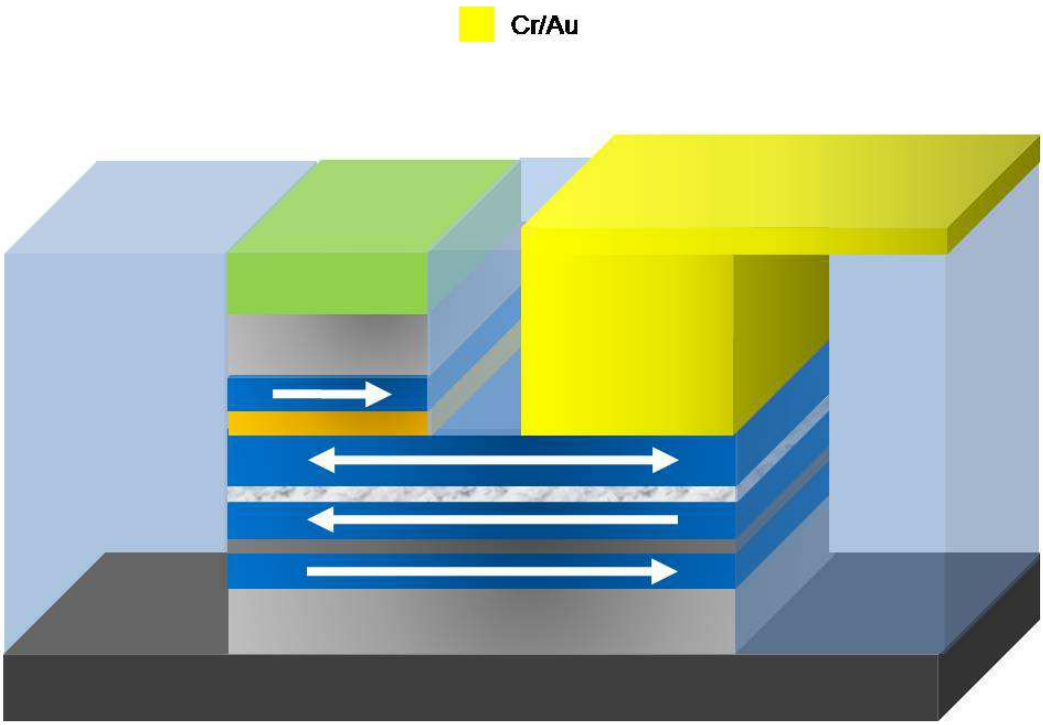

Figure 7.12: Deposition of middle contact. To make contact to the free layer, an adhesion layer of 50 $\mathring{A}$ chrome followed 200 $\mathring{A}$ gold is deposited with ion beam deposition without breaking vacuum from the previous ion mill step, defining the middle electrode of the 3-terminal device.

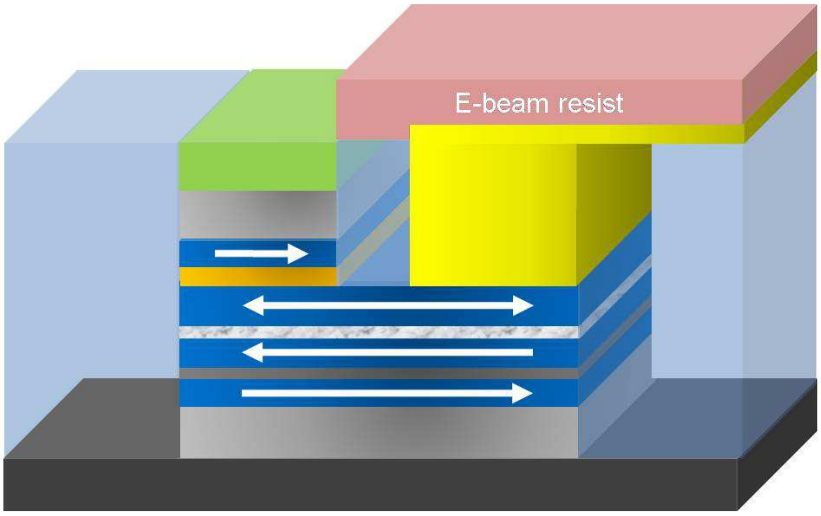

Figure 7.13: Aligned e-beam 2 to define the top electrode. Here, we use EBL to open up the resist above the left edge of the nanopillar, exposing the left half for subsequent deposition steps.

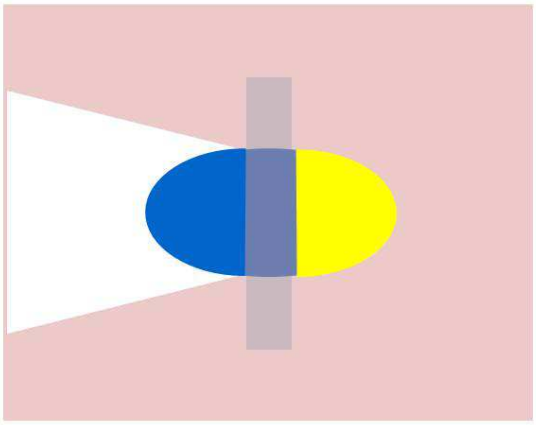

Figure 7.14: Top down view of third aligned e-beam step. Resist is opened up above left half of ellipse.

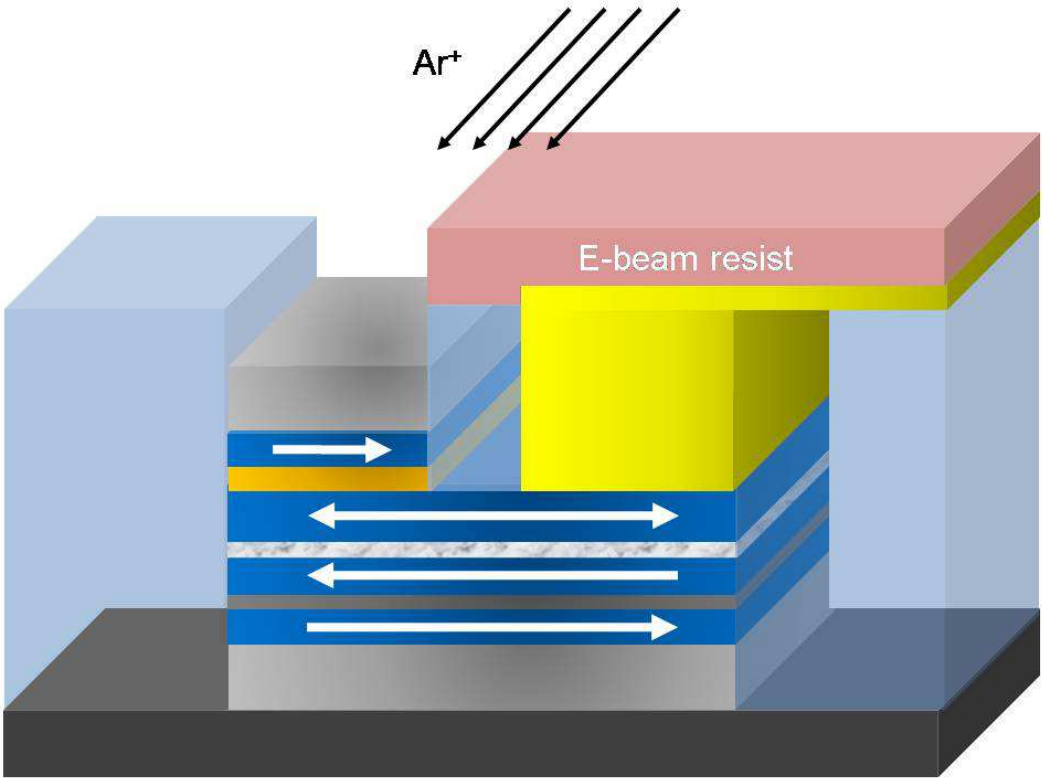

Figure 7.15: Ion mill to define top contact. Here, the Ru capping layer over the left half of the device is milled away to allow for a clean contact to be made.

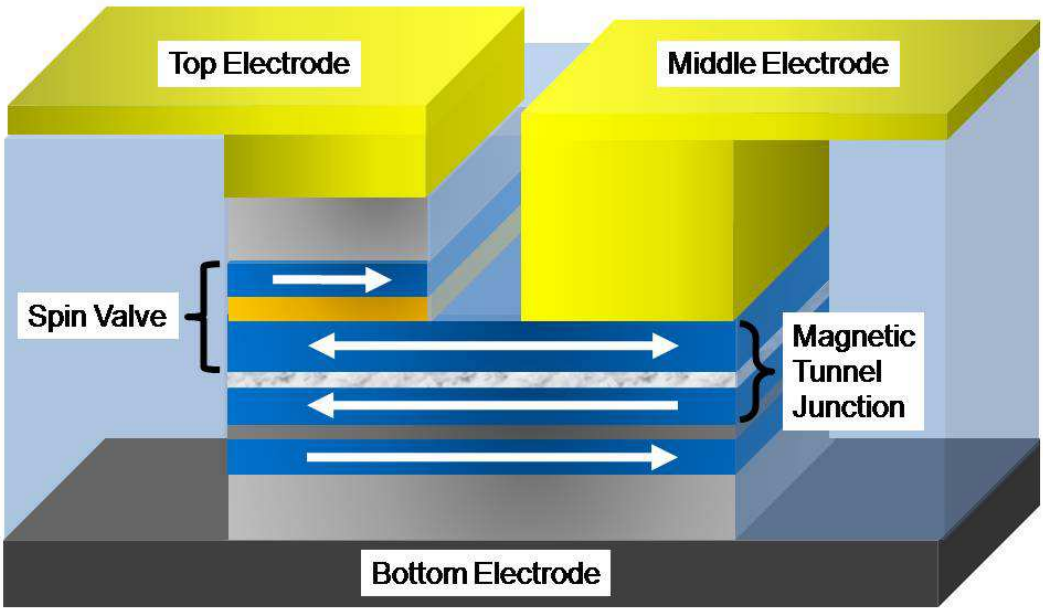

Figure 7.16: Completion of 3-terminal device. Without breaking vacuum from the previous ion mill step, we ion beam deposit 50 $\mathring{A}$ Cr/200 $\mathring{A}$ Au to define the top electrode. At this point, all three electrodes have been defined, the top and middle as described here, and the bottom through standard photolithography performed during nanopillar definition (for further details, see Chapter 3 or [7]). TEM cross sections show that the structure of an actual device processed by these means closely resembles the proposed structure.

7.3 Experimental Results and Discussion

Fabrication of these devices was carried out in two different fabrication runs by Jordan, the first involving a layer structure of 30 Ta/60 NiFe/10 CoFe/30 Cu/25 CoFe/60 IrMn/60 Ru where only the top and middle electrodes were patterned with no tunnel junction. I will refer to this structure as the prototype configuration, where the isolated spin valve was used to verify spin transfer effects originating from nonuniform current injection into the left half of the device. The second stage involved patterning the complete MTJ/SV coupled system involving a layer structure of 70 IrMn/25 CoFe/8 Ru/25 CoFeB/MgO/5 CoFe/60 NiFe/10 CoFe/30 Cu/25 CoFe/60 IrMn/60 Ru using the full process outlined in the previous section. I will refer to this structure as the complete configuration. Figures 7.17-7.20 show SEM micrographs of these devices at various points in the fabrication process. These indicate the level of precision that can be achieved with aligned EBL for positioning the electrodes, which is a major accomplishment enabling fabrication of this complicated device. Fig. 7.21 shows a TEM cross section of a long patterned line processed to define middle and top electrodes[1]. Here, ion milling together with secondary ion mass spectrometry (SIMS) used at HGST is successful in controllably milling features down to desired layers with extremely small tolerances.

[1]Note: The tapered sidewalls of the layers above the MgO barrier seen in Fig. 7.21 result from shadowing effects during ion mill definition of the test line. These effects do not play as significant a role when defining the much smaller elliptical patterns, so we expect that a much straighter sidewall profile is present in the actual devices.

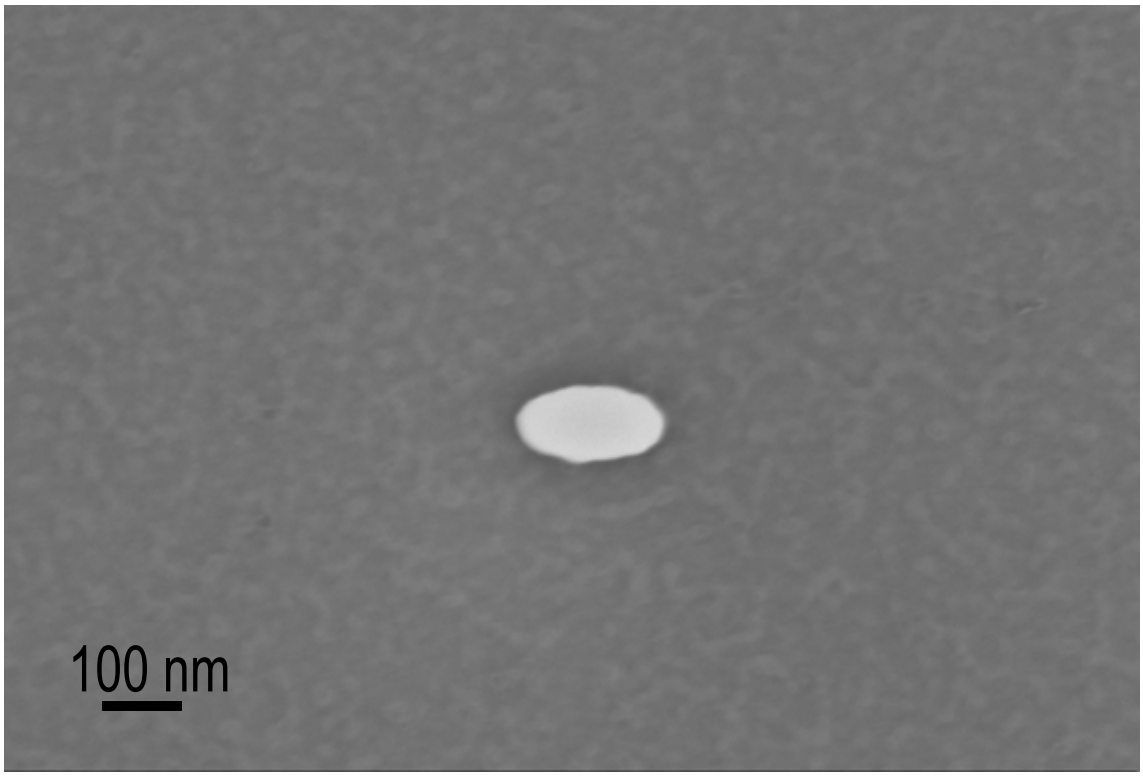

Figure 7.17: Elliptical nanopillar processed using EBL and ion milling in a manner described in [11]. This device represents the starting point in the process I outline to pattern the middle and top electrodes.

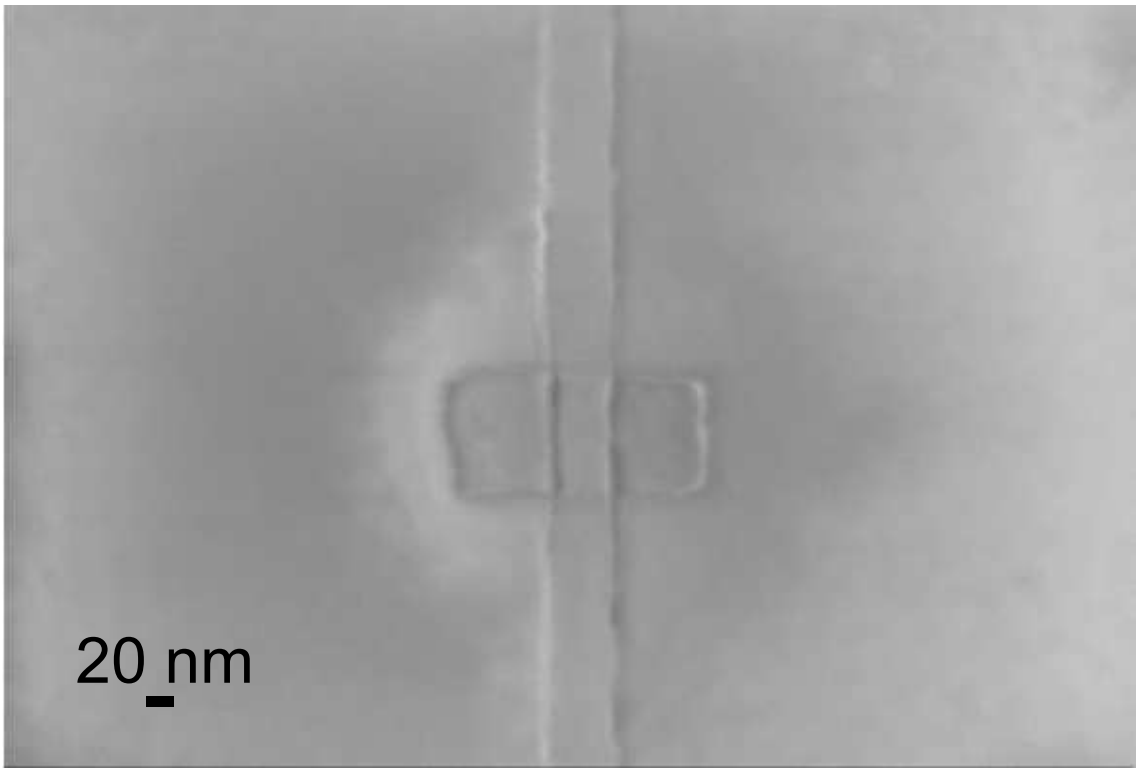

Figure 7.18: Trench ~ 40 nm milled out of the center of the ellipse, down to the free layer of the device as described in the previous section. This trench is then refilled with alumina to isolate the left edge of the ellipse from the right.

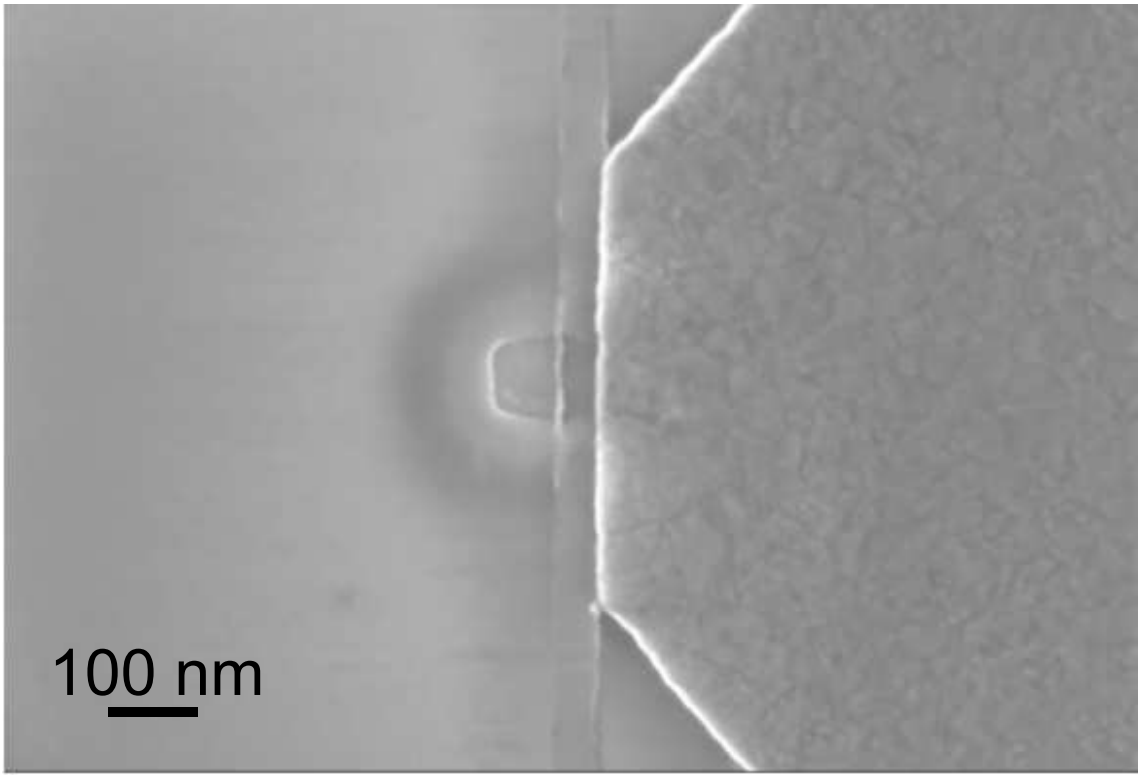

Figure 7.19: Aligned EBL defines the right contact, which was milled to the free layer before depositing the Cr/Au contact.

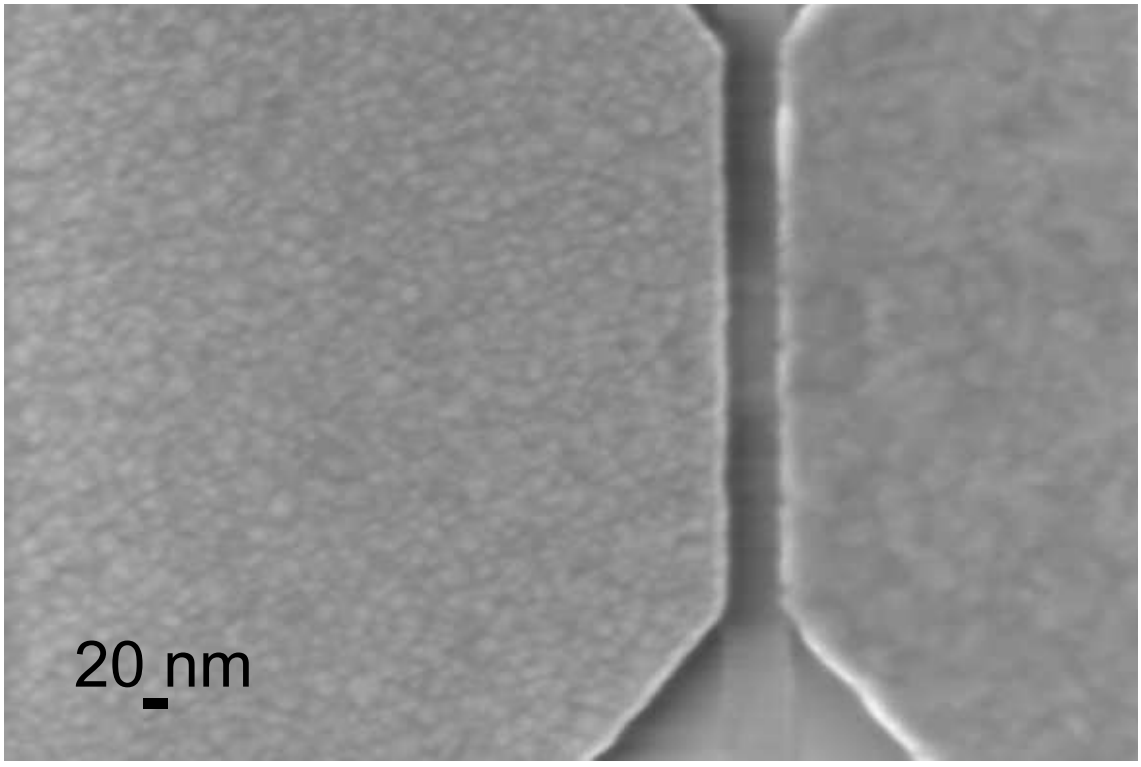

Figure 7.20: Aligned EBL defines the left contact, which had the Ru cap milled before depositing the Cr/Au contact.

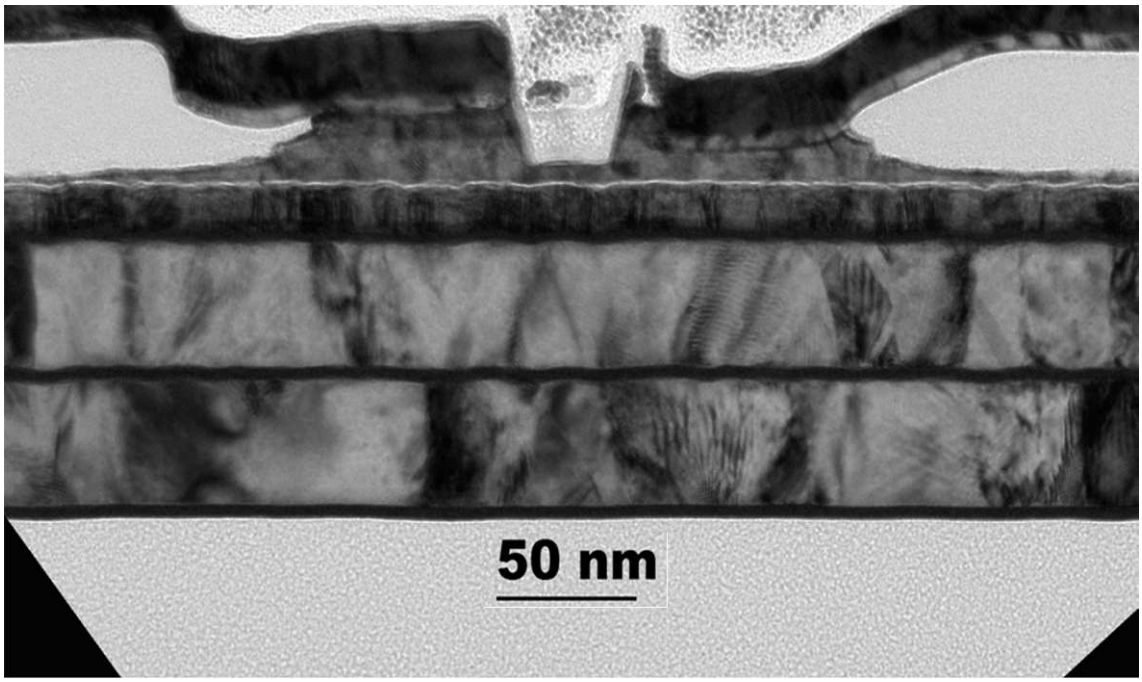

Figure 7.21: TEM cross section of an EBL defined line patterned simultaneously with the elliptical devices. Here, I note that both the insulating trench and the right contact have been milled to the NiFe layer directly above the MgO barrier (represented by the thin white line), which verifies that the electrodes can be controllably placed anywhere within the multilayer stack.

For both device configurations, elliptical nanopillars of various dimensions were defined prior to top and middle electrode definition. Optimal device performance occurred for nanopillars with $\sim 70\times200$ nm^2 dimensions, for reasons outlined below. First, the isolation trench milled into the nanopillar (Fig. 7.21) creates a small conducting channel for electron traveling laterally in the free layer to pass through, thus limiting the amount of current that can be applied across the device to the order of a few milliamps before catastrophic device failure, depending on the thickness and cross sectional area of the channel. Therefore, achieving the critical current densities required for reversal with larger area ellipses is extremely difficult. Decreasing the semimajor axis dimensions introduces the opportunity for shorting between the top and middle electrodes, although further processing characterization could eliminate this negative effect. Decreases in semiminor axis dimensions reduce the cross sectional area of the conducting channel, increasing device resistance and lowering the threshold current for device failure, similarly decreasing the potential of the device for spin transfer applications.

To develop an understanding of the spin torque driven reversal process in this novel nanopillar system, we used a three-dimensional (3D) zero temperature micromagnetic simulation package [10, 12, 13] that includes the Slonczewski spin torque term. Fig. 7.22(a) shows the initial state of the free layer, where to simplify our calculations the magnet has been assumed to be a 40×142.5 nm^2 rectangle and the Oersted field generated by the applied current has not been considered. For simplicity, we only consider the spin torque transmitted by the current flowing perpendicular to the films, so that spin torque is locally exerted at the interface of the free layer directly below RL2 as noted by the outlined region in Fig. 7.22(a). In principle, one should also take into account additional spin-torque interactions between the current flowing laterally across the free layer and any domain walls

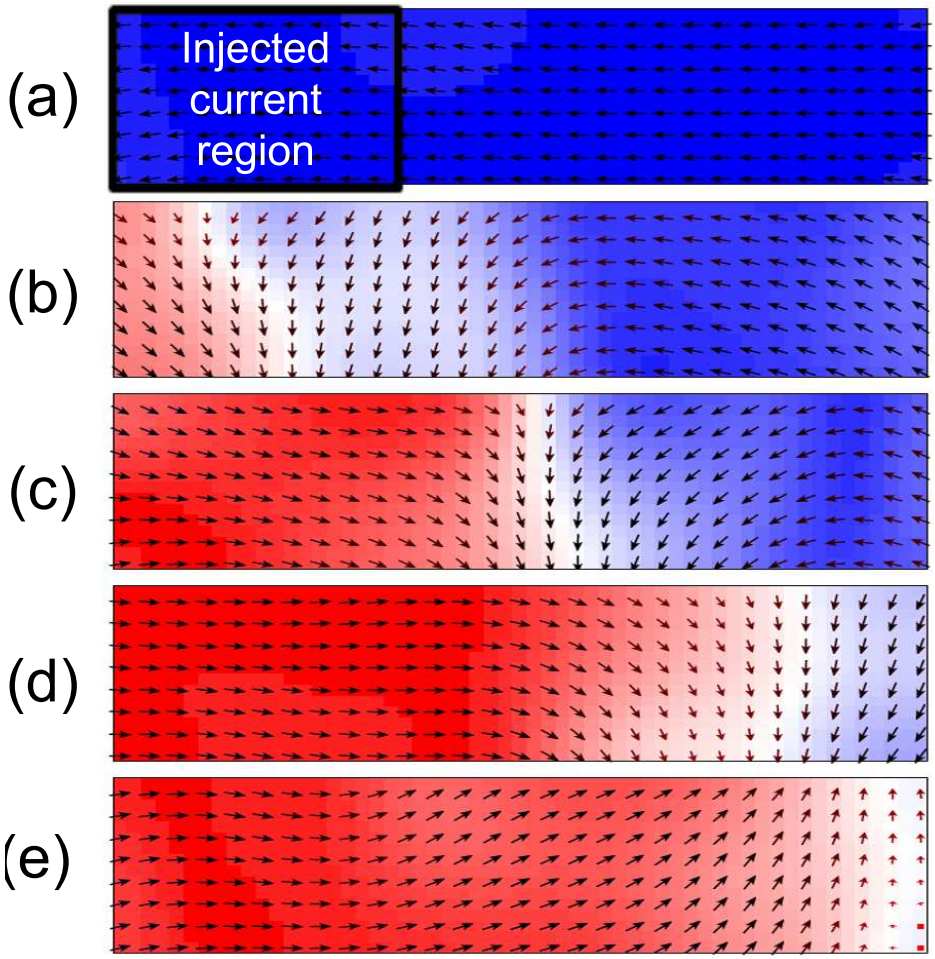

Figure 7.22: (a)-(e) Zero temperature 3D micromagnetic simulations of the SV component of a 3-terminal structure. The initial micromagnetic state of a 40×142.5 nm^2 rectangular nanomagnet is shown in (a) with the region where current is injected perpendicular to the film plane indicated, simulating the reference layer in the left contact shown in Fig. 7.2. For -3 mA with spins polarized antiparallel to the initial magnetization, a reversal domain forms underneath the reference layer (b), which grows in time due to pressure exerted by spin torque (c)-(e). This manifests as a domain wall sweeping across the free layer.

formed in that layer (the domain-wall drag effect) [14–19]. However, we will argue below that this effect is negligible in these devices. Figures 7.22(b)-(e) demonstrate the evolution of the reversal process for a -3 mA current polarized antiparallel to the initial magnetization of the free layer. Switching is initiated by the formation of a reversal domain beneath RL2, creating a head-to-head 180° domain wall within the free layer. This non-stable domain wall then propagates towards the right end of the free layer driven by exchange force, reflects off the right edge of the magnet and decays rapidly away as it travels back towards the left edge, where the magnetization is stabilized by the spin torque exerted on that region. Similar simulation results are obtained for the switching of the free layer magnetization from an orientation parallel to RL2 to one antiparallel by the spin torque exerted by electrons flowing from the free layer to RL2.

Fig. 7.23 shows a typical resistance versus current scan for a 70×200 nm^2 elliptical prototype device measured using standard AC lock-in techniques. During the scan, we apply a constant magnetic field to cancel the small dipole field exerted by the reference layer upon the free layer. Due to the narrow channel in the NiFe layer beneath the isolation trench, the resistance of the SV is significantly larger than is typically observed for current perpendicular to the plane spin valves. We have verified that the current switches the full area of the free layer (and not just the part under RL2) by using an applied magnetic field to set the initial state of the free layer to both the parallel and antiparallel states; the critical currents shown in Fig. 7.23 are the same in both cases. Assuming that the left contact area has an area half that of the ellipse minus half the area of the isolating trench ($\sim 4.1\times10^{-11}$ cm^2), the switching currents shown in Fig. 7.23 correspond to $J_{c,SV} \approx$ -1.2×10^7 A/cm^2, in reasonable agreement with previous ST results in simple spin valve structures. This is somewhat surprising in that it suggests that the exchange

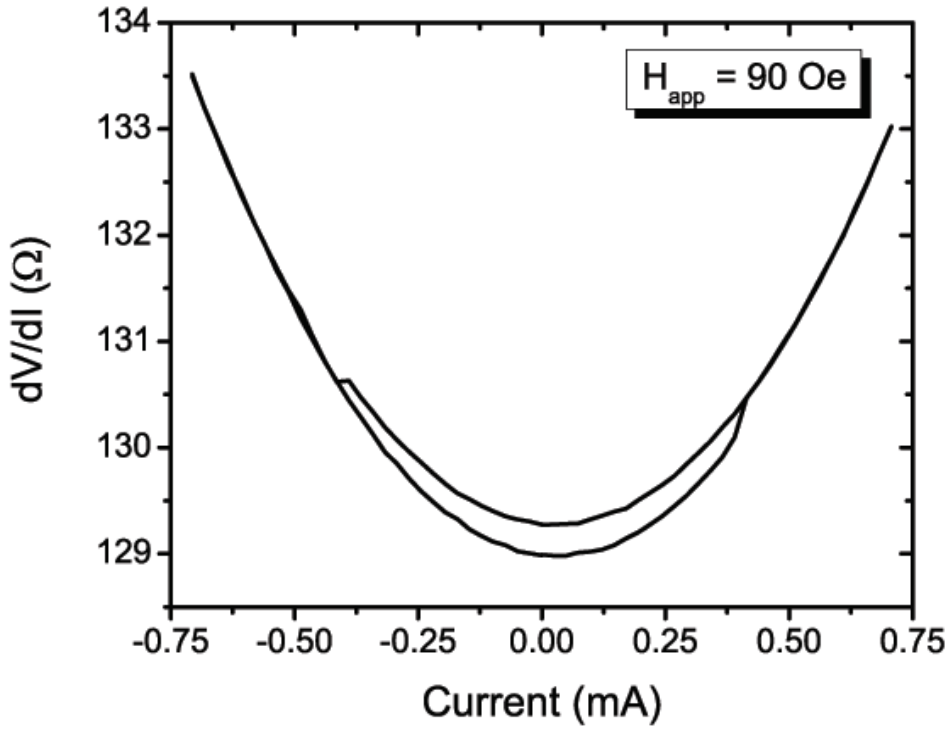

Figure 7.23: dV/dI vs. current for a prototype device patterned from a 70×200 nm^2 elliptical nanopillar.

coupling of the rest of the free layer to the area under the spin valve contact does not substantially impede the reversal process. We will return to this point in the discussion below.

We note in Fig. 7.23 that the critical current amplitude for the antiparallel (AP) to parallel (P) transition (high to low resistance) is very similar to that for the P-to-AP transition. Since any domain drag effect from current flowing laterally within the free layer would decrease the critical current for the AP-to-P transition and increase it for the P-to-AP case, our results indicate that spin torque effects on the domain wall propagation are not significant in this device configuration. We conclude that in this device the spin torque due to current flow across a non-ferromagnet - ferromagnet interface is much more efficient than that due to current flow through a domain wall.

Figures 7.24-7.25 show experimental results for a complete SV/MTJ coupled structure patterned into a 70×200 nm^2 ellipse and processed as described above. Measurement of the SV resistance was accomplished using standard AC lock-in techniques, while the DC resistance of the MTJ was measured simultaneously with a multimeter. By varying the applied magnetic field [Fig. 7.24], we observe steps in resistance in both the SV and MTJ, corresponding to magnetization reversal of the free layer. Due to the antiparallel alignment of RL1 and RL2 with respect to one another, a switch to the high resistance state of the SV corresponds to a switch to the low resistance state of the MTJ.

In Fig. 7.25, we show the results of injecting current through the spin valve while reading the resistance of the MTJ. Spin torque reversal occurs from the high to low resistance state with respect to the SV, and is simultaneously detected by the MTJ. The resistance change of the MTJ initiated by the spin torque effect

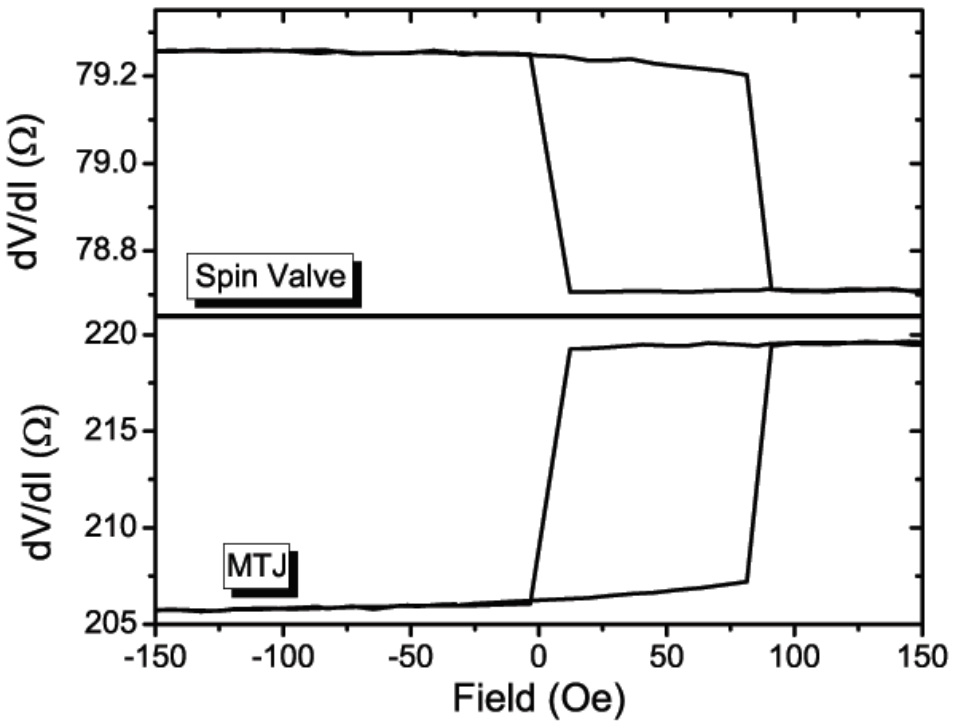

Figure 7.24: Magnetic field vs. resistance measured simultaneously for both the spin valve and magnetic tunnel junction in a completed device. The steps in resistance correspond to reversal of the free layer detected using the giant magnetoresistance (in the SV) and tunneling magnetoresistance (GMR) effects. Since RL1 and RL2 are pinned antiparallel with respect to each other, the high resistance state of the SV is the low resistance state of the MTJ.

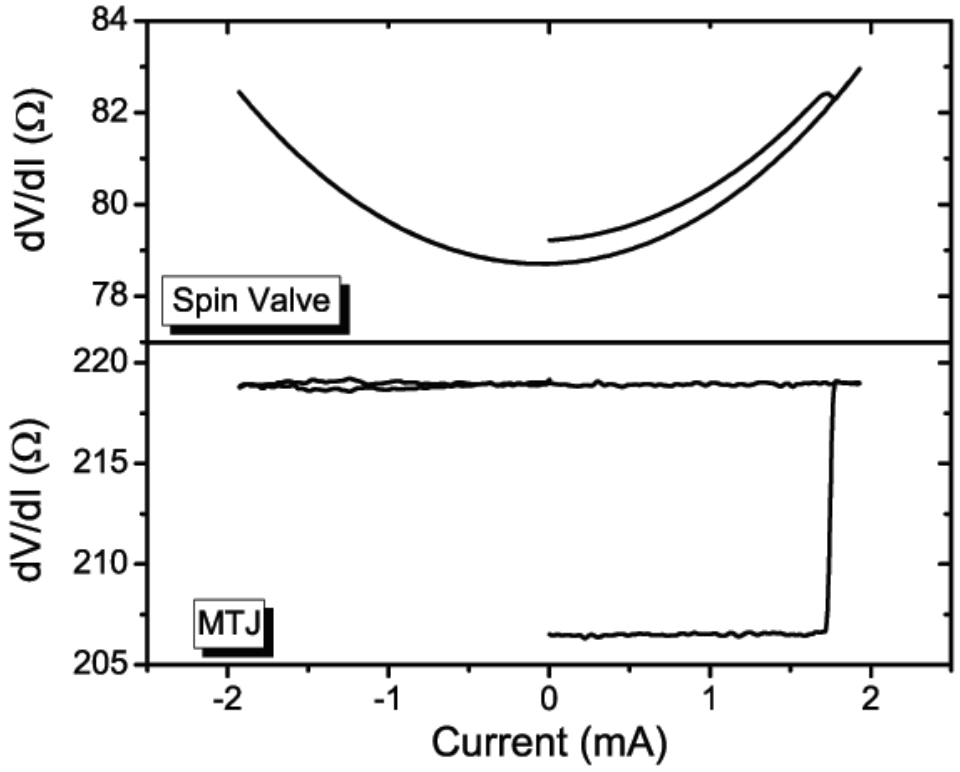

Figure 7.25: Current vs. resistance measured simultaneously for the SV/MTJ. Due to the large currents required for reversal in this structure, RL2 becomes reversed prior to free layer reversal, and so reversal is only observed in one direction.

is equal to the magnetoresistance change observed by sweeping the field, which confirms that the spin torque effect reverses the entire free layer, as predicted by the micromagnetic simulation, and does not result in the formation of a stable domain wall in the free layer, which would result in an intermediate resistance level in the MTJ. We were not able to reverse the spin valve device configuration from the P-to-AP state by flowing current in the positive direction (electrons from free layer to RL2) due to the fact that before the critical current was reached, the circumferential Oersted field acting on RL2 due to the applied current became strong enough to overcome the exchange pinning field from the top IrMn layer and drive the magnetization of the approximately square RL2 into a vortex state. The spin-polarized current generated from such a reference layer configuration is insufficient for reversing the free layer, since spin torques exerted in different spatial regions tend to cancel each other out. The formation of the vortex state occurs because the reversal currents required in the full 3-terminal structures are considerably larger than observed in the isolated SV structure measured in Fig. 7.23. We attribute this difference to an over milling of the isolation trench in the isolated SV structure, resulting in a thinner NiFe channel connecting the left and right ends of the free layer than in the full three-terminal device. As a result, the resistance of the isolated SV structure is found to be $\sim$40% larger than the SV component of the full 3-terminal device, as seen in comparing Fig. 7.25 to Fig. 7.23. We expect thermal effects to play a more significant role in reducing switching currents for the isolated SV structures due to the higher device resistance and lack of a bottom electrode to conduct away heat. This partially etched trench also weakens the net exchange coupling between free layer material under the spin valve contact and the rest of the free layer, which, as indicated by our micromagnetic modeling, can substantially reduce the switching current required to nucleate and

propagate the domain wall in the isolated SV.

7.4 Summary

In conclusion, we have demonstrated a fabrication concept for inserting a third electrode into a nanopillar device, where contact can be made to any layer within the pillar. Fabrication of these devices has allowed us to study a method of spin transfer reversal by nonuniform current injection into the edge of the magnetic free layer. We find that spin transfer mediated by polarized electrons incident on the interface of the free layer dominates reversal by first nucleating a domain under the contact region, and then exerting pressure via the exchange field on the resulting domain wall, forcing it to propagate and complete the reversal. Spin torque from the spin current traveling laterally through the free layer appears to have minimal effect on the reversal process. Free layer reversal initiated by injecting current through the SV can be detected by the resultant resistance change in the MTJ, allowing for a spin transfer writing scheme with a large TMR signal, without tunnel barrier wear-out issues. Further optimization of this system requires enhancing the resistance of the top reference layer RL2 to spin torque effects by increasing its thickness and/or enhancing its exchange bias pinning, fabricating the MTJ with a higher, more appropriate resistance, $\geq 3000\Omega$ that impedance matches a CMOS sense transistor, while choosing the free layer material, thickness, and any trench etch depth so as to minimize the spin valve reversal currents while maintaining good thermal stability. Regardless, we have shown that this 3-T structure offers exiting new opportunities for examining physical effects in magnetic systems, while also providing a possible architecture for future high performance, high speed ST-MRAM applications.

This system offers a wealth of possible opportunities for both applications and basic research. Local injection of spin current into the edge of the nanopillar has been shown to create a domain wall, which could possibly be utilized as a write mechanism for magnetic racetrack memory [20], replacing proposed field writing strategies. Coupling of magnetic and superconducting structures, such as Josephson junctions, could open pathways to novel low power, high density, low temperature memories. Finally, coupling of MTJ devices could advance research in tunnel junctions by creating opportunities for studying various voltage bias effects.

REFERENCES

[1] Slaughter J.M., Dave R.W., DeHerrera M., Durlam M., Engel B.N., Janesky J., Rizzo N.D., & Tehrani S., Fundamentals of mram technology, *Journal of Superconductivity: Incorporating Novel Magnetism* **15**, 19 (2002).

[2] http://http://media.freescale.com/phoenix.zhtml?c=196520&p=irol-newsArticle&ID=880030&highlight=MRAM

[3] Fuchs G.D., Emley N.C., Krivorotov I.N., Braganca P.M., Ryan E.M., Kiselev S.I., Sankey J.C., Ralph D.C., Buhrman R.A., Katine J.A., Spin-transfer effects in nanoscale magnetic tunnel junctions, *Appl. Phys. Lett.* **85**, 1205 (2004).

[4] Huai Y.M., Albert F.J., Nguyen P., Pakala M., Valet T., Observation of spin-transfer switching in deep submicron-sized and low-resistance magnetic tunnel junctions, *Appl. Phys. Lett.* **84**, 3118 (2004).

[5] Slonczewski, J.C., Electronic device using magnetic component, *U.S. Patent No.* 5,695,864 (Dec. 9, 1997).

[6] Slonczewski J.C, Exchange-driven magnetic excitation and integrated magnetoelectronics, *unpublished* (1999).

[7] Emley N.C., Ph.D. thesis, Cornell University (2005).

[8] Kimura T., Otani Y., Hamrle J., Switching magnetization of a nanoscale ferromagnetic particle using nonlocal spin injection, *Phys. Rev. Lett.* **96**, 037201 (2006).

[9] Braganca P.M., Krivorotov I.N., Ozatay O., Garcia A.G.F., Emley N.C., Sankey J.C., Ralph D.C., & Buhrman R.A., Reducing the critical current for short-pulse spin-transfer switching of nanomagnets, *Appl. Phys. Lett.* **87**, 112507 (2005).

[10] Braganca P.M., Ozatay O., Garcia A.G.F., Lee O.J., Ralph D.C., & Buhrman R.A., Enhancement in spin-torque efficiency by nonuniform spin current generated within a tapered nanopillar spin valve, *Phys. Rev. B* **77**, 144423 (2008).

[11] Childress J.R., Carey M.J., Cyrille M.-C., Carey K., Smith N., Katine J.A., Boone T.D., Driskill-Smith A.A.G., Maat S., Mackay K., & Tsang C.H., Fabrication and recording study of all-metal dual-spin-valve CPP read heads, *IEEE Trans. Magn.* **42**, 2444 (2006).

[12] Donahue M.J & Porter D.G., *OOMMF User's Guide, Version 1.0*, *Technical Report No.* NISTIR 6376 (National Institute of Standards and Technology, Gaithersburg, MD, 1999).

[13] Xiao J., Zangwill A., & Stiles M.D., Boltzmann test of Slonczewskis theory of spin-transfer torque, *Phys. Rev. B* **70**, 172405 (2004).

[14] Freita P.P. & Berger L., Observation of s-d exchange force between domain walls and electric current in very thin permalloy films, *J. Appl. Phys.* **57**, 1266 (1985).

[15] Hung C.Y. & Berger L., Exchange forces between domain wall and electric current in permalloy films of variable thickness, *J. Appl. Phys.* **63**, 4276 (1988).

[16] Hayashi M., Thomas L., Bazaliy Y.B, Rettner C., Moriya R., Jiang X., & Parkin S.S.P., Influence of current on field-driven domain wall motion in permalloy nanowires from time resolved measurements of anisotropic magnetoresistance, *Phys. Rev. Lett.* **96**, 197207 (2006).

[17] Li Z. & S. Zhang, Domain-wall dynamics and spin-wave excitations with spin-transfer torques, *Phys. Rev. Lett.* **92**, 207203 (2004).

[18] Li Z. & S. Zhang, Domain-wall dynamics driven by adiabatic spin-transfer torques, *Phys. Rev. B* **70**, 024417 (2004).

[19] Berger L., Exchange interaction between ferromagnetic domain wall and electric current in very thin metallic films, *J. Appl. Phys.* **55**, 1954 (1984).

[20] Parkin S.S.P., Hayashi M., & Thomas L., Magnetic domain-wall racetrack memory , *Science* **320**, 190 (2008).

CHAPTER 8

CONCLUSION

In this thesis, I have discussed magnetic nanostructures designed to maximize spin transfer effects, most notably current induced magnetization reversal for applications in magnetic memory (MRAM). One particular strategy involves the use of low saturation magnetization M_s ferromagnets for the free layer electrodes [1], which theory [2, 3] has predicted to reduce spin transfer critical currents I_c. I chose to examine spin transfer reversal in nanopillars with low M_s NiFe alloys as the ferromagnetic electrodes, using both DC and nanosecond width current pulses. These results are summarized in Chapter 4, where I found that by patterning these nanomagnets into high aspect-ratio elliptical patterns with small areas, the current required for both DC and pulsed current switching could be reduced substantially compared to similar experiments using Co [4–7] electrodes. By varying the thickness of the free layer electrode, I found that the thermal stability of the free layer could be maximized while still maintaining a low switching current, indicating that this could be an enabling strategy for MRAM applications. Comparisons of switching currents required for slow DC current ramps to the current amplitudes necessary for nanosecond pulses indicate that there are two regimes for spin transfer reversal, one for switching times above $\sim$ 10 ns in which stochastic thermal fluctuations act to assist magnetization reversal and lower the switching currents, and one for shorter times, where the current amplitude must be 4-5$\times$ that required for DC reversal as the oscillation period of the magnetization must be greatly increased by the spin torque to ensure it reaches a large enough precession amplitude to reverse during the duration of the current pulse. This verifies that extrapolations of fast switching currents ($\sim$ ns) from slow current ramp data is an inaccurate method of determining these parameters. Finally, macrospin simu-

lation results compared to our experimental results show that the symmetry of the switching currents for AP-P and P-AP reversal are more symmetric than predicted by current spin transfer models [2, 8], requiring us to modify the expression for the angular dependence of the spin torque. From these simulations, we have also found values for the Gilbert damping parameter α to be on the order of 0.03, in reasonable agreement with the results of other experimental studies of patterned Py/Cu/Py nanopillars [9, 10]. Future experiments could be undertaken to examine other low M_s alloys for fast nanosecond magnetization reversal, as well as the examination of patterned shapes other than ellipses, which may further help to boost magnetic anisotropy without increasing I_c. Materials with even lower values for M_s, while not acceptable for room temperature applications, could be useful for low T memory, as kT becomes much smaller, requiring lower anisotropy values for the nanomagnet. Finally, the integration of these low M_s materials into MgO tunnel junctions, while not a trivial exercise, would be extremely beneficial for memory applications.

Another strategy that I have studied and discussed in Chapter 5 involved examining micromagnetic reversal mechanisms excited in Py free layers [11]. Here, I found that the spatially nonuniform demagnetization field of the free layer in these nanopillars lowered I_c at the edges of the free layer, exciting magnetization oscillations locally there that grow in amplitude and drag the center of the nanomagnet into reversal. Surprisingly enough, by comparing micromagnetic simulations to macrospin results modeling the same free layer nanomagnet, this micromagnetic reversal switches faster at lower currents than a uniform reversal. Further enhancement in spin transfer reversal is obtained by tapering the reference layer of the nanopillar, which generates a spatially nonuniform spin current with a spin polarization component polarized partially out of the film plane. Both simulations

and experimental results verify that this tapered pillar structure enhances the effect of the spin torque acting upon the free layer and strongly reduces the current amplitudes required for fast nanosecond magnetization reversal. The curled reference layer magnetization state also affects spin accumulation in the Cu spacer layer and leads to very symmetric reversal currents, which are beneficial for the memory application previously mentioned. This experimental strategy could be carried even further by combining these micromagnetic effects with enhancements generated using a second reference layer oriented antiparallel to the first [12], which should double the torque acting on the free layer. Furthermore, it is likely that other micromagnetic reversal modes could exist caused by different geometric or material considerations. These modes could add additional enhancement to those mentioned in this thesis, and continued exploration of micromagnetic simulations could assist in the discovery of these modes.

Spin transfer enhancements in these tapered nanopillars are not limited to reversal phenomena, as there is a wide range of magnetization dynamics effects excited in these structures, as described in Chapter 6. Out of plane magnetization curling of the reference layer give rise to magnetization oscillations at the edges of this layer, even in the absence of a magnetic field, making these structures extremely useful for on-chip spin torque oscillator (STO) applications, especially since their integrated powers and oscillation frequencies are larger than other structures with similar field characteristics [13–15]. Additional enhancement of the RF output signal occurs with the application of a small hard axis magnetic field, which drives the oscillation frequency of the reference layer into a value roughly $2\times$ the frequency of the free layer. This leads to a phase locking effect known as parametric amplification, resulting in an output signal with large integrated powers (> 100 pW) with linewidths on the order of 1 MHz. Although analysis of these effects

is still ongoing, they verify that the nanopillar can be designed in such a way to create a feedback loop between the free and reference layers, causing phase locking that acts to stabilize the magnets against temperature effects that broaden the linewidth. These enhancements could also be easily incorporated into magnetic tunnel junctions to output huge integrated powers.

Finally, in Chapter 7 I discussed a concept for a three terminal nanopillar structure building on the previous work of Nathan Emley from this group. This device consists of a spin valve and a magnetic tunnel junction (MTJ) sharing a common free layer, such that current can be sent through the spin valve to switch the free layer using spin transfer, and the free layer magnetic state can be detected by reading the resistance of the MTJ. In this manner, we can avoid barrier breakdown effects occurring from biasing MTJs directly for spin transfer writing. Micromagnetic simulations of our device concept indicate that free layer reversal occurs through nucleation of a reversal domain underneath the top electrode of the spin valve and then nucleation of a domain wall across the free layer due to exchange pressure. Fabricated devices exhibit free layer reversal by passing a current through the spin valve, and simultaneous detection by the MTJ, but only AP-P reversal is seen due to an instability in the reference layer at the larger currents necessary for P-AP reversal. Further development is required to optimize this structure for practical applications, but these results verify proof of concept for this design. Additional uses for this device configuration may involve coupling a spin valve or a MTJ with a superconductor device such as a Josephson junction, or a semiconductor structure such as a quantum well.

In closing, the results in this thesis have illustrated the wealth of phenomena that can be explored with spin transfer merely by changing the materials or the

geometric design of a nanopillar device. Significant efforts in improving the micromagnetic simulations have definitely paid off and I strongly encourage future students to take advantage of these simulations as a means of quantifying mechanisms of reversal or dynamics in these systems. I look forward to following the progress of the group for years to come, as I continue my professional journey.

REFERENCES

[1] Braganca P.M., Krivorotov I.N., Ozatay O., Garcia A.G.F., Emley N.C., Sankey J.C., Ralph D.C., & Buhrman R.A., Reducing the critical current for short-pulse spin-transfer switching of nanomagnets, *Appl. Phys. Lett.* **87**, 112507 (2005).

[2] Slonczewski J.C., Current-driven excitation of magnetic multilayers, *J. Magn. Magn. Mater* **159**, L1 (1996).

[3] Sun J.Z., Spin-current interaction with a monodomain magnetic body: A model study, *Phys. Rev. B* **62**, 570 (2000).

[4] Katine J.A, Albert F.J., Buhrman R.A., Myers E.B., & Ralph D.C., Current-driven magnetization reversal and spin-wave excitations in Co/Cu/Co pillars, *Phys. Rev. Lett.* **84**, 3149 (2000).

[5] Albert F.J., Emley N.C., Myers E.B., Ralph D.C., & Buhrman R.A., Quantitative study of magnetization reversal by spin-polarized current in magnetic multilayer nanopillars, *Phys. Rev. Lett* **89**, 226802 (2002).

[6] Kaka S., Pufall M.R., Rippard W.H., Silva T.J., Russek S.E., Katine J.A., & Carey M., Spin transfer switching of spin valve nanopillars using nanosecond pulsed currents, *J. Magn. Magn. Mater.* **286**, 375 (2005).

[7] Devolder T., Tulapurkar A., Yagami K., Crozat P., Chappert C., Fukushima A., & Suzuki Y., Ultra-fast magnetization reversal in magnetic nano-pillars by spin-polarized current, *J. Magn. Magn. Mater.* **286**, 77 (2005).

[8] Xiao J., Zangwill A., & Stiles M. D., Boltzmann test of Slonczewski's theory of spin-transfer torque, *Phys. Rev. B* **70**, 172405 (2004).

[9] Krivorotov I.N., Emley N.C., Garcia A.G.F., Sankey J.C., Kiselev S.I., Ralph D.C., & Buhrman R.A., Temperature dependence of spin-transfer-induced switching of nanomagnets, *Phys. Rev. Lett* **93**, 166603 (2004).

[10] Emley N.C., Krivorotov I.N., Garcia A.G.F., Ozatay O., Sankey J.C., Ralph D.C., & Buhrman R.A., Time-resolved spin torque switching and enhanced damping in Py/Cu/Py spin-valve nanopillars, *Phys. Rev. Lett.* **96**, 247204 (2006).

[11] Braganca P.M., Ozatay O., Garcia A.G.F., Lee O.J., Ralph D.C., & Buhrman R.A., Enhancement in spin-torque efficiency by nonuniform spin current generated within a tapered nanopillar spin valve, *Phys. Rev. B* **77**, 144423 (2008).

[12] Fuchs G.D., Krivorotov I.N., Braganca P.M., Emley N.C., Garcia A.G.F., Ralph D.C., & Buhrman R.A., Adjustable spin torque in magnetic tunnel junctions with two fixed layers, *Appl. Phys. Lett.* **86**, 152509 (2005).

[13] Pribiag V.S., Krivorotov I.N., Fuchs G.D., Braganca P.M., Ozatay O., Sankey J.C., Ralph D.C., & Buhrman R.A., Magnetic vortex oscillator driven by d.c. spin-polarized current, *Nat. Phys.* **3**, 498 (2007).

[14] Pufall M.R., Rippard W.H., Schneider M.L., & Russek S.E., Low-field current-hysteretic oscillations in spin-transfer nanocontacts, *Phys. Rev. B* **75**, 140404 (2007).

[15] Boulle O., Cros V., Grollier J., Pereira L.G., Deranlot C., Petroff F., Faini G., Barnas J., & Fert A., Shaped angular dependence of the spin-transfer torque and microwave generation without magnetic field, *Nature Phys.* **3**, 492 (2007).